REVERSE TIME IMAGING IN SOLID EARTH AND EXPLORATION GEOPHYSICS

EDITED BY: Hua-Wei Zhou, Wei Zhang, Qinya Liu, Zhihui Zou and Hao Hu
PUBLISHED IN: Frontiers in Earth Science

frontiers Research Topics

ISSN 1664-8714
ISBN 978-2-88976-433-4
DOI 10.3389/978-2-88976-433-4

About Frontiers

Frontiers is more than just an open-access publisher of scholarly articles: it is a pioneering approach to the world of academia, radically improving the way scholarly research is managed. The grand vision of Frontiers is a world where all people have an equal opportunity to seek, share and generate knowledge. Frontiers provides immediate and permanent online open access to all its publications, but this alone is not enough to realize our grand goals.

Frontiers Journal Series

The Frontiers Journal Series is a multi-tier and interdisciplinary set of open-access, online journals, promising a paradigm shift from the current review, selection and dissemination processes in academic publishing. All Frontiers journals are driven by researchers for researchers; therefore, they constitute a service to the scholarly community. At the same time, the Frontiers Journal Series operates on a revolutionary invention, the tiered publishing system, initially addressing specific communities of scholars, and gradually climbing up to broader public understanding, thus serving the interests of the lay society, too.

Dedication to Quality

Each Frontiers article is a landmark of the highest quality, thanks to genuinely collaborative interactions between authors and review editors, who include some of the world's best academicians. Research must be certified by peers before entering a stream of knowledge that may eventually reach the public - and shape society; therefore, Frontiers only applies the most rigorous and unbiased reviews.
Frontiers revolutionizes research publishing by freely delivering the most outstanding research, evaluated with no bias from both the academic and social point of view. By applying the most advanced information technologies, Frontiers is catapulting scholarly publishing into a new generation.

What are Frontiers Research Topics?

Frontiers Research Topics are very popular trademarks of the Frontiers Journals Series: they are collections of at least ten articles, all centered on a particular subject. With their unique mix of varied contributions from Original Research to Review Articles, Frontiers Research Topics unify the most influential researchers, the latest key findings and historical advances in a hot research area! Find out more on how to host your own Frontiers Research Topic or contribute to one as an author by contacting the Frontiers Editorial Office: frontiersin.org/about/contact

REVERSE TIME IMAGING IN SOLID EARTH AND EXPLORATION GEOPHYSICS

Topic Editors:
Hua-Wei Zhou, University of Houston, United States
Wei Zhang, Southern University of Science and Technology, China
Qinya Liu, University of Toronto, Canada
Zhihui Zou, Ocean University of China, China
Hao Hu, University of Houston, United States

Citation: Zhou, H.-W., Zhang, W., Liu, Q., Zou, Z., Hu, H., eds. (2022). Reverse Time Imaging in Solid Earth and Exploration Geophysics.
Lausanne: Frontiers Media SA. doi: 10.3389/978-2-88976-433-4

Table of Contents

frontiers | Frontiers in Earth Science

EDITORIAL
published: 01 June 2022
doi: 10.3389/feart.2022.931127

Editorial: Reverse Time Imaging in Solid Earth and Exploration Geophysics

Hua-Wei Zhou[1], *Zhihui Zou*[2]*, *Wei Zhang*[3], *Qinya Liu*[4] *and Hao Hu*[1]

[1]Department of Earth and Atmospheric Sciences, University of Houston, Houston, TX, United States, [2]Key Lab of Submarine Geosciences and Prospecting Techniques MOE, College of Marine Geosciences, Ocean University of China, Qingdao, China, [3]Department of Earth and Space Sciences, Southern University of Science and Technology, Shenzhen, China, [4]Department of Physics and Department of Earth Sciences, University of Toronto, Toronto, ON, Canada

Keywords: reverse time imaging, reverse time imaging, reverse time migration, velocity model building, seismic imaging, imaging fidelity

Editorial on the Research Topic

Reverse Time Imaging in Solid Earth and Exploration Geophysics

BACKGROUND

Our knowledge of Earth's interior structures and properties has been based, for a significant portion, on findings in solid Earth and exploration geophysics. As likely the most popular geophysical tool, seismic imaging has been providing evidences for revealing the nature of Earth structure and geodynamics, for exploring natural resources such as water, petroleum, coal, and minerals, and for mitigating geohazards including land subsidence, landslides, earthquakes, volcanic eruptions, and tsunamis. To better live with the nature, we must balance human activities between taking natural resources and minimizing human impacts on the environment. High fidelity seismic images of Earth's interior are useful to all of these efforts.

MOTIVATION FOR THE TOPIC

Reverse time imaging (RTI) was conceptualized in 1980s as reverse time migration (RTM), to map reflectivity structures and seismic sources *via* modeling time reversed seismic waveforms. Constrained by the limited computing power in the past, RTI has not become a leading way of seismic imaging until this century. With the growing demands for high-fidelity seismic images, it is timely that we present some of the latest advances in RTI.

SUMMARY OF THE PAPERS

The modeling approach enables RTI to map a multitude of seismic sources that were excited in the same time span and at nearby locations, and allows RTM to take multiple scattering wavefields as signals rather than noises. Zhang et al. present here a least-squares RTM (LSRTM) using multiples of OBN data and suppressing crosstalk of multiple wavefields with numerical examples. Zheng et al. take surface multiples in a field walkaway VSP data as the input signal to RTM for monitoring CO_2 injection in NW China, *via* wavefield decomposition and an inverse scattering imaging condition. He et al. propose a P-SV converted-wave RTM *via* 1st-order velocity-dilatation rotation of multi-

OPEN ACCESS

Edited and reviewed by:
Valerio Acocella,
Roma Tre University, Italy

***Correspondence:**
Zhihui Zou
zhzou@126.com

Specialty section:
This article was submitted to Solid Earth Geophysics, a section of the journal Frontiers in Earth Science

Received: *28 April 2022*
Accepted: *12 May 2022*
Published: *01 June 2022*

Citation:
Zhou H-W Zou Z, Zhang W, Liu Q and Hu H (2022) Editorial: Reverse Time Imaging in Solid Earth and Exploration Geophysics. Front. Earth Sci. 10:931127. doi: 10.3389/feart.2022.931127

component data without the source information, and verify their approach *via* numerical simulations.

The versatility of RTI is demonstrated in several case studies of a variety of targets. Huang et al. apply an anisotropic LSRTM to map complex subsurface structures for accurate fault interpretation in geothermal exploration at the Pirouette Mountain and Eleven-Mile Canyon in Nevada. Wang et al. show vertical cable RTM images of hydrate-bearing sediments in South China Sea. Kim et al. present a new way of velocity model building *via* frequency-domain common image gather, and demonstrate it with field data from offshore SW Africa.

Most papers on this Research Topic have an element of improving RTI methodology, especially those focused on numerical studies. After verifying the Kirchhoff modeling is better than the Born modeling in LSRTM, Zhang et al. present an RTM with staggered-grid finite-difference velocity-stress wave equation in pseudo-space domain, to reduce the modeling error of finite-difference meshing. Xu et al. implement a Kirchhoff approximation in LSRTM with L_1 sparse constraint, using a 2D numerical demonstration. Du et al. show a pseudo-Laplace filter to reduce image artifact from using the dot-product scalar imaging condition in vector elastic RTM. Rong and Jia apply deep-learning to reduce the cost of computing the illumination of single-shot RTM, and show some 2D numerical test results. Xie et al. suggest a precondition of LSRTM *via* transmitted wave energy gradient, and test it with the Marmousi and Pluto models. In a second paper, these authors demonstrate an angle-weighted RTM using 2D numerical test and a marine seismic line in the East China Sea.

STATUS OF THE TOPIC

The common occurrence of imaging artifacts and position errors in seismic images based on field data inspires seismic imaging research toward high fidelity, which specifies how accurately each imaging target is resolved at the correct location. To achieve this goal, researchers are making low-frequency vibroseis sources, deploying dense and broadband seismic arrays, developing more advanced and effective numerical simulation algorithms to model seismic wave propagation under more realistic physical conditions, proposing more robust inversion and imaging methods for large volume datasets, and adapting artificial intelligent techniques into seismic imaging. Clearly, the expansion of seismic imaging from high resolution toward high fidelity is an exciting and challenging process. The challenges usually include limited quality and quantity of field data, and more importantly the lack of evidence for verifying imaged features. We expect more interdisciplinary studies to bring in independent evidences for cross checking and corroborating seismic images at processing and interpretation stages.

FUTURE PERSPECTIVES

The desire to better live with our mother Earth demands new ways to overcome the challenges for exploring its interior, and assessing the intricate relationship between our activities of extracting natural resources and the impacts on the environment. We hope the exemplary studies presented here can motivate new research in reverse time imaging, toward providing higher fidelity seismic images for a wider spectrum of applications.

AUTHOR CONTRIBUTIONS

Editorial written by HZ, edited, modified by all other guest editors.

Conflict of Interest: The authors declare that the research was conducted in the absence of any commercial or financial relationships that could be construed as a potential conflict of interest.

Publisher's Note: All claims expressed in this article are solely those of the authors and do not necessarily represent those of their affiliated organizations, or those of the publisher, the editors and the reviewers. Any product that may be evaluated in this article, or claim that may be made by its manufacturer, is not guaranteed or endorsed by the publisher.

frontiers in Earth Science

TECHNOLOGY AND CODE
published: 30 June 2021
doi: 10.3389/feart.2021.669686

Frequency-Domain Common Image Gathers for Quickly Checking the Accuracy of Migration Velocity

Haemin Kim[1], *Yongchae Cho*[2], *Yunseok Choi*[3], *Seungwon Ko*[4] *and Changsoo Shin*[1]*

[1]Department of Energy Resources Engineering, Seoul National University, Seoul, South Korea, [2]Shell International Exploration & Production Inc., Houston, TX, United States, [3]Korea Institute of Geoscience and Mineral Resources, Daejeon, South Korea, [4]Cocolink, Seoul, South Korea

The common image gather (CIG) method enables qualitative and quantitative evaluation of the velocity model through the image. The most common such methods are offset-domain common image gather (ODCIG) and angle-domain common image gather (ADCIG). The challenge is that it requires a great deal of additional computation besides migration. We, therefore, introduce a new CIG method that has low computational cost: frequency-domain common image gather (FDCIG). FDCIG simply rearranges data using a gradient (partial image) calculated in the process of obtaining a migration image to represent it in the frequency-depth domain. We apply the FDCIG method to the layered model to show how FDCIGs behave when the velocity model is inaccurate. We also introduced the 3-D SEG/EAGE salt model to show how to apply the FDCIG method in the hybrid domain. Last, we applied 2-D real data. These sample field data also indicate that even in a complex velocity model, deviant behavior by FDCIG appears intuitively if the background velocity is inaccurate.

Keywords: common image gather, frequency domain, reverse time migration, hybrid domain, acoustic

OPEN ACCESS

Edited by:
Hua-Wei Zhou,
University of Houston, United States

Reviewed by:
Yikang Zheng,
Institute of Geology and Geophysics (CAS), China
Bin He,
University of Toronto, Canada

***Correspondence:**
Changsoo Shin
cssmodel@snu.ac.kr

Specialty section:
This article was submitted to Solid Earth Geophysics, a section of the journal Frontiers in Earth Science

Received: *19 February 2021*
Accepted: *12 May 2021*
Published: *30 June 2021*

Citation:
Kim H, Cho Y, Choi Y, Ko S and Shin C (2021) Frequency-Domain Common Image Gathers for Quickly Checking the Accuracy of Migration Velocity. Front. Earth Sci. 9:669686. doi: 10.3389/feart.2021.669686

INTRODUCTION

Reverse time migration (RTM) produces a high-fidelity subsurface image from seismic data for identification of complex subsurface structures (Baysal et al., 1983; McMechan, 1983; Whitmore, 1983). It is more effective for resolving images of sharply dipping layers or the flank of a salt diapir than ray-based depth imaging. The RTM implementation in the time domain is often preferred due to its lower memory consumption than the frequency domain, and this is a critical factor in handling 3-D problems.

Calculating both wavefields and imaging conditions in the frequency domain nevertheless has advantages over time-domain implementation (Pratt, 1999; Wu and Alkhalifah, 2018). For example, we can easily divide the wavefields into multiple frequencies and acquire the wave solutions of multiple shots through a one-time matrix solving. In the frequency domain, we can also easily perform parallel computation since the frequency components are each independent of each other. In contrast, we need to consider the spatial domain decomposition scheme in the time domain. This is not a trivial task but is essential to facilitate communications between multiple computing processors (He et al., 2020). Also, in the frequency domain, we do not need to apply a reduced time-step to calculate the high frequency wave solutions. One can adjust the scaling of image conditions by applying the frequency-dependent inverse Hessian to obtain better illumination in the deeper part of the subsurface. In this study, we introduce one more

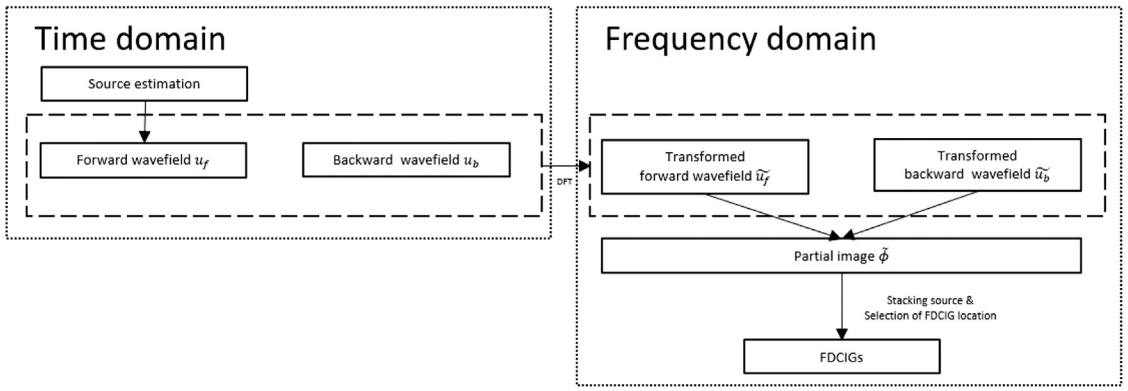

FIGURE 1 | Flowchart of getting FDCIG in hybrid domain. DFT means discrete Fourier transform.

advantage of utilizing the frequency domain, and, that is, efficient quality check called frequency-domain common image gather (FDCIG) for quick quality check of the migration velocity.

Ray theory–based migration such as Kirchhoff or Gaussian-beam migrations is more commonly used for acquiring CIGs in the offset domain due to its relatively low computing cost. However, the offset-domain CIGs often suffer kinematic artifacts (Nolan ad Symes, 1996; Xu et al., 2001; Stolk and Symes, 2004; Wang et al., 2016). This issue could be mitigated by employing angle-domain CIGs—a wave equation–based approach (Prucha et al., 1999; Sava and Fomel, 2003; Biondi and Symes, 2004; Stolk and Symes, 2004). Also cyclic skipping was solved using extended Born modeling, and the migration image was improved with angle-domain LSRTM which uses angle information (He et al., 2019).

Although the ADCIGs provide more reliable CIGs, they require additional operations such as Poynting (Yoon and Marfurt, 2006; Dickens and Winbow, 2011) or Cauchy condition–based polarization (Wang et al., 2016) vectors to calculate subsurface angle information. Also, the ADCIGs may not be suitable for the early stage of velocity model building, which requires repetitive migration for scenario-based model building. Sava and Fomel (2003) introduced a method for converting ODCIGs to ADCIGs in one-way wave equation migration. Hence, we might consider generating corresponding ODCIGs in RTM for obtaining CIGs to make strike a reasonable balance between the pros and cons of ODCIGs vs. ADCIGs; however, this task is nontrivial (Sava and Fomel, 2003; Etgen, 2012; Giboli et al., 2012). In addition, the conversion works efficiently in two dimensions but becomes exorbitantly expensive in three dimensions (Fomel, 2004). Bin He et al. (2019) introduced radon-domain CIGs, which eliminates the picking processes and automatically calculates the focus to obtain a fairly accurate background velocity model.

In this regard, we propose the FDCIG method which extracts CIGs as a function of frequencies (not offset or at an angle) for quick quality check of migration images (Shin and Ko, 2019).

In this study, we briefly summarize the theory of frequency-domain RTM, a means of calculating FDCIGs, and related post-processing flow. We shall demonstrate the FDCIGs using three different models: two synthetic and one of field data. First, we

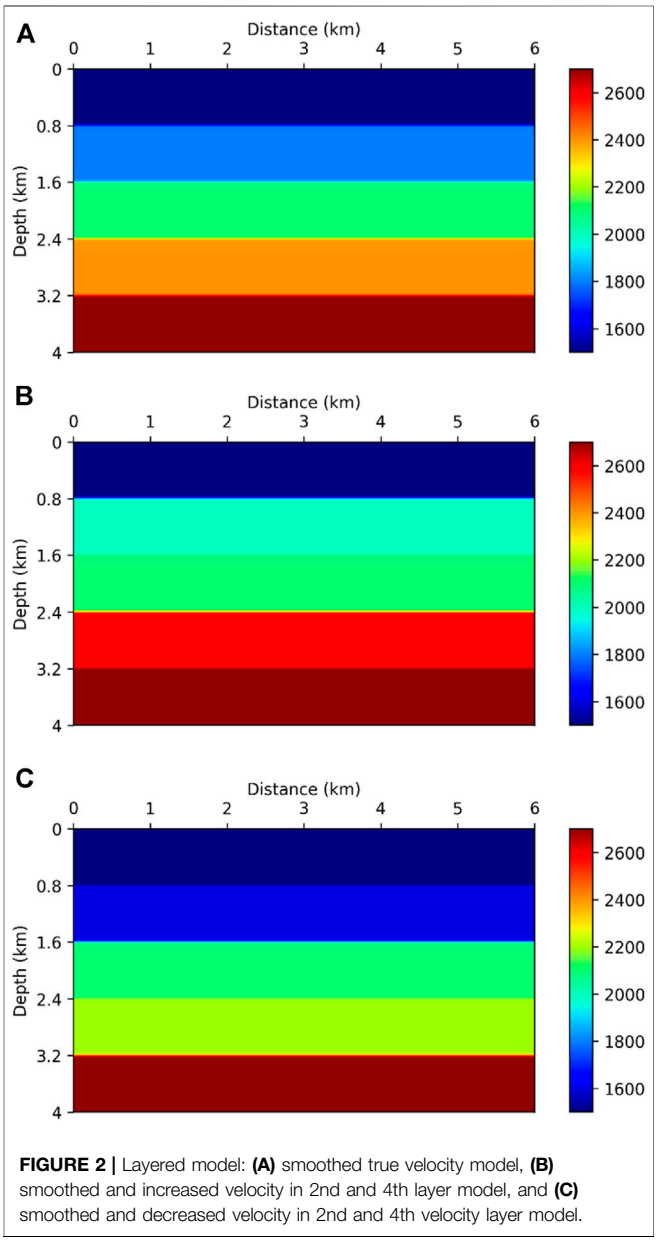

FIGURE 2 | Layered model: **(A)** smoothed true velocity model, **(B)** smoothed and increased velocity in 2nd and 4th layer model, and **(C)** smoothed and decreased velocity in 2nd and 4th velocity layer model.

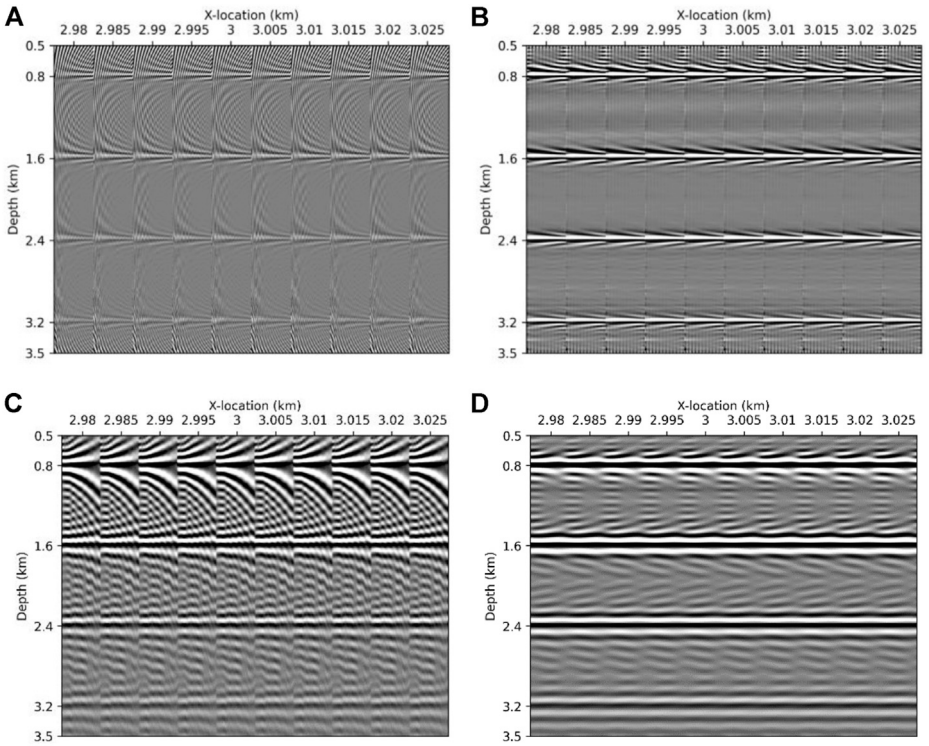

FIGURE 3 | Migration image of **(A)** smoothed true model, **(B)** smoothed and increased velocity in 2nd and 4th layer model, and **(C)** smoothed and decreased velocity in 2nd and 4th velocity layer model.

scrutinize the behavior of FDCIGs *via* a simple layer-cake model. Then, we apply hybrid-domain implementation to acquire the FDCIGs in the SEG/EAGE 3-D salt model. We show that the FDCIGs application is not limited by the domain of the wave simulations *via* this 3-D synthetic example. In the field data examples, we demonstrate how sensitive the FDCIGs are to the inherent noise of the field data.

METHODS

The key step of the proposed method is constructing image gathers along the frequency components. Note that we applied conventional frequency-domain imaging conditions (Pratt et al., 1998; Shin et al., 2003) as summarized below. An RTM image at the k-th model parameter, ϕ_k, can be expressed as a zero-lag cross-correlation between the partial derivative wavefields with respect to the k-th model parameter $\frac{\partial u}{\partial m_k}$ and the measured data vector $\mathbf{d}$ in the time domain (Shin et al., 2003):

$$\phi_k(x) = \sum_{s=1}^{n_s} \int_0^{T_{\max}} \left(\frac{\partial \mathbf{u}_s}{\partial m_k}\right)^T \mathbf{d}_s dt, \tag{1}$$

where s indicates the shot number, T_{max} is the maximum record length, and T is the transpose of the vector. In the frequency domain, ϕ_k can be expressed using the Fourier transform pairs as follows:

$$\phi_k(\boldsymbol{x}) = \sum_{s=1}^{n_s} \int_0^{\omega_{max}} Re\left[\left(\frac{\partial \tilde{\boldsymbol{u}}_s}{\partial m_k}\right)^{\mathrm{T}}\right] \tilde{\boldsymbol{d}}_s^* d\omega, \tag{2}$$

where ω is the angular frequency, the superscript * denotes the complex conjugate, *Re* indicates the real part of a complex value, and the tildes above **u** and **d** indicate that they have been Fourier transformed.

Wave simulations in the frequency domain can be expressed in matrix form (Marfurt, 1984) as follows:

$$\mathbf{S}\tilde{\mathbf{u}}_s = \mathbf{f}, \tag{3}$$

where **S** denotes a complex impedance matrix and **f** means a source vector. One can calculate partial derivative wavefield $\frac{\partial \tilde{\mathbf{u}}_s}{\partial m_k}$ by using a virtual source term $\mathbf{f}_v$ (Pratt et al., 1998) as shown below.

$$\mathbf{S}\frac{\partial \tilde{\mathbf{u}}_s}{\partial m_k} + \frac{\partial \mathbf{S}}{\partial m_k}\tilde{\mathbf{u}}_s = 0, \tag{4}$$

which can be rewritten as

$$\frac{\partial \tilde{\mathbf{u}}_s}{\partial m_k} = \mathbf{S}^{-1}\mathbf{f}_v, \left(\mathbf{f}_v = -\frac{\partial \mathbf{S}}{\partial m_k}\tilde{\mathbf{u}}_s\right), \tag{5}$$

By replacing the partial derivative wavefield term in **Equation 2** with the virtual source shown in **Eq. 5**, we obtain the imaging conditions using the zero-lag cross-correlation between the virtual source and the back-propagated field data:

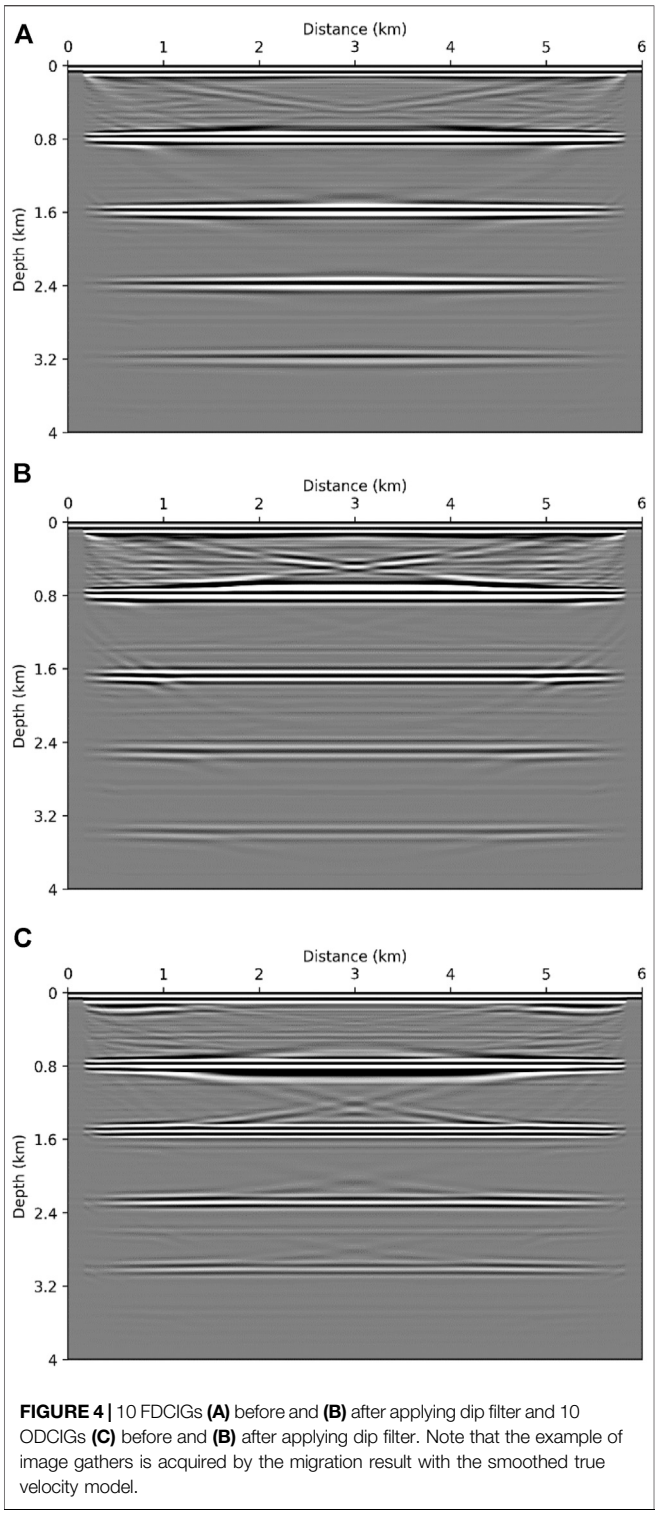

FIGURE 4 | 10 FDCIGs **(A)** before and **(B)** after applying dip filter and 10 ODCIGs **(C)** before and **(B)** after applying dip filter. Note that the example of image gathers is acquired by the migration result with the smoothed true velocity model.

$$\phi_k(\mathbf{x}) = \sum_{s=1}^{n_s} \int_0^{\omega_{max}} Re\left[\mathbf{f}_v^{\mathrm{T}} \left(\mathbf{S}^{\mathrm{T}}\right)^{-1} \tilde{\mathbf{d}}_s\right] d\omega, \tag{6}$$

Because $\mathbf{f}_v$ corresponds to the interaction between forward modeled wavefields and the kinematic properties of the k-th model parameter (Pratt et al., 1998), ϕ_k in the above equation can be viewed as the stacking result of various seismic events sharing the same position m_k. By considering all of the model parameters, the virtual source vector can be replaced with the virtual source matrix F_v. Then, **Eq. 6** can be rewritten as follows:

$$\begin{aligned}\phi(\mathbf{x}) &= \int_0^{\omega_{max}} \widehat{\phi}(\omega, \mathbf{x}) d\omega \\ &= \int_0^{\omega_{max}} \sum_{s=1}^{n_s} Re\left[\mathbf{F}_v^{\mathrm{T}} \left(S^{\mathrm{T}}\right)^{-1} \tilde{\mathbf{d}}_s^*\right] d\omega, \end{aligned} \tag{7}$$

where $\widehat{\phi}(\omega, \mathbf{x})$ are the partial images with various frequencies used for imaging. The time-domain expression of **Eq. 7** can be given as:

$$\phi(\mathbf{x}) = \int_0^{\infty} \mathbf{u}_b(\mathbf{x}, \tau - t) \mathbf{u}_f(\mathbf{x}, \tau) d\tau, \tag{8}$$

where subscript $_{\mathrm{f}}$ and $_{\mathrm{b}}$ denote the forward and backward propagation of the wavefield $\mathbf{u}$.

The Fourier transform of **Eq. 8** can be written as

$$\phi(\mathbf{x}, \omega) = \int_{-\infty}^{\infty} \mathbf{u}_b(\mathbf{x}, t) e^{-i\omega t} dt \int_{-\infty}^{\infty} \mathbf{u}_f(\mathbf{x}, \tau) e^{-i\omega\tau} d\tau, \tag{9}$$

During the time-domain RTM, we compute both the discrete Fourier transform of the backward propagated wavefield and the forward wavefield at a given frequency from minimum frequency to maximum frequency in an interval Δf. Then, we multiply the DFT of the back-propagated wavefield to the DFT of the forward modeled data and take a real part of the above multiplication result, writing a migration image to computer storage at each frequency as a function of frequency. Indeed, we need a huge volume of memory to save both Fourier transformed wavefields: back-propagated and forward modeled data.

By classical migration approaches, we acquire the final migration image by applying **Eq. 7**, which stacks all the images along the entire source-receiver pairs and corresponding frequency components. We propose a novel tool, the so-called FDCIG, for effortless quality check of migration velocity before building the final images; we extract $\omega - z$ sections at selected spatial locations $\mathbf{x}_i = (x_i, y_i)$ as follows:

$$\phi_{\mathbf{x}_i}(\omega, z) = \sum_{s=1}^{n_s} Re\left[\mathbf{F}_v^{\mathrm{T}}(\mathbf{x}_i, z, \omega) \left(\mathbf{S}^{\mathrm{T}}(\mathbf{x}_i, z, \omega)\right)^{-1} \tilde{\mathbf{d}}_s^*(\mathbf{x}_i, z, \omega)\right] d\omega. \tag{10}$$

By interpreting the frequency-oriented common image gathers, we can quickly check the quality of background velocity. Note that the repetitive forward and inverse Fourier transform might generate wrapping artifacts in the image gathers. If the wrapping noise renders target residual move-out difficult to investigate, one can consider applying a dip filter to suppress these artifacts.

As mentioned above, there are a number of advantages to constructing migration images in the frequency domain. However, the high cost of computation is a big hurdle especially when we handle 3-D seismic volume. In this case, one can consider performing wave simulation in the time domain and apply Fourier transform to calculate imaging conditions in

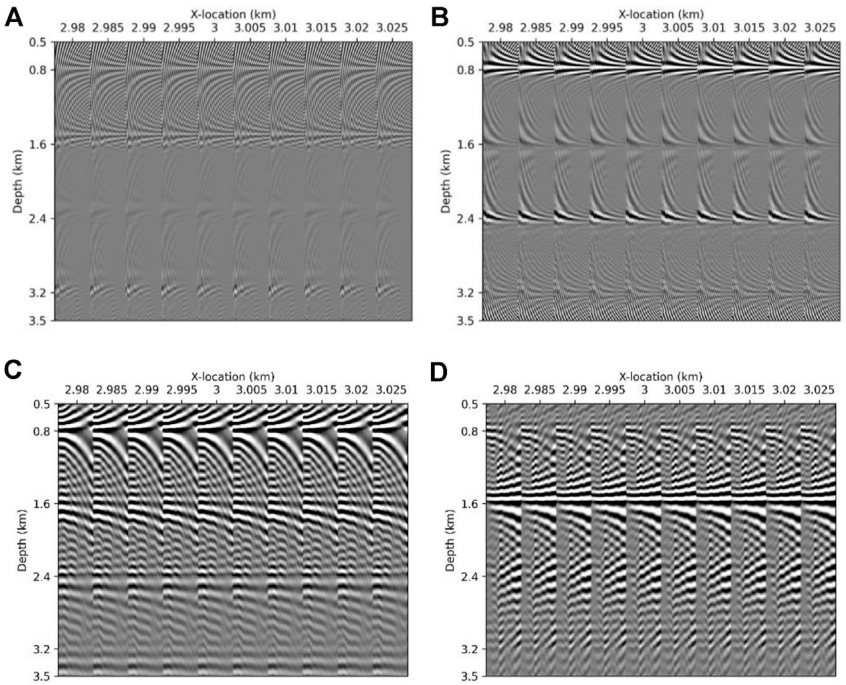

FIGURE 5 | 10 FDCIGs and 10 ODCIGs of **(A)** and **(C)** smoothed and increased 2nd and 4th layer model and **(B)** and **(D)** Smoothed and decreased 2nd and 4th layer model, respectively. Each *x*-axis of FDCIG **(A)** and **(B)** is frequency, ranged from 3 to 20 Hz and that of ODCIG **(C)** and **(D)** is offset, ranged from 100 to 2,800 m.

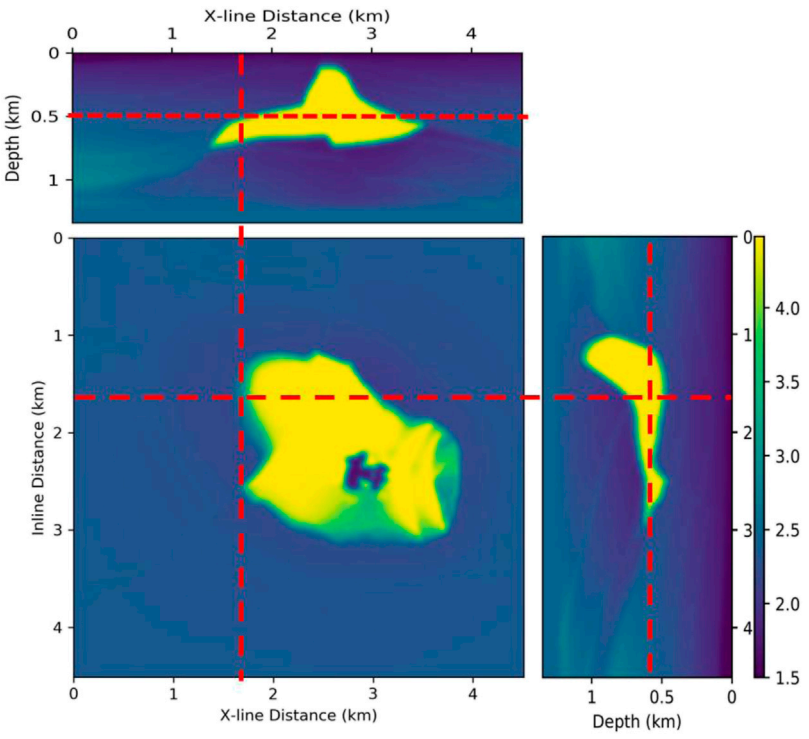

FIGURE 6 | Slices of the P-velocity model of SEG/EAGE 3-D salt model.

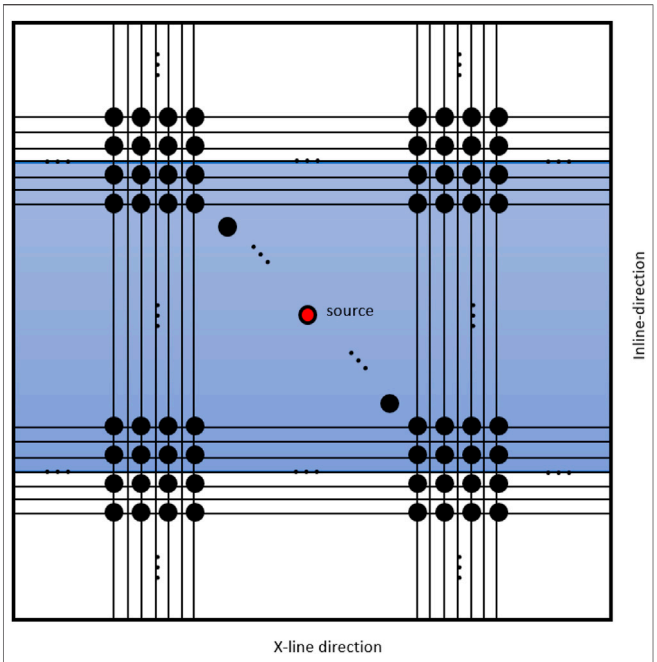

FIGURE 7 | Schematic sketch of the acquisition geometry. Black dots are sources. Blue box shows receivers corresponding to red dot (source).

the frequency domain. Given that the conventional approach (i.e., subsurface angle gather) requires a huge volume of storage capacity, we expect that the FDCIGs can help reduce the computing cost of acquiring image gathers.

The flowchart of the hybrid-domain CIGs is presented in **Figure 1**, where the hybrid domain means that we perform wave simulations in the time domain and then calculate the RTM imaging condition in the frequency domain. This allows us to avoid heavy memory consumption when obtaining solutions of the Helmholtz equation and to take advantage of the frequency-domain imaging. Note that the FDCIGs are constructed between the shot-by-shot imaging condition calculation and the construction of a final migration image without performing any additional operation.

NUMERICAL EXAMPLES

We shall demonstrate the proposed image gathers *via* three different numerical examples: 1) a layered model, 2) a SEG/EAGE 3-D salt model, and 3) 2-D real data. In the layered model, we first show how the FDCIG behaves when the background velocity is inaccurate. When investigating the FDCIGs, the wrapping noise generated by the inverse Fourier transform often hinders investigation of move-out of the reflectors. Therefore, we also briefly explain the post-processing of the FDCIGs using the simple synthetic model. To demonstrate that the proposed method is not limited by the computer memory capacity to store the entire impedance matrix for solving the Helmholtz equation, we show the numerical examples using the SEG/EAGE 3-D salt model by means of

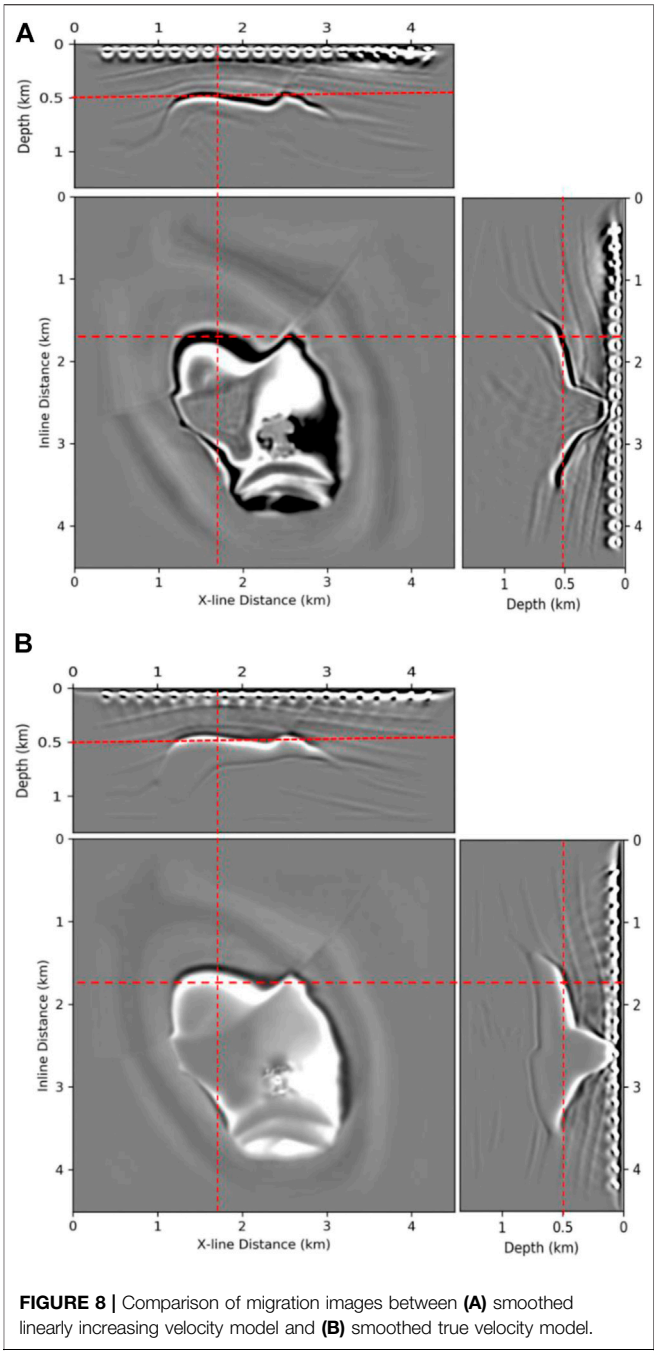

FIGURE 8 | Comparison of migration images between **(A)** smoothed linearly increasing velocity model and **(B)** smoothed true velocity model.

hybrid-domain approaches. Put differently, we can still use time-domain wave modeling schemes to calculate the frequency-domain imaging conditions with corresponding FDCIGs. In the field data examples, we test the robustness of the proposed method using the 2-D real dataset, which also shows the behavior of the CIGs associated with the inherent data noise. Additionally, ODCIG method was used as a comparison for 2-D synthetic and real data to demonstrate the effectiveness of FDCIG method. To obtain the ODCIGs, we calculated imaging conditions at each offset point and merged them in the last step. The computational cost was too high to make

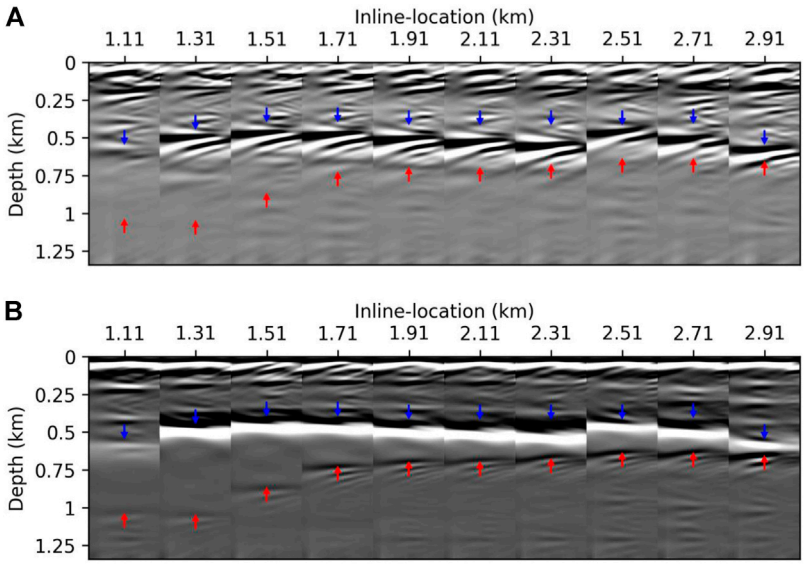

FIGURE 9 | Comparisons of ten FDCIGs spliced between **(A)** linearly increasing velocity model and **(B)** smoothed true velocity model. Each FDCIG has frequency range from 3 to 40 Hz. Blue and red arrows indicate the location of the actual salt top and bottom, respectively.

ODCIGs for all offsets, so the offsets were grouped in units of 100 m.

Simple Synthetic Example: Layered Model

We used the finite element method to calculate the wave solutions in the frequency domain in accordance with Marfurt (1984)'s discretization scheme. To generate the synthetic dataset, we used a 5 m spatial grid size, a frequency range is from 3 to 20 Hz, and a frequency interval of 0.1 Hz. We applied free surface at the top boundary of the model and the PML boundary condition for the other side of the model boundaries. The sources and receivers are located at the 4th grid point (20 m) from the model top in the 5 m interval. The layered model (6 × 4 km) is presented in **Figure 2**. To observe the move-out of the reflectors in FDCIGs, we perturbed the velocity of the 2nd and 4th layers. **Figures 2B,C** show the 200 m/s increased and 200 m/s decreased velocity model, respectively. We applied 20 m smoothing in both the x- and y-direction before performing RTM. Also, to obtain ODCIGs, RTM was performed by limiting and grouping the offset. There are 28 offset groups that are from 100 to 2,900 m at interval 100 m.

Figure 3 exhibits the corresponding RTM images of the velocity model shown in **Figure 2**. The correct depths of the reflectors are 800, 1,600, 2,400, and 3,200 m. Observing the migration image generated by using the true velocity model (**Figure 3A**), all the reflectors are resolved at the right locations of the layer interfaces. In contrast, when the background velocity is inaccurate, the images are contaminated by artifacts and the energy cannot be concentrated at the right position.

For more drastic comparisons of the influence of incorrect background velocity, we displayed the FDCIGs and ODCIGs of the RTM images in **Figure 5**. Again, since the proposed method requires repetitive inverse and forward Fourier transform to generate these image gathers, the FDCIGs might be contaminated by the wrapping noises. In this case, we can utilize dip filters to suppress these artifacts as presented in **Figure 4**. Note that the dip filter can suppress the wrapping noise with much larger angles than the target reflectors.

The FDCIGs generated using the true velocity are displayed in **Figure 5A**. We extracted 10 FDCIGs and 10 ODCIGs from the center point of the model (3 km in distance) at 5~m intervals. The frequency range is 3–20 Hz in each FDCIG, and the offset range is 100–2,800 m in each ODCIG. We could determine from the image gathers that all the reflectors are located at the correct positions as we observed in the migration image. All four reflectors are flat and exhibit strong amplitude throughout the entire frequency band and offset group.

In contrast, when the velocity of the 2nd layer increases, the amplitude of the reflector located at 1,600 m depth is significantly weaker than the one in **Figure 5A** since RTM could not resolve the correct images at the right position. We also observe that the reflector bends downward due to inaccurate background velocity. A similar type of move-out can be observed from the reflector located at 2.400 m depth. This move-out direction reverses when we decrease the velocity (**Figure 2C**) as presented in **Figure 5C**.

It is clear that an inaccurate velocity generates weak amplitude events, deflection, or bent shapes in the image gathers. This is well known and can be observed in the ODCIGs—a classical migration velocity tool, as well. In the proposed method, the level of Gibb's phenomena (or side lobes) located around a target reflection could be a measure of model quality. For example, the amounts of contamination due to side lobes around the reflectors

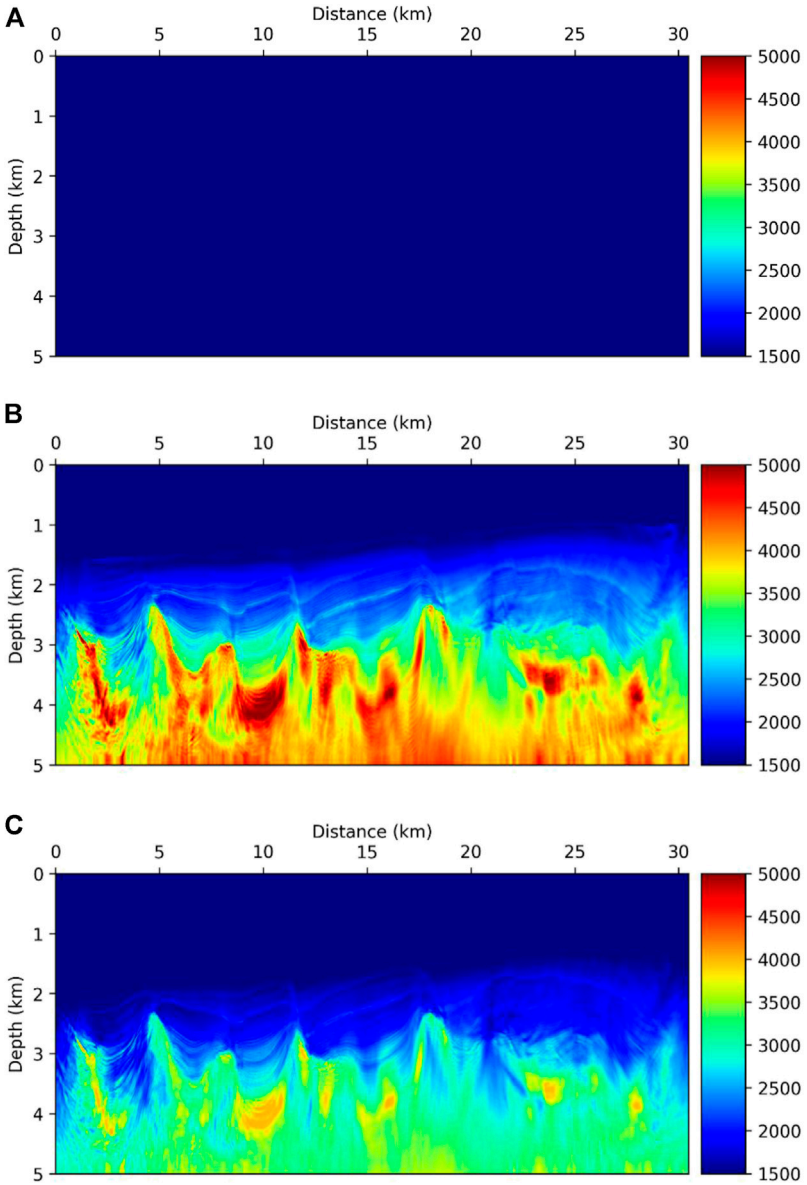

FIGURE 10 | (A) Homogeneous velocity model, **(B)** smoothed velocity inverted model by FWI, and **(C)** smoothed and 20% reduced velocity except sea water velocity model from **(B)**.

are more severe in **Figures 5B,C** than in the FDCIGs generated using the true velocity model (**Figure 5A**). Evaluating the velocity model only by the level of contamination is of limited value in that the level of Gibb's phenomena cannot provide any hint for the direction of move-out. Nevertheless, the proposed method using the FDCIGs provides different perspectives to ascertain the quality of the background velocity model without too much computational effort. However, ODCIGs in **Figures 5C,D**, the pattern appears differently according to the decreased and increased velocity. Comparing the ODCIGs with FDCIGs, the level of distortion in each reflector can be observed more clearly in the FDCIGs than that of ODCIGs.

3-D Synthetic Example: SEG/EAGE 3-D Salt Model

As mentioned above, the goal of this 3-D showcase is to demonstrate that the implementation of the FDCIGs is not limited to the domain of wave modeling. Put differently, we performed time-domain wave modeling, which consumes less memory. Then, we apply a Fourier transform to compute the RTM imaging conditions in the frequency domain. For the time-domain wave simulation, we employed a finite difference method (8th order for spatial derivatives).

To investigate the feasibility of the proposed method, we made comparisons of the FDCIG between the smoothed SEG/EAGE 3-

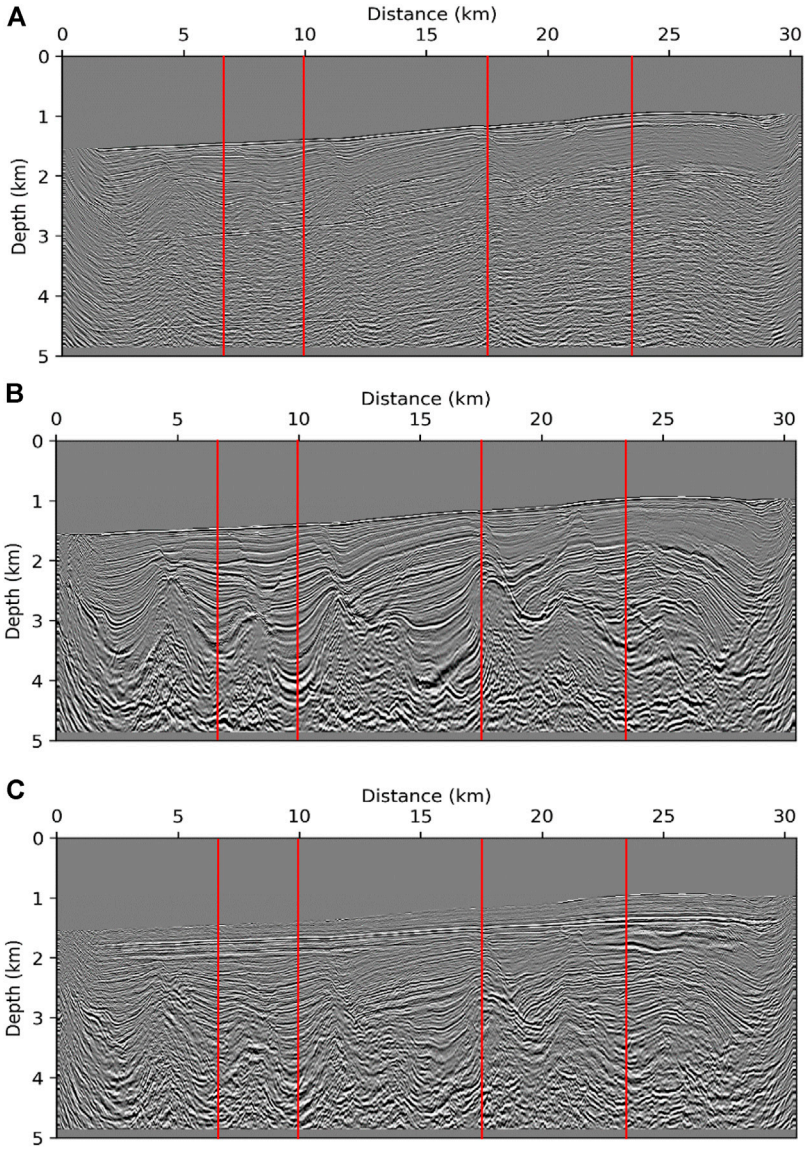

FIGURE 11 | RTM images from **(A)** homogeneous velocity model, **(B)** smoothed velocity inverted model by FWI, and **(C)** smoothed and 20% reduced velocity except sea water velocity model from **(B)**. Four red lines in each RTM images are locations for extracting FDCIGs and ODCIGs.

D salt model and a linearly increasing velocity model. The model size is 451 × 451 × 134 and we applied 10 m grid spacing. The frequency range used for the RTM varies from 3 to 40 Hz. The frequency interval is 0.25 Hz. We applied smoothing to the original velocity model, and **Figure 6** shows the inline, crossline, and depth slice sections, respectively.

Figure 7 exhibits shot-receiver geometry that we used for generating the 3-D synthetic dataset. Four hundred shots are located. The source and receiver spacing are 20 and 10 m, respectively. We used all the receivers in the *x*-axis and 150 receivers (1.5 km) on both sides of the source lines.

Figure 8 shows the intersection of the 3-D migration volumes. **Figure 8A** generated from a linearly increasing model shows a sharper boundary of the salt top with higher impedance contrast than the migration results shown in **Figure 8B** acquired by using a smoothed true velocity. However, observing the bottom line of the salt diapir, the RTM image from a true velocity (**Figure 8B**) could resolve better than the image shown in **Figure 8B**. In addition, analyzing the location of the salt boundary in a map view, **Figure 8B** locates the salt boundaries accurately.

We can perform a further quality check of the migration image by investigating the FDCIGs as shown in **Figure 9**. We displayed the FDCIGs along the inline direction (0° azimuth). The corresponding FDCIGs of **Figures 8A,B** are presented in **Figures 9A,B**, respectively. We can check two different factors to check the model quality: 1) flatness of a reflector and 2) the contamination by side lobes. When observing the near surface (<0.25 km) where all the sediment interfaces exist, the FDCIGs

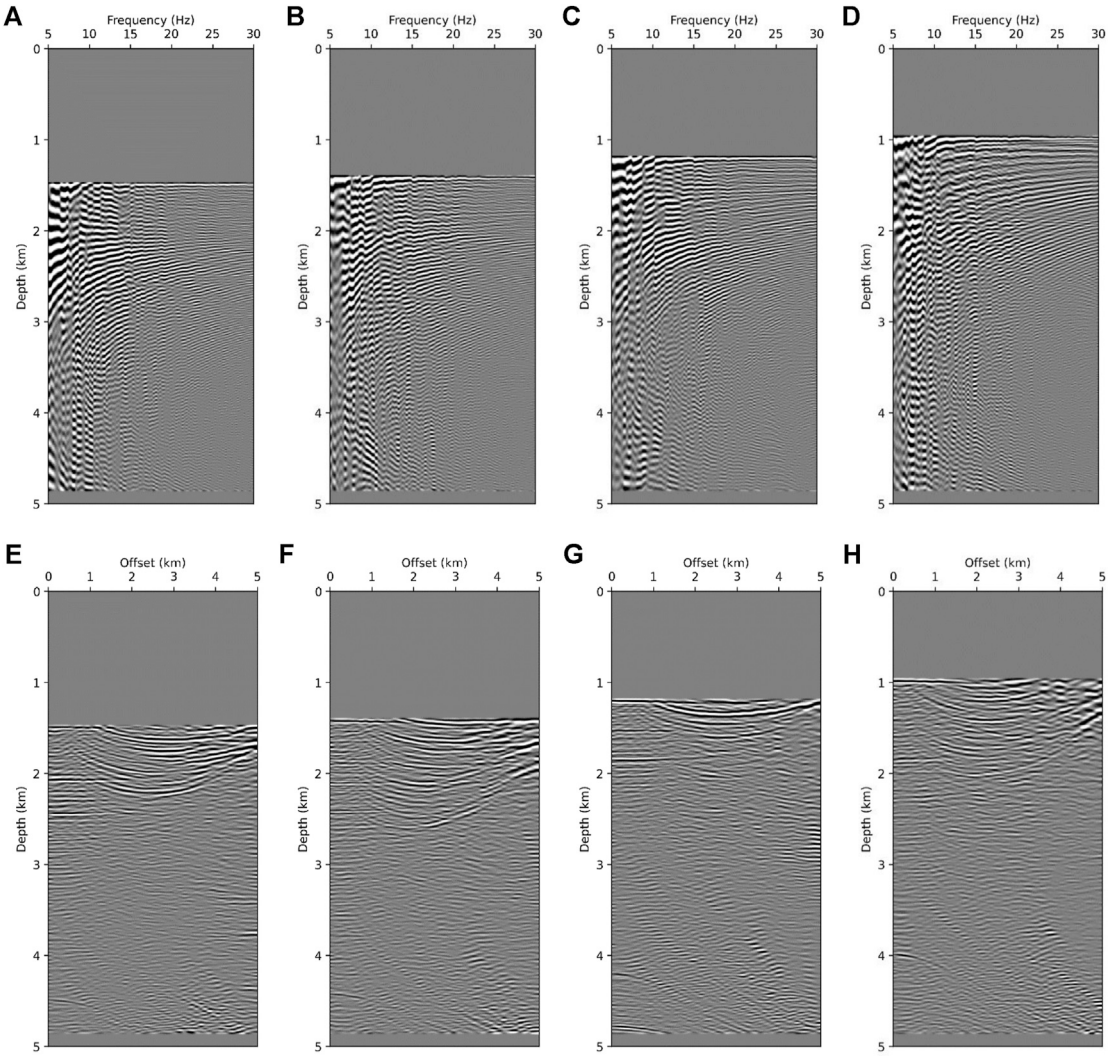

FIGURE 12 | Four FDCIGs of homogeneous velocity model at **(A)** 6.25 km, **(B)** 10 km, **(C)** 17.5 km, and **(D)** 23.75 km. Four ODCIGs of same model as that of FDCIGs at **(E)** 6.25 km, **(F)** 10 km, **(G)** 17.5 km, and **(H)** 23.75 km.

acquired by using a smoothed true velocity model exhibits a better alignment, clearer continuation, and better flatness than the FDCIGs shown in **Figure 9A**. In contrast, FDCIGs generated by applying inaccurate background velocity model shows thicker side lobes and they could not even resolve any salt bottom. In addition, many of the reflectors located above the salt top are obscured by the wrapping noise. Hence, it is difficult to make a correct interpretation of a move-out. We can make sharp comparisons in the right most panel in **Figure 9**, which presents the FDCIGs at the pinch-out points of the salt body. Again, from these FDCIGs, we investigate 1) the separation of the salt top and bottom, 2) the flatness of strata, and 3) the lateral continuity of the frequency gathers.

2-D Real Data Example

The method of calculating the wave solution used a frequency-domain discretization scheme like the layered model. We use a 12.5 m spatial grid size. The minimum and maximum frequency of the data are 5 and 30 Hz, respectively. To calculate the wavefield in the frequency domain, we applied a 0.25 Hz frequency interval. There are 734 shots and 804 receivers in interval 37.5 and 12.5 m, respectively. The sources and receivers are located at 10 m depth. For ODCIGs, we used 50 offset groups that are from 100 to 5,000 m at 100 m intervals.

To demonstrate the effectiveness and robustness of FDCIG in the application of field data, we compared the homogeneous velocity model, the estimated velocity model *via* Laplace–Fourier domain FWI (Shin and Cha, 2009), and the FWI model with 20% velocity reduction (**Figure 10**). Note that the FWI model still bears uncertainties to a certain extent. Nevertheless, the goal of this research is to introduce the first showcase of a model quality check using FDCIGs combined with the migration images. The corresponding RTM images of the models displayed in **Figure 10** are presented in **Figure 11**.

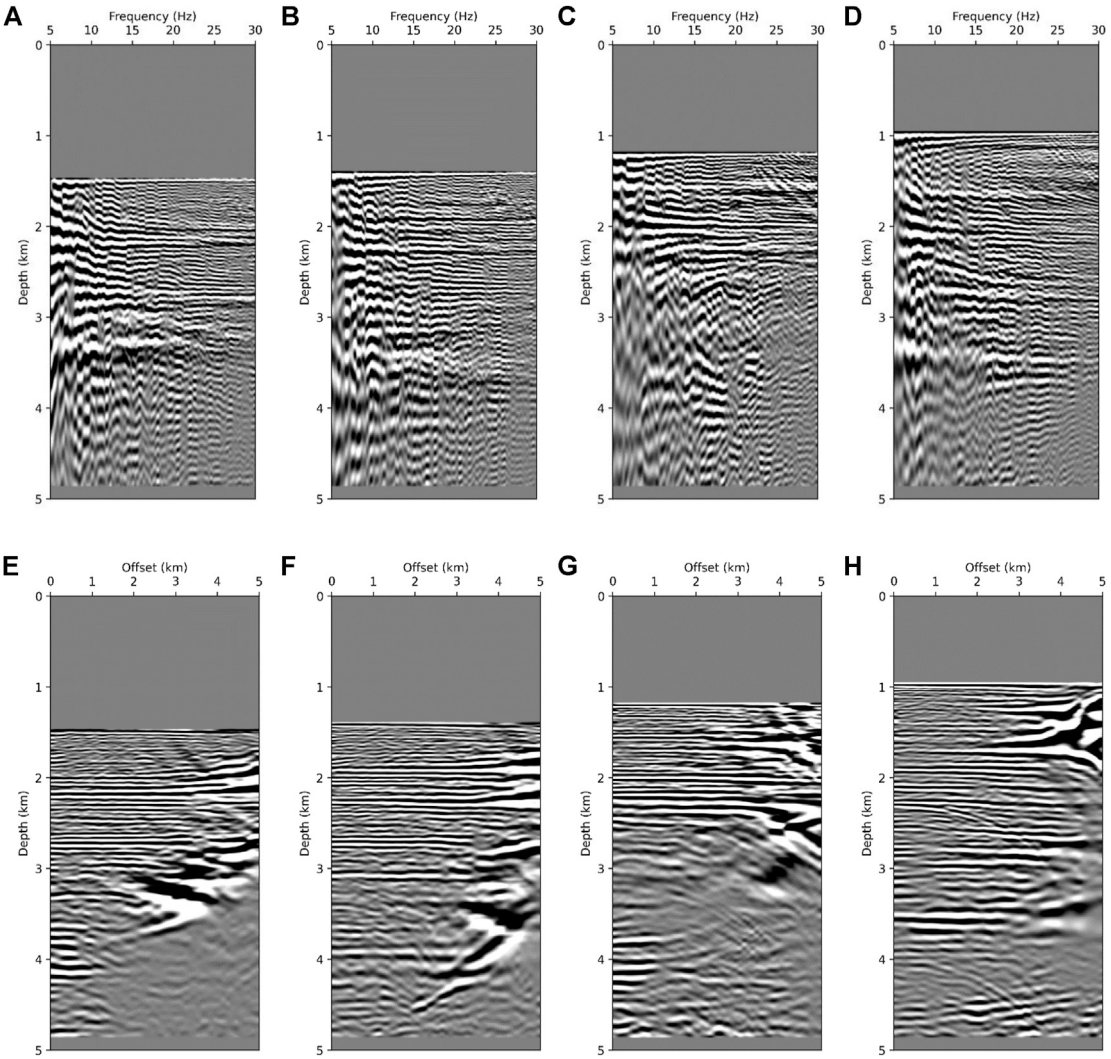

FIGURE 13 | Four FDCIGs of smoothed and inverted velocity model by FWI at **(A)** 6.25 km, **(B)** 10 km, **(C)** 17.5 km, and **(D)** 23.75 km, and four ODCIGs of same model as that of FDCIGs at **(E)** 6.25 km, **(F)** 10 km, **(G)** 17.5 km, and **(H)** 23.75 km.

Figure 12 is the FDCIGs and ODCIGs of **Figure 11A**. Four FDCIGs and four ODCIGs are at 6.25, 10, 17.5, and 23.75 km in order. To demonstrate the change of image gathers, we displayed the image gathers acquired from the homogeneous model with 1,500 m/s in **Figure 12**.

The FDCIGs and ODCIGs were selected from four points in the migration images as highlighted in **Figure 11** with vertical red lines. Observing the gathers shown in **Figure 12**, the FDCIGs (**Figures 12A–D**) are dominated by the low frequency wrapping noise, and the other reflectors are hardly observed due to its discontinuity and weak amplitude. Similarly, the reflectors in ODCIGs (**Figures 12E–H**) are bending upward which means the background velocity needs to be increased. In **Figure 13**, the common image gathers obtained from the full-waveform inversion, a number of reflectors with high amplitude are observable at specific depth. At 6.25 km in **Figure 13A** shows several clear reflectors which are flat and continuous around 2.2, 2.9 and 3.3 km. Likewise, in ODCIG (**Figure 13E**), straight lines are well expressed at 2.2 and 2.9 km. However, around at depth 3.3 km, it is difficult to determine key reflectors due to lack of energy at long offset. Investigating **Figures 13B,F** corresponding to the 10 km point in **Figure 11B**, in this case the reflector should appear at 2.2, 3, and 3.8 km. The FDCIGs (**Figure 13B**) exhibit reflectors at 2.2 and 3.8 km obviously, but reflectors around 3 km are hard to be recognized. Rather, the reflector is well expressed in ODCIG (**Figure 13F**). By investigating **Figures 11A,C** model with intentionally decreased velocity by 20%, we further demonstrate the effectiveness of FDCIGs. Straight lines cannot be found at any depth in FDCIGs (**Figures 14A–D**) due to the inaccurate background velocity model. On the contrary, in ODCIGs (**Figures 14E–H**) there are a number of fake reflectors, which is flat and may possibly mislead by the interpreters. When we need to quality check the migration velocity, utilizing both FDCIGs and ODCIGs may helpful.

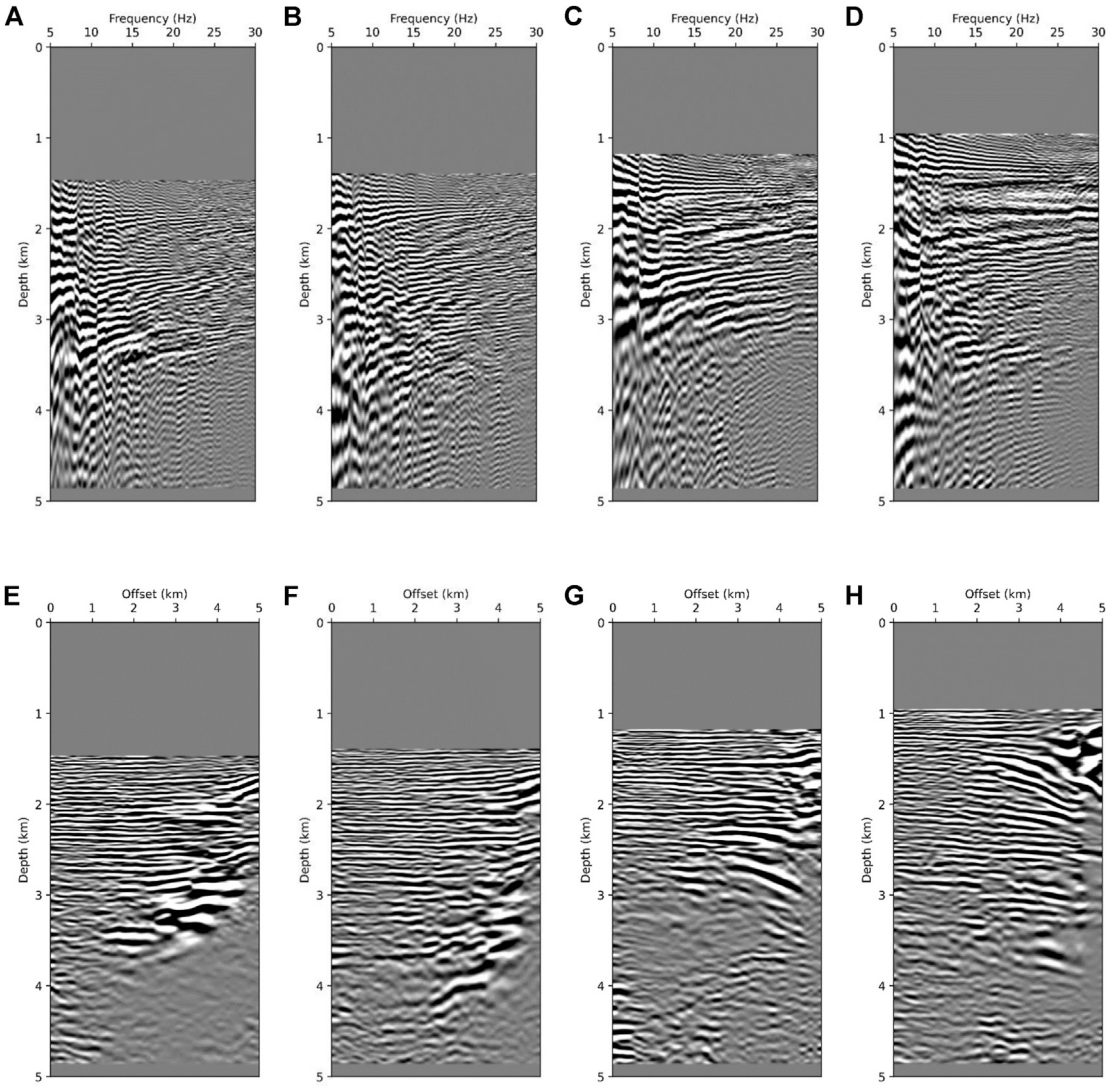

FIGURE 14 | Four FDCIGs of smoothed and inverted and 20% reduced velocity model by FWI at **(A)** 6.25 km, **(B)** 10 km, **(C)** 17.5 km, and **(D)** 23.75 km, and four ODCIGs of same model as that of FDCIGs at **(E)** 6.25 km, **(F)** 10 km, **(G)** 17.5 km, and **(H)** 23.75 km.

Nevertheless, we can quickly determine the accuracy level of the velocity model just by investigating the FDCIGs which add little computational cost to the existing RTM.

CONCLUSION

Validation of the velocity model is essential in identifying unknown subsurface structures. We examined how FDCIGs appear in the true velocity model through the first example (layered model) and also examined how the behavior of the FDCIGs changes when the background velocity is slightly changed. The application to the SEG/EAGE 3-D salt model shows that when performing reverse time migration by modeling in the time domain, FDCIGs can also be obtained quickly and easily by adding only the discrete Fourier transform in the usual process. Finally, in the example applied to real data, it was shown that there was no difficulty in determining the validity of the velocity model with FDCIGs even in a complex velocity model. Through the various examples, it has been sufficiently proven that the newly proposed CIG method can be an effective tool for quickly and intuitively judging the validity of velocity model. In the time-domain RTM, although extra storage of FFT is required, once forward and backward modeled wavefields are saved, we can easily obtain FDCIGs within a relatively short amount of time. For the next step of proposed method, we will investigate a more rigorous and quantitative method to analyze the change of FDCIGs and build a link with the amount of velocity perturbation.

DATA AVAILABILITY STATEMENT

The authors do not have the legal right to release the data as it belongs to TOTAL and is used for research purposes only.

AUTHOR CONTRIBUTIONS

CS, HK, and YC contributed to conception and design of the study. YC and SK contributed to 3-D data modeling and 2-D real data modeling respectively. HK and YC wrote the first draft of the manuscript. HK, YC, and CS contributed to manuscript revision, read, and approved submitted version.

FUNDING

This research was supported by the Basic Research Project (GP 2020-023 and GP 2020-034) of the Korea Institute of Geoscience and Mineral Resources (KIGAM) funded by the Ministry of Science and ICT, Republic of Korea. We thank TOTAL for providing real data.

REFERENCES

Baysal, E., Kosloff, D. D., and Sherwood, J. W. C. (1983). Reverse Time Migration. *Geophysics* 48, 1514–1524. doi:10.1190/1.1441434

Biondi, B., and Symes, W. W. (2004). Angle-domain Common-image Gathers for Migration Velocity Analysis by Wavefield-continuation Imaging. *Geophysics* 69, 1283–1298. doi:10.1190/1.1801945

Dickens, T. A., and Winbow, G. A. (2011). "Rtm Angle Gathers Using Pointing Vectors," in *SEG Technical Program Expanded Abstracts 2011* (Society of Exploration Geophysicists), 3109–3113.

Etgen, J. T. (2012). "3d Wave Equation Kirchhoff Migration," in *SEG Technical Program Expanded Abstracts 2012* (Society of Exploration Geophysicists), 1–5.

Fomel, S. (2004). "Theory of 3-d Angle Gathers in Wave-Equation Imaging," in *SEG Technical Program Expanded Abstracts 2004* (Society of Exploration Geophysicists), 1053–1056.

Giboli, M., Baina, R., Nicoletis, L., and Duquet, B. (2012). "Reverse Time Migration Surface Offset Gathers Part 1: a New Method to Produce 'classical' Common Image Gathers," in *SEG Technical Program Expanded Abstracts 2012* (Society of Exploration Geophysicists), 1–5.

He, B., Liu, Y., and Zhang, Y. (2019). Improving the Least-Squares Image by Using Angle Information to Avoid Cycle Skipping. *Geophysics* 84, 581–598. doi:10.1190/geo2018-0816.1

He, B., Liu, Y., and Zhang, Y. (2020). Wave-equation Migration Velocity Analysis Using Radon-Domain Common-Image Gathers. *J. Geophys. Res. Solid Earth* 125, e2019JB018938. doi:10.1029/2019jb018938

Marfurt, K. J. (1984). Accuracy of Finite-difference and Finite-element Modeling of the Scalar and Elastic Wave Equations. *Geophysics* 49, 533–549. doi:10.1190/1.1441689

McMechan, G. A. (1983). Migration by Extrapolation of Time-dependent Boundary Values*. *Geophys. Prospect* 31, 413–420. doi:10.1111/j.1365-2478.1983.tb01060.x

Nolan, C., and Symes, W. (1996). Imaging in Complex Velocities with General Acquisition Geometry: TRIP Annual Report. doi:10.1190/1.1826642

Pratt, R. G. (1999). Seismic Waveform Inversion in the Frequency Domain, Part 1: Theory and Verification in a Physical Scale Model. *Geophysics* 64, 888–901. doi:10.1190/1.1444597

Pratt, R. G., Shin, C., and Hick, G. (1998). Gauss-newton and Full newton Methods in Frequency-Space Seismic Waveform Inversion. *Geophys. J. Int.* 133, 341–362.

Prucha, M. L., Biondi, B. L., and Symes, W. W. (1999). "Angle-domain Common Image Gathers by Wave-Equation Migration," in *SEG Technical Program Expanded Abstracts 1999* (Society of Exploration Geophysicists), 824–827.

Sava, P. C., and Fomel, S. (2003). Angle-domain Common-image Gathers by Wavefield Continuation Methods. *Geophysics* 68, 1065–1074. doi:10.1190/1.1581078

Shin, C., and Ho Cha, Y. (2009). Waveform Inversion in the Laplace-Fourier Domain. *Geophys. J. Int.* 177, 1067–1079. doi:10.1111/j.1365-246x.2009.04102.x

Shin, C., Min, D., Yangand Lee, S. (2003). Evaluation of Poststack Migration in Terms of Virtual, Source and Partial, Derivative. *J. Seismic Exploration* 12, 17.

Stolk, C. C., and Symes, W. W. (2004). Kinematic Artifacts in Prestack Depth Migration. *Geophysics* 69, 562–575. doi:10.1190/1.1707076

Wang, X., Qian, J., and Wang, H. (2016). Efficient Angle-Domain Common-Image Gathers Using Cauchy-Condition-Based Polarization Vectors. *Geophysics* 81, S69–S77. doi:10.1190/geo2015-0327.1

Whitmore, N. D. (1983). "Iterative Depth Migration by Backward Time Propagation," in *SEG Technical Program Expanded Abstracts 1983* (Society of Exploration Geophysicists), 382–385.

Wu, Z., and Alkhalifah, T. (2018). A Highly Accurate Finite-Difference Method with Minimum Dispersion Error for Solving the Helmholtz Equation. *J. Comput. Phys.* 365, 350–361. doi:10.1016/j.jcp.2018.03.046

Xu, S., Chauris, H., Lambaré, G., and Noble, M. (2001). Common-angle Migration: A Strategy for Imaging Complex media. *Geophysics* 66, 1877–1894. doi:10.1190/1.1487131

Yoon, K., and Marfurt, K. J. (2006). Reverse-time Migration Using the Poynting Vector. *Exploration Geophys.* 37, 102–107. doi:10.1071/eg06102

Conflict of Interest: The author YC was employed by the company Shell. The author SK was employed by Cocolink.

The remaining authors declare that the research was conducted in the absence of any commercial or financial relationships that could be construed as a potential conflict of interest.

frontiers in Earth Science

ORIGINAL RESEARCH
published: 13 August 2021
doi: 10.3389/feart.2021.687835

The Pseudo-Laplace Filter for Vector-Based Elastic Reverse Time Migration

Qizhen Du[1,2]*, *Xiaoyu Zhang*[3,4]*, *Shukui Zhang*[5], *Fuyuan Zhang*[1,2] and *Li-Yun Fu*[1,2]

[1]Key Laboratory of Deep Oil and Gas, China University of Petroleum (East China), Qingdao, China, [2]Laboratory for Marine Mineral Resources, Qingdao National Laboratory for Marine Science and Technology, Qingdao, China, [3]Institute of Oceanographic Instrumentation, Qilu University of Technology (Shandong Academy of Sciences), Qingdao, China, [4]School of Ocean Technology Sciences, Qilu University of Technology (Shandong Academy of Sciences), Qingdao, China, [5]School of Earth Sciences and Engineering, Sun Yat-sen University, Guangzhou, China

The scalar images (PP and PS) can be effectively obtained in vector-based elastic reverse time migration by applying dot product–based scalar imaging conditions to the separated vector wavefields. However, the PP image suffers from polarity reversal issues when opening angles are greater than 90° and backscattering artifacts when opening angles are close to 180°. To address these issues, we propose the pseudo-Laplace filter for the dot product–based scalar imaging condition. Based on the analysis of the Laplace filter in the scalar image of vector-based wavefields, the second-order parallel-oriented partial derivatives of Cartesian components cross-correlation results are selected to construct the pseudo-Laplace filter. In contrast, second-order normal-oriented partial derivatives of the Cartesian component's cross-correlation results are omitted. The theoretical analysis with the plane wave assumption shows that the proposed pseudo-Laplace filter can solve the problems of backscattering artifacts and polarity reversal in PP images by the scalar imaging condition. Due to additional polarity correction and backscattering attenuation, numerical examples show excellent performance in PP images with a pseudo-Laplace filter. Furthermore, the application of the pseudo-Laplace filter requires trivial additional computation or storage.

Keywords: elastic RTM, scalar imaging condition, backscattering suppression, polarity correction, pseudo-Laplace filter

OPEN ACCESS

Edited by:
Hua-Wei Zhou,
University of Houston, United States

Reviewed by:
Aifei Bian,
China University of Geosciences Wuhan, China
Jidong Yang,
China University of Petroleum (Huadong), China

***Correspondence:**
Qizhen Du
multicomponent@163.com
Xiaoyu Zhang
zhxy_upc@126.com

Specialty section:
This article was submitted to Solid Earth Geophysics, a section of the journal Frontiers in Earth Science

Received: *30 March 2021*
Accepted: *21 June 2021*
Published: *13 August 2021*

Citation:
Du Q, Zhang X, Zhang S, Zhang F and Fu L-Y (2021) The Pseudo-Laplace Filter for Vector-Based Elastic Reverse Time Migration. Front. Earth Sci. 9:687835. doi: 10.3389/feart.2021.687835

INTRODUCTION

Reverse time migration (RTM) is a seismic data processing method for migrating seismic reflection data to obtain subsurface images that effectively describe geological structures (Baysal et al., 1983; McMechan, 1983; Whitmore, 1983). Multicomponent seismic data processing techniques have been evolved with seismic acquisition techniques and high-performance computing technologies to acquire more precise images. Elastic reverse time migration (elastic RTM) is one of the most reliable multicomponent seismic data imaging techniques that can provide surface PP and PS reflection information using P-wave and S-wave reflection data. Unlike acoustic RTM, which analyzes P-wave propagation in the subsurface medium, elastic RTM integrates elastic P-wave and S-wave propagation with wave conversion. As a result, the wave conversion-related elastic response and vector-based propagation characteristics are more accurate than the acoustic approximation.

Like acoustic RTM, the early elastic RTM (Sun and McMechan, 1986) used elastic wave equation to forward and backward extrapolation wavefields and extract images by cross-correlation imaging conditions for Cartesian components. For these images, the migration results of different modes are intermixed together. The interference would result in crosstalks in final images and make it difficult to highlight the advantages of S-wave information. The S-wave information can be further used to supplement P-wave images in imaging targets with poor PP reflectivity or under gas clouds. Therefore, in addition to applying wavefield extrapolation and imaging conditions, a more suitable approach for elastic RTM to obtain decoupled elastic wavefield is wavefield separation. Early attempts of wavefield separation use divergence and curl operators. The P wave separated by a divergence operator is usually represented by a scalar-based wavefield, and the S wave separated by a curl operator is usually represented by a scalar-based wavefield in a 2D case or a vector-based wavefield in a 3D case. Their amplitude and phase are different from the original elastic wavefield. Recently, the decoupled wave equation approach has been proposed. The decoupled wave equations (Ma and Zhu, 2003; Li, 2007; Wang and McMechan, 2015; Du et al., 2017) have been proposed to decouple the wavefields of displacement or particle velocity. Zhu (2017) has used Helmholtz decomposition and vector Poisson's equation to decompose P- and S-mode wavefields with correct phases, amplitudes, and physical units similar to the decoupled wave equation. Furthermore, the decoupled wave equation with the assumption of heterogeneous medium (Elita Li et al., 2018; Tang and McMechan, 2018) has also been proposed to handle the wavefield coupling problem at interfaces. The separated P wave and S wave are represented by vector-based wavefields and have the same amplitude and phase as the original elastic wavefield. Therefore, we apply the decoupled wave equations to construct the decoupled source and receiver wavefields.

In addition to wavefield separation, imaging conditions are also the key ingredient for the elastic RTM algorithm to determine the accuracy and quality of imaging results. According to different wavefield separation methods and wavefield representations, imaging conditions are also different. As for scalar-based P wave and vector-based S wave based on divergence and curl operators, various imaging conditions include cross-correlation imaging conditions or divergence- and curl-based imaging conditions (Yan and Sava, 2008; Du et al., 2014). As a result, the migrated PP image may encounter backscattering artifacts whose opening angle is near 180°, and the migrated PS image may encounter a polarity reversal problem at the normal incident, which is caused by the sign change of the S wave from the curl operator on two sides of the normal incident. The Laplace filter (Youn and Zhou, 2001) could suppress backscattering noise in PP images with trivial computation and storage costs.

Furthermore, the S wave's polarization by Poynting vector (Du et al., 2013) or the modified imaging condition (Duan and Sava, 2015) can correct the polarity reversal problem to a certain degree. As for the vector-based P wave and S wave by the decoupled wave equation, the scalar PP and PS images are required to facilitate further interpretation. There are some imaging conditions, such as the cross-correlation imaging condition of Cartesian components (Claerbout, 1971), the scalar imaging condition (Wang and McMechan, 2015; Du et al., 2017; Zhu, 2017; Yang et al., 2018), and energy cross-correlation imaging condition (Rocha et al., 2016). The cross-correlation imaging condition of Cartesian components generates multiple imaging results for interpretation, while the energy cross-correlation imaging condition only generates one image of elastic energy, which misses some important convert-wave information. Therefore, the dot product–based scalar imaging conditions, extended from cross-correlation imaging conditions and sum up these cross-correlation images of Cartesian components together, have been used to obtain the final scalar images (PP and PS).

The scalar imaging condition can output scalar images (PP and PS) of vector wavefields but an encounter with polarity reversal problem and backscattering artifacts in PP images. Different from the polarity reversal in the PS image in which P wave and S wave are separated by divergence and curl operators, the polarity reversal problem is introduced to PP images by scalar imaging conditions while the opening angle exceeds 90°. Du et al. (2017) have used Poynting vectors to analyze the sign change of PP images by scalar imaging conditions versus opening angles. Then, Tang and McMechan (2018) have used Poynting vectors to extract their angle gathers to correct the polarity reversal. These methods, as mentioned above, can solve the polarity reversal problem and lead to a significant extra cost of computation and storage. As for the attenuation of backscattering noise, the angle attenuation factors (Yoon and Marfurt, 2006) and high-pass filters can be used to suppress the image of large opening angles. As a widely used approach, the high-pass filter is easy to implement. Among high-pass filters, the Laplace filter (Youn and Zhou, 2001) has successfully suppressed backscattering noise in PP images by cross-correlation imaging conditions.

In this article, based on the analysis of the Laplace filter in the vector-based scalar image, we select the parallel-oriented partial derivatives and abandon normal-oriented partial derivatives of the Cartesian component's cross-correlation results to propose the pseudo-Laplace filter and produce an optimized image. Theoretical analysis with the plane wave assumption is then carried out to show that the PP image with a pseudo-Laplace filter succeeds in backscattering attenuation and polarity correction. Finally, the numerical experiments prove that the pseudo-Laplace filter can guarantee its stability and practicability without increasing additional computation burdens.

METHODOLOGY

The vector-based elastic RTM algorithms are as follows: 1) forward extrapolated decoupled source wavefields using the decoupled wave equation and retaining their boundary values at imaging time points; 2) back extrapolated decoupled receiver wavefields using the decoupled wave equation and reconstructing the source wavefields by the retained boundary values at the same

imaging time point; 3) applying scalar imaging conditions to construct scalar imaging results (PP and PS). Here, we analyze the scalar imaging condition based on the decoupled wave equation and apply it using a Laplace filter or pseudo-Laplace filter.

The Decoupled Wave Equation

In a homogeneous and isotropic medium, the elastic wave extrapolation (Aki and Richards, 1980) can be expressed as follows:

$$\rho\ddot{\mathbf{u}} = (\lambda + 2\mu)\nabla(\nabla \cdot \mathbf{u}) - \mu\nabla \times \nabla \times \mathbf{u}, \tag{1}$$

where $\mathbf{u}$ and $\ddot{\mathbf{u}}$ are the displacement vector wavefield and its second-order time derivative; λ, μ and ρ are the Lame's moduli and density, respectively. Based on the Helmholtz theorem (Dellinger and Etgen, 1990), the elastic wavefield in an isotropic case can be separated into a curl-free P wavefield ($\nabla \times \mathbf{u}_P = \mathbf{0}$) and a divergence-free S wavefield ($\nabla \cdot \mathbf{u}_S = 0$). $\mathbf{u}_P$ and $\mathbf{u}_S$ are the P-wave and S-wave displacement vector wavefields. Analogous to the separation of displacement wavefield, the second-order time derivative of displacement wavefield can be decomposed as $\ddot{\mathbf{u}} = \ddot{\mathbf{u}}_P + \ddot{\mathbf{u}}_S$, where

$$\begin{cases} \ddot{\mathbf{u}}_P = (\lambda + 2\mu)\nabla(\nabla \cdot \mathbf{u}) \\ \ddot{\mathbf{u}}_S = -\mu\nabla \times \nabla \times \mathbf{u} \\ \mathbf{u} = \mathbf{u}_P + \mathbf{u}_S \end{cases}. \tag{2}$$

Decoupled **Equation 2** is embedded in the update of the displacement wavefield. The P and S wavefields are constructed by the first two equations, respectively, and their summation can obtain the total elastic wavefield in the third equation (Ma and Zhu, 2003; Li, 2007; Zhu, 2017). In contrast to the summing of decoupled P wavefield and S wavefield, the decoupled S wavefield can be constructed by subtracting the P wavefield from the total elastic wavefield. Decoupled **Equation 2** produces displacement vector wavefields of pure P- and S-waves. Correspondingly, the first-order stress-particle velocity wave equation has been proposed (Li, 2007; Du et al., 2017; Zhou et al., 2018):

$$\begin{cases} \dot{\boldsymbol{\tau}} = (\lambda + 2\mu)\nabla \cdot \mathbf{v} - \mu(\nabla\mathbf{v} + \nabla\mathbf{v}^T) \\ \rho\dot{\mathbf{v}} = \nabla \cdot \boldsymbol{\tau} \\ \dot{\tau}_p = (\lambda + 2\mu)\nabla \cdot \mathbf{v} \\ \rho\dot{\mathbf{v}}_P = \nabla\tau_p \\ \mathbf{v}_S = \mathbf{v} - \mathbf{v}_P \end{cases}, \tag{3}$$

where $\mathbf{v}$ and $\boldsymbol{\tau}$ are particle velocity and stress of elastic wave, ∇ and $\nabla\cdot$ represent the operators of gradient and divergence, superscripted T represents the transpose, and subscripted P and S represent the P wave and S wave, respectively. Firstly, the particle velocity and stress tensor of elastic wave and the synthetic seismic records are computed by the first two equations, the conventional stress-particle velocity wave equation. Then, the auxiliary wavefield τ_p can be constructed by the third equation $\dot{\tau}_p = (\lambda + 2\mu)\nabla \cdot \mathbf{v}$ and is used to compute the P-wave particle velocity$\mathbf{v}_P$. Finally, the S-wave particle velocity can be constructed by subtracting P wavefield particle velocity $\mathbf{v}_P$ from total elastic wavefield particle velocity $\mathbf{v}$. The source and receiver wavefield can be generated by the forward and backward extension, respectively, based on the decoupled wave equation. The decoupled wavefields are all vector, and their amplitude and phase are consistent with the original elastic wavefield.

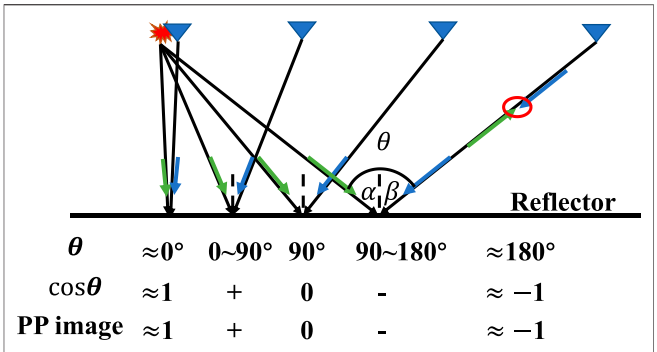

FIGURE 1 | Sign distributions of PP images via the opening angles. The green arrows and blue arrows represent the P-wave incident vectors of the source wavefield and the reflected vectors of the receiver wavefield, respectively. Regardless of the incident and reflected vector's modulus, the amplitude of PP images by the dot product scalar imaging condition implicitly depends on the scaling factor cos θ, where the opening angle θ is equal to the sum of the P-wave incident angle α and the reflected angle β. As for the unconverted reflection wave, the reflected angle β is equal to the incident angle α. The sign reversal of the factorcos θ = cos 2 α is observed when the incident angle αapproaches the critical angle 45°, which indicates that polarity reversal occurs in the PP image. As marked by the red circle, the factor cos θ reaches -1 while the incident angle is near 90°, which exists in the propagation path of the backscattering wave. The backscattering artifacts with 180° or near 180° scattering angles (i.e., opening angles) also contaminate the PP image.

The Scalar Imaging Condition for the PP Mode

For the decoupled vector wavefields, we obtain scalar imaging results by imaging conditions, including cross-correlation imaging condition of Cartesian components generating too many results to interpret, and dot product–based scalar imaging conditions. Regardless of source normalization, the dot product–based scalar imaging condition (Du et al., 2017; Zhu, 2017; Yang et al., 2018) for the PP wave can be written as follows:

$$I_{pp}(\mathbf{x}) = \int \mathbf{s}^p(\mathbf{x}, t) \cdot \overline{\mathbf{r}}^p(\mathbf{x}, t)dt \tag{4}$$

in terms of source particle velocity vector $\mathbf{s}^p$ and receiver particle velocity vector $\mathbf{r}^p$. Here, I_{pp} is the migrated PP image by integrating the dot product over time t, symbol "·" denotes the dot product of two vectors, and tilde above wavefield variable denotes its conjugation.

Algebraically, the dot product is the sum of some related Cartesian components products, which means $\mathbf{s}^p \cdot \mathbf{r}^p = s_x^p\overline{r}_x^p + s_y^p\overline{r}_y^p + s_z^p\overline{r}_z^p$. Since the Cartesian components are independent over time t, the migrated PP image I_{pp} can be disintegrated into three parts I_{ppxx}, I_{ppyy}, and I_{ppzz}, where $I_{ppxx} = \int s_x^p\overline{r}_x^p dt$, $I_{ppyy} = \int s_y^p\overline{r}_y^p dt$, and $I_{ppzz} = \int s_z^p\overline{r}_z^p dt$ represent

cross-correlation imaging results of the x-axis, y-axis, and z-axis Cartesian components, respectively.

By introducing the opening angle θ shown in **Figure 1**, the dot product scalar imaging condition can be equivalently expressed as follows:

$$I_{pp} = \int |\mathbf{s}^p||\overline{\mathbf{r}}^p| \cos\,\theta dt. \tag{5}$$

Here, $|\cdot|$ is the modulus of a vector. The amplitude of the PP image depends on the modulus of the incident wave, modulus of the reflected wave, and the extra weighting factor $\cos\,\theta$. Depending on the seismic source and Green function between the source and scattering point, the modulus of the incident wave is desired in the PP image. The modulus of a reflected wave depends on the Green function between the receiver and scattering point and the reflection coefficient R_{pp}. The reflection coefficient R_{pp} quantitatively describes the amplitude and phase of the reflected wave while P wave is incidence on the interface. The modulus of the incident and reflected waves is desired information in an image to provide a reliable basis for seismic interpretation inversion. Regardless of wavefields modulus, the additional factor $\cos\,\theta$ will cause destructive interference in the final PP image. On the one hand, this extra factor $\cos\,\theta$ changes its sign when the opening angle $\theta > 90°$ or the incident angle $\alpha > 90°$, which will cause the polarity reversal problem (Du et al., 2017; Zhou et al., 2018) at a large incident angle. On the other hand, I_{pp} is also contaminated by backscattering artifacts with the incident angles close to 90° or opening angles near 180°.

The Scalar Imaging Condition With the Laplace Filter

In acoustic RTM or scalar-based elastic RTM, the Laplace filter (Youn and Zhou, 2001) has been used to suppress the backscattering artifacts in the PP image. As for the PP image in vector-based elastic RTM, the scalar imaging condition with a Laplace filter can be expressed as follows:

$$\begin{aligned} I_{pp}^{lap} &= \nabla^2 I_{PP} \\ &= \nabla^2 \int (\mathbf{s}^p(\mathbf{x},t) \cdot \overline{\mathbf{r}}^p(\mathbf{x},t))dt. \end{aligned} \tag{6}$$

Here, I_{pp}^{lap} is the migrated PP image with a Laplace filter, $\nabla^2 = \partial_x^2 + \partial_y^2 + \partial_z^2$ is the Laplace filter operator, ∂_x^2, ∂_y^2, and ∂_z^2 are the second-order partial derivatives along the x-axis, y-axis, and z-axis direction, respectively. Since partial derivatives are independent of time integration, the PP image I_{pp}^{lap} can also be disintegrated by Cartesian components' cross-correlation imaging results. As for 2D vector-based wavefields, the PP image I_{pp}^{lap} can be separated into four items:

$$\begin{aligned} I_{pp}^{lap} &= \partial_x^2 \int s_x^p \overline{r}_x^p dt + \partial_x^2 \int s_z^p \overline{r}_z^p dt + \partial_z^2 \int s_x^p \overline{r}_x^p dt + \partial_z^2 \int s_z^p \overline{r}_z^p dt \\ &= \partial_x^2 I_{ppxx} + \partial_x^2 I_{ppzz} + \partial_z^2 I_{ppxx} + \partial_z^2 I_{ppzz}. \end{aligned} \tag{7}$$

Here, $\partial_x^2 I_{ppxx}$ and $\partial_z^2 I_{ppxx}$ are second-order derivatives of x-axis Cartesian component cross-correlation imaging result along the x-axis direction and z-axis direction, respectively; $\partial_x^2 I_{ppzz}$ and $\partial_z^2 I_{ppzz}$ are second-order partial derivatives of z-axis Cartesian component cross-correlation imaging result along the x-axis direction and z-axis direction, respectively. Thereinto, $\partial_x^2 I_{ppxx}$ and $\partial_z^2 I_{ppzz}$ are parallel-oriented partial derivatives of Cartesian component cross-correlation imaging result. Meanwhile, $\partial_z^2 I_{ppxx}$ and $\partial_x^2 I_{ppzz}$ are normal-oriented partial derivatives of Cartesian component cross-correlation imaging result. The fault model (shown in **Figure 2**) has been introduced for reverse time migration to highlight the interaction characteristics of these decoupled migrated results on the flat and inclined interface. **Figures 3A–D** are the decoupled migrated results of $\partial_x^2 I_{ppxx}$, $\partial_x^2 I_{ppzz}$, $\partial_z^2 I_{ppxx}$, and $\partial_z^2 I_{ppzz}$, respectively.

Backscattering noise has been suppressed in all decoupled images. Moreover, these decoupled images have different migration capabilities. On the one hand, the decoupled items $\partial_x^2 I_{ppxx}$ (shown in **Figure 3A**) and $\partial_x^2 I_{ppzz}$ (shown in **Figure 3B**) related to second-order partial derivative associated with x-axis direction show similar migrated images sensitive to inclined structures. Compared with the ideal parallel-oriented result $\partial_x^2 I_{ppxx}$, the decoupled normal-oriented item $\partial_x^2 I_{ppzz}$ would encounter severe crosstalks, causing destructive interference in the final stacked image. On the other hand, the decoupled items $\partial_z^2 I_{ppxx}$ (**Figure 3C**) and $\partial_z^2 I_{ppzz}$ (**Figure 3D**) related to second -order partial derivatives along the z-axis direction migrate good images in flat-layer structures. Compared with the ideal parallel-oriented migrated result $\partial_z^2 I_{ppzz}$, the decoupled normal-oriented item $\partial_z^2 I_{ppxx}$ fails to image near-zero offset, contrary to the final PP wave image. Furthermore, the phase of $\partial_z^2 I_{ppxx}$ is opposite to $\partial_z^2 I_{ppzz}$. The opposite phase between $\partial_z^2 I_{ppzz}$ and $\partial_z^2 I_{ppxx}$ will result in the Laplace filter's disability in correcting the polarity reversal problem in the PP image. The scalar imaging condition with the Laplace filter successfully suppresses backscattering but fails to correct the polarity reversal.

The Scalar Imaging Condition With the Pseudo-Laplace Filter

Since normal-oriented partial derivative related items of the Laplace filter are greatly affected by crosstalk noise, the horizontal derivative related decoupled items have been selected to migrate the PP image. Analogous to the scalar imaging condition with the Laplace filter, we propose the scalar imaging condition with the pseudo-Laplace filter. To characterize the scalar imaging condition with a pseudo-Laplace filter mathematically, we first define the pseudo-Laplace operator $\widetilde{\nabla}^2$ as follows:

$$\widetilde{\nabla}^2 = \left(\partial_x^2, \partial_y^2, \partial_z^2\right) \tag{8}$$

and the PP wave's Hadamard product image $\mathbf{I}_{PP}$ as follows:

$$\mathbf{I}_{PP} = \int \mathbf{s}^p \circ \overline{\mathbf{r}}^p dt = \left(I_{ppxx}, I_{ppyy}, I_{ppzz}\right), \tag{9}$$

where $\circ$ is the Hadamard operator (see also **Appendix A**). The pseudo-Laplace operator $\widetilde{\nabla}^2$ comprises three array components, which are second-order partial derivatives along the x-, y- and

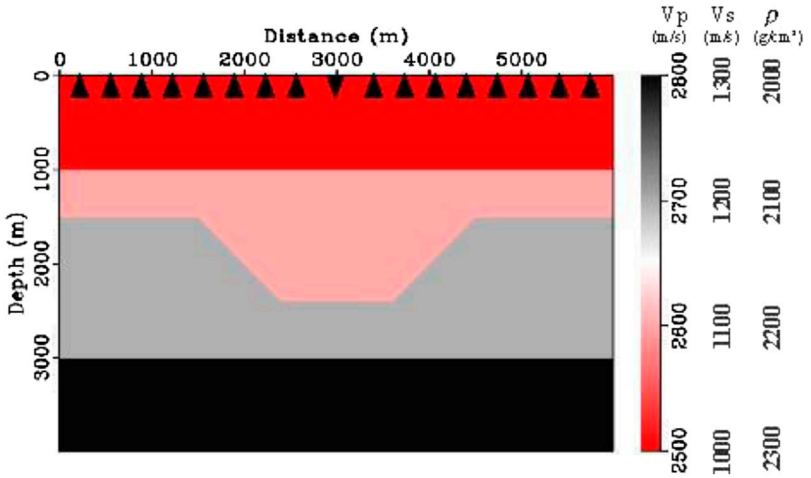

FIGURE 2 | The P-wave velocity, S-wave velocity, and density of a fault model. The model contains 600 points of dx = 10$m$in the x-axis and 400 points of dz = 10$m$in the z-axis. The inverted triangle marks the location of the explosive source with a Ricker wavelet of 30 Hz, and triangle represents receivers with 20 m interval.

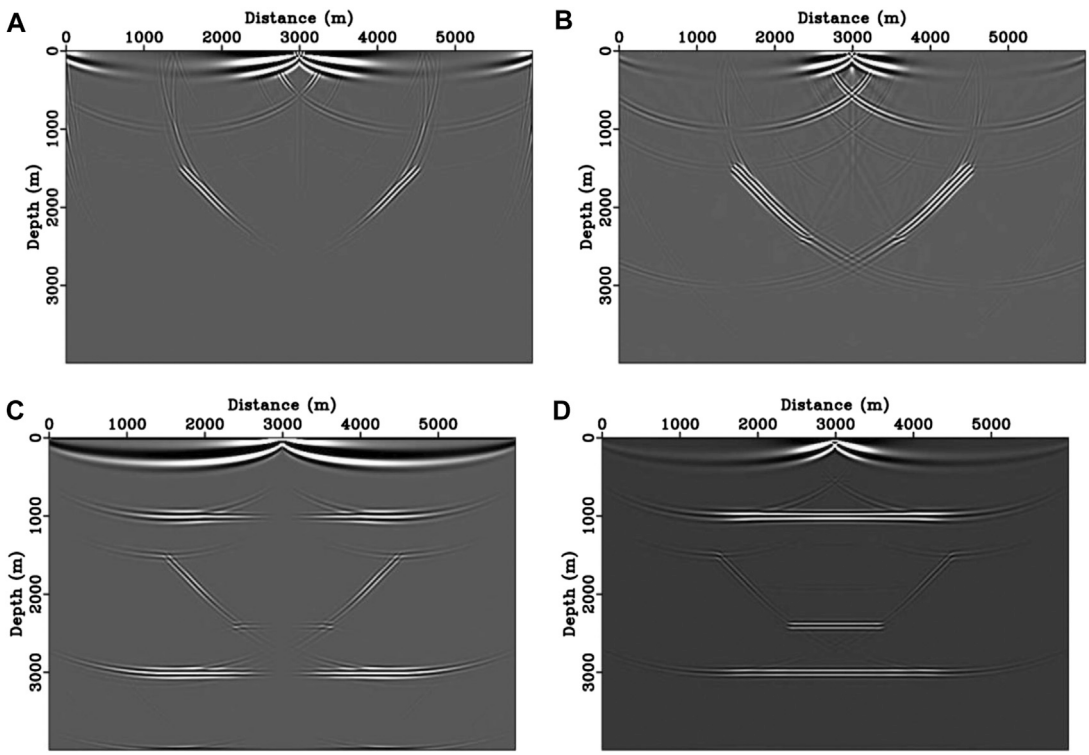

FIGURE 3 | The decoupled migrated images of $\partial_x^2 I_{ppxx}$ **(A)**, $\partial_x^2 I_{ppzz}$ **(B)**, $\partial_z^2 I_{ppxx}$ **(C),** and $\partial_z^2 I_{ppzz}$ **(D)**. The sum of decoupled migrated images $\partial_x^2 I_{ppxx}$, $\partial_x^2 I_{ppzz}$, $\partial_z^2 I_{ppxx}$, and $\partial_z^2 I_{ppzz}$ is equal to the scalar imaging condition with a Laplace filter I_{pp}^{lap}. Otherwise, the sum of decoupled migrated images $\partial_x^2 I_{ppxx}$ and $\partial_z^2 I_{ppzz}$ is equal to the scalar imaging condition with a pseudo-Laplace filter $I_{pp}^{pse-lap}$.

z-axis, respectively. Their summation is just the Laplace operator. Meanwhile, the PP wave Hadamard product images $\mathbf{I}_{PP}$ are composed of three array components: cross-correlation imaging results of the x-axis, y-axis, and z-axis Cartesian components. The summation of array components is just a PP wave scalar product image I_{pp}. There is some specific connection between the pseudo-Laplace operator $\widetilde{\nabla}^2$ and the Laplace operator $\widetilde{\nabla}^2$ and between the PP wave Hadamard product image $\mathbf{I}_{PP}$ and the PP wave scalar product image I_{pp}. Unlike the scalar Laplace operator ∇^2 and PP wave scalar product image

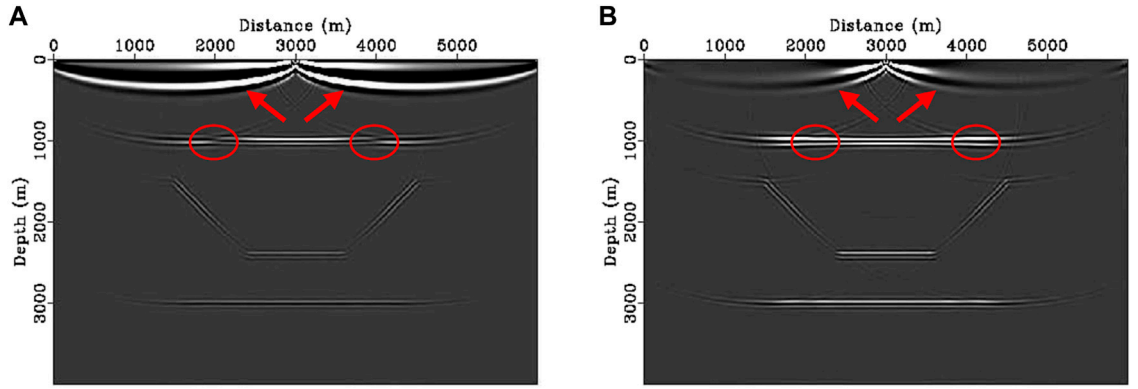

FIGURE 4 | PP images by the scalar imaging condition with a Laplace filter **(A)** and with a pseudo-Laplace filter **(B)**. Compared with the PP image with a Laplace filter (Panel A), backscattering noise suppression (marked by red arrows) and polarity reversal correction (marked by red circles) have been shown in the PP image with a pseudo-Laplace filter (Panel B).

I_{pp}, the pseudo-Laplace operator $\tilde{\nabla}^2$ and PP wave Hadamard product image $\mathbf{I}_{PP}$ are both vectors.

Combining the pseudo-Laplace operator with the PP wave Hadamard product image vector, we propose a scalar imaging condition with a pseudo-Laplace filter for vector-based wavefields as follows:

$$I_{pp}^{pse-lap} = \tilde{\nabla}^2 \cdot \mathbf{I}_{PP} \qquad = \tilde{\nabla}^2 \cdot \left(\int \mathbf{s}^p \circ \bar{\mathbf{r}}^p dt \right). \tag{10}$$

Here, $I_{pp}^{pse-lap}$ is the PP image by the scalar imaging condition with a pseudo-Laplace filter. As for 2D vector-based wavefield, the scalar imaging condition with a pseudo-Laplace filter for the PP wave should be simplified, and components related to y-axis should be neglected:

$$\begin{aligned} I_{pp}^{pse-lap} &= \partial_x^2 \int s_x^p \bar{r}_x^p dt + \partial_z^2 \int s_z^p \bar{r}_z^p dt \\ &= \partial_x^2 I_{ppxx} + \partial_z^2 I_{ppzz}. \end{aligned} \tag{11}$$

The scalar imaging conditions with a Laplace filter (**Eq. 4**) and a pseudo-Laplace filter (**Eq. 8**) depend on second-order partial derivatives of Cartesian components cross-correlation results. Different from the Laplace filter composed of parallel-oriented and normal-oriented items, only the parallel-oriented items are selected to form the pseudo-Laplace filter. As shown in **Figure 4**, we migrate the PP images of the fault model by the scalar imaging condition with the Laplace filter and with the pseudo-Laplace filter. **Figure 4A** is the migrated PP scalar image with a Laplace filter, the sum of **Figures 3A–D**. Similarly, the sum of **Figures 3A,D** is just one scalar migrated PP image with a pseudo-Laplace filter, as shown in **Figure 4B**. Compared with the PP image with a Laplace filter (**Figure 4A**), backscattering noise suppression (marked by red arrows) and polarity reversal correction (marked by red circles) have been shown in the PP image with a pseudo-Laplace filter (**Figure 4B**).

For the application in elastic RTM, we should migrate three Cartesian component's images (or two images in a 2D case) by time integration and then sum second-order derivatives of three images together. Compared with the scalar imaging condition, additional storage of three Cartesian component's images and computation of second-order derivative operation are introduced in scalar imaging conditions with a pseudo-Laplace filter. Compared with the storage and computation costs consumed by the wavefield extrapolation of elastic RTM, the additional calculation introduced by the proposed filter can be ignored to a certain degree. Thus, the scalar imaging condition with a pseudo-Laplace filter is easy to perform and does not require additional processing or storage, which is essential for elastic RTM.

Backscattering Attenuation and Polarity Correction

Based on the above-tested fault model, the suppression of backscattering and correction of polarity reversal have been shown in the PP scalar image with the proposed pseudo-Laplace filter. The section will theoretically illustrate how the pseudo-Laplace filter suppresses backscattering noise and correct polarity reversal in PP images with the assumption of a plane wave.

For the vector-based elastic wavefields, the source-side particle velocity vector $\mathbf{s}^p$ and receiver-side particle velocity vector $\mathbf{r}^p$ are related to the polarization and propagation of the P wave. Decomposing the particle velocity wavefield of pure P wave in plane waves, we obtain the following:

$$\mathbf{s}^p = |\mathbf{s}^p| \mathbf{p}^s e^{ik\left(\mathbf{n}^s \cdot \mathbf{x} - v_p t\right)}, \tag{12A}$$

and

$$\bar{\mathbf{r}}^p = |\mathbf{r}^p| R_{pp} \mathbf{p}^r e^{ik\left(v_p t - \mathbf{n}^r \cdot \mathbf{x}\right)}. \tag{12B}$$

Here, $|\mathbf{s}^p|$and $|\mathbf{r}^p| = |\mathbf{s}^p| R_{pp}$ are the modulus of the incident and reflected wave, respectively. $\mathbf{p}$ and $\mathbf{n}$ are polarization unit vector and propagation unit vector, respectively. Superscripts s and r represent incident wave and reflected wave. v_p, $k = \omega / v_p$, and ω are P wave's propagated velocity, wavenumber and angular frequency, respectively. Assuming that vectors $\mathbf{n}$ and $\mathbf{p}$ vary

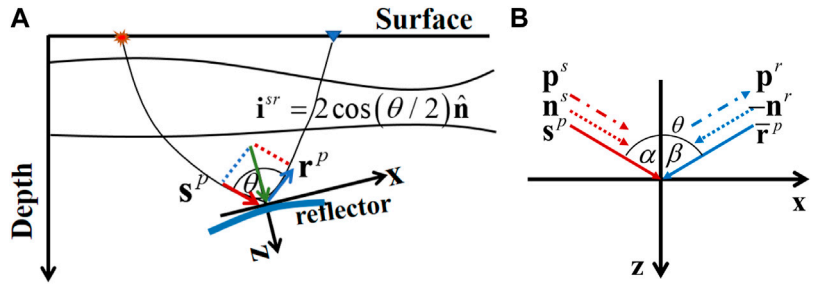

FIGURE 5 | The incident vector and reflected vector of pure P wave in observation coordinate system **(A)** and local coordinate system **(B)**. The coordinate observation system is constructed along the horizontal surface and vertical depth. The illumination vector $\mathbf{i}^{sr}$, used to describe the relationship between the incident wave and reflected wave, is related to the vertical directions of the reflector and opening angle. To simplify their representation, the local coordinate system is constructed along with tangential and vertical directions of the reflector. In a local coordinate system, the incident vector and reflected vector can be described by the incident angle α or opening angle θ.

slowly in the space-time domain, their temporal and spatial derivatives are small enough to be ignored.

Substituting the plane wave definitions (**Eq. 12**) into **Eqs 4**, **7**, **11**, we obtain an expression with the assumption of the plane wave as follows:

$$I_{pp} = \int |\mathbf{s}^p||\mathbf{r}^p| R_{pp} (\mathbf{p}^s \cdot \mathbf{p}^r) e^{ik(\mathbf{n}^s - \mathbf{n}^r)\cdot\mathbf{x}} dt, \tag{13A}$$

$$I_{pp}^{lap} = -\int |\mathbf{s}^p||\mathbf{r}^p| R_{pp}\omega^2 \left\{ \left[(n_x^s - n_x^r)^2 + (n_z^s - n_z^r)^2 \right] (p_x^s p_x^r + p_z^s p_z^r) \right\} e^{ik(\mathbf{n}^s - \mathbf{n}^r)\cdot\mathbf{x}} dt, \tag{13B}$$

and

$$I_{pp}^{pse-lap} = -\int |\mathbf{s}^p||\mathbf{r}^p| R_{pp}\omega^2 \left[(n_x^s - n_x^r)^2 p_x^s p_x^r + (n_z^s - n_z^r)^2 p_z^s p_z^r \right] e^{ik(\mathbf{n}^s - \mathbf{n}^r)\cdot\mathbf{x}} dt. \tag{13C}$$

In the 2D case of incident pure P wave, the reflected P wave without wave conversion would be obtained in an observation coordinate system along the horizontal surface and vertical depth. As shown in **Figure 5A**, the geological structure information of the reflector has been introduced in the descriptions of particle velocity vectors in the observation coordinate system. A local coordinate system (as shown in **Figure 5B**) is constructed along with tangential and vertical directions of the reflector to simplify the representation of vectors in the source and receiver wavefield. As for pure P wave, the polarization vector $\mathbf{p}^s$ is parallel to the propagation vector $\mathbf{n}^s$ with the same positive direction. In the local coordinate system, the polarization vector $\mathbf{p}^s$ and propagation vector $\mathbf{n}^s$ of incident vector $\mathbf{s}^p$ in source wavefield should be described by the incident angle α as follows:

$$\mathbf{p}^s = \sin\alpha\,\vec{i} + \cos\alpha\,\vec{k}, \tag{14A}$$

and

$$\mathbf{n}^s = \sin\alpha\,\vec{i} + \cos\alpha\,\vec{k}. \tag{14B}$$

Unlike source wavefield, the pure P wave in receiver wavefield should be described by conjugation of a reflected vector $\bar{\mathbf{r}}^p$. Its propagation direction is the opposite to that of the reflected wave, and polarization direction is the same as the reflected wave. The polarization vector $\mathbf{p}^s$ is parallel to the propagation vector $\mathbf{n}^s$ with the same positive direction for reflected pure P wave $\mathbf{r}^p$. When it comes to reflected pure P wave, the polarization vector $\mathbf{p}^r$ and propagation vector $\mathbf{n}^r$ should be described in the local coordinate system by the reflected angle α as follows:

$$\mathbf{p}^r = -\sin\alpha\,\vec{i} + \cos\alpha\,\vec{k}, \tag{15A}$$

and

$$\mathbf{n}^r = \sin\alpha\,\vec{i} - \cos\alpha\,\vec{k}. \tag{15B}$$

According to the descriptions of incident vector (**Eq. 14**) and conjugation of reflected vector (**Eq. 15**), we can rewrite the scalar imaging condition, the scalar imaging condition with a Laplace filter, and the scalar imaging condition with a pseudo-Laplace filter in the local Cartesian coordinate system as follows:

$$I_{pp} = \int |\mathbf{s}^p||\mathbf{r}^p| R_{pp} \cos\theta e^{ik(\mathbf{n}^s - \mathbf{n}^r)\cdot\mathbf{x}} dt, \tag{16A}$$

$$I_{pp}^{lap} = -\int |\mathbf{s}^p||\mathbf{r}^p| R_{pp}\omega^2 2\cos\theta(\cos\theta + 1) e^{ik(\mathbf{n}^s - \mathbf{n}^r)\cdot\mathbf{x}} dt, \tag{16B}$$

and

$$I_{pp}^{pse-lap} = -\int |\mathbf{s}^p||\mathbf{r}^p| R_{pp}\omega^2 (\cos\theta + 1)^2 e^{ik(\mathbf{n}^s - \mathbf{n}^r)\cdot\mathbf{x}} dt. \tag{16C}$$

Here, $\theta = 2\alpha$ is the opening angle. The above-mentioned imaging algorithms need to be separated into terms related to amplitude and phase. As for the phase-related item, they agree with each other by the form of $e^{ik(\mathbf{n}^s - \mathbf{n}^r)\cdot\mathbf{x}}$. The phase-related item is dependent on the illumination vector $\mathbf{i}^{sr} = \mathbf{n}^s - \mathbf{n}^r$, defined by Lecomte (2008). The illumination vector $\mathbf{i}^{sr}$ satisfies the following relationship $\mathbf{i}^{sr} = \mathbf{n}^s - \mathbf{n}^r = 2\cos(\theta/2)\hat{\mathbf{n}}$, where $\hat{n}$ is a unit normal vector at each reflector. In a local coordinate system, a unit normal vector can be described as $\hat{\mathbf{n}} = (0, 1)$ regardless of the inclination of a reflector. Phase-related items are dependent on the opening angle θ. In particular, $\mathbf{i}^{sr} = 0$ while $\theta = 180°$. It indicates that $\mathbf{i}^{sr}$ will be zero at the reflectors when the incident wave and reflected wave are with the same propagating path.

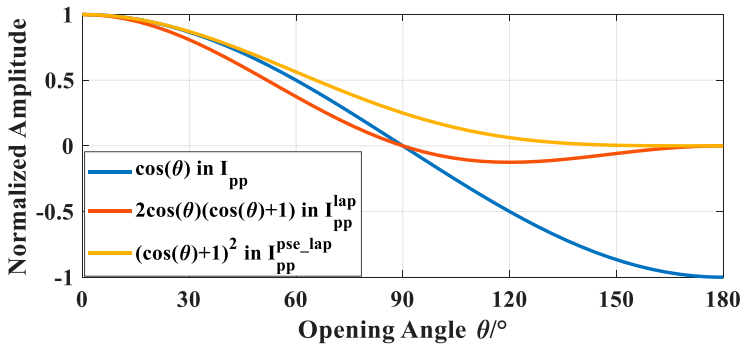

FIGURE 6 | The variation of a weighting factor in the scalar imaging condition, the scalar imaging condition with a Laplace filter and with a pseudo-Laplace filter. Note that the blue curve of the weighting factor cos θ will cross through the axis whose amplitude is zero and reach -1 while the opening angle is 180°. The red curve of the weighting factor 2 cos θ(cos θ + 1) goes through the axis whose amplitude is zero and reaches 0 while the opening angle is 180°. The yellow curve of the weighting factor (cos θ + 1)^2 range 1–0 without change of positive and negative sign.

Otherwise, the amplitude-related items in I_{pp}, I_{pp}^{lap}, and $I_{pp}^{pse-lap}$ imaging algorithms are different from each other. Factor $|\mathbf{s}^p||\mathbf{r}^p|R_{pp}$, coexisting in The above-mentioned imaging conditions, is useful for seismic inversion interpretation. Once the Laplace filter and pseudo-Laplace filter are introduced, the scalar imaging algorithms are influenced by angular frequency ω^2. The introduction of ω^2 weakens the amplitude of low-frequency data and enhances the amplitude of high-frequency data, changing the spectrum of images and damaging effective low-frequency information. To maintain the spectrum of images and recover their effective low-frequency information, reasonable time integration is needed (Liu et al., 2010). Furthermore, the above-mentioned imaging algorithms are dependent on different weighting factors:

$$w_{pp} = \cos\theta, \tag{17A}$$

$$w_{pp}^{lap} = -2\cos\theta(\cos\theta + 1), \tag{17B}$$

and

$$w_{pp}^{pse-lap} = -(\cos\theta + 1)^2. \tag{17C}$$

Here, w_{pp},w_{pp}^{lap}, and $w_{pp}^{pse-lap}$ are the introduced weighting factor of the scalar imaging condition, the scalar imaging condition with a Laplace filter, and the scalar imaging condition with a pseudo-Laplace filter, respectively. From **Eq. 17**, we can see that weighting factors vary with the opening angle θ.

The variation of the weighting factor for the opening angle θ is shown in **Figure 6**. For visual display, the amplitude is normalized by the corresponding max value. When the opening angle θ increases from 0° to 180°, the weighting factor w_{pp} (represented by the blue curve) in the scalar imaging condition ranges from 1 through 0 to −1. The polarity of the image is reversed while the sign of weight factor changes from positive to negative near 90°, and the backscattering noise is generated by dot product cross-correlation of two wavefields with an opening angle of 180° or close to 180°. By introducing the Laplace filter, the weighting factor w_{pp}^{lap} (represented by the red curve) will be 0 near 180°, which indicates that backscattering noise has been suppressed. However, the sign of the weighting factor w_{pp}^{lap} still changes from positive to negative around 90°. In other words, the Laplace filter fails to correct the polarity reversal in PP images by scalar imaging conditions. Furthermore, the pseudo-Laplace filter has been introduced in scalar imaging conditions, and its weighting factor $w_{pp}^{pse-lap}$ (represented by the yellow curve) is in the range of 1–0. Similar to the Laplace filter, for backscattering waves with 180° or near 180° opening angles, the weighting factor $w_{pp}^{pse-lap}$ is zero. Unlike the Laplace filter, the weighting factor $w_{pp}^{pse-lap}$ only ranges from 1 to 0, and its sign is always positive. Therefore, the weighting factor can suppress backscattering noise and correct the reversed polarity. As for the PP image by the scalar imaging condition with a pseudo-Laplace filter, the backscattering noise has been suppressed and polarity reversal has been corrected.

NUMERICAL EXAMPLES

This section presents a two-layer flat model and a four-layer inclined model to demonstrate the challenges of backscattering noise and polarity reversal in PP images caused by scalar imaging conditions. Moreover, it shows how to suppress them by the pseudo-Laplace filter. Then, using numerical values, we investigate the amplitude variation versus the opening angle to demonstrate the consistency of the pseudo-Laplace filter. The Marmousi 2 model (Martin et al., 2006) is then used to demonstrate the effectiveness and advantages of the pseudo-Laplace filter in the suppression of backscattering artifacts and correction of polarity reversal.

When it comes to vector-based elastic RTM, the decoupled elastic wave equation (Xiao and Leaney, 2010; Du et al., 2017) generates source and receiver wavefield of decoupled P wave. Furthermore, the source normalization by decoupled P-wave source wavefield should be introduced to balance the energy between the shallow and deep layers.

The Two-Layer Flat Model

The two-layer flat model shown in **Figure 7** is $10 \times 2km$. At a depth of 1 km, there is one flat interface. The first and second layer's P-wave velocities would be 2400 m/s and 2700 m/s,

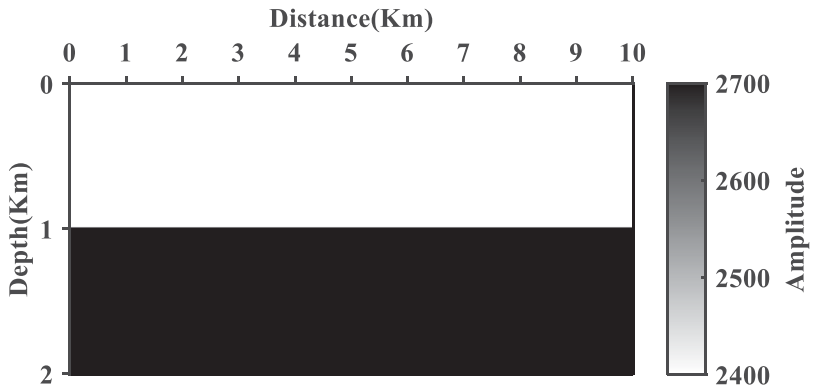

FIGURE 7 | The P-wave velocity of the two-layer flat model, whose S-wave velocity and density are satisfied with $v_s = v_p/1.73$ and $\rho = 2300g/cm^2$, respectively.

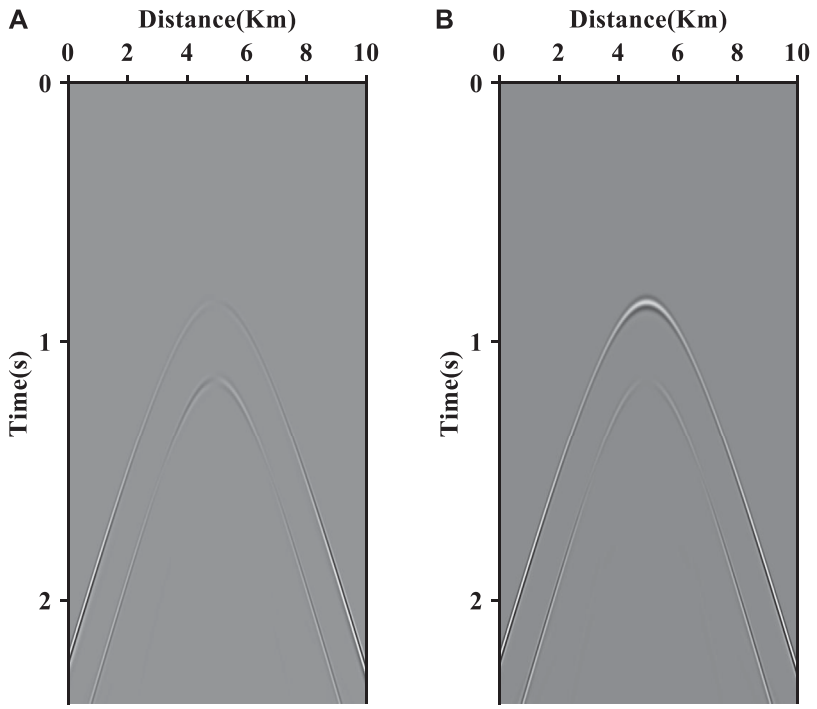

FIGURE 8 | The synthetic multicomponent seismic record without direct wave: **(A)** x-component and **(B)** z-component.

respectively. The S-wave velocity is consistent with the relationship $v_s = v_p/1.73$, and density is set to 1.0 g/cm^3. It contains 1000 points in the horizontal direction and 200 points in the vertical direction, with a space interval of 10 m. **Figure 8** shows a synthetic seismic record generated using double receiving observation geometry, with a shot located at a depth of 10 m. At a depth of 10 m, there are 500 receivers with a 20 m receiver interval. As a result, the maximum offset is up to 5 km. The synthetic seismic data are generated using an explosive source of Ricker wavelet with a peak frequency of 20 Hz. The time interval is 0.8 ms, and the total record time is 2.4 s.

The migrated PP images by scalar imaging conditions, scalar imaging conditions with a Laplace filter, and scalar imaging conditions with a pseudo-Laplace filter are shown in **Figure 9**. It is evident that backscattering artifacts (marked by the red arrow) influence the PP image by the scalar imaging condition (shown in **Figure 9A**) and have been attenuated effectively in the PP image with the application of a Laplace filter (shown in **Figure 9B**) and with a pseudo-Laplace filter (shown in **Figure 9C**). Apart from backscattering noise, the other noise, such as polarity reversal, also occurs at the interface. As for the interface of 1 km depth, the maximum incident angle reaches 68.2°, over critical angle $\arcsin(v_{p1}/v_{p2}) = 62.73°$ and polarity reversed angle 45°. Thus, all

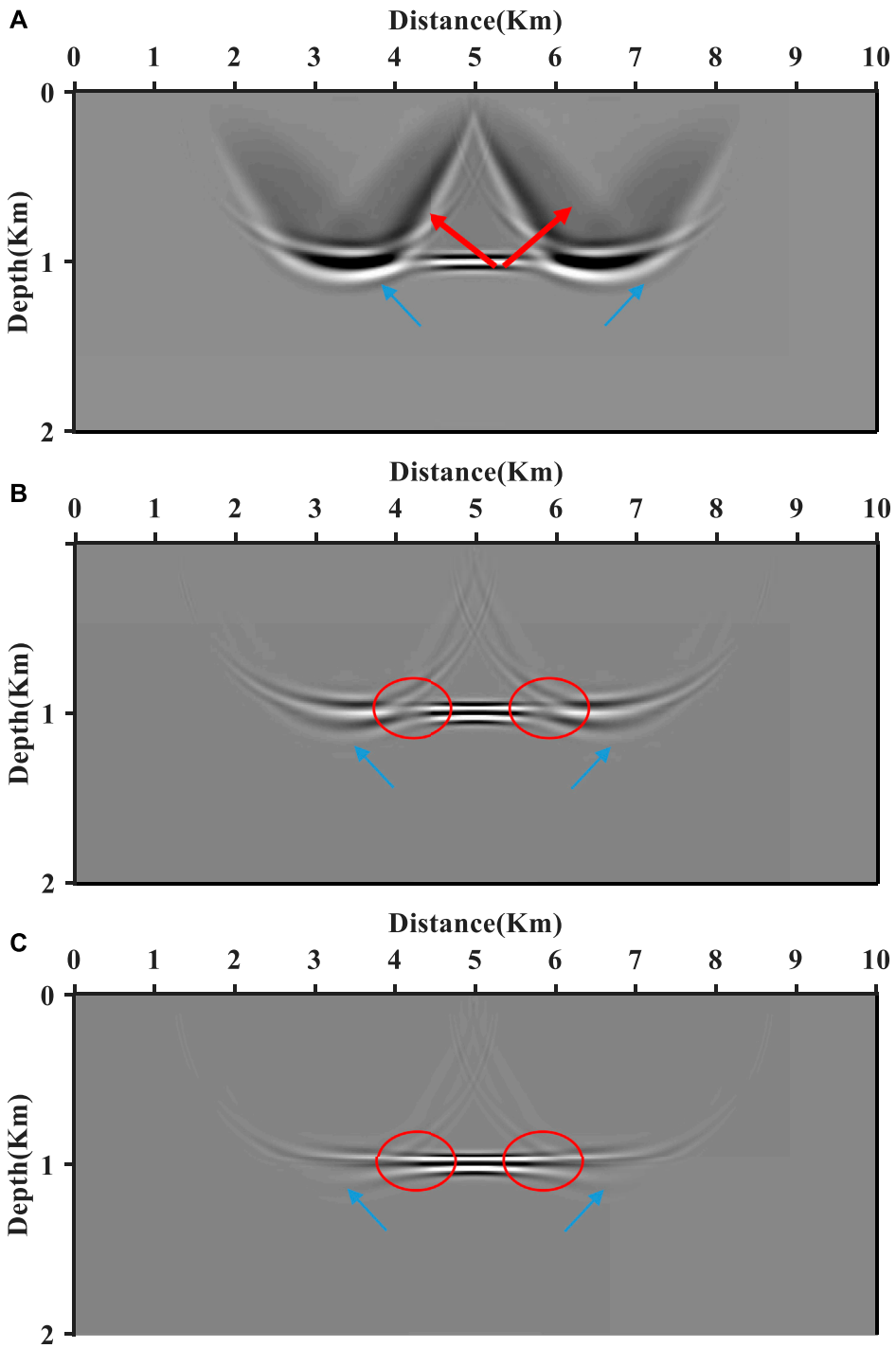

FIGURE 9 | PP migrated images of the two-layer flat model by the scalar imaging condition **(A)**, the scalar imaging condition with a Laplace filter **(B)**, and the scalar imaging condition with a pseudo-Laplace filter **(C)**. The backscattering noise (marked by the red arrow) has been effectively suppressed in PP images by scalar imaging conditions with a Laplace filter and a pseudo-Laplace filter. Furthermore, the polarity reversal (marked by the red circle) has been corrected in the PP image by the scalar imaging condition with a pseudo-Laplace filter.

three migrated PP images are similar and encounter phase-distorted inhomogeneous waves, such as refracted waves (marked by blue arrows) around 1.9 km distance. Besides, only PP images without or with the Laplace filter suffer from the polarity reversal around 1 km distance (marked by red circles), which would have been corrected in the PP image with a pseudo-Laplace filter. Therefore, the phase axis of the PP image with the pseudo-Laplace filter is more continuous than the PP image with the Laplace filter.

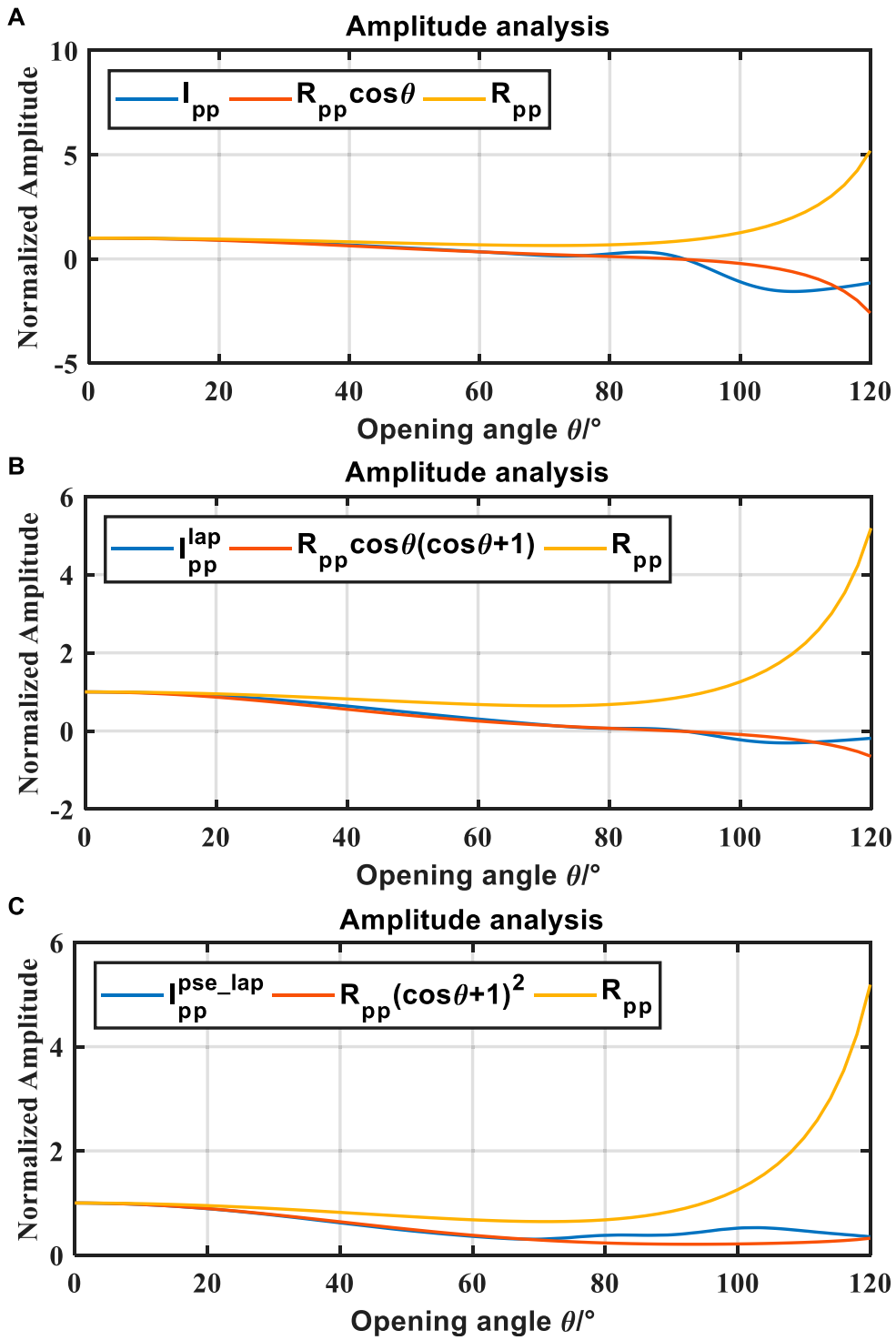

FIGURE 10 | The comparison between the analytical reflection coefficient R_{pp} (yellow curves), the weighting theoretical reflection coefficient (red curves) and normalized amplitudes (blue curves) extracted from PP images by the scalar imaging condition **(A)**, the scalar imaging condition with a Laplace filter **(B)**, and the scalar imaging condition with a pseudo-Laplace filter **(C)** in **Figure 9**. The reflection coefficient (yellow curves) is solved by the Zoeppritz equation with the elastic parameters of the two-layer layer model, and the normalized amplitudes in PP images have been converted to variation with the opening angle.

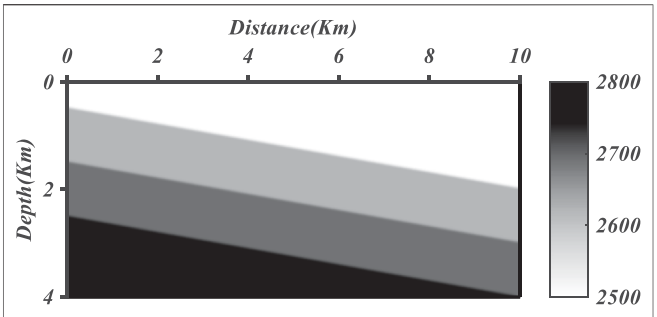

FIGURE 11 | The P-wave velocity of the four-layer inclined model, whose S-wave velocity and density are satisfied with $v_s = v_p/1.73$ and $\rho = 2300g/cm^2$, respectively.

Additionally, we measure the amplitudes of these images at the interface at a depth of 1 km and convert the offset variable to the opening angle variable using geological and elastic parameters. Then, we compare these amplitudes (blue curves) from **Figure 9** with the theoretical reflection coefficient R_{pp} (yellow curves) and the corresponding weighting factor (red curves), respectively. The analytical solution R_{pp} (yellow curves) is calculated by solving the Zoeppritz equation with the elastic parameters of the two-layer layer model. The opening angle ranges from 0 to 120° to avoid phase distortion when the incidence angle is greater than the critical angle of 62.73°. The extracted amplitudes (blue curves) match well with the weighting theoretical reflection coefficient (red curves) up to approximately 80°, verifying the correctness of the theoretical analysis.

What is more, the extracted amplitudes have higher values than the corresponding weighting theoretical reflection coefficient at large angles of incidence and then decline to zero due to the limited acquisition space. Both Laplace and pseudo-Laplace filters would fail to maintain the amplitude of images at large incidence. **Figure 10A** shows the extracted amplitudes from **Figure 9A** and weighting theoretical reflection coefficient $R_{pp}\cos\theta$; **Figure 10B** shows the extracted amplitudes from **Figure 9B** and weighting theoretical reflection coefficient $R_{pp}\cos\theta(\cos\theta + 1)$. They both change their signs at approximately 90° angle of incidence. However, **Figure 10C** shows the extracted amplitudes from **Figure 9C** and weighting theoretical reflection coefficient $R_{pp}(\cos\theta + 1)^2$, and its sign remains unchanged at any opening angle. Therefore, the consistency of the pseudo-Laplace filter has been demonstrated by the analysis of amplitude variation versus the opening angle, which indicated that polarity reversal had been corrected.

The Four-Layer Inclined Model

The four-layer inclined model, as shown in **Figure 11**, is $10 \times 4km$. There are three inclined interfaces with a 10° dip angle at 1.5, 2.5, and 3.5 km depth, respectively. The P-wave velocity of the first layer, second layer, third layer, and fourth layer would be 2500 m/s, 2600 m/s, 2700 m/s, and 2800 m/s, respectively. The S-wave velocity satisfies the relationship $v_s = v_p/1.73$, and density is set to constant 1 g/cm^3. It contains 1000 points and 400 points in the horizontal and vertical directions with a space interval of 10 m. Synthetic data are generated with double receiving observation geometry, where the shot is located at a depth of 10 m and a distance of 7 km. There are 500 receivers with a receiver interval of 20 m at a depth of 10 m. Therefore, the maximum offset is 7 km. The explosive source of the Ricker wavelet with 30 Hz peak frequency is set to generate the synthetic seismic data. The time interval is 1.0 ms, and the total record time is 3 s.

The migrated PP images by scalar imaging conditions with a Laplace filter and scalar imaging conditions with a pseudo-Laplace filter are shown in **Figure 12**. It is evident that backscattering artifacts (marked by the red arrow) influence the PP image by scalar imaging conditions (shown in **Figure 12A**) and have been attenuated effectively in the PP image with the application of a Laplace filter (shown in **Figure 12B**) and with a pseudo-Laplace filter (shown in **Figure 12C**). Apart from backscattering noise, the other noise, such as polarity reversal, also occurs at images along with the interfaces. As for the first interface, the maximum incident angle reaches 75°, which is over critical angle $\arcsin(v_{p1}/v_{p2}) = 74.05°$, and polarity reversed angle 45° at the maximum offset of 7 km. Therefore, the polarity reversal around 5 km (marked by a red circle) and phase-distorted homogeneous wave such as refracted wave (marked by the blue arrow) would be introduced in PP images without or with a Laplace filter. As for the second interface, the maximum incident angle of 58°, equal to 116° opening angle, is less than the critical angle $\arcsin(v_{p2}/v_{p3}) = 74.35°$ and bigger than the polarity reversed angle of 45°. PP images without or with the Laplace filter of the second interface only encounter a polarity reversal problem around 4 km without phase aberration. As for the third interface, the maximum incident angle of 43° is near the polarity reversed angle of 45° and less than the critical angle $\arcsin(v_{p2}/v_{p3}) = 74.64°$. The amplitude of the phase-reversed image is too little to influence the final stacked result. Furthermore, the polarity reversals at three interfaces have been corrected in the PP image with a pseudo-Laplace filter. Therefore, the phase axis of the PP image with a pseudo-Laplace filter is more continuous than the PP image with a Laplace filter.

To analyze the amplitude variation versus opening angle, we pick up the max amplitude of these images along the second interface and convert the offset variable to the opening angle variable with a geological structure. Since the first interface is affected by the direct wave and heterogeneous wave such as refracted wave, the second interface has been utilized. Once the amplitude variation has been picked up, the smoothing and normalization are required to avoid interference of other factors such as phase. As shown in **Figure 13**, the variations of normalized amplitude in three images match the variations of normalized weighting with an opening angle ranging from 0 to near 116°, the maximum opening angle of the geometry. Once the opening angle exceeds the maximum, normalized amplitudes would be zero. Around 90° opening angle, change the numerical symbols of amplitude that occurs in the PP image (represented by the blue curve) and the PP image with a Laplace filter (represented by the red curve). However, the yellow curve, representing the PP image with a

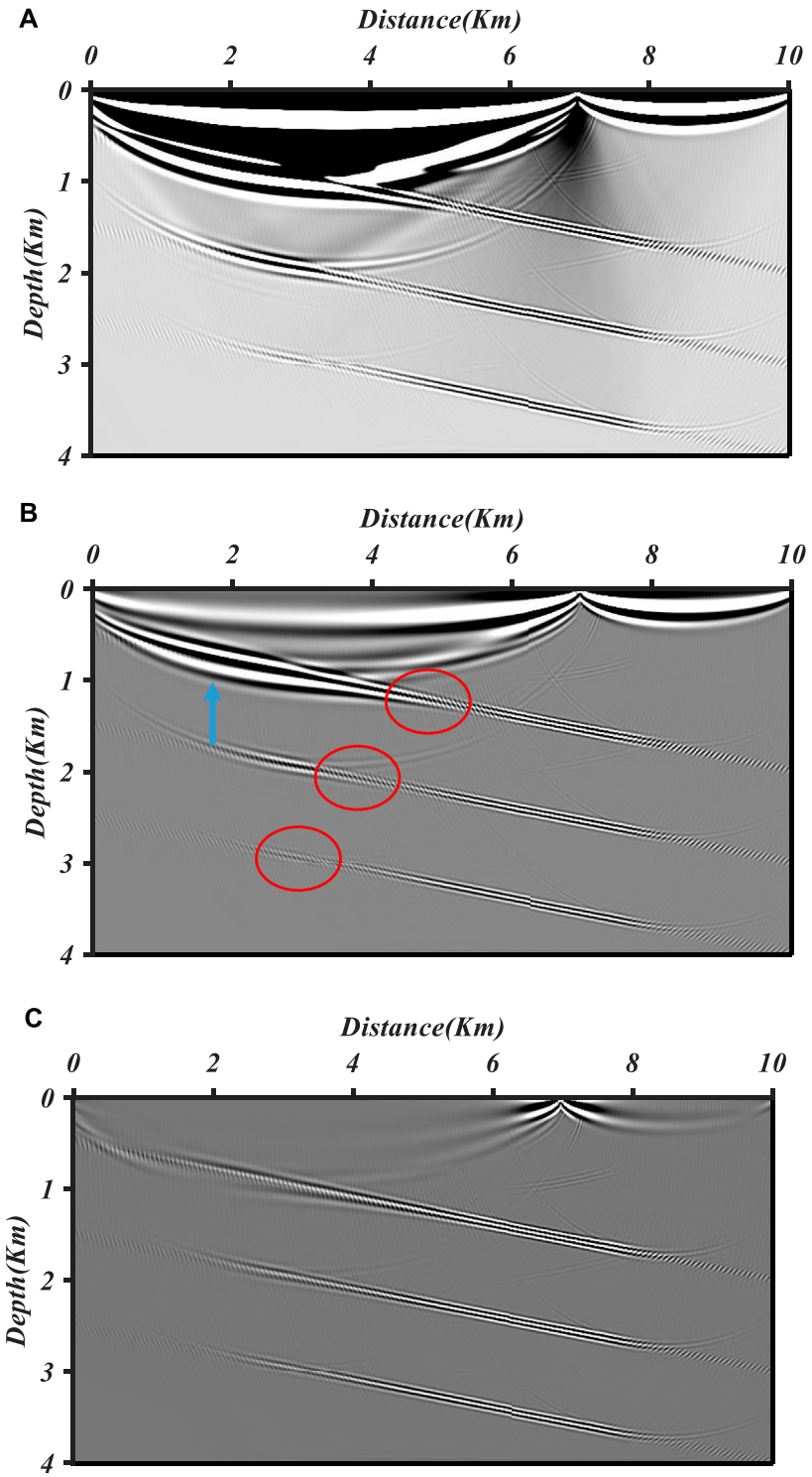

FIGURE 12 | PP migrated images of the four-layer inclined model by the scalar imaging condition **(A)**, the scalar imaging condition with a Laplace filter **(B)**, and the scalar imaging condition with a pseudo-Laplace filter **(C)**. The backscattering noise (marked by the red arrow) has been effectively suppressed in PP images by scalar imaging conditions with a Laplace filter and a pseudo-Laplace filter. Furthermore, the polarity reversal (marked by the red circle) has been corrected in the PP image by the scalar imaging condition with a pseudo-Laplace filter.

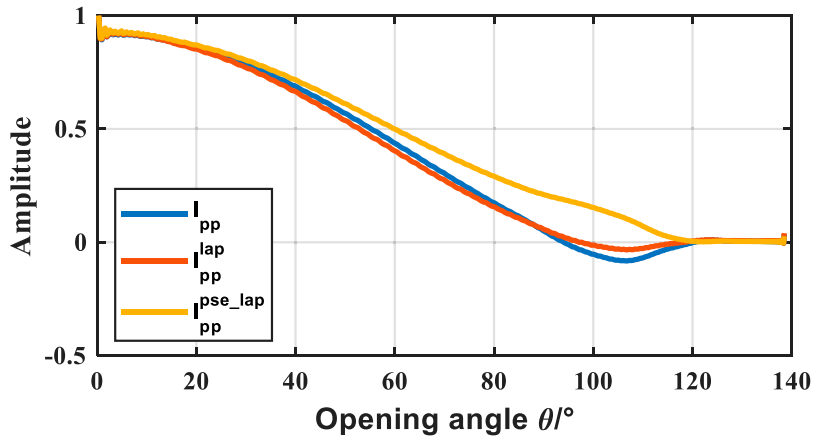

FIGURE 13 | The variation of normalized amplitude in PP images with the opening angle. Numerically, amplitude symbols change with the P-wave incident angle reaching 45°, and the offset is around 3500 m in both the PP image by the scalar imaging condition (blue curve) and the scalar imaging condition with a Laplace filter (red curve). In contrast, amplitude symbols are consistent in the PP image by the scalar imaging condition with a pseudo-Laplace filter (yellow curve).

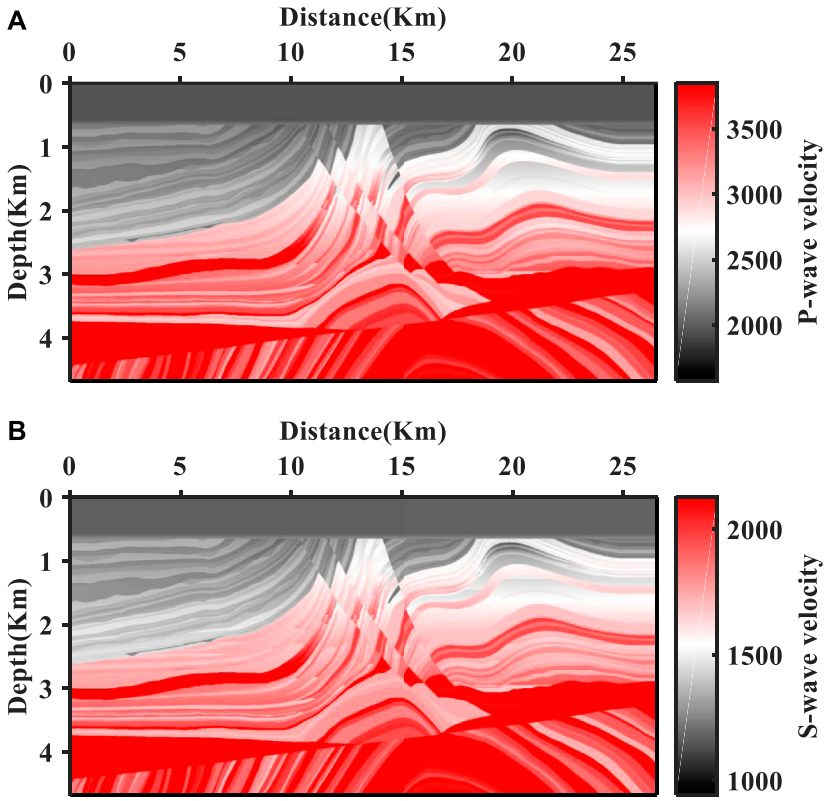

FIGURE 14 | The P-wave velocity of the elastic Marmousi 2 model **(A)** and the S-wave velocity of the elastic Marmousi 2 model **(B)** and the density is constant of 1 g/cm^3.

pseudo-Laplace filter, has a consistent numerical symbol in amplitude. Therefore, the consistency of the pseudo-Laplace filter has been demonstrated by the analysis of amplitude variation versus the opening angle, which indicated that polarity reversal had been corrected.

Marmousi 2 Model

The Marmousi 2 model is used in this example to show how the pseudo-Laplace filter can effectively suppress backscattering noise, resolve polarity reversal, and generate a high-quality PP image in complex geological structures.

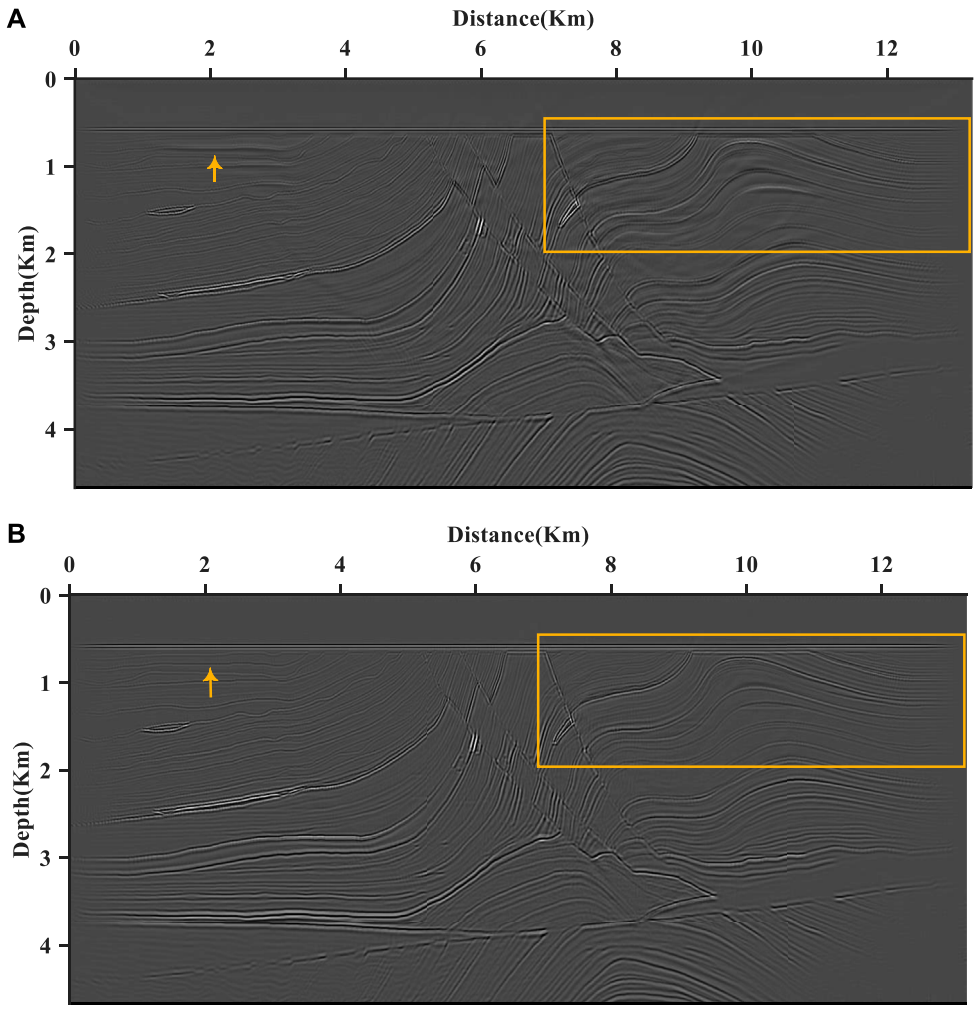

FIGURE 15 | The PP images of the Marmousi 2 model by the scalar imaging condition with the Laplace filter **(A)** and with the pseudo-Laplace filter **(B)**. The two images embody the structural characteristics of the model. The overall appearance of Panel B is more apparent and events in the shallow layer are more continuous than those in Panel A. Furthermore, the backscattering noise of Panel A is more serious than that in Panel B.

As shown in **Figure 14**, the modified Marmousi 2 model (Martin et al., 2006) contains 1325 points in the horizontal direction with 10 m sample interval and 934 points in the vertical direction with 5 m sample interval. Thus, the size of the Marmousi 2 model is $13.25 \times 4.67km$. The P-wave velocity ranges from 1800 m/s to 4600 m/s, the S-wave velocity ranges from 1000 m/s to 2000 m/s, and density is the constant of 1 g/cm^3. The full-receiving geometry, where 265 shots are excited with a 50 m shot interval at a depth of 10 m, and 1325 receivers are located with a 10 m receiver interval at the surface, is constructed to generate the seismic record. The source function is a Ricker wavelet with a peak frequency of 30 Hz. The recording time interval is 1.0 ms, and the recording length is 4.3 s.

Figure 15A is the migrated PP image by the scalar imaging condition with the Laplace filter, and **Figure 15B** is the migrated PP image by the scalar imaging condition with a pseudo-Laplace filter. The backscattering noise contamination has been suppressed successfully in these two images, while some backscattering noise still resides in the PP image with Laplace (marked by the red arrow). Furthermore, both of them have embodied the structural character of the model. Compared with the PP image with Laplace of **Figure 15A**, the overall appearance of **Figure 15B** is more apparent, including the shallow fault in detail. That is related to the weighting factor of the pseudo-Laplace filter is stronger than that of the Laplace filter. Furthermore, the events in the shallow layer of **Figure 15B** are more continuous than those of **Figure 15A**.

We further extracted the traces from PP images with a Laplace filter (**Figure 15A**) and a pseudo-Laplace filter (**Figure 15B**) at a depth of 1.32 km. As shown in **Figure 16**, we compare the amplitude of trace extracted from **Figure 15A** (blue curve) and **Figure 15B** (red curve) with the theoretical reflection coefficient R_{pp} (yellow curves). The Zoeppritz equation calculates the theoretical reflection coefficient R_{pp} at normal incidence. The variation trends of traces are consistent with

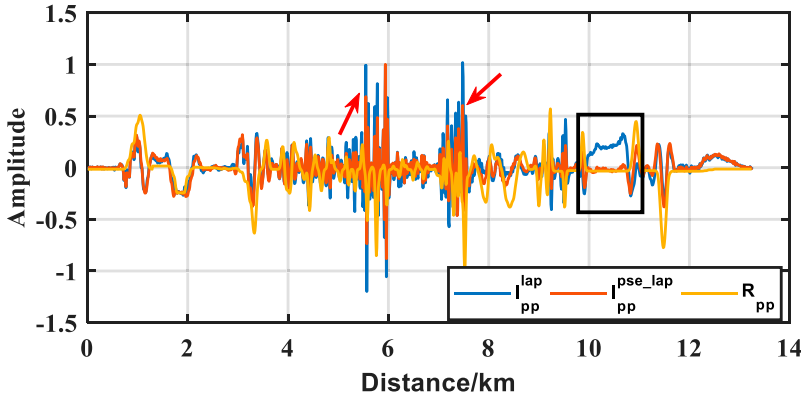

FIGURE 16 | The comparison between normalized amplitudes of theoretical reflection coefficient R_{pp} (yellow curves) calculated by Zoeppritz equation and traces extracted from **Figure 15A** (blue curve) and **Figure 15B** (red curve) at a depth of 1.32 km. The variation trends of traces are consistent with the theoretical reflection coefficient, and the amplitude of trace from $I_{pp}^{pse\_lap}$ (red curve) is generally slightly larger than that from I_{pp}^{lap} (blue curve). However, the amplitude of trace from $I_{pp}^{pse\_lap}$ (red curve) is smaller than that from I_{pp}^{lap} (blue curve) in the fault area (marked by the red arrow). Moreover, the phase of I_{pp}^{lap} (blue curve) is opposite to that of $I_{pp}^{pse\_lap}$ (red curve) and theoretical solution (yellow curve) at the cover of anticline where sub-cover oil and gas reservoirs develop, marked by a black rectangular box.

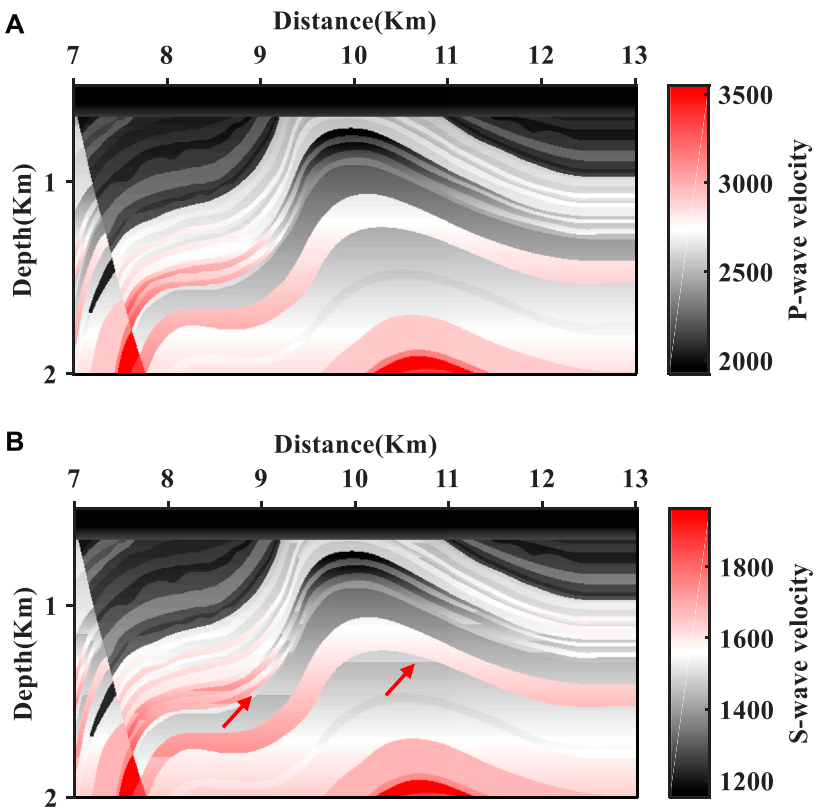

FIGURE 17 | The partial enlargements of the P-wave velocity of the elastic Marmousi 2 model **(A)** and the S-wave velocity of the elastic Marmousi 2 model **(B)**.

the theoretical reflection coefficient. Moreover, the amplitude of trace from $I_{pp}^{pse\_lap}$ (red curve) is generally slightly larger than that from I_{pp}^{lap} (blue curve) because the weighting factor $2\cos\theta(\cos\theta+1)$ of PP images with a Laplace filter is stronger than the weighting factor $(\cos\theta+1)^2$ of PP images with the pseudo-Laplace filter at small incident angles. However, there is a big difference between amplitudes and theoretical value in the fault area at 5–6 km and 7–8 km. The inaccuracy is caused by a false reflected wave where diffraction wave and multiple waves exist. Moreover, at the cover of anticline where sub-cover

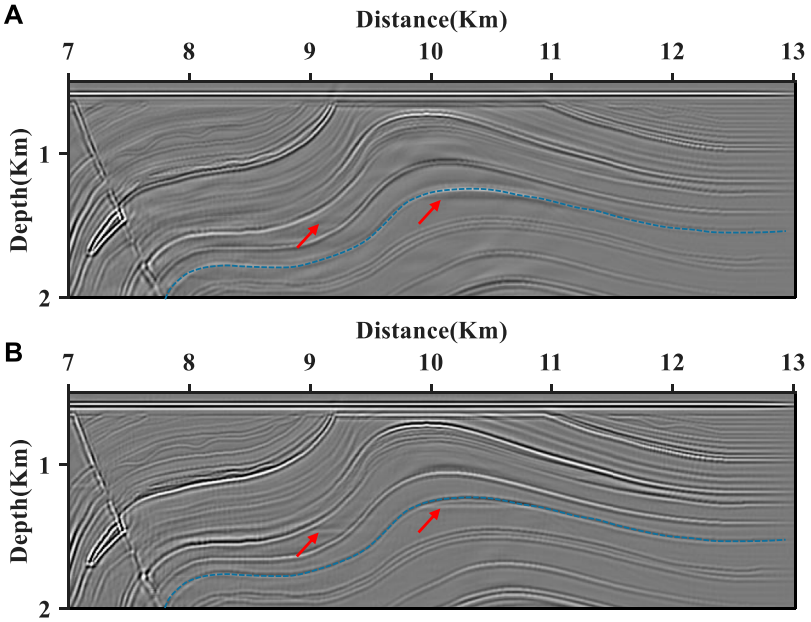

FIGURE 18 | The partial enlargements of PP images of the Marmousi 2 model by the scalar imaging condition with the Laplace filter (Panel A) and with the pseudo-Laplace filter (Panel B). The polarity of the event (such as events marked by the blue curve) in Panel B is more continuous than that in Panel A. Furthermore, clearer interfaces and less disturbance of the oil and gas reservoirs at sub-cover (marked by the red arrow), indicated by the partial enlargements of the elastic Marmousi 2 model in **Figure 17B**, are located in Panel B.

oil and gas reservoirs develop with 10–11 km distance, the phase of stacked I_{pp}^{lap} (blue curve) is opposite to that of stacked $I_{pp}^{pse\_lap}$ (red curve) and theoretical solution (yellow curve), as marked by a black rectangular box. The phase reversal originates from polarity reversal in the PP image with the Laplace filter and polarity correction in the PP image with the pseudo-Laplace filter at large incidence.

To observe clearly, we intercept the part of the Marmousi 2 model with a distance from 7–13 km and a depth from 0.5 to 4 km. **Figures 17A,B** are the partial enlargements of the P-wave velocity of the elastic Marmousi 2 model and S-wave velocity of the elastic Marmousi 2 model amplified, respectively. Correspondingly, **Figure 18A** is a partial enlargement of the PP image of the Marmousi 2 model by the scalar imaging condition with a Laplace filter (**Figure 15A**), and **Figure 18B** is a partial enlargement of the PP image of the Marmousi 2 model by the scalar imaging condition with the pseudo-Laplace filter (**Figure 15B**). Even as the polarity reversal described by **Figure 16**, the phase of the stacked PP image with a Laplace filter is opposite to that of the stacked PP image with a pseudo-Laplace filter and is no longer continuous at the cover of the anticline. As marked by the blue curve, the phase of the event in **Figure 18B** is more persistent than in **Figure 18A**, especially at the cover of an anticline. Furthermore, there is an oil and gas reservoir at sub-cover with the variation of S-wave velocity in **Figure 17B**. The disturbance at sub-cover (marked by the red arrow) succeeds to be imaged in **Figure 18A** but fails to be imaged in **Figure 18A**. Overall, the scalar imaging condition with a pseudo-Laplace filter generates a high-quality PP image in complicated geological structures.

DISCUSSIONS

The dot product cross-correlation scalar imaging condition, similar to the cross-correlation scalar wave field imaging condition, is a simple and effective imaging condition for vector-based wavefields. Naturally, the PP image by the dot product scalar imaging condition encounters backscattering noise, also being in cross-correlation imaging results, and polarity reversal problem caused by the weighting factor $\cos\theta$. The scalar imaging condition with a pseudo-Laplace filter has been developed as an analogy to the cross-correlation imaging condition with the Laplace filter. Analogous to the cross-correlation imaging condition with the Laplace filter, the scalar imaging condition with pseudo-Laplace filter has been proposed.

Table 1 is the comparative table for the Laplace filter and pseudo-Laplace filter characters from the backscattering noise, the polarity reversal, the spectral variation, and the computation cost. Overall, the pseudo-Laplace filter is similar to the Laplace filter in backscattering suppression, spectral variation, and computation cost. However, it is only the pseudo-Laplace filter that could correct the polarity reversal problem at large incidence. Therefore, the field data with large offset are suitable for the proposed pseudo-Laplace filter. As for the filters composed of second-order spatial derivatives, the angular frequency ω^2 has been introduced into the final image. Similar to spectrum modification of a Laplace filter, some low-frequency effective information of the PP image with a pseudo-Laplace filter would be suppressed due to the introduction of ω^2. Further study of the low-frequency compensation should be carried out.

TABLE 1 | The comparison between the Laplace filter and pseudo-Laplace filter.

	The Laplace filter	The pseudo-Laplace filter
Backscattering noise	Succeeds to suppress the backscattering noise	Succeeds to suppress the backscattering noise
Polarity reversal problem	**Fails** to correct polarity reversal problem	**Succeeds** to correct polarity reversal problem caused by the weighting factor $\cos\theta$
Spectral variation	Attenuates the low-frequency information and	Attenuates the low-frequency information
Additional computation or storage	Trivial additional storage or computation is required	Trivial additional storage or computation is required

The bold values emphasizes the difference between the Laplace filter and the pseudo-Laplace filter.

Once the low-frequency information is compensated, the weighting factor $(\cos\theta + 1)^2$ can be extracted by deciding the modulus of the incident wave and reflected wave. The weighting factor $(\cos\theta + 1)^2$is in a linear relationship with the opening angle. Furthermore, the scalar imaging condition with pseudo-Laplace can be used to extract common imaging point gathers. The SS image by the dot product–based scalar imaging condition suffers from the backscattering and polarity reversal, whose generating mechanism is similar to the PP image. The pseudo-Laplace filter can be extended to the SS image.

CONCLUSION

The PP image by the dot product–based scalar imaging condition will encounter the problem of polarity reversal when the opening angle exceeds 90° and backscattering noise when the opening angle is close to 180°. Based on the application of the Laplace filter for vector-based wavefield, we propose the pseudo-Laplace filter. Unlike the Laplace filter, the scalar imaging condition with a pseudo-Laplace filter only consists of second-order parallel-oriented partial derivatives of Cartesian components cross-correlation results and omits normal-oriented partial derivatives of Cartesian components cross-correlation result. Derivation with plane wave assumption shows that the proposed pseudo-Laplace filter, which depends on the weighting factor $(\cos\theta + 1)^2$, can correct polarity reversal and attenuate backscattering artifacts in the PP image. Numerical experiments of the two-layer flat model, four-layer inclined model, and Marmousi 2 model have verified the efficiency and accuracy of the pseudo-Laplace filter. The proposed pseudo-Laplace filter can provide the image with backscattering suppression and continuous phase, which can be further used to extract common imaging point gathers.

DATA AVAILABILITY STATEMENT

The original contributions presented in the study are included in the article/Supplementary Material; further inquiries can be directed to the corresponding authors.

AUTHOR CONTRIBUTIONS

QD and XZ contributed to the conception and design of the study. SZ organized the database and performed the statistical analysis. FZ and L-YF modified the manuscript. All authors contributed to manuscript revision and read and approved the submitted version.

FUNDING

This research was supported by the National Science Foundation of China (41930429 and 41774139), the China National "111" Foreign Experts Introduction Plan for Tight Oil & Gas Geology and Exploration, and the Deep-Ultradeep Oil & Gas Geophysical Exploration and Qingdao Applied Research Projects.

ACKNOWLEDGMENTS

The authors are grateful to the associate editor H-WZ and reviewers for reviewing this manuscript and Qamar Yasin for revising this manuscript.

REFERENCES

Aki, K., and Richards, P. (1980). *Quantitative Seismology[M]*. New York: W. H. Freeman.

Baysal, E., Kosloff, D. D., and Sherwood, J. W. C. (1983). Reverse Time Migration. *Geophysics* 48 (11), 1514–1524. doi:10.1190/1.1441434

Claerbout, J. F. (1971). Toward a Unified Theory of Reflector Mapping. *Geophysics* 36 (3), 467–481. doi:10.1190/1.1440185

Dellinger, J., and Etgen, J. (1990). Wave-field Separation in Two-Dimensional Anisotropic media. *Geophysics* 55 (7), 914–919. doi:10.1190/1.1442906

Du, Q., Gong, X., Zhang, M., Zhu, Y., and Fang, G. (2014). 3D PS-Wave Imaging With Elastic Reverse-Time Migration. *Geophysics* 79 (5), S173–S184. doi:10.1190/geo2013-0253.1

Du, Q., Guo, C., Zhao, Q., Gong, X., Wang, C., and Li, X.-y. (2017). Vector-based Elastic Reverse Time Migration Based on Scalar Imaging Condition. *Geophysics* 82 (2), S111–S127. doi:10.1190/geo2016-0146.1

Du, Q. Z., Zhu, Y. T., Zhang, M. Q., and Gong, X. F. (2013). A Study on the Strategy of Low Wavenumber Noise Suppression for Prestack Reverse Time Depth Migration. *Chin. J. Geophys.* 56 (7), 2391–2401. doi:10.6038/cjg20130725

Duan, Y., and Sava, P. (2015). Scalar Imaging Condition for Elastic Reverse Time Migration. *Geophysics* 80 (4), S127–S136. doi:10.1190/geo2014-0453.1

Elita Li, Y., Du, Y., Yang, J., Cheng, A., and Fang, X. (2018). Elastic Reverse Time Migration Using Acoustic Propagators. *Geophysics* 83 (5), S399–S408. doi:10.1190/geo2017-0687.1

Lecomte, I. (2008). Resolution and Illumination Analyses in Psdm: A ray-Based Approach. *Leading Edge* 27 (5), 650–663. doi:10.1190/1.2919584

Li, Z. C. (2007). Numeric Simulation of Elastic Wavefield Separation by Staggering Grid High-Order Finite-Difference Algorithm (In Chinese). *Oil Geophys. Prospect.* 42 (5), 510–515. doi:10.1016/S1872-5813(08)60001-8

Liu, H. W., Liu, H., Zou, Z., and Cui, Y. F. (2010). The Problem of Denoise and Storage in Seismic Reverse Time Migration (In Chinese): Chinese. *J. Geophys.* 53 (9), 2171–2180. doi:10.1002/cjg2.1530

Ma, D., and Zhu, G. (2003). Numerical Modeling of P-Wave and S-Wave Separation in Elastic Wavefield. *Oil Geophys. Prospect.* 38 (5), 482–486. doi:10.1007/BF02974893

Martin, G. S., Wiley, R., and Marfurt, K. J. (2006). Marmousi2: An Elastic Upgrade for Marmousi. *The Leading Edge* 25 (2), 156–166. doi:10.1190/1.2172306

McMechan, G. A. (1983). Migration by Extrapolation of Time-dependent Boundary Values*. *Geophys. Prospect* 31 (3), 413–420. doi:10.1111/j.1365-2478.1983.tb01060.x

Rocha, D., Tanushev, N., and Sava, P. (2016). Isotropic Elastic Wavefield Imaging Using the Energy Norm. *Geophysics* 81 (4), S207–S219. doi:10.1190/geo2015-0487.1

Sun, R., and McMechan, G. A. (1986). Pre-Stack Reverse-Time Migration for Elastic Waves With Application to Synthetic Offset Vertical Seismic Profiles. *Proc. IEEE* 74 (3), 457–465. doi:10.1109/PROC.1986.13486

Tang, C., and McMechan, G. A. (2018). Multidirectional-vector-based Elastic Reverse Time Migration and Angle-Domain Common-Image Gathers with Approximate Wavefield Decomposition of P- and S-Waves. *Geophysics* 83 (1), S57–S79. doi:10.1190/geo2017-0119.1

Wang, W., and McMechan, G. A. (2015). Vector-based Elastic Reverse Time Migration. *Geophysics* 80 (6), S245–S258. doi:10.1190/geo2014-0620.1

Whitmore, N. D. (1983). Iterative Depth Migration by Backward Time Propagation: SEG Technical Program Expanded Abstracts 1983. *Soc. Expl. Geophys.*, 382–385.

Xiao, X., and Leaney, W. S. (2010). Local Vertical Seismic Profiling (VSP) Elastic Reverse-Time Migration and Migration Resolution: Salt-Flank Imaging with Transmitted P-To-S Waves. *Geophysics* 75 (2), S35–S49. doi:10.1190/1.3309460

Yan, J., and Sava, P. (2008). Isotropic Angle-Domain Elastic Reverse-Time Migration. *Geophysics* 73 (6), S229–S239. doi:10.1190/1.2981241

Yang, J., Zhu, H., Huang, J., and Li, Z. (2018). 2D Isotropic Elastic Gaussian-Beam Migration for Common-Shot Multicomponent Records. *Geophysics* 83 (2), S127–S140. doi:10.1190/geo2017-0078.1

Yoon, K., and Marfurt, K. J. (2006). Reverse-Time Migration Using the Poynting Vector. *Geophys. Explor.* 59 (1), 102–107.

Youn, O. K., and Zhou, H. W. (2001). Depth Imaging with Multiples. *Geophysics* 66 (1), 246–255. doi:10.1190/1.1444901

Zhou, X., Chang, X., Wang, Y., and Yao, Z. (2018). Scalar Pp and Ps Imaging of Elastic Rtm by Wavefield Decoupling Method: SEG Technical Program Expanded Abstracts 2018. *Soc. Expl. Geophys.*, 2417–2421. doi:10.1190/segam2018-2995359.1

Zhu, H. (2017). Elastic Wavefield Separation Based on the Helmholtz Decomposition. *Geophysics* 82 (2), S173–S183. doi:10.1190/geo2016-0419.1

Conflict of Interest: The authors declare that the research was conducted in the absence of any commercial or financial relationships that could be construed as a potential conflict of interest.

Publisher's Note: All claims expressed in this article are solely those of the authors and do not necessarily represent those of their affiliated organizations, or those of the publisher, the editors and the reviewers. Any product that may be evaluated in this article, or claim that may be made by its manufacturer, is not guaranteed or endorsed by the publisher.

APPENDIX A: HADAMARD PRODUCT AND ITS APPLICATION

For the vectors **s** and **t** with the same dimension, we can obtain a new vector **w** by the Hadamard product $\circ$. The new vector **w** of Hadamard product, whose element is equal to the element-wise product of vectors s and t, is described as follows:

$$\mathbf{w} = \mathbf{s} \circ \mathbf{t} = \left(s_x t_x, s_y t_y, s_z t_z\right). \tag{A1}$$

By introducing the Hadamard product into vectors $\mathbf{s}^p$ and $\mathbf{r}^p$, the imaging vector $\mathbf{s}^p \circ \mathbf{r}^p$ at each imaging time can be expressed by the components as follows:

$$\left(s_x^p \overline{r}_x^p, s_y^p \overline{r}_y^p, s_z^p \overline{r}_z^p\right). \tag{A2}$$

frontiers in Earth Science

METHODS
published: 03 September 2021
doi: 10.3389/feart.2021.731697

Sparse Constrained Least-Squares Reverse Time Migration Based on Kirchhoff Approximation

Xu Hong-Qiao[1,2,3], *Wang Xiao-Yi*[1,2,3], *Wang Chen-Yuan*[1,2,3] *and Zhang Jiang-Jie*[1,2]*

[1]*Key Laboratory of Petroleum Resources Research, Institute of Geology and Geophysics, Chinese Academy of Sciences, Beijing, China,* [2]*Innovation Academy for Earth Science, Chinese Academy of Sciences, Beijing, China,* [3]*University of Chinese Academy of Sciences, Beijing, China*

Least-squares reverse time migration (LSRTM) is powerful for imaging complex geological structures. Most researches are based on Born modeling operator with the assumption of small perturbation. However, studies have shown that LSRTM based on Kirchhoff approximation performs better; in particular, it generates a more explicit reflected subsurface and fits large offset data well. Moreover, minimizing the difference between predicted and observed data in a least-squares sense leads to an average solution with relatively low quality. This study applies L1-norm regularization to LSRTM (L1-LSRTM) based on Kirchhoff approximation to compensate for the shortcomings of conventional LSRTM, which obtains a better reflectivity image and gets the residual and resolution in balance. Several numerical examples demonstrate that our method can effectively mitigate the deficiencies of conventional LSRTM and provide a higher resolution image profile.

Keywords: least-squares reverse time migration (LSRTM), kirchhoff approximation, L1-norm regularization, sparsity constraint, born approximation

OPEN ACCESS

Edited by:
Hao Hu,
University of Houston, United States

Reviewed by:
Jincheng Xu,
Southern University of Science and Technology, China
Chuang Li,
Xi'an Jiaotong University, China

****Correspondence:***
Zhang Jiang-Jie
zhangjj@mail.iggcas.ac.cn

Specialty section:
This article was submitted to Solid Earth Geophysics, a section of the journal Frontiers in Earth Science

Received: *28 June 2021*
Accepted: *17 August 2021*
Published: *03 September 2021*

Citation:
Hong-Qiao X, Xiao-Yi W, Chen-Yuan W and Jiang-Jie Z (2021) Sparse Constrained Least-Squares Reverse Time Migration Based on Kirchhoff Approximation. Front. Earth Sci. 9:731697. doi: 10.3389/feart.2021.731697

INTRODUCTION

Seismic migration is an inverse procedure of forward modeling, which can restore the interior of the earth medium with record data. Specifically, migration attempts to eliminate the effects caused by the process of physical propagation and obtain an image that clearly depicts the structural information of interest. Reverse time migration (RTM), a state-of-the-art seismic imaging method (Baysal et al., 1983; McMechan, 1983), identifies the aforementioned acausal procedure appropriately. Based on two-way wave equation, RTM is powerful for handling complex geological settings and velocity with dramatic variation in the lateral direction. Therefore, it can deal with steep dips and salt dome better than conventional migration (Zhu and Lines, 1998; Yoon et al., 2003; Liu et al., 2010). However, most migration methods, including RTM, use the adjoint operator to compute the image instead of the inverse operator (Tarantola, 1984). Practical data suffers from many factors, such as irregular acquisition geometry and limited aperture of the acquisition system. These deficiencies generate artifacts and degrade the resolution. To overcome these limitations, least-squares migration (LSM) was proposed to combine with RTM (Liu et al., 2011; Dai et al., 2012). Therefore, seismic imaging can be regarded as a linearized inverse problem. With a proper initial velocity model, seismic records can be inverted to a more accurate profile. LSRTM iteratively reduces the residual between predicted data and observed data in a least-squares framework; therefore, the adjoint operator can keep approaching the inverse operator. Many results have indicated that LSRTM has a better performance than conventional RTM and migration (Zhang et al., 2015; Dutta and Schuster, 2014; Liu et al., 2016).

The precondition of seismic inversion is forward modeling, which maps the parameter model to seismic data. There are two main approaches to build linear approximation between physical model and wavefield (Yang and Zhang, 2019). One is the most commonly used Born approximation based on small perturbation (Beylkin, 1985; Bleistein, 1987). This requires that high-order scattered wavefields are much weaker than primary field. The Born operator describes a linear relationship between model perturbation and primary reflected wave. It divides the wavefield into two parts: background wavefield and perturbation wavefield. LSRTM based on Born approximation can achieve model perturbation with these two fields. In addition, an alternative scheme for modeling is Kirchhoff approximation (Bleistein, 1987). Compared with Born modeling, the Kirchhoff operator delineates the connection between primary reflected wave and reflectivity. Different operators lead to distinctive results under these two physical contexts. However, neither Born nor Kirchhoff approximation can avoid the impact on seismic image in a least-squares sense. Because minimizing the L2 norm only provides an average solution (Wang, 2016; Wu et al., 2016). It is essential to seek a balance between the residual and resolution. According to geological recognition, the earth medium usually presents a layered spatial distribution. The reflection coefficient that mirrors strata attributes should be sparsity, that is, the part of model that does not generate reflected wave ought to be zero. Therefore, the inverted model needs a sparse limitation.

This study implements a Kirchhoff modeling formula for LSRTM promoted by sparsity. The reflectivity model should be regularized with L1 norm while minimizing the residual of wavefield in the form of the L2 norm. Referring to 'least absolute shrinkage and selection operator' (Lasso) problem (Tibshirani, 1996), this reformed LSRTM can be solved by the algorithm of spectral projected gradient for L1 minimization (SPGL1), which is designed to solve sparse least squares (van den Berg and Friedlander, 2011). Examples show that our method can effectively overcome the problems mentioned above.

METHOD

RTM has great advantages in imaging steep strctures such as salt dome. However, it suffers from low-frequency noise compared to conventional migration. Least-squares migration can get closer iteratively to the optimal solution and eventually obtain a relatively high signal-to-noise ratio, high resolution and amplitude equalized profile that eliminates the influence of the acquisition system. It contains three steps: constructing a linear modeling problem first, using the forward and backward propagation wavefields to image, and finally updating the physics model according to the residual.

Linear Modeling Operators

The linearization of nonlinear forward problem is essential to seismic inversion, making the physical progress more explicit; moreover, converting the medium parameter becomes easier. The choice of a linear operator will lead to different physical significance and images. It is a common way to use Born approximation to realize linearization. The real velocity model is divided into two parts: background velocity v_0 and velocity perturbation δv. Given a perturbation δv, it generates a corresponding wavefield perturbation δu. The Born operator describes the relationship between reflected wave and model perturbation. Specifically, the incident wave interacting with model perturbation becomes a new source, namely the Huygens principle, and then the new source generates wavefield perturbations. This can be expressed as follows in time domain:

$$\left(\frac{1}{v_0(\boldsymbol{x})^2}\frac{\partial^2}{\partial t^2}-\nabla^2\right)u_0(\boldsymbol{x},t;\boldsymbol{x}_s)=f(t;\boldsymbol{x}_s) \tag{1}$$

$$\left(\frac{1}{v_0(\boldsymbol{x})^2}\frac{\partial^2}{\partial t^2}-\nabla^2\right)\delta u_b(\boldsymbol{x},t;\boldsymbol{x}_s)=m(x)\frac{1}{v_0(\boldsymbol{x})^2}\frac{\partial^2 u_0(\boldsymbol{x},t;\boldsymbol{x}_s)}{\partial t^2} \tag{2}$$

where u_0 represents the background field propagating in v_0, $f(t;\boldsymbol{x}_s)$ is the source signature located at $\boldsymbol{x}_s$ and excited at t, the model perturbation is denoted by $m(\boldsymbol{x})=2\delta v(\boldsymbol{x})/v_0(\boldsymbol{x})$, which describes velocity changes compared to background velocity. $\boldsymbol{x}$ is a point in model. This study assumes that the density ρ is a constant **(Eq. 1)** and **(Eq. 2)** can be rewritten in form of an integral using Green's theorem:

$$u_0(\boldsymbol{x},t;\boldsymbol{x}_s)=f(t;\boldsymbol{x}_s)G_0(\boldsymbol{x},t;\boldsymbol{x}_s) \tag{3}$$

$$\delta u_b\left(\boldsymbol{x}_g,t;\boldsymbol{x}_s\right)=\int m(\boldsymbol{x})\frac{1}{v_0^2(\boldsymbol{x})}\frac{\partial^2 u_0(\boldsymbol{x},t;\boldsymbol{x}_s)}{\partial^2 t}G_0\left(\boldsymbol{x}_g,t;\boldsymbol{x}\right)d\boldsymbol{x} \tag{4}$$

where $G_0(\boldsymbol{x},t;\boldsymbol{x}_s)$ is the Green's function from $\boldsymbol{x}_s$ to $\boldsymbol{x}$, $G_0(\boldsymbol{x}_g,t;\boldsymbol{x})$ propagates from $\boldsymbol{x}$ to $\boldsymbol{x}_g$. Green's function is governed by:

$$\left(\frac{1}{v_0(\boldsymbol{x})^2}\frac{\partial^2}{\partial t^2}-\nabla^2\right)G_0(\boldsymbol{x},t;\boldsymbol{x}_s)=\delta(t;\boldsymbol{x}_s) \tag{5}$$

where the $\delta(t;\boldsymbol{x}_s)$ is Dirac function.

Born approximation represents scattered phenomenon caused by model perturbation, which could be a means of linearizing seismic inversion. However, this approximation is accurate when scattered field δu is much weaker than background field u_0 (Schuster, 2017), which is a disadvantage of Born approximation. It cannot describe kinematic and dynamic information of seismic waves well with strong reflector. And studies have shown that Born approximation has limited angle validity and it cannot appropriately predict the reflections generated with large incident angle (Yang and Zhang, 2019).

Compared to the Born operator, the Kirchhoff operator relates the reflectivity to wavefield perturbation. Therefore, it depicts the interaction between the incident field and reflectivity rather than velocity perturbation. There is a relationship between reflectivity and model perturbation when the perturbation and incident angle are small (Stolt and Weglein, 2012):

$$r(\boldsymbol{x},\alpha)=\frac{i\omega}{2v_0(\boldsymbol{x})\cos(\boldsymbol{x},\alpha)}m(\boldsymbol{x}) \tag{6}$$

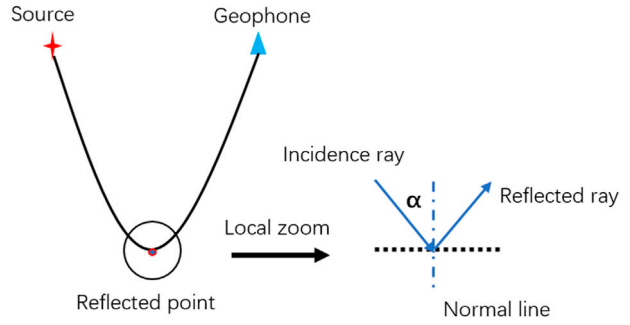

FIGURE 1 | Schematic illustration of incident wave and reflected wave. And α is the incident angle.

where the $r(\boldsymbol{x}, \alpha)$ is the reflection coefficient at point $\boldsymbol{x}$ with incident angle α between the incidence and the normal line (**Figure 1**). This means that we can obtain the wavefield perturbation under the Kirchhoff approximation by substituting (**Eq. 6**) into (**Eq. 4**), and we have

$$\delta u_b\left(\boldsymbol{x}_g, t; \boldsymbol{x}_s\right) = \int \frac{2v_0(\boldsymbol{x})}{i\omega} r(\boldsymbol{x}, \alpha) \cos(\boldsymbol{x}, \alpha) \frac{1}{v_0^2(\boldsymbol{x})} \frac{\partial^2 u_0(\boldsymbol{x}, t; \boldsymbol{x}_s)}{\partial^2 t} G_0\left(\boldsymbol{x}_g, t; \boldsymbol{x}\right) d\boldsymbol{x} \tag{7}$$

Here we turn Kirchhoff modeling equation into the same form as Born approximation. Then **Eq. 7** can be rewritten as.

$$\left(\frac{1}{v_0(\boldsymbol{x})^2}\frac{\partial^2}{\partial t^2} - \nabla^2\right) u_0(\boldsymbol{x}, t; \boldsymbol{x}_s) = -\int f(t; \boldsymbol{x}_s) dt \tag{8}$$

$$\left(\frac{1}{v_0(\boldsymbol{x})^2}\frac{\partial^2}{\partial t^2} - \nabla^2\right) \delta u_k(\boldsymbol{x}, t; \boldsymbol{x}_s) = 2v_0(\boldsymbol{x}) r(\boldsymbol{x}, \alpha) \cos(\boldsymbol{x}, \alpha) \frac{1}{v_0(\boldsymbol{x})^2} \frac{\partial^2 u_0(\boldsymbol{x}, t; \boldsymbol{x}_s)}{\partial t^2} \tag{9}$$

It should be noted that the term $r(\boldsymbol{x}, \alpha)$ can be replaced by the generalized angle-dependent reflectivity model to get rid of the limitations of small perturbation and incident angle. Although there are some methods to solve the propagation direction of wave, such as Poynting vector and Plane Wave Decomposition (PWD), it is still tedious and time-consuming to obtain the angle term. Here we give an approximate scheme (Yang and Zhang, 2019).

Each shot can invert a reflectivity image, here we sum the images obtained by all shots. Then, we regard the summation as the final reflectivity model and use it to iterate. Approximately, we can get an averaged reflectivity model by multiple shots stacking. Therefore, we can get the predicted data by using this stacked reflectivity $R(\boldsymbol{x})$ rather than the angle-dependent term $r(\boldsymbol{x}, \alpha)\cos(\boldsymbol{x}, \alpha)$. Note that $R(\boldsymbol{x})$ is an averaged reflectivity over all illuminated angles.

$$R(\boldsymbol{x}) \approx \sum_{shot} r(\boldsymbol{x}, \alpha) \cos(\boldsymbol{x}, \alpha) \tag{10}$$

With this approximate reflectivity $R(\boldsymbol{x})$, we can express **Eq. 9** as

$$\left(\frac{1}{v_0(\boldsymbol{x})^2}\frac{\partial^2}{\partial t^2} - \nabla^2\right) \delta u_k(\boldsymbol{x}, t; \boldsymbol{x}_s) = 2v_0(\boldsymbol{x}) R(\boldsymbol{x}) \frac{1}{v_0(\boldsymbol{x})^2} \frac{\partial^2 u_0(\boldsymbol{x}, t; \boldsymbol{x}_s)}{\partial t^2} \tag{11}$$

In sum, with the relationship of reflectivity and model perturbation, two linear approximations have a similar form, which expresses their common ground. The difference between two approximations is also evident. From **Eq. 6**, $\cos\alpha$ approximately equals to one and can be ignored for a small incident angle. Therefore, reflectivity can be regarded as the spatial derivative of model perturbation. The inverted model after spatial derivation has a higher resolution, that is, the spectrum has been improved. More details are provided in the numerical tests.

Least-Squares With Sparse Optimization

In contrast to full waveform inversion (FWI) (Liu, et al., 2020), LSRTM first establishes a linear relationship between physical model and corresponding response (Tarantola, 1984), then it implements the inverse problem. The least-squares method (LSM) only requires the construction of a migration operator and inverse migration operator, which is conjugated to each other. It can reduce the residual between the observed and predicted data iteratively to approach the optimal solution of the inverse problem gradually. According to the linear approximation above, we can express them in the form of a matrix:

$$\mathbf{d} = \mathbf{Lm} \tag{12}$$

where the $\boldsymbol{d}$ is predicted data, such as background or perturbation fields. $\boldsymbol{L}$ represents modeling operator and $\boldsymbol{m}$ is the physics model. Usually, it is assumed that the background velocity has been obtained in advance, and then the data can be predicted. Hence, the misfit function can be expressed as:

$$E(\boldsymbol{m}) = \|\boldsymbol{Lm} - \boldsymbol{d}_{obs}\|_2 \tag{13}$$

The model $\boldsymbol{m}$, which makes $\frac{\partial E(\boldsymbol{m})}{\partial \boldsymbol{m}}$ (the Jacobian matrix) equal to 0, is the optimal solution of **Eq. 13**. However, the computation of the Jacobian matrix is quite time consuming, particularly for seismic exploration. We adopt the adjoint-state method to calculate the adjoint operator $\boldsymbol{L}^T$ of modeling operator $\boldsymbol{L}$, Specifically, the gradient of $E(\boldsymbol{m})$ can be obtained by back propagation of the wavefield residual and background field, here we give the gradient based on Kirchhoff approximation (Plessix, 2006; Wang et al., 2021):

$$\boldsymbol{m}_{mig} = \boldsymbol{L}^{\mathrm{T}}\boldsymbol{d} = 2v_0(\boldsymbol{x}) \sum_{shot} \int \frac{1}{v_0(\boldsymbol{x})^2} \frac{\partial^2 u_0(\boldsymbol{x}, t; \boldsymbol{x}_s)}{\partial t^2} q(\boldsymbol{x}, t; \boldsymbol{x}_s) \mathrm{d}t \tag{14}$$

Where $q(\boldsymbol{x}, t; \boldsymbol{x}_s)$ is the adjoint wavefield governed by:

$$\frac{1}{v_0(\boldsymbol{x})^2} \frac{\partial^2 q(\boldsymbol{x}, t; \boldsymbol{x}_s)}{\partial t^2} - \nabla^2 q(\boldsymbol{x}, t; \boldsymbol{x}_s) = \delta u(\boldsymbol{x}_r, t; \boldsymbol{x}_s) \tag{15}$$

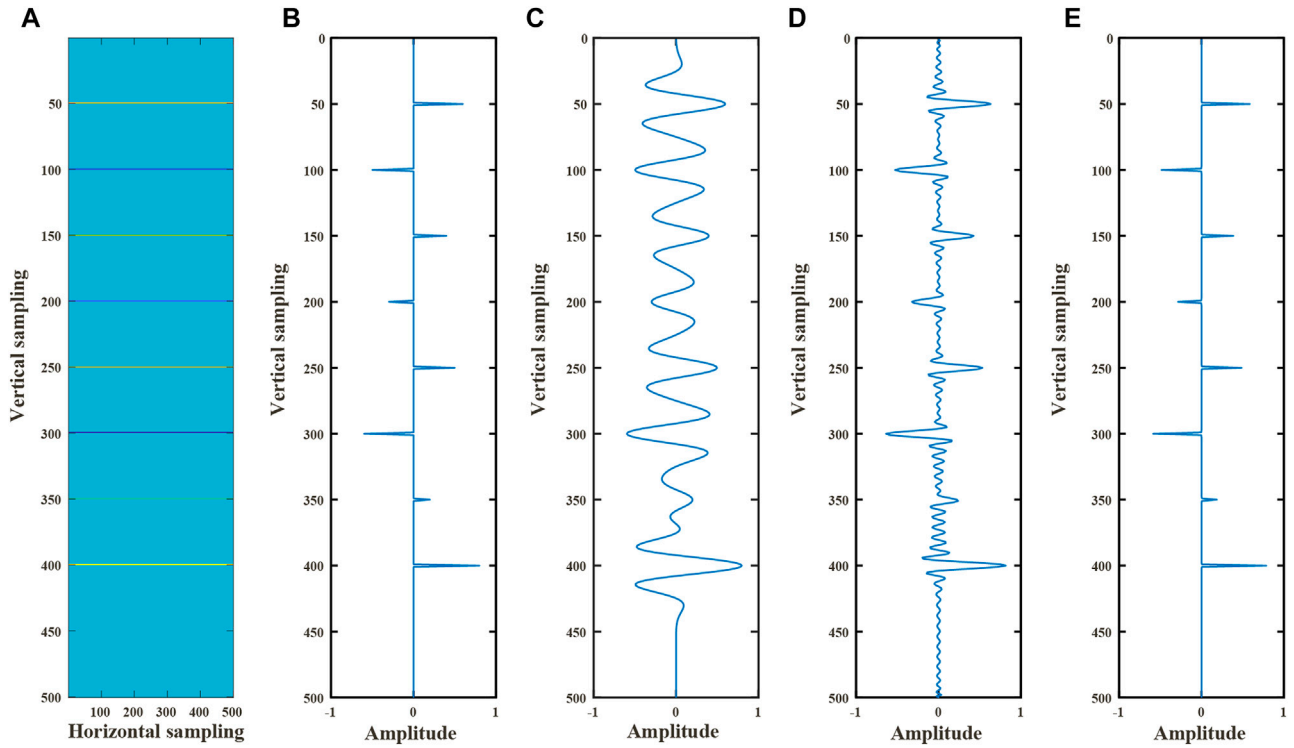

FIGURE 2 | (A) reflectivity model; **(B)** reflection coefficient series extracted in **Figure 2A**; **(C)** deconvolution of single record; **(D)** the result inverted by LSM; **(E)** the result inverted by sparse constrained LSM.

According to **Eq. 13**, we can obtain a least-squares solution $\boldsymbol{m} = (\boldsymbol{L}^T\boldsymbol{L})^{-1}\boldsymbol{L}^T\boldsymbol{d}$. Note that LSM provides a smooth solution of the model, which is determined by the properties of the L2 norm. As a result, LSM has a limited ability to improve the quality of the image. Here we give a simple model to display the impact of LSM. In this example, we use the Ricker wavelet with a center frequency of 30 Hz and a time sampling interval of 1 ms. With convolution model theory, we can get seismic records via the convolution of Ricker wavelet and reflection coefficients, which can be obtained by $\boldsymbol{d} = \boldsymbol{Lm}$. Conversely, reflection coefficients can be obtained by the deconvolution of seismic records and wavelet, that is, $\boldsymbol{m}_{mig} = \boldsymbol{L}^{\mathrm{T}}\boldsymbol{d}$. **Figure 2C** is the result of deconvolution, and it is hard to identify the reflectors. Compared to deconvolution, **Figure 2D** shows that LSM improves the resolution obviously. However, many oscillations caused by $(\boldsymbol{L}^T\boldsymbol{L})^{-1}$ near the real reflection coefficients should not exist. That's why we regard the least-squares solution as a smooth or average solution. The actual model indicates that the medium presents a layered spatial distribution, as shown in **Figure 2A** or **Figure 2B**, that is, the sub-surfaces are sparse. In **Figure 2E**, the inversion result with sparse constrained LSM performs quite well, and these oscillations generated by LSM are suppressed; thus, the resolution and sparsity of the reflection coefficient series are improved effectively.

Due to the feasibility and sparse property of L1-norm, we modify the objective function with L1 norm to realize sparse reconstruction of the model in this study. Generally, **Eq. 13** can be reformed with two new problems.

1 Basis Pursuit (BP) problem

$$(BP) \quad min \|\boldsymbol{m}\|_1, \quad subject\ to\ \boldsymbol{Lm} = \boldsymbol{d} \tag{16}$$

Eq. 16 depicts a BP problem that comes from compressed sense theory, and it aims to seek a sparse solution that satisfies $\boldsymbol{Lm} = \boldsymbol{d}$. However, practical seismic data inevitably contain noise, and **Eq. 16** can be modified as a basis pursuit denoising (BPDN) problem:

$$(BP_\sigma) \quad min \|\boldsymbol{m}\|_1, \quad subject\ to \|\boldsymbol{Lm} - \boldsymbol{d}_{obs}\|_2 \le \sigma \tag{17}$$

where the σ describes the noise level in the data, and **Eq. 16** and **Eq. 17** are equivalent to each other when $\sigma = 0$.

2 Least Absolute Shrinkage and Selection Operator (LASSO) problem

$$(LS_\tau) \quad min \|\boldsymbol{Lm} - \boldsymbol{d}_{obs}\|_2, \quad subject\ to \|\boldsymbol{m}\|_1 \le \tau \tag{18}$$

where the $\tau \ge 0$ is an explicit limitation of sparsity on $\boldsymbol{m}$. Problems (BP_σ) and (LS_τ) are different descriptions of the same question. They are equivalent in the sense that there exists a solution $\boldsymbol{m}^*$ of (BP_σ) for a given σ, and there exists a corresponding τ that makes $\boldsymbol{m}^*$ also be a solution of (LS_τ).

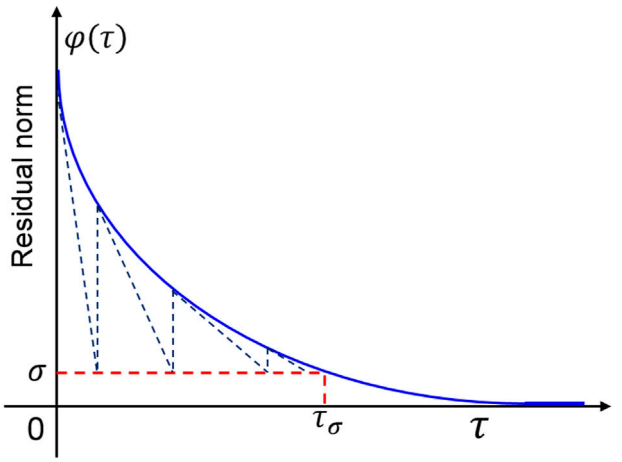

FIGURE 3 | Schematic diagram of the Pareto curve. A Newton-based root-finding method is used to update the solution of **Eq. 20**.

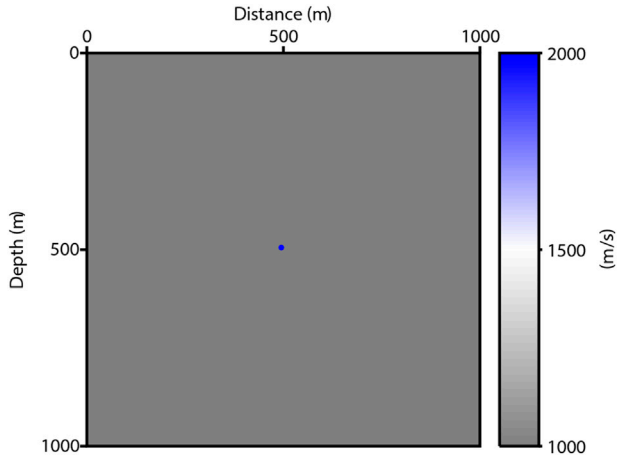

FIGURE 4 | A simple diffraction point velocity model.

Both problems mentioned above can be solved by the algorithm of spectral projected gradient for L1 minimization (SPGL1). Given a constraint τ, we can obtain the residual norm from **Eq. 18**:

$$\varphi(\tau) = \|\boldsymbol{r}_\tau\|_2 \quad with \quad \boldsymbol{r}_\tau = L\boldsymbol{m}_\tau - \boldsymbol{d}_{obs} \tag{19}$$

Let

$$\varphi(\tau) = \sigma \tag{20}$$

Eq. 20 recasts (LS_τ) as a problem of finding the root of a nonlinear equation and defines a continuous curve, the Pareto curve (**Figure 3**).

For a given σ, SPGL1 uses the Newton method to approach the root, and as the τ updates iteratively, the optimal solution $\boldsymbol{m}_{\tau_\sigma}$ of problems (BP_σ) and (LS_τ) can be obtained. Therefore, we balance the 2-norm of the residual against the 1-norm of the solution eventually (van den Berg and Friedlander, 2009). From **Figure 3**, the question is degraded to a simple Lasso problem (LS_τ) when the noise level factor σ is equal to 0. In this study, we set $\sigma = 0$. Note that synthetic seismic records do not contain noise in general, so we set the noise level factor to be zero. Actually, the algorithm of SPGL1 can deal with noisy data, and we can add some random noise or set some traces to be zero in synthetic data. Besides, the determination of parameter τ is quite important. According to the theoretical model, we can calculate the perturbation model or reflectivity model and make a rough estimate of τ. In general, it is appropriate to set the value of tau to tens of times that of the calculated perturbation model or reflectivity model. Then, the parameter τ can be adjusted according to the inversion results.

Here we summarize the workflow of L1-regularized LSRTM as follows:

1) Obtain the predicted data $\boldsymbol{d}_0$ with migration velocity v_0, and get the $\boldsymbol{d}_{res}$ with $\boldsymbol{d}_{res} = \boldsymbol{d}_{obs} - \boldsymbol{d}_0$;
2) Set the initial model $\boldsymbol{m}_0$ and predict the data $\boldsymbol{L}\boldsymbol{m}_0$ based on Born or Kirchhoff approximation, therefore we can get the residual $\boldsymbol{r}_0 = \boldsymbol{L}\boldsymbol{m}_0 - \boldsymbol{d}_{res}$ and gradient operator $\boldsymbol{g}_0 = \boldsymbol{L}^T\boldsymbol{r}_0$;
3) Input the parameters of τ, σ and set $k = 0$;
4) Solve the Lasso problem (LS_τ) with the algorithm of SPGL1, and update the $\boldsymbol{m}_k$, $\boldsymbol{r}_k$ and $\boldsymbol{g}_k$ until $k = k_{max}$;
5) Output the result $\boldsymbol{m}_{k_{max}}$.

NUMERICAL EXAMPLE

In this study, two theoretical models are used to test the validity of the proposed method, including a single diffraction point and complex fault model. Both are based on the two-way acoustic wave equation. Here we use the finite difference method on regular grid.

Single-Diffraction Point

To verify the effectiveness of this method, we first set a simple model with a diffraction point of 2000 m/*s* embedded in the background velocity of 1,000 *m*/*s* (**Figure 4**), and the entire model has been discretized into 201 × 201 grids in the horizontal and vertical directions, respectively, with the same interval of 5*m*. The geometry system is arranged as follows: a total of 21 shots are uniformly distributed on the surface of this model with an interval of 50*m*. Geophones are also placed on each grid point on the surface. We use the Ricker wavelet with a center frequency of 25 Hz for modeling, and the sampling interval is 0.5 ms. In this example, we set 1,000 *m*/*s* as the migration velocity.

As shown in **Figure 5A**, the image is obtained by LSRTM based on Born approximation. This is consistent with the actual situation to a certain degree. The single scatter point is blurred with a disturbing cross pattern (marked by a yellow arrow). However, it should be a dot on the image (Lecomte and Kjeller, 2008). This is because we use the adjoint operator to migrate rather than the inverse operator in **Eq. 14**. Specifically, **Eq. 13** defines a normal equation with $\boldsymbol{L}^T\boldsymbol{L}\boldsymbol{m} = \boldsymbol{L}^T\boldsymbol{d}$. The term $\boldsymbol{L}^T\boldsymbol{L}$, Hessian matrix, is equivalent to a blur operator acting on the true image $\boldsymbol{m}$. Furthermore, $\boldsymbol{L}^T\boldsymbol{L}$ includes the influence of irregular acquisition, limited acquisition aperture, band

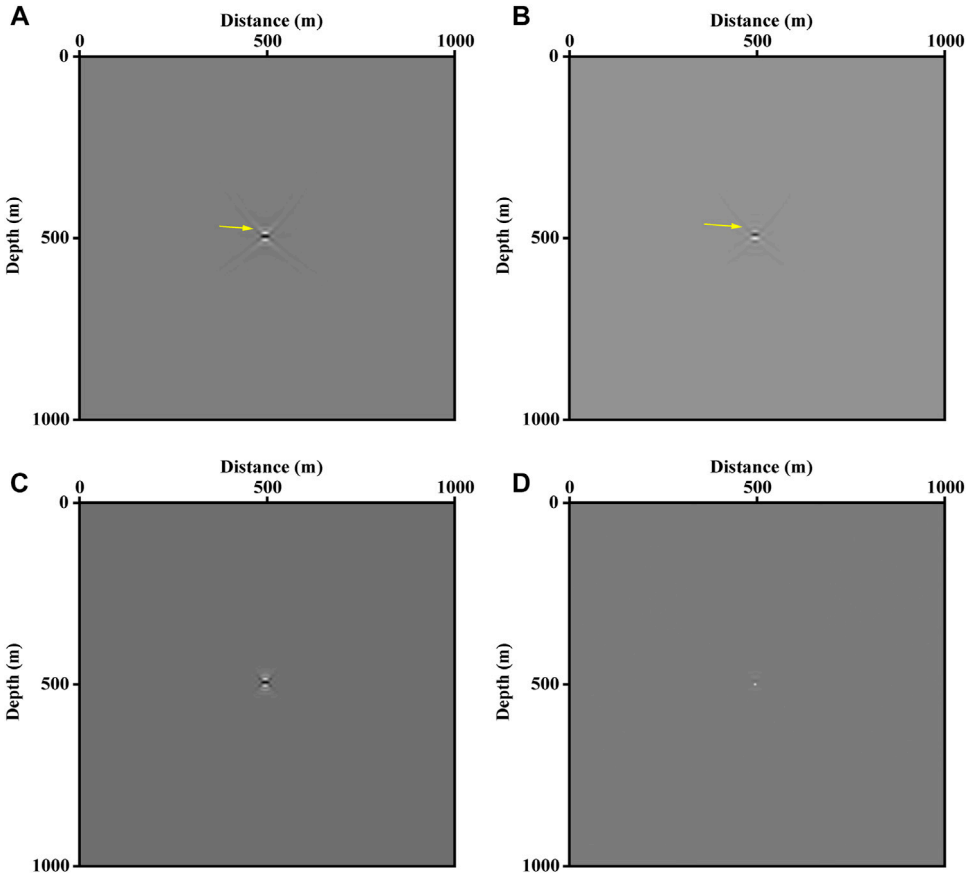

FIGURE 5 | The images invert by LSRTM and LSRTM with L1 norm constraint based on Born and Kirchhoff approximation. **(A)** Unconstrained LSRTM based on Born approximation. **(B)** Unconstrained LSRTM using Kirchhoff approximation. **(C)** The image of the LSRTM with L1 norm regularization based on Born approximation. **(D)** The migrated image with sparse constrained LSRTM based on Kirchhoff approximation.

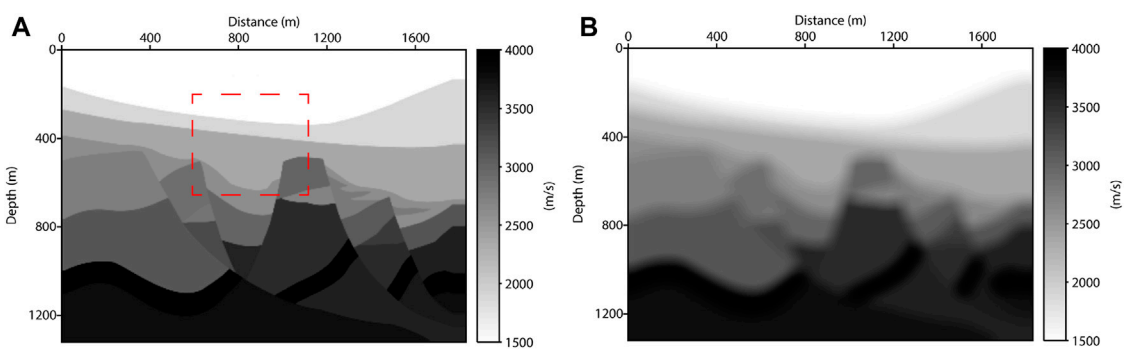

FIGURE 6 | (A) The real velocity of fault model. **(B)** the background velocity model after smooth.

limited source, etc., which generate artifacts and degrade the resolution of the image (Jiang and Zhang, 2019). Compared to LSRTM, the same method in **Figure 5C** with the L1 constraint performs better; it mitigates the distortion caused by the blur operator. Therefore, with the promotion of sparsity, the resolution in the least-squares method has been improved significantly, and the image looks more like a scatter point.

The LSRTM based on the Kirchhoff operator inverts the reflectivity directly from the seismic records. **Figure 5B** displays the image produced by Kirchhoff approximation. Compared to **Figure 5A**, least-squares RTM based on Kirchhoff operator suffers from the same problems. Similarly, we implement the L1 norm on LSRTM, which is shown in **Figure 5D**. The cross pattern is eliminated clearly, and we

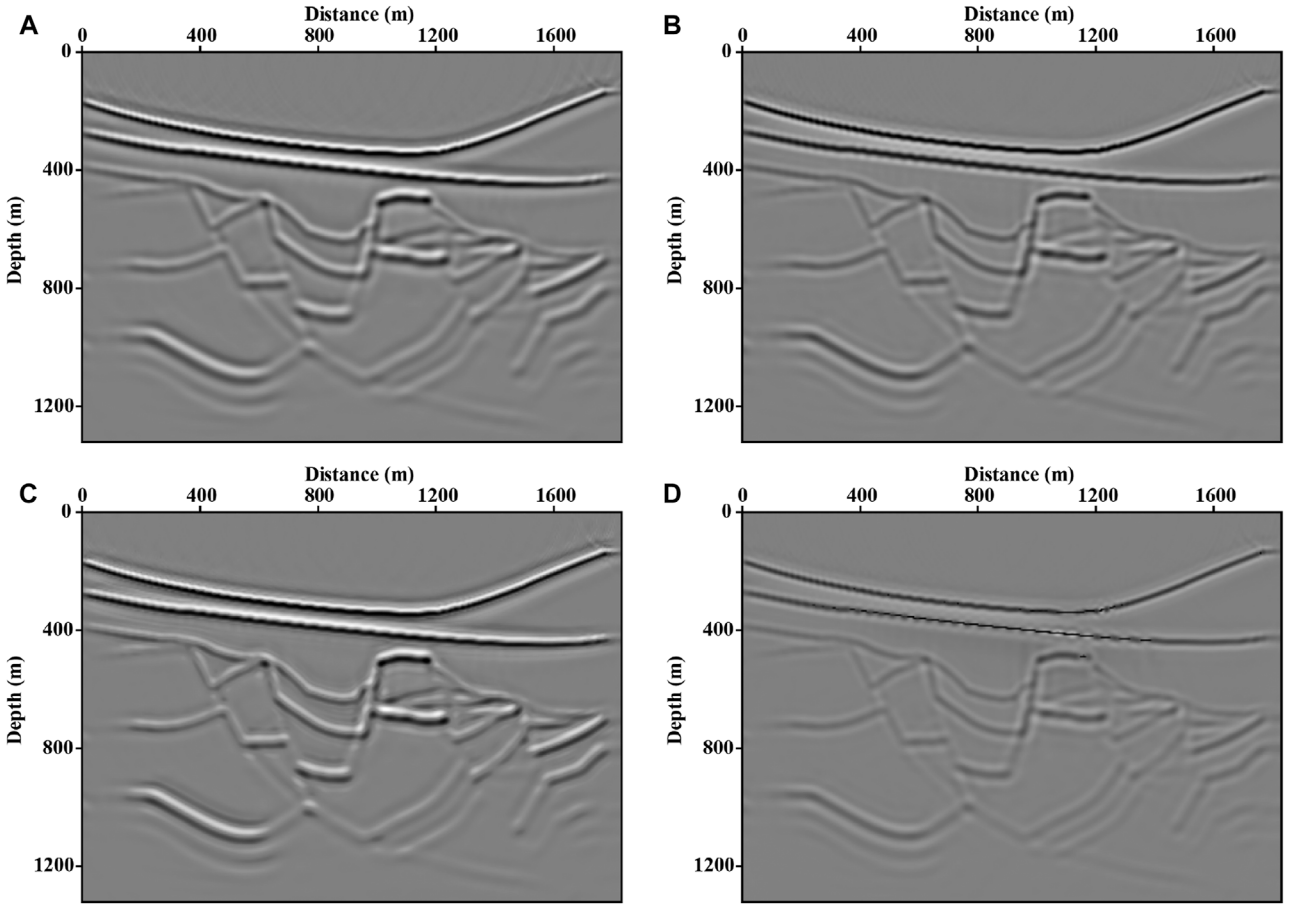

FIGURE 7 | Fault images inverted by **(A)** Unconstrained LSRTM based on Born approximation. **(B)** Unconstrained LSRTM with Kirchhoff approximation. **(C)** LSRTM with L1 norm regularization based on Born approximation. **(D)** sparse constrained LSRTM based on Kirchhoff approximation.

obtain an explicit dot rather than a blurred spot. Therefore, for a simple model, the sparsity-promoting LSRTM based on Kirchhoff approximation can effectively improve the resolution of the image. The results calculated by LSRTM in **Figures 5A,B** iterate 5 times. **Figures 5C,D** use the SPGL1 algorithm for iterating 10 times with $\tau = 2$.

Fault Model

We also test the other relative complex model. In this fault model (**Figure 6A**), there are some classical geological structures, including folds, fault blocks, and depressions. Therefore, it appropriately shows the complex structure of near-surface media. The maximum and minimum velocities are 4,000 m/s and 1,500 m/s, respectively. Similarly, we discretize it into 265 × 367 grids with an interval of 5 m. Thus, a total of 25 shots are uniformly located at the surface of this model. The modeling seismic wavelet is same to last experiment.

As shown in **Figures 7A,B**, images inverted by LSRTM based on two approximations fit the fault model well, and the contact relationship between structures can be clearly depicted. To further improve the resolution of these images, we combined L1 norm regularization with LSRTM to reconstruct the model. From **Figures 7C,D**, the method based on Kirchhoff approximation recovers the stratum's sparsity more effectively. The results in **Figures 7A,B** are calculated by LSRTM with 10 iterations. **Figures 7C,D** use the SPGL1 algorithm for iterating 10 times with $\tau = 2000$ and $\tau = 500$, respectively. Note that the amplitude of inverted results is different because of the value of parameter τ.

Furthermore, we enlarge the model framed by red rectangle in **Figure 6A**, which has step-like strata (marked by yellow arrows in **Figure 8A**). After inverting, the reflectivity image in **Figure 8D** produced by constrained LSRTM based on Kirchhoff operator agrees with the actual situation.

Furthermore, images inverted by two different approximations have different phases. According to **Eq. 6**, reflectivity can be derived from model perturbation. With the assumption of a small incident angle, $\cos(\boldsymbol{x}, \alpha)$ is roughly equivalent to 1 and can be ignored. Then, **Eq. 6** can be rewritten as $r(\boldsymbol{x}) = ikm(\boldsymbol{x})/2$, where the wavenumber $k = \frac{\omega}{c}$. Therefore, reflectivity $r(\boldsymbol{x})$ is the spatial derivative of model perturbation $m(\boldsymbol{x})$. As a result, the image inverted by Kirchhoff performs sparser and sharper, and there is a phase shift of 90° between perturbation model and reflectivity model.

Figure 9 shows the amplitude spectra of the images in **Figures 7B–D**, respectively. The spectra curves are the sum of each trace by the spatial Fourier transform along the depth. The

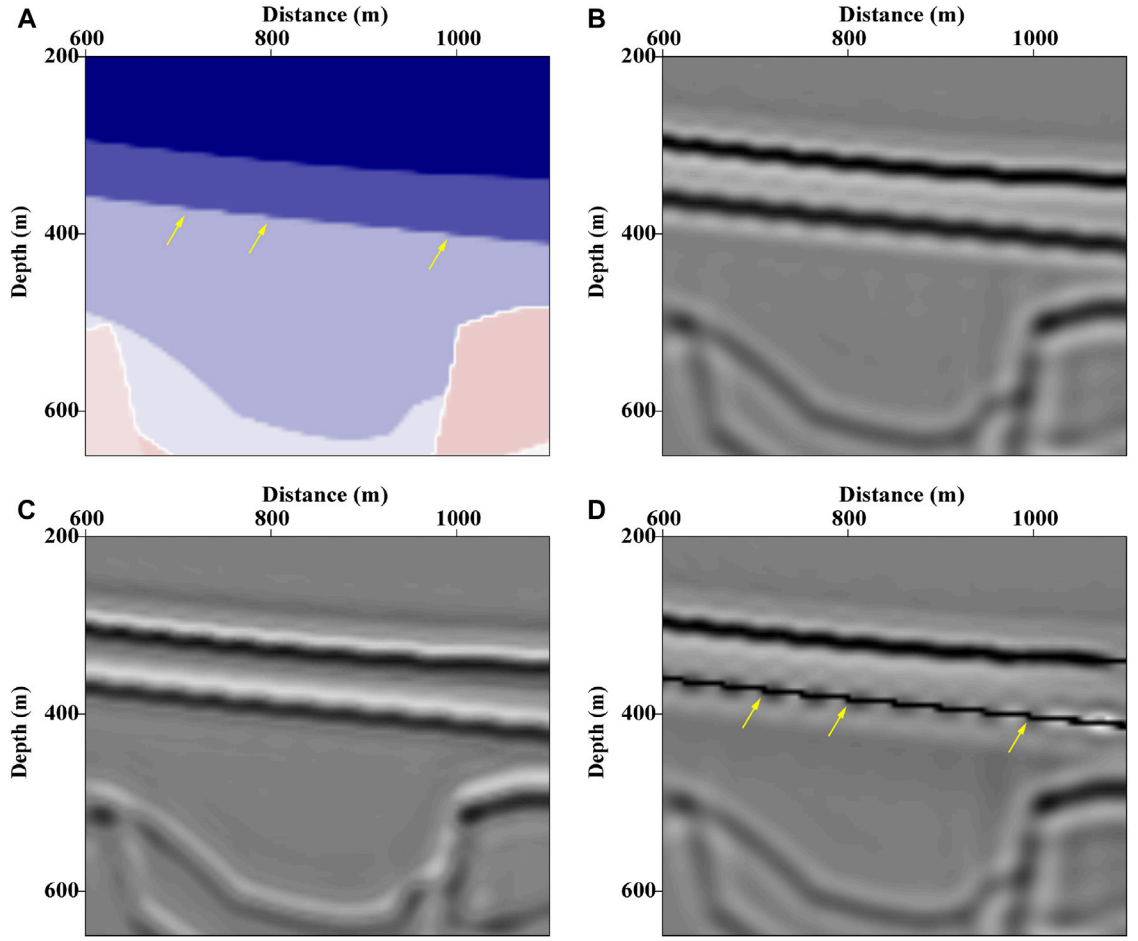

FIGURE 8 | (A) true velocity model in the red rectangle in **Figure 6A**, **(B)** corresponding image inverted by LSRTM based on Kirchhoff approximation, **(C)** LSRTM with sparse constraint based on Born approximation, **(D)** LSRTM with sparse constraint based on Kirchhoff approximation.

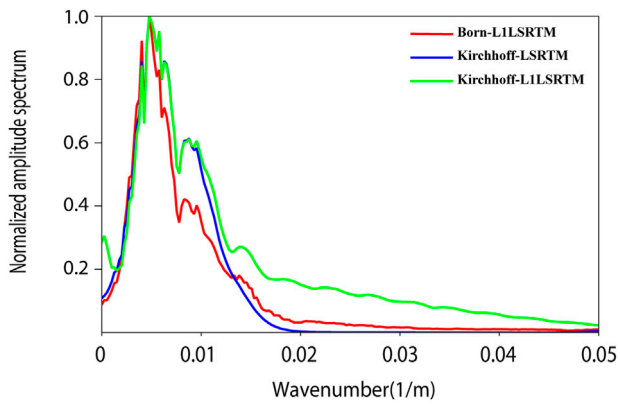

FIGURE 9 | The spectrum of inverted images form **Figure 6**.

red one is generated from the image inverted by L1-regularized LSRTM based on Born approximation. The blue and green spectrum curves are produced by unconstrained and constrained LSRTM with Kirchhoff approximation, respectively. Because of the spatial derivative and sparse constraint, the spectrum of the image inverted by L1-LSRTM with Kirchhoff approximation has more high-wavenumber components than that of Born approximation, which explains that Kirchhoff approximation improves the resolution of the image.

CONCLUSION

The LSRTM recasts classical seismic inversion as a linear inverse problem. By means of linear approximation, physical model is related to the corresponding wavefield. Thereafter, we can reduce the residual between predicted and observed data iteratively to directly invert the interest parameters. This study introduces two linearization methods. Born approximation obtains the relationship between the model and physical response based on perturbation theory. With the help of the Born operator, we derive another type of linear method, namely the Kirchhoff operator, which relates the reflectivity to wavefield explicitly. Moreover, these two methods have a relationship of a spatial derivative, and there is a phase shift

between perturbation model and reflectivity model. Although two operators are different physical quantities, the resolution can be improved by Kirchhoff approximation.

LSRTM can mitigate the shortcomings of other migration methods, while the solution is smooth and deviates from the true model. Specifically, there are redundant oscillatory axes in the strata that should be sparsely distributed. Therefore, we reform the question as a sparsity-promoting LSRTM. The SPGL1 algorithm can effectively solve this problem and invert a sparse image that matches the model well. Examples prove the validity of our study.

DATA AVAILABILITY STATEMENT

The raw data supporting the conclusions of this article will be made available by the authors, without undue reservation.

AUTHOR CONTRIBUTIONS

XH-Q: Methodology, Investigation, Formal analysis, Visualization, Writing—Original Draft WX-Y: Conceptualization, Writing—Review and Editing, Project administration WC-Y: Validation, Data Curation, Writing—Review and Editing ZJ-J: Supervision, Writing—Review and Editing, Funding acquisition.

ACKNOWLEDGMENTS

We thank the National Natural Science Fund of China (under grant 42074158) for supporting this work. And we are grateful for the comments provided by reviewers, which improve the quality of this paper a lot.

REFERENCES

Baysal, E., Kosloff, D. D., and Sherwood, J. W. C. (1983). Reverse Time Migration. *Geophysics* 48, 1514–1524. doi:10.1190/1.1441434

Beylkin, G. (1985). Imaging of Discontinuities in the Inverse Scattering Problem by Inversion of a Causal Generalized Radon Transform. *J. Math. Phys.* 26, 99–108. doi:10.1063/1.526755

Bleistein, N., Cohen, J. K., and Hagin, F. G. (1987). Two and One-half Dimensional Born Inversion with an Arbitrary Reference. *Geophysics* 52, 26–36. doi:10.1190/1.1442238

Bleistein, N. (1987). On the Imaging of Reflectors in the Earth. *Geophysics* 52, 931–942. doi:10.1190/1.1442363

Dai, W., Fowler, P., and Schuster, G. T. (2012). Multi-source Least-Squares Reverse Time Migration. *Geophys. Prospecting* 60, 681–695. doi:10.1111/j.1365-2478.2012.01092.x

Dutta, G., and Schuster, G. T. (2014). Attenuation Compensation for Least-Squares Reverse Time Migration Using the Viscoacoustic-Wave Equation. *Geophysics* 79, S251–S262. doi:10.1190/geo2013-0414.1

Jiang, B., and Zhang, J. (2019). Least-squares Migration with a Blockwise Hessian Matrix: A Prestack Time-Migration Approach. *Geophysics* 84, R625–R640. doi:10.1190/geo2018-0533.1

Lecomte, I. (2008). Resolution and Illumination Analyses in PSDM: A ray-based Approach. *The Leading Edge* 27, 650–663. doi:10.1190/1.2919584

Liu, H. W., Li, B., Liu, H., Tong, X. -L., and Liu, Q. (2010). The Algorithm of High Order Finite Difference Pre-stack Reverse Time Migration and GPU Implementation. *Chin. J. Geophys.* 53, 1725–1733. doi:10.1002/cjg2.1530(in Chinese)

Liu, Y., Chang, X., Jin, D., He, R., Sun, H., and Zheng, Y. (2011). Reverse Time Migration of Multiples for Subsalt Imaging. *Geophysics* 76, WB209–WB216. doi:10.1190/geo2010-0312.1

Liu, Y., He, B., and Zheng, Y. (2020). Controlled-order Multiple Waveform Inversion. *Geophysics* 85, R243–R250. doi:10.1190/geo2019-0658.1

Liu, Y., Liu, X., Osen, A., Shao, Y., Hu, H., and Zheng, Y. (2016). Least-squares Reverse Time Migration Using Controlled-Order Multiple Reflections. *Geophysics* 81, S347–S357. doi:10.1190/geo2015-0479.1

McMechan, G. A. (1983). Migration by Extrapolation of Time-dependent Boundary Values*. *Geophys. Prospect* 31, 413–420. doi:10.1111/j.1365-2478.1983.tb01060.x

Plessix, R.-E. (2006). A Review of the Adjoint-State Method for Computing the Gradient of a Functional with Geophysical Applications. *Geophys. J. Int.* 167, 495–503. doi:10.1111/j.1365-246X.2006.02978.x

Schuster, G. T. (2017). *Seismic Inversion*. Tulsa: Society of Exploration Geophysicists. doi:10.1190/1.9781560803423

Stolt, R. H., and Weglein, A. B. (2012). *Seismic Imaging and Inversion: Application of Linear Inverse Theory*. New York: Cambridge University Press, 1–404. doi:10.1017/CBO9781139056250

Tarantola, A. (1984). Inversion of Seismic Reflection Data in the Acoustic Approximation. *Geophysics* 49, 1259–1266. doi:10.1190/1.1441754

Tibshirani, R. (1996). Regression Shrinkage and Selection via the Lasso. *J. R. Stat. Soc. Ser. B (Methodological)* 58, 267–288. doi:10.1111/j.2517-6161.1996.tb02080.x

van den Berg, E., and Friedlander, M. P. (2009). Probing the Pareto Frontier for Basis Pursuit Solutions. *SIAM J. Sci. Comput.* 31, 890–912. doi:10.1137/080714488

van den Berg, E., and Friedlander, M. P. (2011). Sparse Optimization with Least-Squares Constraints. *SIAM J. Optim.* 21, 1201–1229. doi:10.1137/100785028

Wang, X. Y., Zhang, J. J., Xu, H. Q., and Tian, B. Q. (2021). Least-squares Reverse Time Migration with Wavefield Decomposition Based on the Poynting Vector. *Chin. J. Geophys. (in Chinese)* 64, 645–655. doi:10.6038/cjg2021O0120

Wang, Y. H. (2016). *Seismic Inversion: Theory and Applications*. Oxford: Wiley, 85–86. doi:10.1002/9781119258032.ch7

Wu, D., Yao, G., Cao, J., and Wang, Y. (2016). Least-squares RTM with L1 Norm Regularisation. *J. Geophys. Eng.* 13, 666–673. doi:10.1088/1742-2132/13/5/666

Yang, K., and Zhang, J. (2019). Comparison between Born and Kirchhoff Operators for Least-Squares Reverse Time Migration and the Constraint of the Propagation of the Background Wavefield. *Geophysics* 84, R725–R739. doi:10.1190/geo2018-0438.1

Yoon, K., Shin, C., Suh, S., Lines, L. R., and Hong, S. (2003). 3D Reverse-Time Migration Using the Acoustic Wave Equation: An Experience with the SEG/EAGE Data Set. *The Leading Edge* 22, 38–41. doi:10.1190/1.1542754

Zhang, Y., Duan, L., and Xie, Y. (2015). A Stable and Practical Implementation of Least-Squares Reverse Time Migration. *Geophysics* 80, V23–V31. doi:10.1190/geo2013-0461.1

Zhu, J., and Lines, L. R. (1998). Comparison of Kirchhoff and Reverse-time Migration Methods with Applications to Prestack Depth Imaging of Complex Structures. *Geophysics* 63, 1166–1176. doi:10.1190/1.1444416

Conflict of Interest: The authors declare that the research was conducted in the absence of any commercial or financial relationships that could be construed as a potential conflict of interest.

Publisher's Note: All claims expressed in this article are solely those of the authors and do not necessarily represent those of their affiliated organizations, or those of the publisher, the editors and the reviewers. Any product that may be evaluated in this article, or claim that may be made by its manufacturer, is not guaranteed or endorsed by the publisher.

frontiers in Earth Science

ORIGINAL RESEARCH
published: 06 September 2021
doi: 10.3389/feart.2021.732803

An efficient local imaging strategy based on illumination analysis with deep learning

*Chao Rong and Xiaofeng Jia**

School of Earth and Space Sciences, University of Science and Technology of China, Hefei, China

We propose a deep-learning-based illumination analysis and efficient local imaging method. Based on the wavefield forward modeling, seismic illumination can intuitively express the energy propagation of direct waves, reflected waves, and transmitted waves, while it requires high calculation costs. We use a series of convolution operations in deep learning to establish the nonlinear relationship between the model and the illuminations to realize single-shot illumination result of the model. Stacking the single shot illumination results obtained by the network prediction can further help determine the target area. For the target area, we use a deep learning method to obtain the low illumination area of the geological model. Each shot has contribution to the low illuminated area; single shot is selected based on the contribution of the shot being greater than the average illuminance, and the low illumination area is imaged by reverse time migration on the selected shot gather. The trained convolutional neural network can help us quickly obtain the single shot illumination result of the model, which is convenient to analyze the energy distribution of various areas of geological model, and do further imaging for target areas. Using part of the shot gathers to image a local area can recover the complex geological structure of the area and improve the efficiency of reverse time migration especially for 3D problems. This method has universal applicability and is suitable for local imaging of various complex models such as subsalt areas and deep regions.

Keywords: Deep learning, Local imaging, Illumination analysis, low illumination area, Reverse time migration

OPEN ACCESS

Edited by:
Wei Zhang,
Southern University of Science and Technology, China

Reviewed by:
Hejun Zhu,
The University of Texas at Dallas, United States
Yibo Wang,
Chinese Academy of Sciences (CAS), China

****Correspondence:***
Xiaofeng Jia
xjia@ustc.edu.cn

Specialty section:
This article was submitted to Solid Earth Geophysics, a section of the journal Frontiers in Earth Science

Received: *29 June 2021*
Accepted: *23 August 2021*
Published: *06 September 2021*

Citation:
Rong C and Jia X (2021) An efficient local imaging strategy based on illumination analysis with deep learning. Front. Earth Sci. 9:732803. doi: 10.3389/feart.2021.732803

1 INTRODUCTION

Seismic imaging is to return the reflected wave or the diffracted wave to the underground location where it is generated. It mainly includes two parts: determining the spatial position of the reflection or diffraction point, and reproducing its waveform and amplitude characteristics. As the main step of seismic imaging, seismic migration is the process of moving the data signal from the receiver point to the underground position. In the 1960s, without considering the waveform characteristics of the reflected wave, seismic migration relied on manual operation to draw the spatial position of the reflection point. Claerbout (1971) proposed the wave equation migration technique. They used the finite difference method to solve the one-way wave equation, and reconstructed the wavefield propagating in the subsurface through observed data recorded by the geophone on the surface. The wavefield was extracted from the subsurface reflection interfaces to construct the migration profile. In the late 1970s, Stolt (1978) solved the wave equation in the frequency-wavenumber domain and extrapolated the seismic wavefield. The algorithm was called F-K domain migration. It had the characteristics of simple calculation and high efficiency, and had been quickly promoted in industry.

The reverse time migration method was developed by solving the full wave equation for wavefield propagation (Baysal et al., 1983; McMechan, 1983). Chang et al. (1990) extended the reverse time migration method to the three-dimensional situation, and came up with the challenge of improving the accuracy and efficiency for 3D problems. Moreover, Wu et al. (1996) used high-order finite difference operators to achieve reverse time migration in three dimensions, and compared the features of high-order and low-order schemes. To compensate for poorly imaged areas, Chen and Jia (2014) proposed a staining algorithm for seismic modeling and imaging. This method performs dye marking on the target area and defines the staining wavefield. By imaging the target area with the staining wavefield, more accurate geology structures in the target area can be obtained. The staining algorithm based on reverse time migration establishes the connection between the real geological structure and its related wavefield and reflection data. Apart from reverse time migration, ray-based migration (Gray, 1986; Hill, 1990; Albertin et al., 2002) and one-way wave-equation-based migration (Ristow and Ruhl, 1994; Mulder and Plessix, 2004) are also commonly used in current practice.

Because of limited acquisition apertures, complex overburden structures, and large dipping angles, seismic migration often generates a distorted image of actual subsurface structures. (Lecomte, 1998) proposed the method of calculating the number of ground scattered wave coverage using ray tracing. The ray tracing-based illumination analysis provided directional illumination information, and the calculation speed was fast. The method only allowed for the seismic wave kinematic characteristics, and the calculation results are reliable when the medium is not seriously heterogeneous. In order to avoid the shortcomings of the ray-tracing based algorithm, wave theory is introduced into illumination analysis and has been successively applied to study illumination conditions under complex geology (Wu et al, 1996; Xie et al., 2003; Chen et al., 2007). Furthermore, Yang et al. (2008) put forward the idea of optimizing the design and acquisition system parameters by means of illumination analysis. Seismic illumination analysis can optimize the observation system so that the energy in the subsurface medium is evenly distributed (Xie et al., 2013). Moreover, Sun et al. (2018) proposed the multiple-wave-based illumination analysis method which is more powerful in evaluating and optimizing the observation system when dealing with complex geological models, and can make preliminary predictions on the imaging quality.

Machine learning (ML) offers algorithms designed to learn the features and relationships hidden in large datasets (Jia and Ma, 2017). As a branch of ML, deep learning has been widely applied to seismic model building, e.g., a prior models building from seismic images for full waveform inversion (Vigh et al., 2016), building detection framework based on deep learning model (Liu et al., 2018) and seismic tomography directly from shot gathers (Mauricio et al., 2018). In this paper, we first use deep learning method to establish the nonlinear relationship between the model and the illuminations, after training, it can help us got single-shot illumination result when inputting background velocity with shot information. Then, illumination results obtained by the network prediction can help us select the target area in which low illumination occurs densely. We further determine the low illumination area in target area of the geological model and select partial shot sets to achieve high-resolution and high-efficiency imaging in low illumination areas.

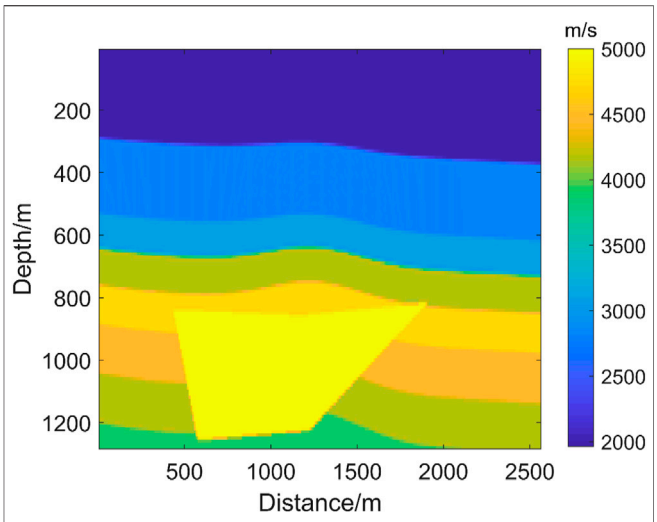

FIGURE 1 | Randomly generated velocity model.

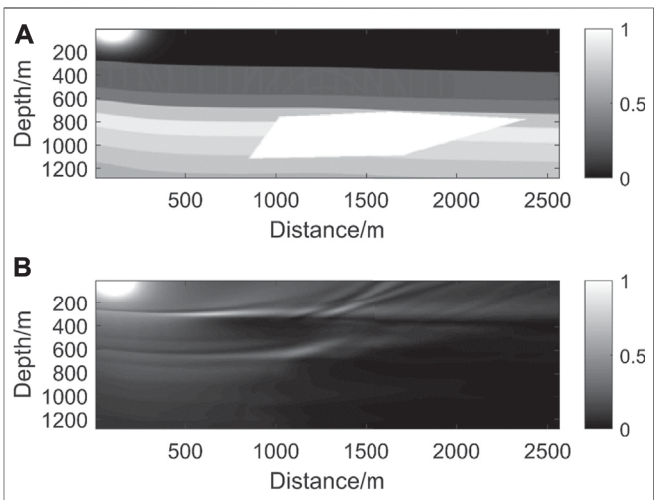

FIGURE 2 | Training dataset. **(A)** is the velocity model with shot information and **(B)** is the corresponding illumination result calculated by **Eq. 2.2**.

2 ALGORITHM

2.1 Illumination theory

The two-dimensional constant density time domain acoustic wave equation has the form of:

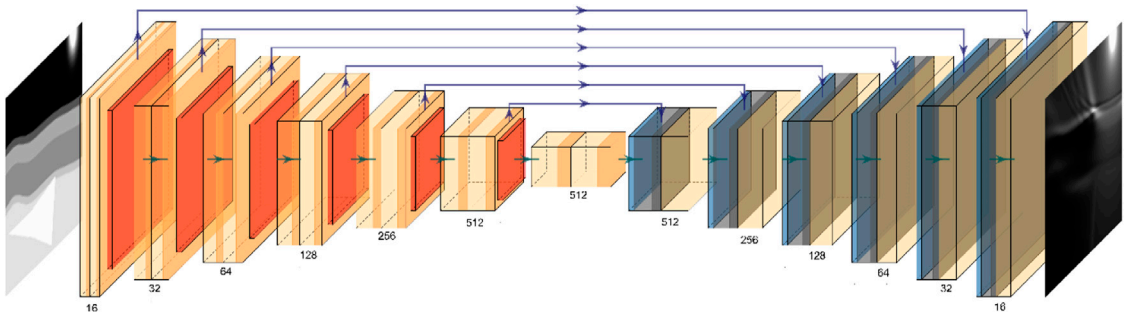

FIGURE 3 | Constructed UNet network with 6 downsampling layers.

$$\frac{1}{v(x,z)^2}\frac{\partial^2 u(x,z,t)}{\partial t^2} - \nabla^2 u(x,z,t) = s(t) \tag{2.1}$$

where $v(x,z)$ is the seismic wave velocity, $u(x,z,t)$ refers to the wavefield, and s(t) is the source.

The illumination intensity at point (x,z) for a shot is defined as (Chen et al.,2013):

$$I_s^{(i)}(x,z) = \sum_t u^{(i)}(x,z,t).\, u^{(i)}(x,z,t), \tag{2.2}$$

where $I_s^{(i)}$ is the source illumination intensity for the i-th shot.

The source illuminance for N shots can be regarded as the sum of the illuminance for singleshot:

$$I_s(x,z) = \sum_{i=1}^{N} I_s^{(i)}(x,z). \tag{2.3}$$

By obtaining the one-way (i.e., source-way) illumination intensity of single shot or multiple shots, we can investigate the distribution characteristics of the seismic wave energy propagating in the subsurface region. It provides a reference for redesigning the excitation position of the shot and the receiving range of the geophone. Although the distribution of subsurface energy can be seen through the one-way illumination diagram, it only indicates that the source energy can reach the specified subsurface location. Since not all these energy can be received by the surface geophone, it is necessary to consider factors such as the correspondence between excitation and detection, and the distribution of geophones on the surface.

As mentioned above, for a specified subsurface scattering point (x,z), the energy intensity of the i-th shot is $I_s(x,z)$. We assume the energy received by the surface geophone for this point is $I_r^{'}(x_r,0)$ where x_r is the receiver location. According to the principle of wave reciprocity, the energy of the scattering point to the detection point can be converted into the energy $I_r(x,z)$ received at (x,z) with the excitation point of $(x_r,0)$.

We define the two-way illumination intensity of each source for a space point (x,z) as:

$$I_i(x,z) = \sqrt{I_s^{(i)}(x,z) I_r^{(i)}(x,z)}. \tag{2.4}$$

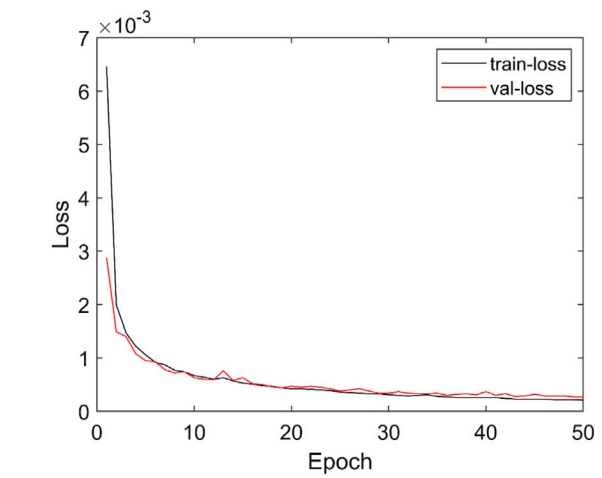

FIGURE 4 | Curve of loss function during training (black is training dataset; red is validation dataset).

The shots are independent of one another, and the same for geophones. Therefore, the two-way illumination intensity of M pairs of source and receiver can be regarded as the sum of each source-receiver pair, namely

$$I(x,z) = \sum_{i=1}^{M} I_i(x,z). \tag{2.5}$$

2.2 Illumination analysis based on deep learning

For demonstration of combining deep learning and illumination analysis, we employ a simple method (**Equations 2.2-2.5**) to calculate the illumination, which costs little extra computational time in migration. When the geological model is large and complicated, it is necessary to adopt high-resolution illumination analysis methods, e.g., the local directional approaches (Mao et al., 2010; Yan & Xie, 2016), which require a lot of calculation time. The deep learning method can build the nonlinear mapping between the model and its corresponding single shot illumination result, and therefore efficient illumination analysis can be realized.

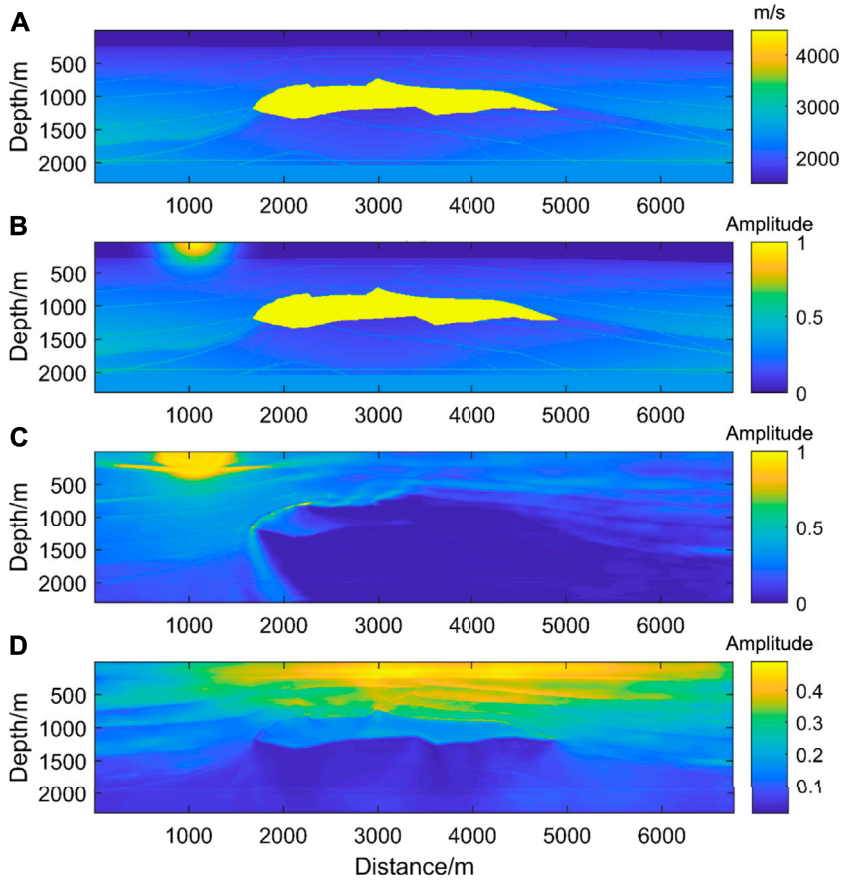

FIGURE 5 | (A) is SEG salt velocity model. **(B)** is the velocity with shot position information and **(C)** is the Network prediction of single shot illumination result. **(D)** is the stack of multi-shot one-way illumination results.

2.2.1 Building dataset

Since our illumination analysis is for geological models, we need to build a series of velocity models. In order to make the model represent as many complex subsurface features as possible, we randomly include flat layers, inclined formations, folds, faults, and high-velocity anomalies in the model. **Figure 1** shows an example model generated by this means.

The desired output of the neural network is the single-shot source illuminance. The position information of the shot is crucial to the source illuminance. In order to include the shot information in the input of the network, we add a Gaussian function of point source at the shot position. For the shot position (x_0, y_0), a two-dimensional Gaussian function is defined by

$$f(x,y) = 255 * e^{-\left(\frac{(x-x_0)^2}{2c_1^2} + \frac{(y-y_0)^2}{2c_2^2}\right)}, \quad (2.6)$$

where c_1 and c_2 are two variables in the x and y directions empirically determined by the radius of source illuminance.

In this way, we have the input of the neural network and calculate its corresponding output, with an example shown in **Figure 2**. From **Figure 2A** we see that the point source Gaussian function simulates the propagation mode of the seismic source very well. In the single-shot illumination result shown in **Figure 2B**, the energy near the sharp edge and below the high-velocity body is relatively weak. In this research, we built a total of 1,000 velocity models and got 25,000 single shot illumination results; therefore, the number of the training dataset including input and output is 25,000*2. The data set

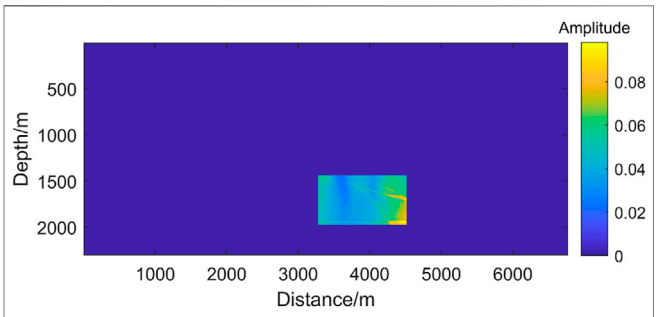

FIGURE 6 | The location of target area which is artificially selected according to the illumination result.

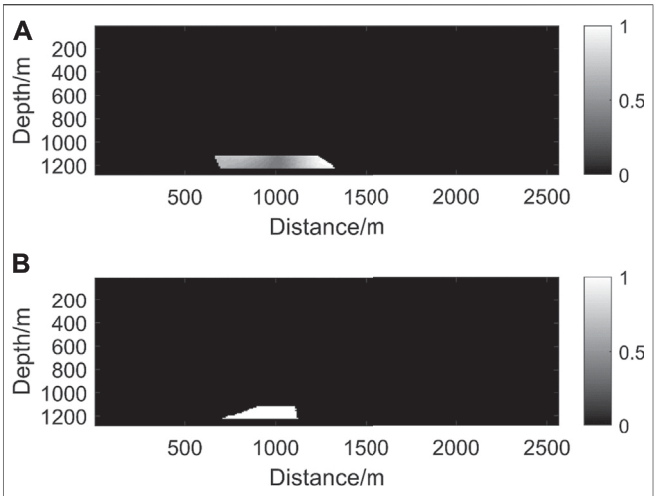

FIGURE 7 | Determination of the low illumination area. **(A)** The illumination results as network input. **(B)** The picked low illumination area as network output.

needs to be normalized before being applied to the network model. After data normalization, the process of searching for the best parameters of the network model will become smoother, and the normalization effectively prevents the local value from being too large, which will be easier to correctly converge to the optimal solution.

2.2.2 Network Construction

The UNet network takes the feature information of different scales into account and combines them with each other, so that more features, especially some detailed features are better preserved (Ronneberger et al., 2015). As the illumination is closely related to the subsurface structure, the UNet network was chosen to retain more background geological features. Based on the traditional UNet network, we constructed a network architecture with 6 downsampling layers and upsampling layers. The stride of the pooling layer is 2, and the stride of the convolutional layer is 1. The convolution kernels of the entire network are all the same size as 3x3. The UNet network is show in **Figure 3**. The final single shot illumination result is obtained through the input of the model with the shot position information at the leftmost.

2.2.3 Training of UNet

In training process, we set the batchsize as 32, and the learning rate lr=0.001 which decreases with the number of training epoch. The data in the constructed dataset is divided into the training dataset and the validation dataset at a ratio of 17:3. The mean square error function is selected as the loss function. The loss function of training dataset is shown in black line of **Figure 4**. According to the curve trend in **Figure 4**, the network matches the constructed dataset well, and the parameter selection in training is relatively correct. The abscissa of the graph is the number of training. With the training number increases, the loss value of the validation dataset in red of **Figure 4** initially decreases quickly, mainly caused by the mean square error function, and then slowly decreases. For the test dataset, after epoch reaches 30, the value of the loss function tends to be stable.

3 RESULT

We perform trial calculations on the SEG salt dome model with the trained network. The resampled sources start with the location of 1050 m on the surface, and the shot interval is 50 m. The shot is on the right end of the spread. The spread length is 1000 m, and the receiver spacing is 10 m. As shown in **Figure 5A**, the SEG salt dome model contains a large high-velocity anomaly. Underneath the anomaly, there are complex structures such as folds and faults. It is difficult for the traditional reverse time migration method to obtain a clear geological image globally.

The one-way illumination of the seismic source is shown in **Figure 5**. **Figure 5B** is the input of the network, and **Figure 5C** is the single shot illumination result predicted by the network. The average time of calculating a single illumination result by using the regular theory and the deep learning method is 10s and 0.4s, respectively. From **Figure 5C**, most of the energy propagated from the seismic

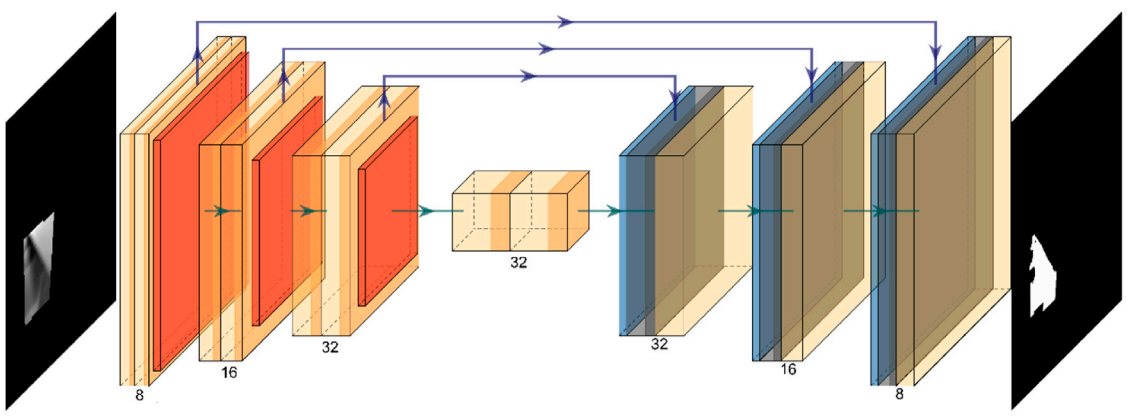

FIGURE 8 | Constructed UNet network with 3 downsampling layers.

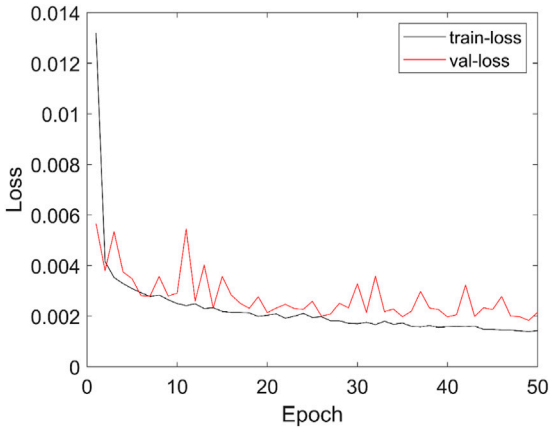

FIGURE 9 | Curves of loss function during training (black—training dataset; red—validation dataset).

source is blocked by the high-velocity salt dome. There is a low-energy area below the salt dome. The source has better illumination results above the salt dome. Therefore, it can be preliminarily predicted that the artillery source has strong illumination energy above the salt dome and near the seismic source, and the imaging results also have relatively high resolution in these areas.

Single-shot illumination result can hardly show the overall energy distribution, so we stack all the shots to get full shots illumination in **Figure 5D**. The overlying stratum above the high-velocity salt dome has strong illumination, and the energy distribution is relatively uniform in the lower left and lower right of the model. The illumination is significantly weak below the high-velocity salt dome. The size of the low illumination area decreases with the distance from the salt dome, and the existence of the salt dome has a key impact on the illumination of the structure below it. According to these predicted illumination results, we believe that the imaging results below the salt dome will have relatively poor quality and low resolution. Without considering whether the geophone can receive the wavefield propagated from the seismic source, the one-way illumination of the seismic source energy does not fit the complete situation of data acquisition well. It is necessary to allow for the receiver impact on the illumination analysis by using **Eq. 2.4**.

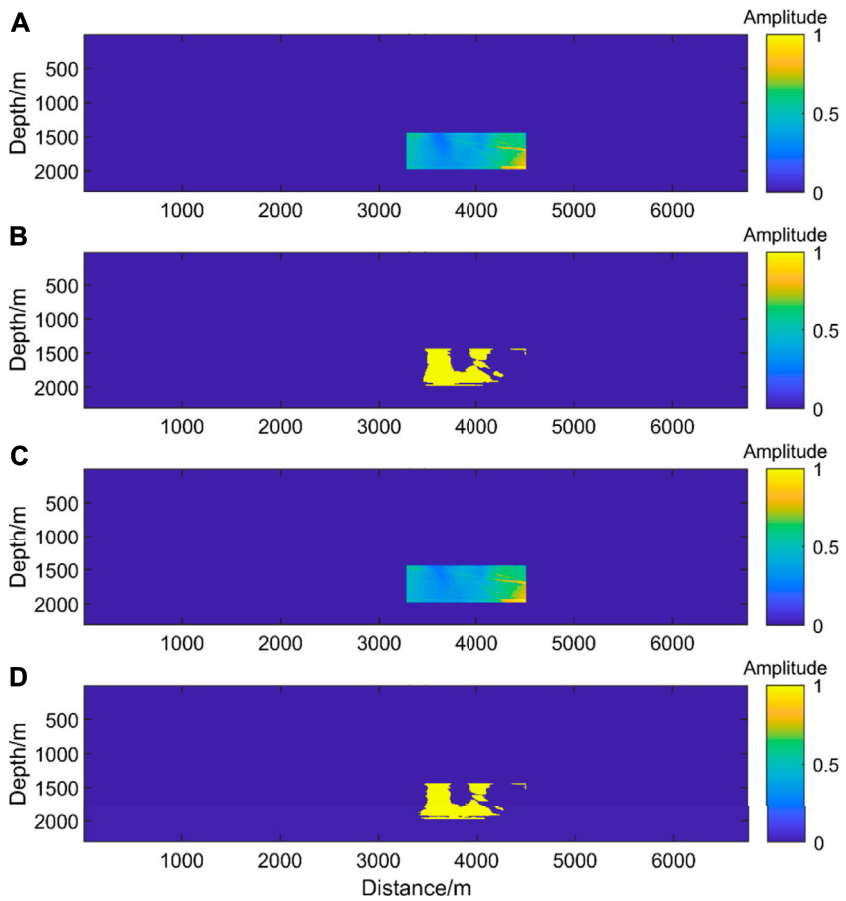

FIGURE 10 | The location of low illumination area predicted by the network under the guidance of one-way and two-way illumination. **(A)** is the target area and **(B)** is the weak illumination area of one-way illumination. **(C)** is the target area and **(D)** is the weak illumination area of two-way illumination.

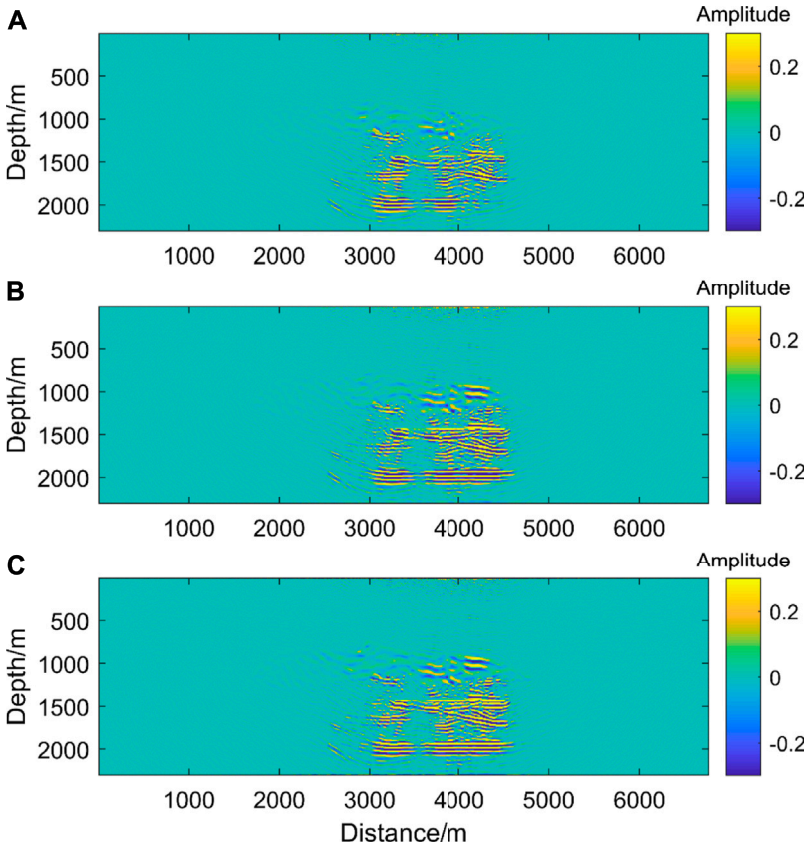

FIGURE 11 | (A) is the image result for the target area with shots selected by the one-way illumination. **(B)** is the image result for the target area with shots selected by the two-way illumination. **(C)** is the image result for the target area with all shots.

3.1 Determining low illumination area from the target area

According to the one-way illumination result of **Figure 5d**, we can see the distribution of the low illumination area is relatively wide below the salt body. To be more specified, we manually select an area in **Figure 5D** as the target area. For example, the box position in **Figure 6** is defined as the research area. This area contains fault structures, and it is a challenge for migration to obtain a clear image of this region.

In order to further extract the specific location of the low illuminated area in the target area, deep learning can be used to identify the low illuminated area. The dataset used for this model is shown in **Figure 7A,B**. The upper panel shows the energy illumination of the target area, and the lower one illustrates the marked low illumination area. The marked low illumination area is selected based on the relative average strength in the target area. The total number of training datasets is 1,000*2.

In order to fast identify the contour of the low illuminated area in the local area of the picture, a UNet network with three layers of downsampling and three layers of upsampling is constructed. The stride of the pooling layer is 2, and the stride of the convolutional layer is 1. The convolution kernels of the entire network are all the same size as 3*3. The UNet network is show in **Figure 8**. Considering that the network only needs to further filter the pixel values in the selected target area, it is similar to the recognition of medical images. The input of the network is only the illumination result of the target area, and the output of the network is the position of the identified low illuminated area.

During network training, the loss function is defined by the root mean square error function. **Figure 9** is the loss function curve for network training. It can be seen that the losses of the training and testing are both rapidly decline at the beginning, and after the epoch reaches 20, the value of the loss function tends to be stable.

The stack energy map of one-way or two-way illumination in the target area is input into the trained network model. The result obtained by edge smoothing is shown in the **Figure 10A,B** (one-way illumination) and **Figure 10C,D** (two-way illumination), respectively. It can be seen that the weak illumination area is a part of the target area.

3.2 Selection of shot based on low illumination area

Based on single-shot illumination results, when its energy intensity of the low illumination area is greater than average,

Table 1 | Calculation efficiency comparison.

Strategies	Calculation time for local imaging
One-way illumination selection	2, 478s
Two-way illumination selection	2, 786s
Allshots	4, 410s

the shot will be kept. By this means we only retain the shots which have dominant contributions on the illumination of the area. The selected shots are successively distributed, and only a few shots are selected separately. For the shot selection results obtained under the two-way illumination situation, the shots are evenly distributed directly above the target area. The shot range is wider, with only one separate shot near the right end. On the whole, the selected shots is about half of the total shot.

3.3 Local imaging based on shot selection

We perform regular reverse time migration for the selected shots above in the target area. In the partial imaging results with one-way illumination in **Figure 11A**, most of the interface information can be obtained for the restoration of subsurface structures. Due to the constraint of one-way illumination-based shot selection, the results of geological structure imaging in low-illumination areas are clear, while the imaging results of other locations in the target area are relatively poor.

Similarly, the shot gathers selected by the two-way illumination are employed for reverse time migration. In the partial imaging results with two-way illumination in **Figure 11B**, most of the interface information can be obtained for the restoration of subsurface structures. Compared with **Figure 11A**, the overall imaging result of the target area is clearer in the non-low illumination area.

We compare the imaging results based on one-way and two-way illumination analysis with the normal all-shots local imaging result as shown in **Figure 11C**. The approaches with one-way and two-way illumination constraints can recover the subsurface structures very well. The result with one-way illumination is relatively poor in interface continuity, while two-way illumination can overcome this and its imaging result has almost the same accuracy as the all-shots result. The two-way illumination strategy can achieve a balance between accuracy and computational cost.

By comparing the calculation efficiency as shown in **Table 1**, we see that the local imaging algorithms based on shot selection greatly save the calculation time, and the imaging quality is equivalent to the integrated image results of all shots.

4 DISCUSSION

The illumination analysis based on deep learning provides a preliminary prediction for subsurface seismic energy distribution. According to this, the acquisition system can be optimized to obtain seismic data related to difficult subsurface regions. This method considers various of structures in the training of the network, and can be applied to complex models.

Based on the results of deep learning illumination, we can select the target area to be studied, and further use neural network for the target area to quickly pick out the low illumination area.

By applying the principle of energy intensity filtering to select shot at low illumination area and implement local imaging, the subsurface structures can be imaged well, and the calculation efficiency has also been significantly improved. In the case of 3D model, the number of shots selected by the 3D illumination will be further reduced, and employing the shot selection results for 3D imaging will have a dramatic improvement in computational efficiency compared with regular all-shots imaging.

5 CONCLUSION

The illumination analysis method with deep learning allows us to efficiently compute single-shot illumination results to be employed for shot selection. Compared with the regular wave equation illumination method, the calculation efficiency is significantly improved. By dumping less related shots to the weakly illuminated area, the computational time is reduced furthermore without affecting the imaging quality.

DATA AVAILABILITY STATEMENT

The raw data supporting the conclusions of this article will be made available by the authors, without undue reservation.

AUTHOR CONTRIBUTIONS

CR programmed with illumination analysis, migration, and deep learning training and prediction; he wrote the manuscript. XJ presented the whole idea and revised the manuscript.

FUNDING

This study received support from the Joint Open Fund of Mengcheng National Geophysical Observatory (No. MENGO-202005) and the National Natural Science Foundation of China (42074125 & 41774121).

REFERENCES

Albertin, U., Watts, D., Chang, W., Kapoor, S. J., Stork, C., Kitchenside, P., et al. (2002). Near-salt-flank imaging with Kirchhoff and wavefield extrapolation migration. *72nd SEG Technical Program Expanded Abstracts*, 1328–1331. doi:10.1190/1.1816901

Baysal, E., Kosloff, D. D., and Sherwood, J. W. C. (1983). Reverse time migration. *Geophysics* 48, 1514–1524. doi:10.1190/1.1441434

Chang, K.-H., Han, M.-H., Roh, J.-K., Kim, I.-O., Han, M.-C., Choi, K.-S., et al. (1990). Gd-dtpa enhanced mr imaging in intracranial tuberculosis. *Neuroradiology* 32 (1), 19–25. doi:10.1007/bf00593936

Chen, B., and Jia, X. (2014). Staining algorithm for seismic modeling and migration. *Geophysics* 79 (4), S121–S129. doi:10.1190/geo2013-0262.1

Chen, S.-C., Ma, Z.-T., and Wu, R.-S. (2007). Illumination compensation for wave equation migration shadow. *Chinese J. Geophys.* 50 (3), 729–736. doi:10.1002/cjg2.1087

Chen, Y. R., Li, Z., Qin, N., and Zhang, K. (2013). Full waveform inversion with wave equation bi-directional illumination optimization. *Progress in Geophysics (in Chinese)* 28 (006), 3015–3021.

Claerbout, J. F. (1971). Toward a unified theory of reflector mapping. *Geophysics* 36 (3), 467–481. doi:10.1190/1.1440185

Gray, S. H. (1986). Efficient traveltime calculations for Kirchhoff migration. *Geophysics* 51, 1685–1688. doi:10.1190/1.1442217

Hill, N. R. (1990). Gaussian beam migration. *Geophysics* 55, 1416–1428. doi:10.1190/1.1442788

Jia, Y., and Ma, J. (2017). What can machine learning do for seismic data processing? an interpolation application. *Geophysics* 82 (3), V163–V177. doi:10.1190/geo2016-0300.1

Lecomte, I. (1998). Have a look at the resolution of prestack depth migration for any model, survey and wavefields. *68th SEG Technical Program Expanded Abstracts*, 1112–1115. doi:10.1190/1.1820082

Liu, Y., Zhang, Z., Zhong, R., Chen, D., Ke, Y., Peethambaran, J., Chen, C., and Sun, L. (2018). Multilevel building detection framework in remote sensing images based on convolutional neural networks. *IEEE J. Sel. Top. Appl. Earth Observations Remote Sensing* 11, 3688–3700. doi:10.1109/jstars.2018.2866284

Mao, J., Wu, R.-S., and Gao, J.-H. (2010). Directional illumination analysis using the local exponential frame. *Geophysics* 75, S163–S174. doi:10.1190/1.3454361

Mauricio, A. P., Jennings, J., Adler, A., and Dahlke, T. (2018). Deep-learning tomography. *Leading Edge* 37 (1), 58–66.

McMechan, G. A. (1983). Migration by Extrapolation of Time-dependent Boundary Values*. *Geophys Prospect* 31, 413–420. doi:10.1111/j.1365-2478.1983.tb01060.x

Mulder, W. A., and Plessix, R. E. (2004). A comparison between one-way and two-way wave-equation migration. *Geophysics* 69, 1491–1504. doi:10.1190/1.1836822

Ristow, D., and Rühl, T. (1994). Fourier finite-difference migration. *Geophysics* 59, 1882–1893. doi:10.1190/1.1443575

Ronneberger, O., Fischer, P., and Brox, T. (2015). U-net: convolutional networks for biomedical image segmentation. *LNCS* 9351, 234–241. doi:10.1007/978-3-319-24574-4_28

Stolt, R. H. (1978). Migration by fourier transform. *Geophysics* 43 (1), 23–48. doi:10.1190/1.1440826

Sun, J., Wang, D. L., Wang, T., Zhang, Y. B., Wang, T. X., and Tian, M. (2018). Study of multiples illumination analysis method based on two-way wave equation. *Progress in Geophysics* 033 (001), 243–249.

Vigh, D., Jiao, K., Cheng, X., Sun, D., and Lewis, W. (2016). Earth-model building from shallow to deep with full-waveform inversion. *The Leading Edge* 35 (12), 1025–1030. doi:10.1190/tle35121025.1

Wu, W. J., Lines, L. R., and Lu, H. X. (1996). Analysis of higher-order, finite-difference schemes in 3-D reverse-time migration. *Geophysics* 61 (3), 845–856. doi:10.1190/1.1444009

Xie, X. B., Jin, S, and Wu, R. S. (2003). Three-dimensional illumination analysis using wave equation based propagator. *73rd SEG Technical Program Expanded Abstracts*, 989–992.

Xie, X. B., He, Y. Q., and Li, P. M. (2013). Seismic illumination analysis and its applications in seismic survey design. *Chinese Journal of Geophysics-Chinese Edition* 56 (5), 1568–1581.

Yan, Z., and Xie, X.-B. (2016). Full-wave seismic illumination and resolution analyses: A Poynting-vector-based method. *Geophysics* 81, S447–S458. doi:10.1190/geo2016-0003.1

Yang, H., Xie, X. B., Luo, M., and Jin, S. (2008). Target oriented full-wave equation based illumination analysis. *78th SEG Technical Program Expanded Abstracts*, 2216–2220.doi:10.1190/1.3059326

Conflict of Interest: The authors declare that the research was conducted in the absence of any commercial or financial relationships that could be construed as a potential conflict of interest.

frontiers in Earth Science

ORIGINAL RESEARCH
published: 14 September 2021
doi: 10.3389/feart.2021.730476

Fast Least-Squares Reverse Time Migration of OBN Down-Going Multiples

Yanbao Zhang[1], *Yike Liu*[2]*, *Jia Yi*[3] *and Xuejian Liu*[4]

[1]Institute of Geophysics, China Earthquake Administration, Beijing, China, [2]Key Laboratory of Petroleum Resources Research, Institute of Geology and Geophysics, Chinese Academy of Sciences, Beijing, China, [3]China Earthquake Disaster Prevention Center, China Earthquake Administration, Beijing, China, [4]Department of Geosciences, The Pennsylvania State University, University Park, PA, United States

Nowadays the ocean bottom node (OBN) acquisition is widely used in oil and gas resource exploration and seismic monitoring. Conventional imaging algorithms of OBN data mainly focus on the processing of up-going primaries and down-going first-order multiples. Up-going multiples and higher-order down-going multiples are generally regarded as noise and should be eliminated or ignored in conventional migration methods. However, multiples carry abundant information about subsurface structures where primaries cannot achieve. To take full advantage of multiples, we propose a migration method using OBN down-going all-order multiples. And then the least-squares optimization algorithm is used to suppress crosstalks. Finally, a phase-encoding-based migration algorithm is developed to cut down the computational cost by blending several common receiver gathers together using random time delays and polarity reversals. Numerical experiments on the complex Marmousi model illustrate that the developed approach can enlarge the imaging area evidently, reduce the computational cost effectively, and enhance the image quality by suppressing crosstalks and improving the resolution.

Keywords: LSRTM, OBN, multiples imaging, phase-encoding, down-going multiples

OPEN ACCESS

Edited by:
Hua-Wei Zhou,
University of Houston, United States

Reviewed by:
Changsoo Shin,
Seoul National University, South Korea
Xiaohong Chen,
China University of Petroleum, China
Bingshou He,
Ocean University of China, China

***Correspondence:**
Yike Liu
ykliu@mail.iggcas.ac.cn

Specialty section:
This article was submitted to Solid Earth Geophysics, a section of the journal Frontiers in Earth Science

Received: *25 June 2021*
Accepted: *30 August 2021*
Published: *14 September 2021*

Citation:
Zhang Y, Liu Y, Yi J and Liu X (2021) Fast Least-Squares Reverse Time Migration of OBN Down-Going Multiples. Front. Earth Sci. 9:730476. doi: 10.3389/feart.2021.730476

INTRODUCTION

Many advanced imaging algorithms have been developed over the past few decades, among which reverse time migration (RTM) can provide quality images of subsurface complex structures aided by the two-way wave equation. Conventional RTM only accounts for primaries and regards multiples as noise. RTM using the raw data containing primaries and multiples will produce serious crosstalks in non-structural subsurface areas, which results in the reduction of the signal-to-noise (S/N) ratio of final imaging results and the incorrect geological interpretation. Therefore, many researchers concentrated on the suppression of multiples (Verschuur et al., 1992; Dragoset et al., 2010; Liu et al., 2010). However, multiples also carry lots of useful information about strata. Compared with primaries, multiples can provide extra illumination in areas where primaries cannot achieve for their smaller reflection angles and longer travel paths (Berkhout and Verschuur, 2006; Liu et al., 2011; Lu et al., 2015). To obtain higher-precision imaging results of subsurface structures, geophysical researchers have developed a variety of imaging approaches using multiples (Jiang et al., 2007; Muijs et al., 2007; Liu et al., 2011, 2015; Verschuur and Berkhout, 2011; Lu et al., 2015; Liu X. et al., 2016; Liu et al., 2018; Zhang et al., 2019). Among these techniques, reverse time migration of multiples (RTMM) Liu et al. (2011) combining the advantages of multiples and RTM can correctly

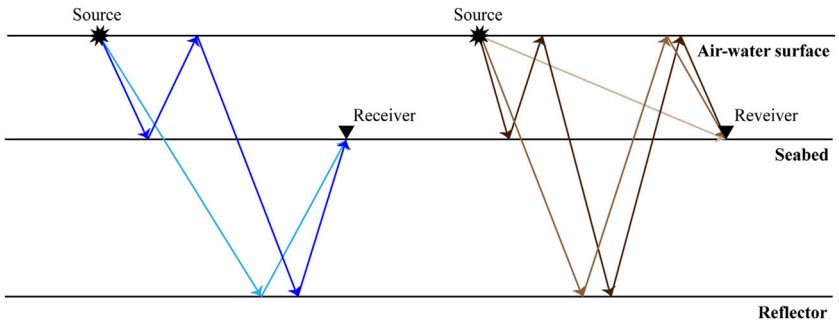

FIGURE 1 | Illustrations of OBN up-going reflections and down-going reflections denoted by the blue raypaths and the brown raypaths, respectively.

migrate the multiple reflections and image the subsalt structures. RTMM is currently one of the easiest and most widely used algorithms to migrate multiples (Zuberi and Alkhalifah, 2013; Liu Y. et al., 2016; Li et al., 2017; Liu and Liu, 2018; Zhang et al., 2020).

Due to the existence of interfaces with large impedance differences such as the air-water surface, seabed, and salt boundaries, marine seismic data often contain plenty of multiples with strong energy. The imaging results with satisfactory accuracy cannot be obtained if multiples are not effectively processed. Traditionally, marine seismic data are acquired using the towed streamer, ocean bottom cable (OBC), or OBN. Equipped with a geophone and a hydrophone, OBN is a seismometer that is placed at the seabed. For the flexible deployment and the abundant wavefield information, the OBN acquisition is widely used in oil and gas resource exploration, seismic monitoring, detection of deep structures, etc. (Katzman et al., 1994; Dash et al., 2009; Mathias et al., 2009). In the OBN acquisition, the record is composed of up-going and down-going components, as shown in **Figure 1**. The up-going record includes the up-going primaries and multiples, while the down-going record contains the direct wave and down-going multiples. And the two components can be separated using the hydrophone recording (P) and the vertical component of the geophone (Z) aided by PZ summation technique (Barr and Sander, 1989; Schalkwijk et al., 2003).

Traditional imaging algorithms using up-going primaries have limits in imaging the seabed and the illumination range. The migration using the down-going first-order multiples is developed to solve the problems mentioned above. And it is also called mirror migration (Grion et al., 2007; Dash et al., 2009; Wong et al., 2015). In mirror migration, the virtual OBN position is obtained by turning the real OBN up with the sea surface as a mirror, followed by implementing conventional migration procedures. Regardless of the conventional migration or the mirror migration, the up-going multiples and down-going high-order multiples are regarded as noise and should be suppressed before or during migration. Compared with primaries and first-order down-going multiples, higher-order multiples possess longer travel paths and sufficient smaller reflection angles, which can guarantee that imaging using multiples can supply quality results with a wider illumination range (Liu et al., 2011; Lu et al., 2015; Wong et al., 2015). To make full use of the structural information contained in multiples and further increase the illumination range, we proposed RTM using down-going multiples for OBN acquisition, in which the lower-order multiples are recognized as the secondary sources of the higher-order multiples. However, the biggest challenge of RTMM is the suppression of crosstalks (Liu et al., 2011). Further, the least-squares algorithm is introduced to suppress the crosstalk noise (Nemeth et al., 1999; Dai et al., 2012; Liu et al., 2017; He et al., 2019).

The calculation cost of the migration process is linear with the total number of shot gathers. Therefore, combining several shot gathers into a supergather can effectively reduce the calculation unit and improve the calculation efficiency. However, when migrating one supergather, the interactions between the unrelated sources wavefield and the receivers wavefield will cause serious crosstalk noise, which decreases the S/N ratio of the imaging results tremendously (Romero et al., 2000; Dai et al., 2012). For example, by combining two shot gathers into one supergather and then implementing the migration, the crosscorrelation between the source wavefield activated by the first source and the receiver wavefield generated by the unrelated second backward-penetrating receiver data will produce strong crosstalks. To mitigate the above-mentioned crosstalk noise, Romero et al. (2000) first applied the phase encoding strategies in the migration procedures and showed a variety of encoding strategies. Among the commonly used encoding strategies, the random phase encoding technology Schuster et al. (2011), combining random time delays and random polarity reversals, has a better crosstalk suppression effect because it can shift and discrete crosstalk noise randomly. Krebs et al. (2009) introduced the random phase encoding scheme into the full waveform inversion and obtained results of the same quality as conventional methods, while the amount of calculation is reduced by an order of magnitude. The multi-source least-squares reverse time migration (LSRTM) proposed by Dai et al. (2012) is even more efficient than RTM, although there are some random artifacts in the imaging results. It is worth noting that to avoid convergence problems caused by the incomplete matching between the predicted data and observed data, the application of random phase encoding is generally limited to the fixed-spread acquisition geometries (Krebs et al., 2009; Dai et al., 2012; Liu et al., 2018). In the RTM of OBN

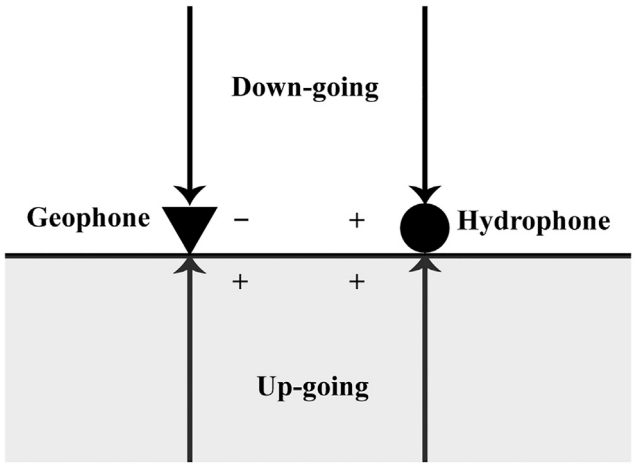

FIGURE 2 | Schematic diagram of PZ summation. The hydrophone and geophone record down-going and up-going wavefield with different polarities.

down-going multiples, the lower-order multiples are recognized as the sources of the higher-order multiples, and the lower- and higher-order multiples share the same receivers. Therefore, the random phase encoding scheme can be introduced into the migration of multiples for OBN acquisition conveniently. To save the computational cost, we developed a phase-encoding-based LSRTM of OBN down-going multiples.

In this paper, we first specify the principle of RTM using OBN down-going multiples and then introduce least-squares technology to suppress crosstalks, followed by the explicit description of the phase-encoding-based LSRTM of OBN down-going multiples. Numerical experiments on the Marmousi model are used to verify the effectiveness and efficiency of the proposed approach, and the results demonstrate that the proposed approach can effectively suppress crosstalks, improve the imaging resolution, and save the computational cost. Finally, the discussion and conclusion are provided.

Theory

Common Receiver Domain RTM of OBN Down-Going Multiples

The seismic record in OBN acquisition consists of up-going and down-going components, which can be separated using PZ summation:

$$\begin{cases} U = (P + \rho c Z)/2 \\ D = (P - \rho c Z)/2 \end{cases} \tag{1}$$

where U and D denote the up-going and down-going records, respectively. P and Z represent the pressure recorded on the hydrophone and particle velocity recorded on the vertical geophone, respectively. ρ and c are the density and the acoustic velocity of water, respectively. As shown in **Figure 2**, the basic principle of PZ summation is that the geophone and the hydrophone data record opposite polarity for the down-going propagating wavefield. If the wavefield is propagating upward, they will record the same polarity.

In OBN acquisition, receivers are placed at the seabed sparsely, while sources are activated on the sea surface densely. For the sake of computational efficiency, the seismic reciprocal principle Knopoff and Gangi (1959) is implemented and migrations for OBN data are usually performed in the common receiver gather (CRG) domain. The data is converted from the common shot gather (CSG) into the CRG by exchanging the source and receiver locations during imaging. After conversion, the sources and nodes are regarded as the virtual receivers and the virtual sources, respectively. The conventional migration algorithms for OBN data often account for up-going primaries or down-going first-order multiples, as shown in **Figures 3A,B**. For the imaging of up-going primaries, the virtual sources are arranged at the seabed, which results in serious aliasing noise around the real node locations. And the subsurface coverage area of primaries is limited to the vicinity of the node positions. The mirror migration, utilizing down-going first-order multiples, can image the seabed well and enlarge the imaging range by turning the OBNs to the mirror OBNs taking the sea surface as the axis of symmetry. Both the above-mentioned migration approaches regard the up-going multiples and down-going high-order multiples as the data noise and suppress them before migration. The structural information of high-order multiples has not been fully exploited. To take full advantage of higher-order multiples, we propose RTM using down-going multiples for the OBN acquisition. Prior to the migration procedure, the down-going record is separated using PZ summation, and then the down-going multiples are acquired by muting the direct wave from the down-going record. The RTM of down-going multiples can be accomplished through the following three steps:

1 Producing the source wavefield by forward-propagating the separated down-going record including the direct wave and multiples:

$$\begin{cases} \dfrac{1}{v_0(x,z)^2}\dfrac{\partial^2 P_s(x,z,t)}{\partial t^2} = \nabla^2 P_s(x,z,t) \\ P_s(x_r, z=0, t) = d(x_r,t) + m(x_r,t) \end{cases}, \tag{2}$$

where x_r is the horizontal location of virtual receivers, $v_0(x,z)$ is the migration velocity model, and $P_s(x,z,t)$ is the generated source wavefield. $d(x_r,t)$ and $m(x_r,t)$ are the direct wave and the down-going multiples in the CRG domain, respectively.

2 Backward-extrapolating the down-going multiples to obtain the receiver wavefield $M_r(x,z,t)$:

$$\begin{cases} \dfrac{1}{v_0(x,z)^2}\dfrac{\partial^2 M_r(x,z,t)}{\partial t^2} = \nabla^2 M_r(x,z,t) \\ M_r(x_r, z=0, t) = m(x_r,t) \end{cases}, \tag{3}$$

3 Implementing the zero-lag crosscorrelation imaging condition to the source and receiver wavefield:

$$I(x,z) = \sum_{t=0}^{t_{max}} P_s(x,z,t) M_r(x,z,t), \tag{4}$$

where $I(x,z)$ represents the migrated image and t_{max} is the total recording time. Compared to the imaging point of mirror

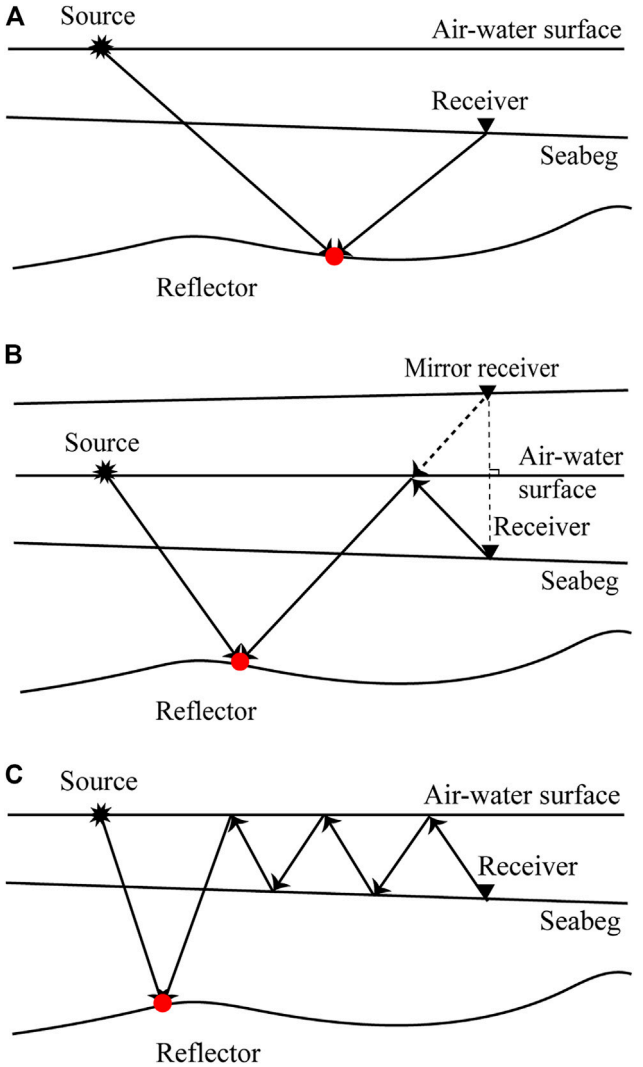

FIGURE 3 | Raypath diagrams of RTM using **(A)** the up-going primaries **(B)** the down-going first-order multiples (mirror migration), and **(C)** all-order down-going multiples. And the red points represent the imaging points of different approaches.

migration (the red solid point in **Figure 3B**), the imaging point of the proposed RTM using down-going multiples in **Figure 3C** is located at the left of that in **Figure 3B** (the shadow zone of mirror migration), which means wider illumination range. And theoretically with the order of multiples gets larger, the illumination can be further expanded.

Unlike conventional RTM, RTMM correlates the complex forward- and backward-penetrated records, thus the interactions among unrelated multiples will cause undesired crosstalk artifacts which critically degrade the S/N ratio of the final imaging results. **Figure 4** illustrates the representative crosstalks in RTMM for OBN acquisition. In **Figure 4**, the red solid lines, the black solid lines, and the red dotted lines represent the wavepaths of the forward-propagating data, the backward-propagating data, and the crosscorrelation, respectively. As shown in **Figure 4**, the forward-propagating direct wave recorded at S3 can be regarded as the secondary source of the backward-propagating second-order multiples recorded at S1, and the crosscorrelation between the two multiples will produce crosstalk point A1 denoted by the magenta point. In **Figure 4B**, the crosscorrelation between the forward-propagating first-order multiples recorded at S2 and the backward-propagating first-order multiples recorded at S1 will cause the crosstalk point A2.

LSRTM of OBN Down-Going Multiples

Compared with RTM, the LSRTM has been extensively researched to enhance the imaging quality by suppressing RTM imaging artifacts, improving the imaging resolution, and balancing the energies of imaging events. LSRTM also can be extended to the migration of multiples to suppress the severe crosstalks of RTMM. Unlike the conventional LSRTM using primaries, LSRTM of multiples (LSRTMM) Zhang and Schuster (2014), Wong et al. (2015), Liu X. et al. (2016) regards multiples data as the secondary source and tries to find a reflectivity model that minimizes the misfit function between predicted and observed multiple reflections. The Born modeling operator (see **Appendix A**) that corresponds to the multiples can be represented as

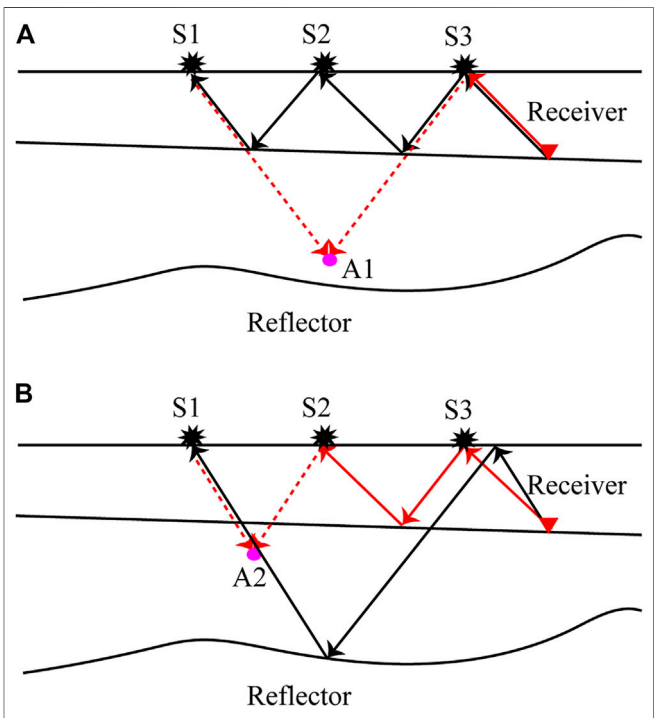

FIGURE 4 | Illustrations of representative crosstalks in RTMM. As shown in panel **A**, the crosscorrelation between the forward-propagating direct wave recorded at S3 and the backward-propagating second-order multiples recorded at S1 will generate the crosstalk point A1 denoted by the magenta point. In panel **B**, the first-order multiple recorded at S2 can be regarded as the secondary source of the backward-propagating first-order multiple recorded at S3, and the crosscorrelation of the two multiples will cause crosstalk point A2.

$$\begin{cases} \dfrac{1}{v_0(x,z)^2}\dfrac{\partial^2 M(x,z,t)}{\partial t^2} - \nabla^2 M(x,z,t) = d(x_r,t) + m(x_r,t) \\ \dfrac{1}{v_0(x,z)^2}\dfrac{\partial^2 M_r(x,z,t)}{\partial t^2} - \nabla^2 M_r(x,z,t) = -R(x,z)\dfrac{\partial^2 M(x,z,t)}{\partial t^2}\cdot \\ m_{pre}(x_r,t) = M_r(x_r,z=0,t) \end{cases} \tag{5}$$

Eq. (5) contains three steps: 1) The down-going record of OBN data $d(x_r,t) + m(x_r,t)$ are treated as the virtual sources and injected into the subsurface background model v_0, which will produce the incident wavefield M. 2) The interaction between the incident wavefield M and the subsurface reflectivity R will generate the scattered wavefield M_r. 3) Through saving the boundary wavefield of the scattered wavefield M_r, we can obtain the predicted down-going multiples m_{pre}. **Eq. (5)** can be depicted compactly using a matrix-vector notation:

$$m_{pre,i} = L_i R \tag{6}$$

where L_i and $m_{pre,i}$ represent the linear Born modeling operator and the predicted OBN down-going multiples for the ith CRG, respectively. The RTM operator can be treated as the adjoint of the forward-modeling operator, thus the final migrated image R_{mig} can be obtained by:

$$R_{mig} = \left[L_1^T L_2^T \cdots L_n^T\right]\begin{bmatrix} m_1 \\ m_2 \\ \vdots \\ m_n \end{bmatrix} = \sum_{i=0}^{n} L_i^T m_i \tag{7}$$

where the superscript T is the conjugate transpose operation. L_i^T and m_i are the migration operator and the observed down-going multiples for the ith CRG, respectively.

Based on the Born modeling operator defined in **Eq. 5** and its adjoint RTM operator in **Eq. (7)**, we can minimize the difference between the modeled/predicted multiples and the observed multiples via the misfit function $f(R)$,

$$f(R) = \frac{1}{2}\sum_{i=0}^{n}\|L_i R - m_i\|_2^2 \tag{8}$$

which can be iteratively solved aided by any gradient-based inversion approach.

LSRTM of OBN Down-Going Multiples With Random Phase Encoding

However, in LSRTM, each iteration contains migration, de-migration and gradient calculation steps, the calculation cost of which is several times of that of RTM. And the computational cost of LSRTM for OBN down-going multiples may be larger for more iterations are needed to achieve better crosstalk artifacts suppression effect. Therefore, we introduce the random phase encoding scheme into LSRTM of OBN down-going multiples to improve the computational efficiency. By encoding the forward modeling operators (in **Eq. (6)**), OBN down-going multiples of different CRGs can be simultaneously modeled as

$$[\alpha_1 + \alpha_2 + \cdots + \alpha_n]m_{pre,i} = [\alpha_1 L_1 + \alpha_2 L_2 + \cdots + \alpha_n L_n]R \tag{9}$$

where α_n is the phase encoding function. **Eq. (9)** can be written in a compact form of

$$\check{m}_{pre} = \check{L}R \tag{10}$$

where $\check{L}$ and $\check{m}_{pre}$ represent the encoded forward modeling operator and predicted data for one supergather, respectively. The image of a supergather of observed OBN down-going multiples $\check{m}$ can be produced by

$$\check{R}_{mig} = \check{L}^T\check{m} \tag{11}$$

where $\check{R}_{mig}$ represents the phase-encoded image of OBN down-going multiples. **Eq. (12)** is the expanded form of **Eq. (11)**

$$\begin{aligned} \check{R}_{mig} &= \left[\alpha_1^* L_1^T + \alpha_2^* L_2^T + \cdots + \alpha_n^* L_n^T\right]\times\left[\alpha_1\check{m}_1 + \alpha_2\check{m}_n + \cdots + \alpha_n\check{m}_n\right] \\ &= \sum_{i=1}^{n}\alpha_i^*\alpha_i L_i^T\check{m}_i + \sum_{i=1}^{n}\sum_{j\neq i}^{n}\alpha_i^*\alpha_j L_i^T\check{m}_i \\ &= \underbrace{\sum_{i=1}^{n} L_i^T\check{m}_i}_{valid\ term} + \underbrace{\sum_{i=1}^{n}\sum_{j\neq i}^{n}\alpha_i^*\alpha_j L_i^T\check{m}_i}_{noise\ term} \end{aligned} \tag{12}$$

where for any integer value i, we assume that $\alpha_i^*\alpha_i = 1$. In **Eq. (12)**, the valid term, which is identical with **Eq. (7)**, will produce the correct imaging result and crosstalks. The noise term only generates crosstalk noise, which is caused by the interaction between the encoded CRGs. For phase-encoding-based RTM of OBN down-going multiples, the crosstalk noise generated by the noise term is much stronger than the noise generated by the valid term (Liu et al., 2018). In the numerical experiment section, we will illustrate the different crosstalks caused by the valid and noise terms of **Eq. (12)**. Through encoding ns supergathers from original CRGs and based on **Eqs (10)** and **(11)**, the objective function of phase-encoding-based LSRTM of OBN down-going multiples is expressed as

$$f(R) = \frac{1}{2}\sum_{i=1}^{ns}\|\check{L}R - \check{m}_i\|_2^2 \tag{13}$$

The implementation details of the proposed migration approach are illustrated in **Figure 5**. One of the key steps to the proposed approach is the choice of the phase encoding functions. In this paper, the phase encoding function is designed as

$$\alpha_n = e^{-iw\tau_n}S_n \tag{14}$$

where τ_n and S_n denote the random time delay and random polarity reversal for a blended CRG, respectively. The random time delays τ_n follows the normal distribution with a standard deviation of σ and a mean of zero, expressed as:

$$\tau_n \sim N(0,\sigma^2). \tag{15}$$

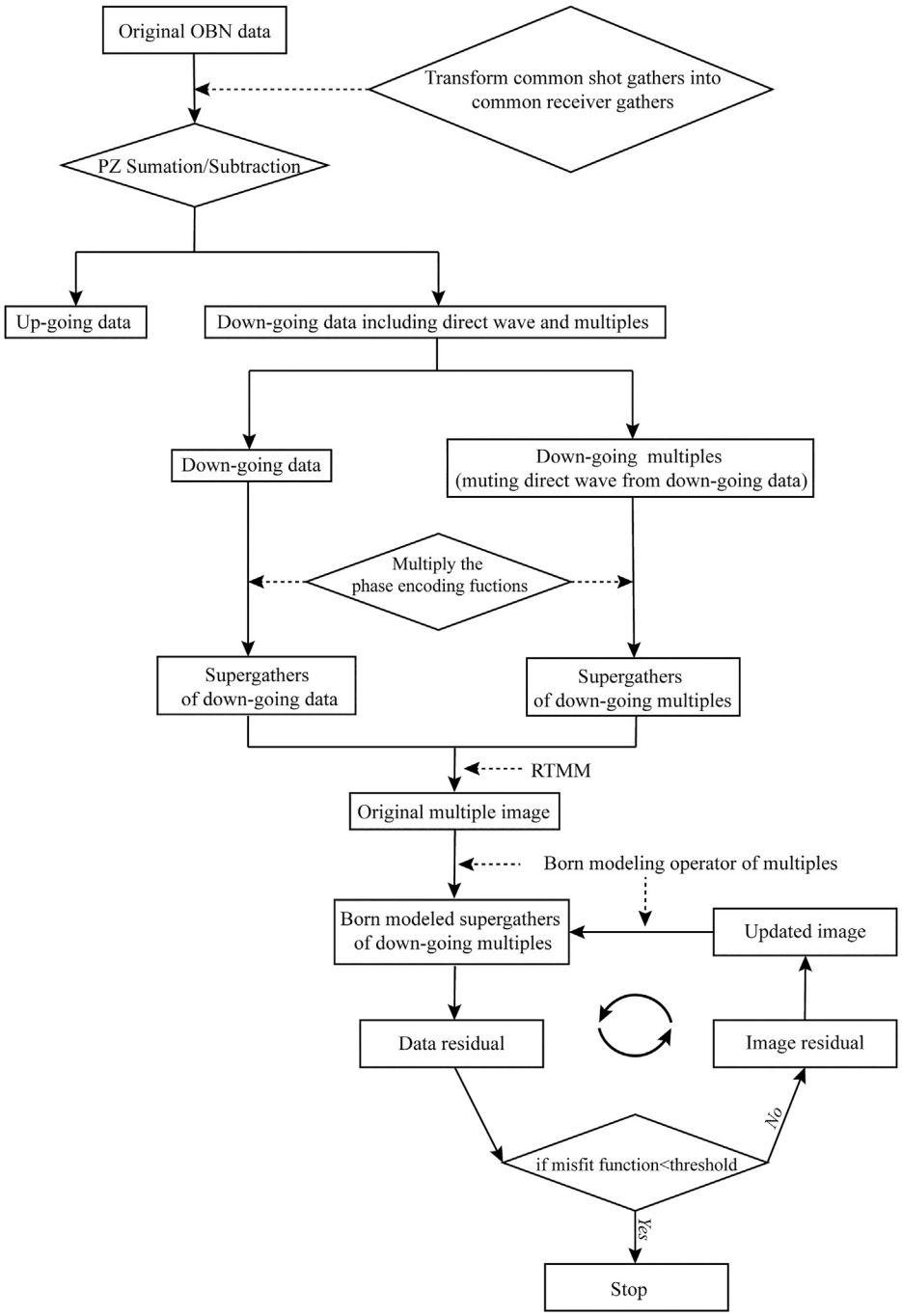

FIGURE 5 | The workflow of the fast LSRTM using down-going multiples.

The probability that the polarity reversal function S_n takes a value of 1 or -1 for each blended CRG is 1/2. According to the property of normal distribution, the polarity reversal function S_n can be defined by the following:

$$S_n = sgn(\tau_n), \tag{16}$$

where *sgn* represents the sign function. If $\tau_n \geq 0$ $S_n = 1$, otherwise $S_n = -1$.

Numerical Examples

In this section, we apply the proposed phase-encoding-based LSRTM of OBN down-going multiples on the Marmousi model. A high-order staggered-grid finite-difference algorithm with PML absorbing boundaries is utilized to solve the first-order velocity-stress acoustic wave equations and produce the OBN data. The results of conventional RTM using primaries and mirror migration are also used to verify the effectiveness of the proposed approach.

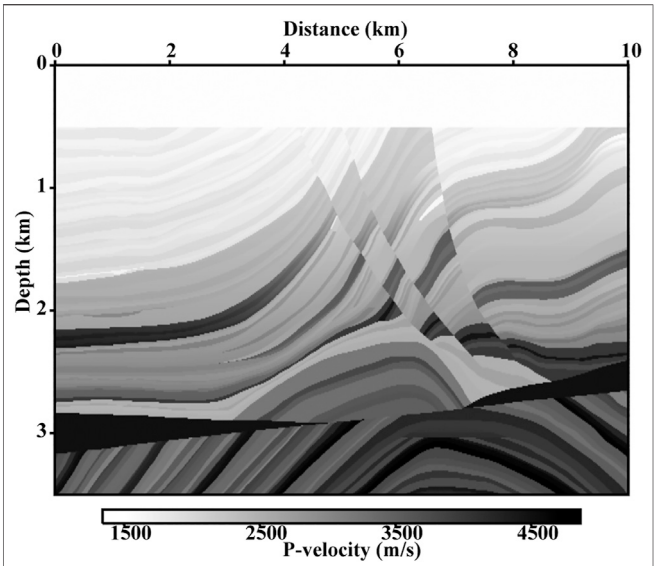

FIGURE 6 | The Marmousi velocity model.

The Behavior of Conventional LSRTM of OBN Down-Going Multiples

Figure 6 shows the Marmousi velocity model. The model is discretized into 351 grids in the vertical direction and 1,001 grids in the horizontal direction both with a 10 m grid interval. The seismic source is selected as the Ricker wavelet with a peak frequency of 20 Hz. A set of 1,001 CSGs with a source interval of 10 m are simulated to certify the performance of the novel approach. The total recording time of each CSG is 4s with a sampling interval of 4 m s. First, we make use of 20 OBNs, distributed evenly from 2.98 to 6.78 km in the horizontal direction with a 200-m node interval, to test the imaging performances of RTM and LSRTM of down-going multiples. The pressure components of a CSG and a converted CRG are illustrated in **Figure 7A,B** respectively. The up-going and down-going records after PZ summation are displayed in **Figure 8A,B**, respectively. The down-going multiples after muting the direct wave from the down-going record (**Figure 8**) are shown in **Figure 8C**.

In the CRG domain, since the seismometers are placed at the seabed and they act as the virtual sources, there is strong aliasing noise around the seabed in the image of the conventional RTM using up-going primaries as shown by the arrow in **Figure 9A**. Moreover, the illumination range of **Figure 9A** is limited to the vicinity of the node positions due to the insufficient subsurface coverage of up-going primaries. To settle the above-mentioned problems, the RTM using the down-going first-order multiples (mirror migration) is developed. As shown in **Figure 9B**, the imaging quality of the seabed has been greatly improved pointed out by the arrow, and the illumination range has also been expanded compared with the imaging result of up-going primaries in **Figure 9A**. To make full advantage of higher-order multiples, the proposed RTM of OBN down-going multiples algorithm is implemented, and the imaging result is displayed in **Figure 9C**. Compared with the results in **Figures 9A,B**, the imaging result of all-order multiples in **Figure 9C** shows a much wider illumination range. However, the interferences among unrelated multiples cause crosstalk artifacts which degrade

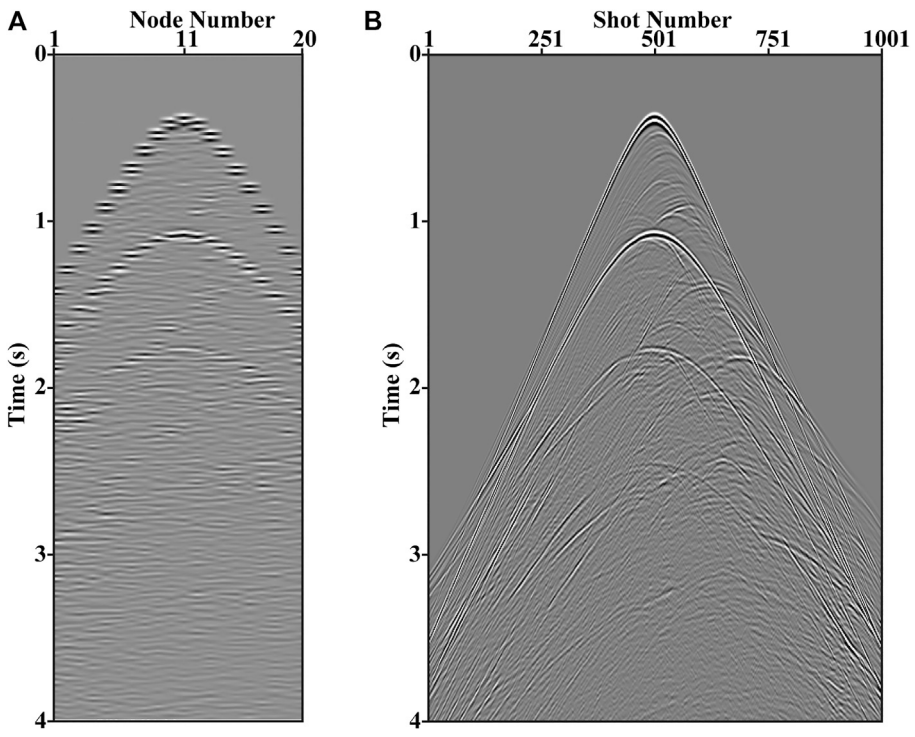

FIGURE 7 | The hydrophone pressures of **(A)** a CSG and **(B)** a converted CRG with a node interval.

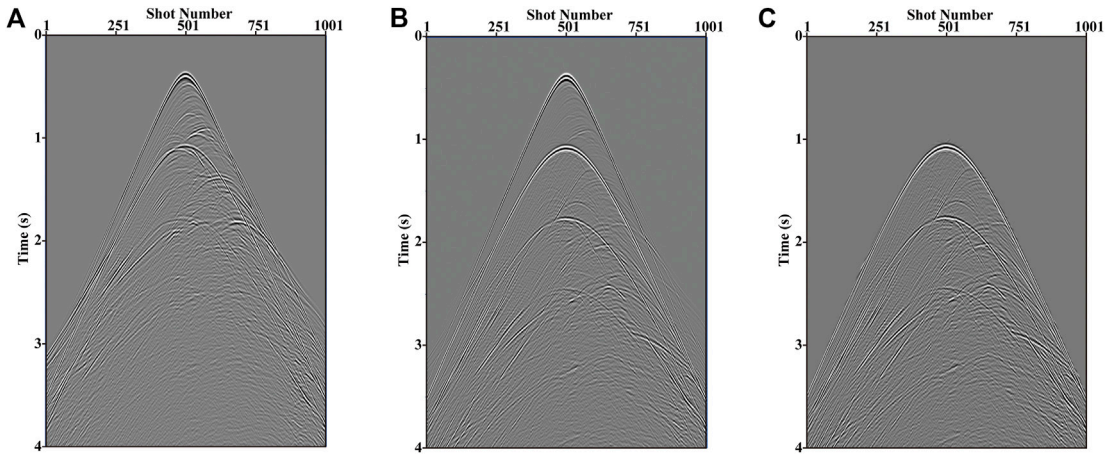

FIGURE 8 | The CRGs of **(A)** the up-going and **(B)** down-going pressures obtained after applying PZ summation **(C)** the down-going multiples acquired by muting direct wave from panel B.

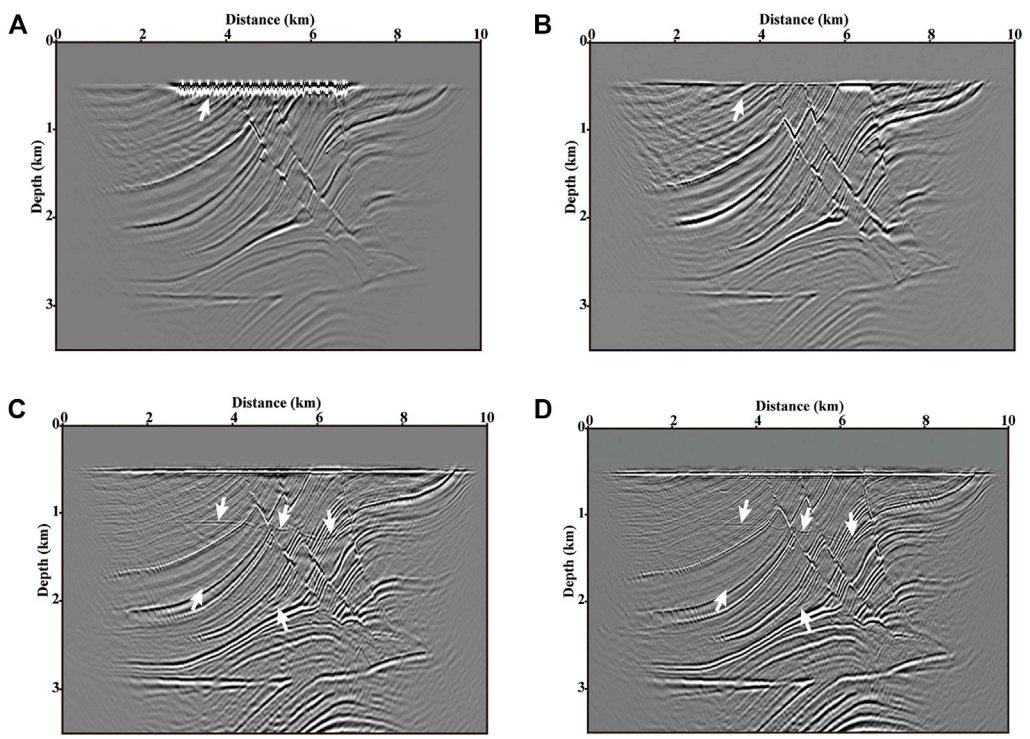

FIGURE 9 | Migration results of **(A)** up-going primaries **(B)** down-going first-order multiples, and down-going all-order multiples **(C)** with and **(D)** without least-squares algorithm (10 iterations) with a node interval of 100 m. The arrows in panels C and D denote the inherent crosstalks which can be suppressed effectively by LSRTMM.

the imaging fidelity as denoted by the arrows in **Figure 9C**. The kind of crosstalks is inherent in conventional RTMM results (**Eq. (7)** or the valid term of **Eq. (12)**) (Liu et al., 2011). Compared with RTM of down-going multiples, the developed LSRTM of down-going multiples can suppress the crosstalks effectively as pointed out by the arrows in **Figures 9C,D**, and produce a higher-resolution image (**Figure 9D**).

The Behavior of the Proposed Phase-Encoding-Based LSRTM of OBN Down-Going Multiples

Subsequently, the node interval is reduced from 200 to 100 m, and a total of 40 nodes are evenly placed at the seabed from 2.98 to 6.88 km. After the simulation and PZ summation, 40 CRGs are encoded into 1,

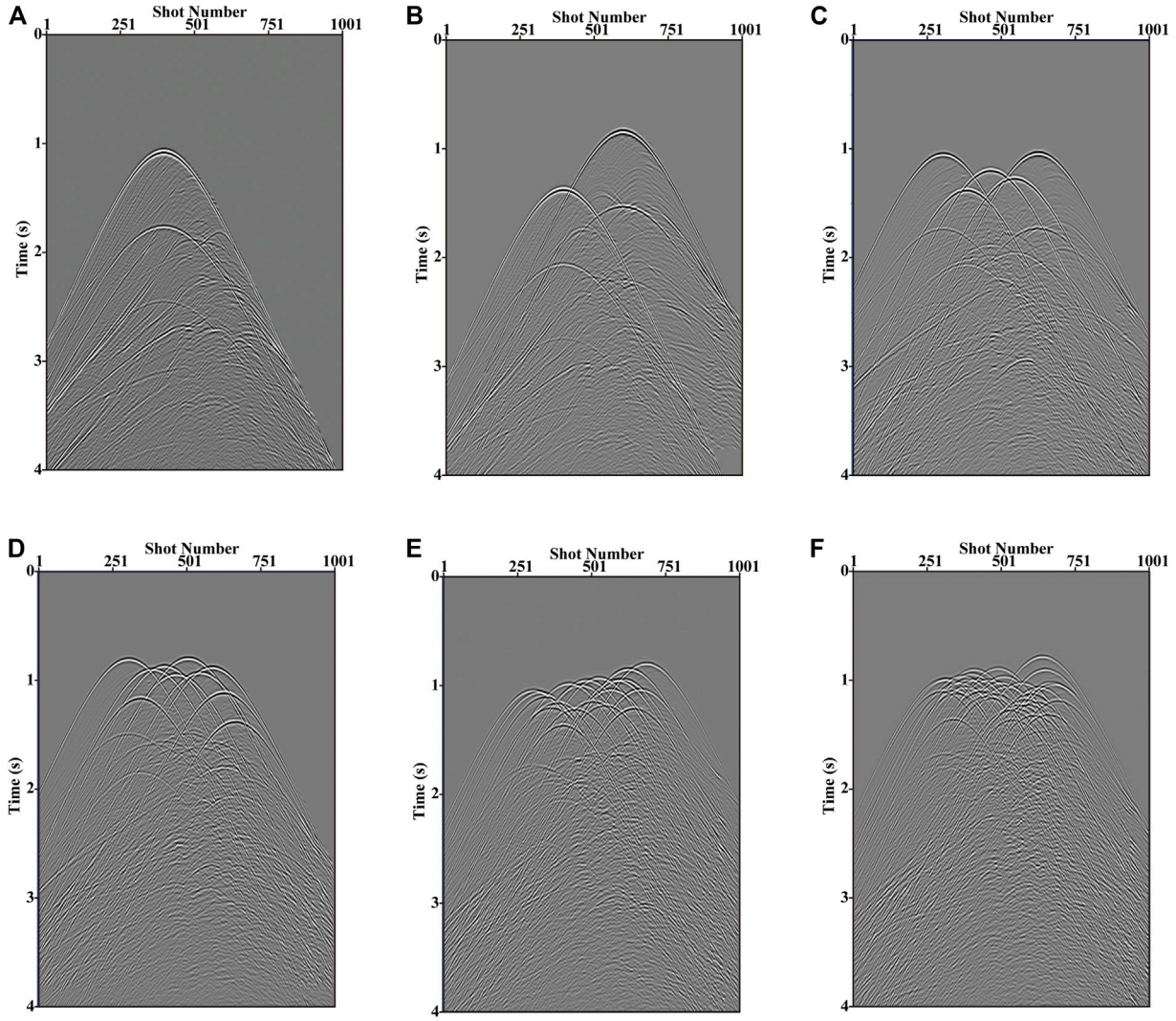

FIGURE 10 | The blended supergathers by encoding **(A)** 1 **(B)** 2 **(C)** 5 **(D)** 10 **(E)** 20, and **(F)** 40 CRGs of down-going multiples with a node interval of 100 m.

2, 4, 8, 20 supergathers to verify the effectiveness and efficiency of the proposed phased-encoding-based algorithm. The random encoding function which combines the random time delays and polarity reversals is utilized to blend different CRGs. The random time delay sequences distribute normally with a 0.5 standard deviation and zero mean. The blended supergathers of 1, 2, 5,10, 20, and 40 CRGs of down-going multiples are illustrated in **Figure 10**, respectively. Images generated by RTM of up-going primaries, down-going first-order multiples (mirror migration), and down-going multiples are shown in **Figures 11A–C**, respectively. **Figure 11D** represents the result of LSRTM of down-going multiples. Compared with the images with the 200 m node interval in **Figure 9**, the corresponding images with the 100 m node interval provide more sufficient subsurface coverage, more continuous strata, and a higher S/N ratio.

In the following, we use five sets of supergathers that regard the number of encoding CRGs as the variable to present the effectivity and efficiency of the proposed phase-encoding-based LSRTM of down-going multiples. **Figures 12–16** display the RTM and LSRTM (10 iterations) images using the supergathers in **Figures 10B–F**, respectively. Compared with the RTM, the LSRTM can effectively suppress the noise caused by the interferences among encoded CRGs (the noise term of **Eq. 12**) and significantly improve the imaging resolution as shown by the arrows in panels **A** and **B** of **Figures 12–16**. From the five pairs of migration results, as the number of encoding CRGs decreases, the imaging results are getting closer to those of conventional migrations (**Figures 11C,D**). The trend is caused by the decrease of the energy proportion of the noise term in **Eq. (12)**. However, as the number of encoding CRGs decreases, the computational cost will increase. In the last two experiments, the original 40 shot gathers are encoded into 8 and 20 supergathers, respectively. And the final results (**Figures 15**, **16**) show better imaging qualities and a higher S/N ratio compared with those results in **Figures 12–14**. Therefore, we choose them to conduct the calculation comparison

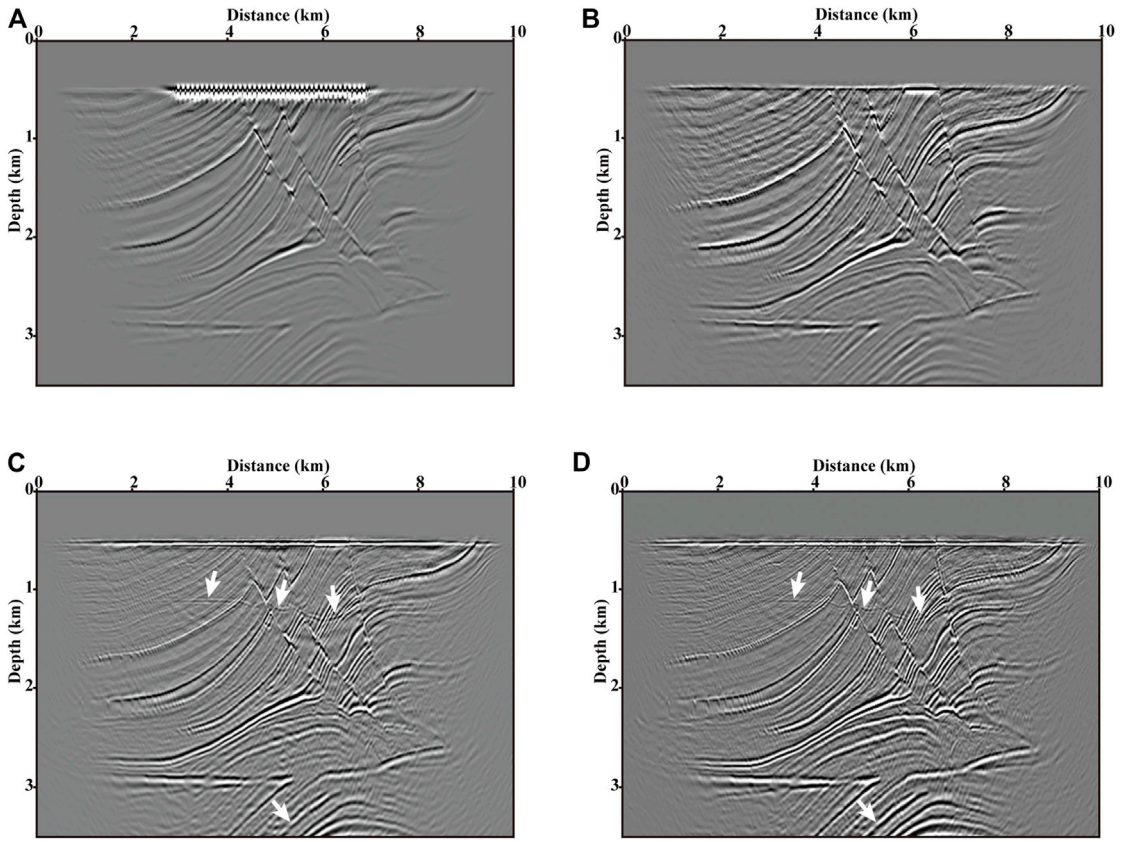

FIGURE 11 | Migration images of **(A)** up-going primaries **(B)** down-going first-order multiples, and down-going all-order multiples **(C)** with and **(D)** without least-squares algorithm (10 iterations) with a node interval of 100 m. As denoted by the arrows in panels C and D, the LSRTM can improve the imaging quality effectively.

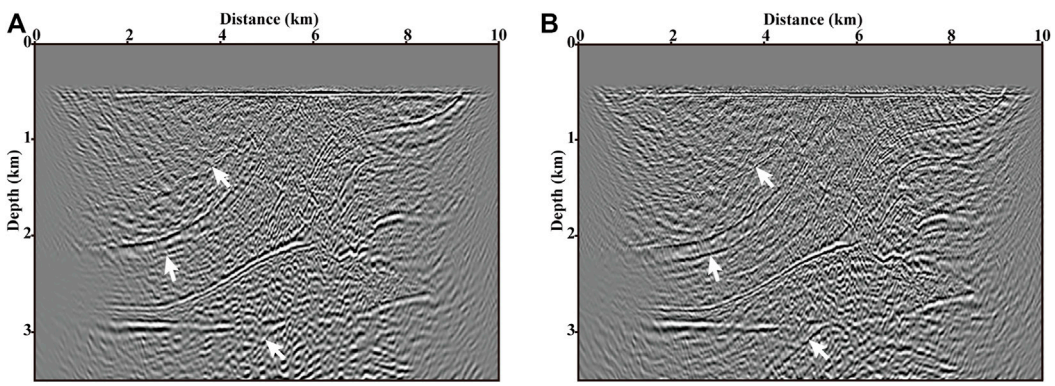

FIGURE 12 | Images provided by **(A)** RTM and **(B)** LSRTM of one blended supergather of 40 CRGs after 10 iterations.

with conventional LSRTM of down-going multiples. Scaling all calculations to the forward modeling, each iteration of the LSRTM requires 6 forward modelings including two for the RTM, two for the de-migration, and two for the gradient calculation. The conventional LSRTM of down-going multiples with 40 supergathers and 10 iterations (see **Figure 11D**) requires a computational cost of $40 \times 6 \times 10 = 2{,}400$ forward modelings. The computational costs for LSRTM images in **Figure 15B** (8 supergathers) and **Figure 16B** (20 supergathers) are $8 \times 6 \times 10 = 480$ and $20 \times 6 \times 10 = 1{,}200$ forward modelings, respectively. The comparison of computational cost demonstrates that the proposed phased-encoded LSRTM method can provide the results which can meet the requirement of interpretation and improve the computational efficiency manyfold.

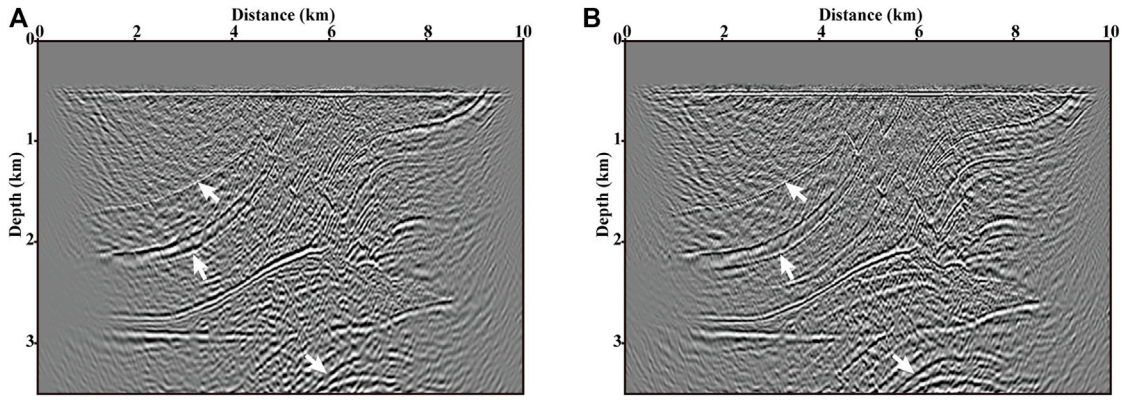

FIGURE 13 | Images provided by **(A)** RTM and **(B)** LSRTM of two blended supergathers of 20 CRGs after 10 iterations.

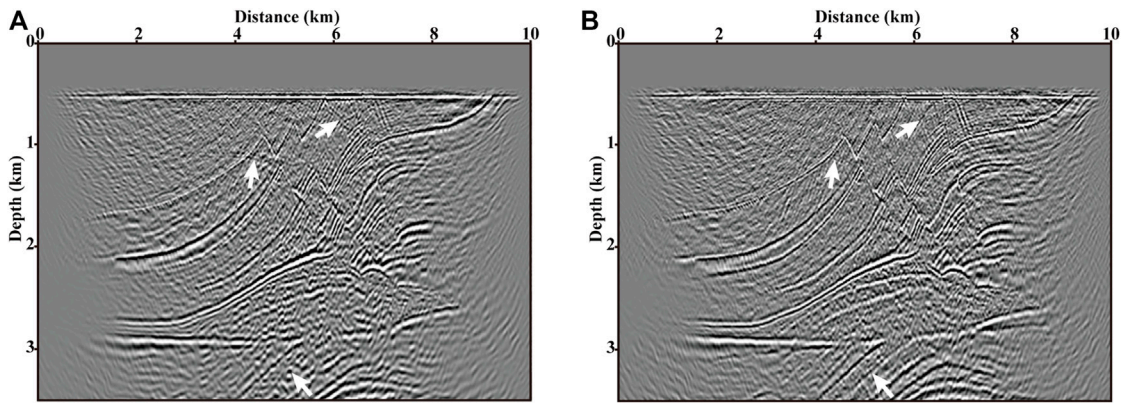

FIGURE 14 | Images provided by **(A)** RTM and **(B)** LSRTM of four blended supergathers of 10 CRGs after 10 iterations.

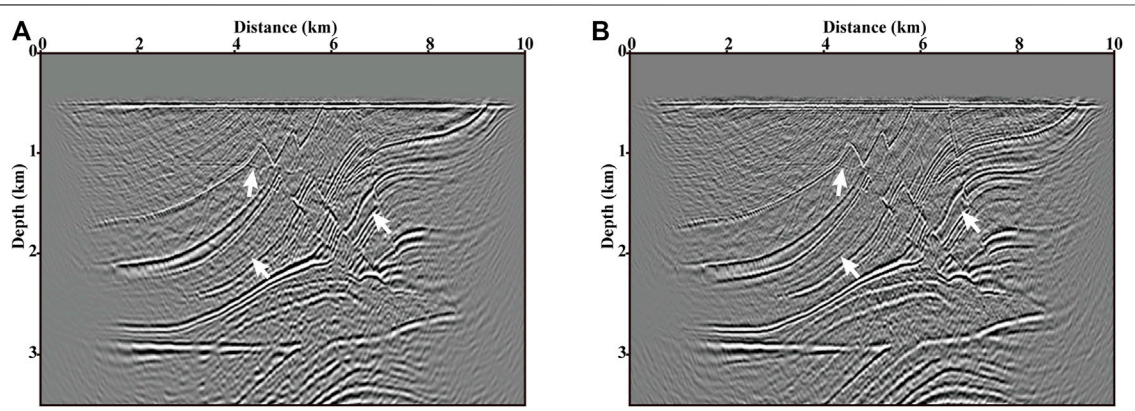

FIGURE 15 | Images provided by **(A)** RTM and **(B)** LSRTM of eight blended supergathers of 5 CRGs after 10 iterations.

DISCUSSION

Up to now, there are two widely used crosstalk suppression methods in the migration of multiples. The first one is the LSRTMM which introduces least-squares optimal algorithms to suppress crosstalks and obtains higher-precision images of multiples migration. The second one is the RTM of controlled-order multiples (RTM-CM) in which the different orders of multiples are extracted before migration procedures and the separated nth-order and (n+1)th-order multiples respectively

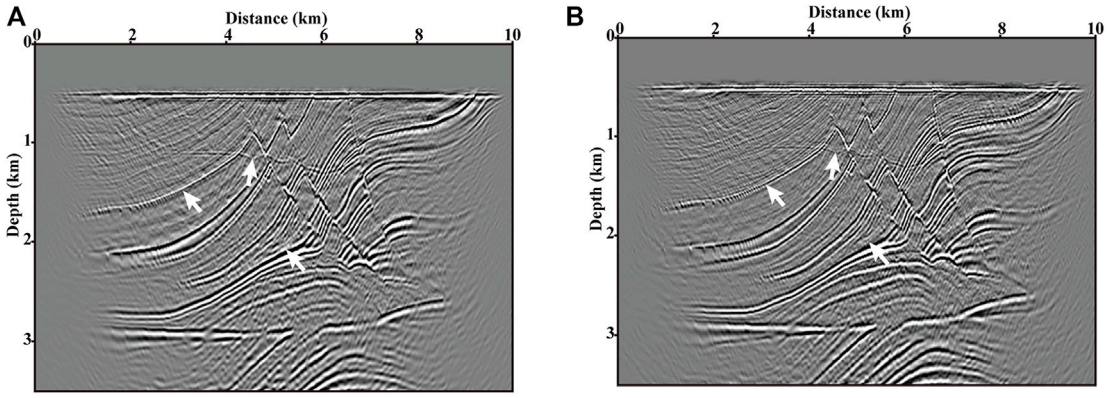

FIGURE 16 | Images provided by **(A)** RTM and **(B)** LSRTM of twenty blended supergathers of two CRGs after 10 iterations.

act as the source and receiver data. RTM-CM can significantly reduce the crosstalks due to the simplifies of the forward- and backward-propagating data. Liu Y. et al. (2016) separated different orders of multiples using surface-related multiple elimination (SRME) and then proposed LSRTM-CM. Compared with LSRTMM, LSRTM-CM obtains images with a higher S/N ratio. When extracting multiples of different orders by conventional SRME, the locations of sources and receivers must keep coincident. However, in OBN acquisition, shots are activated densely on the sea surface and seismometers are sparsely placed at the seabed, which makes it difficult to isolate different-order up- or down-going multiples. Therefore, in this study, LSRTMM is utilized to suppress crosstalks rather than RTM-CM. The least-squares algorithms can not only suppress the inherent crosstalks of multiple imaging but also reduce the noises caused by interactions among the encoding CRGs.

In this paper, we select the static phase encoding strategy, that is, during the entire least squares implementation the encoding function remains constant, which will result in the undesired suppression of the crosstalk noise generated by the encoded CRGs. In the following research, we will design an optimal dynamic phase encoding scheme to achieve a better noise suppression effect. It should be illustrated that we assumed that the geophones and the hydrophones are placed above the seabed. Consequently, the acquired synthetic data only contain P-wave components. And the pressure component P and the particle velocity component Z directly can be obtained directly by using the first-order velocity-stress acoustic wave equation. S-wave information is the key to the data processing of OBN acquisition, and the availability and efficiency of the proposed method on S-wave remain to be verified. In the following researches, we will concentrate on the exploitation of S-wave information.

CONCLUSION

Conventional imaging approaches of OBN data account for the up-going primaries and the down-going first-order multiples. However, OBN data contain the up-going multiples and down-going higher-order multiples, and the information carried by those multiples could also be used to enhance the imaging quality. In this paper, we developed a CRG-domain LSRTM of OBN down-going multiples with a random phase encoding scheme in which the full down-going data and down-going multiples are recognized as secondary sources and observed data. The encoding function is composed of random time delay sequences and random polarity reversals which are designed as a normal distribution. Synthetic experiments demonstrate that the proposed approach can efficiently produce images with a wide illumination range and high resolution. Our approach has the potential to serve as a powerful tool for imaging OBN data of complex subsurface structures.

DATA AVAILABILITY STATEMENT

The original contributions presented in the study are included in the article/Supplementary Material, further inquiries can be directed to the corresponding author.

AUTHOR CONTRIBUTIONS

YZ and YL contributed as the major authors of the manuscript. JY did a part of writing and coding works. XL provided some constructive ideas and polished the manuscript. All authors contributed to the article and improved the submitted version.

FUNDING

The research was partially funded by the National Nature Science Foundation of China (Grant No. 41730425), the Special Fund of the Institute of Geophysics, China Earthquake Administration (Grant No. DQJB20K42), and the Institute of Geology and Geophysics, Chinese Academy of Sciences Project (Grant No. IGGCAS-2019031).

REFERENCES

Alerini, M., Traub, B., Ravaut, C., and Duveneck, E. (2009). Prestack Depth Imaging of Ocean-Bottom Node Data. *Geophysics* 74 (6), WCA57–WCA63. doi:10.1190/1.3204767

Barr, F. J., and Sanders, J. I. (1989). Attenuation of Water-column Reverberations Using Pressure and Velocity Detectors in a Water-bottom cable. *59th Annu. Int. Meet. SEG, Expanded Abstr.* 8, 653–655. doi:10.1190/1.1889557

Berkhout, A. J., and Verschuur, D. J. (2006). Imaging of Multiple Reflections. *Geophysics* 71 (4), SI209–SI220. doi:10.1190/1.2215359

Dai, W., Fowler, P., and Schuster, G. T. (2012). Multi-source Least-Squares Reverse Time Migration. *Geophys. Prospect.* 60, 681–695. doi:10.1111/j.1365-2478.2012.01092.x

Dash, R., Spence, G., Hyndman, R., Grion, S., Wang, Y., and Ronen, S. (2009). Wide-area Imaging from OBS Multiples. *Geophysics* 74, Q41–Q47. doi:10.1190/1.3223623

Dragoset, B., Verschuur, E., Moore, I., and Bisley, R. (2010). A Perspective on 3D Surface-Related Multiple Elimination. *Geophysics* 75 (5), 75A245–75A261. doi:10.1190/1.3475413

Grion, S., Exley, R., Manin, M., Miao, X., Pica, A. L., Wang, Y., et al. (2007). Mirror Imaging of OBS Data. *First Break* 25, 37–42. doi:10.3997/1365-2397.2007028

He, B., Liu, Y., and Zhang, Y. (2019). Improving the Least-Squares Image by Using Angle Information to Avoid Cycle Skipping. *Geophysics* 84 (6), S581–S598. doi:10.1190/geo2018-0816.1

Jiang, Z., Sheng, J., Yu, J., Schuster, G. T., and Hornby, B. E. (2007). Migration Methods for Imaging Different-Order Multiples. *Geophys. Prospect.* 55, 1–19. doi:10.1111/j.1365-2478.2006.00598.x

Katzman, R., Holbrook, W. S., and Paull, C. K. (1994). Combined Vertical-Incidence and Wide-Angle Seismic Study of a Gas Hydrate Zone, Blake Ridge. *J. Geophys. Res.* 99 (B9), 17975–17995. doi:10.1029/94JB00662

Knopoff, L., and Gangi, A. F. (1959). Seismic Reciprocity. *Geophysics* 24, 681–691. doi:10.1190/1.1438647

Krebs, J. R., Anderson, J. E., Hinkley, D., Neelamani, R., Lee, S., Baumstein, A., et al. (2009). Fast Full-Wavefield Seismic Inversion Using Encoded Sources. *Geophysics* 74 (6), WCC177–WCC188. doi:10.1190/1.3230502

Li, Z., Li, Z., Wang, P., and Zhang, M. (2017). Reverse Time Migration of Multiples Based on Different-Order Multiple Separation. *Geophysics* 82 (1), S19–S29. doi:10.1190/geo2015-0710.1

Liu, X., Liu, Y., Hu, H., Li, P., and Khan, M. (2016a). Imaging of First-Order Surface-Related Multiples by Reverse-Time Migration. *Geophys. J. Int.* 208 (2), 1077–1087. doi:10.1093/gji/ggw437

Liu, X., Liu, Y., and Khan, M. (2018). Fast Least-Squares Reverse Time Migration of VSP Free-Surface Multiples with Dynamic Phase-Encoding Schemes. *Geophysics* 83 (4), S321–S332. doi:10.1190/geo2017-0419.1

Liu, X., Liu, Y., Lu, H., Hu, H., and Khan, M. (2017). Prestack Correlative Least-Squares Reverse Time Migration. *Geophysics* 82 (2), S159–S172. doi:10.1190/geo2016-0416.1

Liu, X., and Liu, Y. (2018). Plane-wave Domain Least-Squares Reverse Time Migration with Free-Surface Multiples. *Geophysics* 83 (6), S477–S487. doi:10.1190/geo2017-0570.1

Liu, Y., Chang, X., Jin, D., He, R., Sun, H., and Zheng, Y. (2011). Reverse Time Migration of Multiples for Subsalt Imaging. *Geophysics* 76 (5), WB209–WB216. doi:10.1190/geo2010-0312.1

Liu, Y., Hu, H., Xie, X.-B., Zheng, Y., and Li, P. (2015). Reverse Time Migration of Internal Multiples for Subsalt Imaging. *Geophysics* 80, S175–S185. doi:10.1190/geo2014-0429.1

Liu, Y., Jin, D., Chang, X., Li, P., Sun, H., and Luo, Y. (2010). Multiple Subtraction Using Statistically Estimated Inverse Wavelets. *Geophysics* 75 (6), WB247–WB254. doi:10.1190/1.325549910.1190/1.3494082

Liu, Y., Liu, X., Osen, A., Shao, Y., Hu, H., and Zheng, Y. (2016b). Least-squares Reverse Time Migration Using Controlled-Order Multiple Reflections. *Geophysics* 81 (5), S347–S357. doi:10.1190/geo2015-0479.1

Lu, S., Whitmore, D. N., Valenciano, A. A., and Chemingui, N. (2015). Separated-wavefield Imaging Using Primary and Multiple Energy. *The Leading Edge* 34, 770–778. doi:10.1190/tle34070770.1

Muijs, R., Robertsson, J. O., and Holliger, K. (2007). Prestack Depth Migration of Primary and Surface-Related Multiple Reflections: Part I - Imaging. *Geophysics* 72 (2), S59–S69. doi:10.1190/1.2422796

Nemeth, T., Wu, C., and Schuster, G. T. (1999). Least-squares Migration of Incomplete Reflection Data. *Geophysics* 64, 208–221. doi:10.1190/1.1444517

Romero, L. A., Ghiglia, D. C., Ober, C. C., and Morton, S. A. (2000). Phase Encoding of Shot Records in Prestack Migration. *Geophysics* 65, 426–436. doi:10.1190/1.1444737

Schalkwijk, K. M., Wapenaar, C. P. A., and Verschuur, D. J. (2003). Adaptive Decomposition of Multicomponent Ocean-bottom Seismic Data into Downgoing and Upgoing P- and S-waves. *Geophysics* 68, 1091–1102. doi:10.1190/1.1581081

Schuster, G. T., Wang, X., Huang, Y., Dai, W., and Boonyasiriwat, C. (2011). Theory of Multisource Crosstalk Reduction by Phase-Encoded Statics. *Geophys. J. Int.* 184, 1289–1303. doi:10.1111/j.1365-246X.2010.04906.x

Verschuur, D. J., and Berkhout, A. J. (2011). Seismic Migration of Blended Shot Records with Surface-Related Multiple Scattering. *Geophysics* 76 (1), A7–A13. doi:10.1190/1.3521658

Verschuur, D. J., Berkhout, A. J., and Wapenaar, C. P. A. (1992). Adaptive Surface-related Multiple Elimination. *Geophysics* 57, 1166–1177. doi:10.1190/1.1443330

Wong, M., Biondi, B. L., and Ronen, S. (2015). Imaging with Primaries and Free-Surface Multiples by Joint Least-Squares Reverse Time Migration. *Geophysics* 80 (6), S223–S235. doi:10.1190/geo2015-0093.1

Zhang, D., and Schuster, G. T. (2014). Least-squares Reverse Time Migration of Multiples. *Geophysics* 79 (1), S11–S21. doi:10.1190/geo2015-0479.110.1190/geo2013-0156.1

Zhang, Y., Liu, Y., and Liu, X. (2019). Reverse Time Migration Using Controlled-Order Water-Bottom-Related Multiples. *89th Annu. Int. Meet. SEG, Expanded Abstr.*, 4261–4265. doi:10.1190/segam2019-3206145.1

Zhang, Y., Liu, Y., Liu, X., and Zhou, X. (2020). Reverse Time Migration Using Water-bottom-related Multiples. *Geophys. Prospecting* 68 (2), 446–465. doi:10.1111/1365-2478.12851

Zuberi, A., and Alkhalifah, T. (2013). Imaging by Forward Propagating the Data: Theory and Application. *Geophys. Prospect.* 61, 248–267. doi:10.1111/1365-2478.12006

Conflict of Interest: The authors declare that the research was conducted in the absence of any commercial or financial relationships that could be construed as a potential conflict of interest.

APPENDIX A: BORN MODELING FOR OBN DOWN-GOING DATA

The LSRTM is generally utilized to enhance the quality of an image R by minimizing the difference between the observed data $d_{obs}(x_r, t)$ and the predicted data $d_{pre}(x_r, t)$ via the following misfit function:

$$f(R) = \frac{1}{2}\sum_{i=0}^{n} \|d_{obs}(x_r, t) - d_{pre}(x_r, t)\|_2^2. \tag{A1}$$

The acoustic wave equation in the time t and space (x, z) domain is provided in a reference medium as

$$\frac{1}{v_0(x,z)^2}\frac{\partial^2 P_0(x,z,t)}{\partial t^2} - \nabla^2 P_0(x,z,t) = \delta(x - x_s, z - z_s)S(t) \tag{A2}$$

where $v_0(x, z)$ represents the acoustic wave propagation velocity in the background/reference medium, $P_0(x, z, t)$ denotes the pressure wavefield. (x_s, z_s) is the location of a source, and $S(t)$ indicates the source function. The perturbation method is used to explain the wavefield $P(x, z, t)$ in the real medium $v(x, z)$. A velocity perturbation $\delta v(x, z) = v - v_0$ between the real and background medium can cause a wavefield perturbation $\delta P(x, z, t) = P - P_0$, which can be estimated by Born modeling:

$$\frac{1}{v_0(x,z)^2}\frac{\partial^2 \delta P(x,z,t)}{\partial t^2} - \nabla^2 \delta P(x,z,t) \approx R(x,z)\frac{\partial^2 P_0(x,z,t)}{\partial t^2}. \tag{A3}$$

where $R(x, z) = -2\delta v(x, z)/v_0(x, z)^3$ is the reflectivity model which is corresponding to the velocity perturbation $\delta v(x, z)$. The wavefield perturbation $\delta P(x, z, t)$ can be obtained by solving **Eqs A2** and **A3**, and then the predicted data can be acquired by $d_{pre}(x_r, t) = \delta P(x_r, 0, t)$.

In imaging with multiples, the lower-order multiples can be recognized as the virtual secondary source, and then they are forward extrapolated into the earth to produce higher-order multiples. Consequently, for OBN down-going multiples, we adjust **Eq. A2** by incorporating direct wave $d(x_r, t)$ and down-going multiples $m(x_r, t)$ in the right side of the equation and combine it with **Eq. A3**. The Born modeling operator associated with the OBN down-going data is thus given by:

$$\begin{cases} \dfrac{1}{v_0(x,z)^2}\dfrac{\partial^2 M(x,z,t)}{\partial t^2} - \nabla^2 M(x,z,t) = d(x_r,t) + m(x_r,t) \\ \dfrac{1}{v_0(x,z)^2}\dfrac{\partial^2 M_r(x,z,t)}{\partial t^2} - \nabla^2 M_r(x,z,t) = -R(x,z)\dfrac{\partial^2 M(x,z,t),}{\partial t^2} \\ m_{pre}(x_r,t) = M_r(x_r, z=0, t) \end{cases} \tag{A4}$$

where $m_{pre}(x_r, t)$ denotes the predicted down-going multiples. M and M_r represents the background and perturbation wavefields, respectively.

frontiers in Earth Science

ORIGINAL RESEARCH
published: 14 October 2021
doi: 10.3389/feart.2021.730184

VSP Imaging Using Free-Surface Multiples With Wavefield Decomposition: Synthetic and Field Data Examples

Yikang Zheng[1,2], *Yibo Wang*[1,2]* *and Xu Chang*[1,2]

[1]Key Laboratory of Petroleum Resource Research, Institute of Geology and Geophysics, Chinese Academy of Sciences, Beijing, China, [2]Innovation Academy for Earth Science, Chinese Academy of Sciences, Beijing, China

Vertical seismic profiling (VSP) is an effective technique to provide high-resolution seismic images of the reservoir area. However, the quality of the images is limited by the poor illumination of primary reflection wave. In conventional VSP imaging, only the upgoing primaries are used. Adding free-surface–related multiples into the imaging process can significantly improve the coverage of the illuminated area. Conventional migration methods using multiples need the complex process of multiple prediction. Data-to-data migration (DDM) is an effective imaging technique for multiples in which the recorded data is migrated directly. To improve the imaging quality of DDM in VSP imaging, we propose separating the wavefield into downgoing and upgoing components using Hilbert transform when reverse-time migration (RTM) is implemented in DDM, and the inverse-scattering imaging condition is further applied to the decomposed wavefields. The proposed method eliminates low-frequency noises and false images generated from the conventional cross-correlation imaging condition, and further enhance the illumination in the VSP imaging. Synthetic examples and application to a walkaway field data demonstrate that it can attenuate the noise and improve the imaging resolution effectively. By using DDM with inverse scattering imaging condition and wavefield decomposition based on Hilbert transform, VSP imaging using free-surface–related multiples becomes a practical complement for conventional VSP imaging.

Keywords: VSP, data-to-data migration, wavefield decomposition, inverse-scattering imaging condition, Hilbert transform

OPEN ACCESS

Edited by:
Zhihui Zou,
Ocean University of China, China

Reviewed by:
Shaoping Lu,
Sun Yat-sen University, China
Lele Zhang,
Delft University of Technology, Netherlands
Yue Ma,
Aramco Beijing Research Center, China

***Correspondence:**
Yibo Wang
wangyibo@mail.iggcas.ac.cn

Specialty section:
This article was submitted to Solid Earth Geophysics, a section of the journal Frontiers in Earth Science

Received: *24 June 2021*
Accepted: *19 August 2021*
Published: *14 October 2021*

Citation:
Zheng Y, Wang Y and Chang X (2021) VSP Imaging Using Free-Surface Multiples With Wavefield Decomposition: Synthetic and Field Data Examples. Front. Earth Sci. 9:730184. doi: 10.3389/feart.2021.730184

INTRODUCTION

Vertical seismic profiling (VSP) surveys differ from surface seismic surveys or crosswell surveys in that the surface sources and the borehole receivers are used to record both upgoing and downgoing wavefields (Stewart et al., 1984; Hardage, 1985; Chang and McMechan, 1986; Hinds et al., 1996). The receiver well is placed near the target area to obtain sufficient reflection waves generated from the reservoir (Burch et al., 2010). The configuration of VSP gives the benefits to understand corresponding geologic logs and provide additional seismic interpretation insights. However, the results of VSP imaging are restricted by the illuminated area of the primary reflections (O'Brien, et al., 2013). To greatly extend the subsurface illumination, free-surface related multiples recorded in the VSP surveys are also used in the migration of VSP data (Yu and Schuster, 2001). Jiang et al. (2005)

use the mirror imaging condition to migration the first-order multiples in the VSP data. But the method needs to calculate the traveltimes of the raypath. To avoid the picking of traveltimes, seismic interferometry theory (Wapenaar and Fokkema, 2006; Schuster, 2009) is employed to transform different orders of free-surface related multiples into virtual primaries and then applied in the migration process (Yu and Schuster, 2002; Jiang et al., 2007). He et al. (2007) demonstrated the wave-equation interferometric migration generates an image volume with wide coverage for 3D VSP data. Soni and Verschuur (2015) used full-wavefield migration to enhance the illumination for VSP measurements. Recently Marchenko imaging also emerges as an alternative tool to analyze the response of multiple reflections (Singh et al., 2015; Wapenaar et al., 2017; Lomas et al., 2018; Zhang and Slob, 2019) and include the contribution for VSP imaging.

Several methods have been developed to image free-surface related multiples directly in surface seismic surveys. Instead of taking as coherent noise, the multiples are used as areal sources in the migration process (Guitton, 2002; Shan 2003; Verschuur and Berkhout, 2005; Artman, 2006; Muijs et al., 2007). Recently, migration of multiples has shown the significant advantages for enhancing areal illumination to image subsurface structures (Lu et al., 2015; Li et al., 2017; Liu et al., 2018; Zhang et al., 2020). However, most methods involve the process to separate the surface-related multiples from the original data, which is complex and prone to error for real data applications. To avoid the separation of the primaries and free-surface related multiples, Wang et al. (2014a) propose an approach that can simultaneously migrate the primaries and free-surface related multiples. The recorded data containing primaries and free-surface related multiples are backward-propagated as the receiver wavefield, and the recorded data, together with a synthetic wavelet, are forward-propagated as the source wavefield. Wang et al. (2014b) isolate the contribution of multiples and name it as data-to-data migration (DDM), in which the recorded data containing primaries and free-surface related multiples are forward and backward propagated simultaneously. The algorithm is designed for surface seismic profile and can also be applied in the VSP data processing. Using the source-receiver reciprocity, the common receiver gathers is similar to the common shot gathers in the surface seismic surveys except that the virtual source is located in the borehole.

Kirchhoff migration (Keho and Beydoun, 1988; Gray and May 1994; Bevc, 1997; Hua and McMechan, 2003) and wave-equation migration (Gazdag, 1978; Stoffa et al., 1990; Ristow and Rühl, 1994; Sava and Vasconcelos, 2011) are the most common migration algorithms in the migration of free-surface related multiples for VSP (Jiang et al., 2005; He et al., 2007). For the surface seismic surveys, reverse-time migration (RTM, Baysal et al., 1983; McMechan, 1983) has shown its superiority in handling complex geologic structures and potential for true-amplitude, high-resolution migration. The main problem for RTM is that low-frequency noise and false images are generated when the source and receiver wavefields are cross-correlated near the strong velocity gradients (Liu et al., 2011; Fei et al., 2015). This is due to the two-way wave-equation is used in the wavefield simulation. To eliminate the high-amplitude, low-frequency noise along the wave paths, Fletcher et al. (2005) propose to apply the directional damping factor. Yoon and Marfurt (2006) use the Poynting vector to calculate the direction of the wavefields and cross-corelate the desired component. The most practical method is the Laplace filter proposed by Zhang and Sun (2009), which has been widely applied in the applications of RTM. Liu et al. (2011) use Hilbert transform to separate the upgoing and downgoing components and avoid the storage of the entire wavefields. Fei et al. (2015) point out that only the cross-correlation of the downgoing source wavefield and upgoing receiver wavefield are the correct imaging condition when strong velocity contrasts exist in the velocity model. Wang et al. (2017) show the wavefield decomposition method based on Hilbert transform can eliminate the noises and false images in the DDM for surface seismic survey. Zheng et al. (2018) use the similar approach to separate the upgoing and downgoing components in the 3D forward modeling and 3D RTM. The method can be also applied in the migration of VSP data. With the decomposed wavefields, it is possible to apply some advanced imaging condition to obtain better estimation of subsurface reflectivity, such as the deconvolution imaging condition (Valenciano and Biondi, 2003; Guitton et al., 2007; Lu et al., 2015) and inverse-scattering imaging condition (Whitmore and Crawley, 2012; Suh and Wang, 2013). The inverse-scattering imaging condition is derived from the inverse theory and high-frequency approximation, which can generate subsurface images with preserved amplitudes and high resolution (Pestana et al., 2014; Duprat et al., 2015). The wavefield separation used in the imaging can be achieved with high accuracy with Hilbert transform instead of Poynting vectors (Yoon and Marfurt, 2006).

In the following sections, we first introduce the theory of DDM for VSP data, and then we illustrate how to use inverse-scattering imaging condition and wavefield decomposition with Hilbert

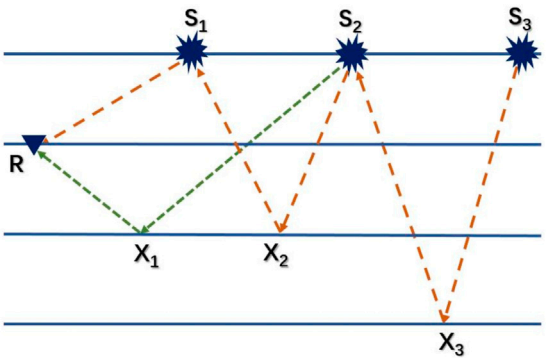

FIGURE 1 | Schematic diagram of DDM method for VSP data. In conventional migration of walkaway VSP data, the upgoing component recorded at R is backward propagated and cross-correlated with the forward-propagated source wavelet excited at S_2 to image X_1; In migration of multiples. In migration of multiples, the receivers are considered to be virtual sources in the borehole and the sources located at the surface are taken as receivers for imaging multiples. The fist-order multiples are backward extrapolated from S_2 and cross-correlated with the forward-propagated direct wave from S_1 to image X_2; Similarly, the second-order multiples are backward extrapolated and cross-correlated with the forward-propagated first-order multiple to image X_3.

transform to improve the results. Synthetic examples are used to validate the effectiveness of our approach. Then the method is applied to walkaway field data which is collected to monitor the injection process of CO_2. The final part is the conclusion of our work.

METHODOLOGY

DDM for VSP Data

The DDM method for surface seismic data has been demonstrated by Wang et al. (2014b). Using the source-receiver reciprocity theory, if the VSP data are resorted into common receiver gathers and the receiver in the borehole is taken as a source. They are similar to the common shot gathers of surface seismic survey except that the source in reciprocal domain is located in the well. **Figure 1** illustrates the wavepath in the VSP surveys with free surface. In the gathers recorded at R, the data contains the direct wave excited at S_1, the primary excited at S_2, first-order free-surface related multiple excited at S_2 and second-order free-surface related multiple excited at S_3. Only the primary is the upgoing components and can be separated from the original data by f-k filtering. In the conventional migration of VSP data, the primary is backward propagated and cross-correlated with the forward-propagated source wavelet excited at R to image X_1. Here the source-receiver reciprocity is used. In migration of free-surface related multiples, the first-order free-surface related multiple excited at S_2 is backward propagated and cross-correalted with the direct wave excited at S_1 to image the reflector X_2. And the second-order free-surface related multiple excited at S_3 is backward propagated and cross-correalted with the first-order free-surface related multiple excited at S_2 to image the reflector X_3. From the comparison of the wavepaths in the diagram illustration, the imaging results of free-surface related multiples has wider coverage than the conventional migration. Moreover, it can clarify the shallow reflectors, which are usually not imaged when using primaries only.

The imaging condition of DDM is (Wang et al., 2014b)

$$I = D_F * D_B \tag{1}$$

For VSP data, D represents the downgoing components in the common receiver gathers. The subscript F denotes forward propagated, and B denotes backward propagated. The same data are forward and backward propagated and cross-correlated to form the subsurface image. The results of DDM contain some artifacts related with the undesired cross-correlations, such as the cross-correlation of direct waves from different shots or the cross-correlation of the direct wave and second-order free-surface related multiple. The first type mainly exists at the surface and can be muted easily. The second has longer wavepath and much weaker energy.

DDM With Inverse-Scattering Imaging Condition

There are different algorithms to implement DDM, such as one-way wave-equation (Zheng et al., 2016) or two-way wave-equation (Wang et al., 2014b). Now RTM based on two-way wave-equation has shown its benefits in offering high-resolution images and handling complex subsurface structures. The original imaging condition in RTM is

$$I(\boldsymbol{x}) = \int S(\boldsymbol{x},t)R(\boldsymbol{x},t)dt \tag{2}$$

where $\boldsymbol{x}$ represents the space location and t represents the time. In the DDM for VSP data, $S(\boldsymbol{x},t)$ and $R(\boldsymbol{x},t)$ are the forward and backward propagated wavefields of the common receiver gathers from the shot locations.

As the two-way wave-equation is used in the wavefield simulation of $S(\boldsymbol{x},t)$ and $R(\boldsymbol{x},t)$, the upgoing and downgoing components both exist in the wavefields. The subscripts d and u are used to represent the downgoing and upgoing components respectively. Then the image in RTM can be divided into four parts

$$\begin{aligned} I(\boldsymbol{x}) = &\int S_d(\boldsymbol{x},t)R_u(\boldsymbol{x},t)dt + \int S_u(\boldsymbol{x},t)R_d(\boldsymbol{x},t)dt \\ &+ \int S_d(\boldsymbol{x},t)R_d(\boldsymbol{x},t)dt + \int S_u(\boldsymbol{x},t)R_u(\boldsymbol{x},t)dt \end{aligned} \tag{3}$$

The last two terms, $S_d(\boldsymbol{x},t)R_d(\boldsymbol{x},t)$ and $S_u(\boldsymbol{x},t)R_u(\boldsymbol{x},t)$, generate the high-amplitude, low-frequency noise in the RTM results. Liu et al. (2011) use Hilbert transform to eliminate such kind of noise. Fei et al. (2015) show that the second term, $S_u(\boldsymbol{x},t)R_d(\boldsymbol{x},t)$, generates false images near the velocity interface or strong velocity contrasts. Thus the de-primary imaging condition is proposed (Fei et al., 2015; Wang et al., 2016; Wang et al., 2017):

$$I(\boldsymbol{x}) = \int S_d(\boldsymbol{x},t)R_u(\boldsymbol{x},t)dt \tag{4}$$

It is the cross-correlation imaging with wavefield decomposition. True-amplitude imaging is an attractive topic for RTM. Based on the high-frequency asymptotic and the imaging/inversion theory, it is possible to obtain the estimation of slowness perturbations in wave-equation migration (Kiyashchenko et al., 2007). In RTM, the inverse-scattering imaging condition is proposed and shown the benefit of better amplitude recovery and higher resolution (Whitmore and Crawley, 2012; Pestana et al., 2014; Duprat et al., 2015). The imaging formula can be expressed as:

$$\begin{aligned} I(\boldsymbol{x}) &= \frac{\int \left[\frac{1}{v^2(\boldsymbol{x})}I_1 - I_2\right]dt}{\int |S_d(\boldsymbol{x},t)|^2 dt}, \\ I_1 &= \partial_t S_d(\boldsymbol{x},t)\partial_t R_u(\boldsymbol{x},t)\,,\; I_2 = \nabla S_d(\boldsymbol{x},t)\cdot\nabla R_u(\boldsymbol{x},t) \end{aligned} \tag{5}$$

where $v(\boldsymbol{x})$ represents the velocity. ∂_t and ∇ are the time derivative and spatial gradient operator, respectively. Compared to the conventional cross-correlation imaging condition, **Eq. 5** can preserve the amplitudes and improve the resolution. In the imaging process, it is necessary to separate the wavefields to attenuate the backscattered noise introduced by two-way wave-equation. Pestana et al. (2014) uses the Poynting vector to obtain the separated components. However, their results show that the method may damage some reflections and has poor performance on receiver field. In this work, we followed the approach based on Hilbert transform to decompose the wavefield effectively.

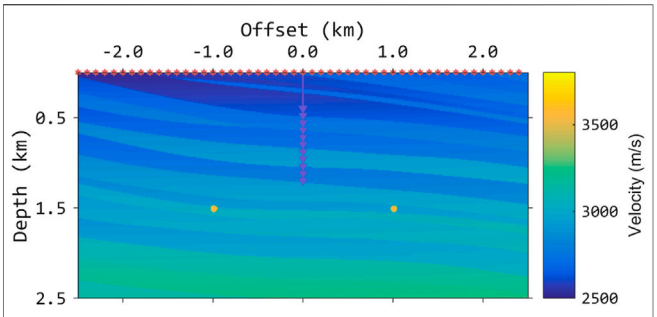

FIGURE 2 | A part of Sigsbee 2A model. The VSP survey consists of 80 geophones evenly placed in the borehole between a depth of 400–1,200 m. 500 shots are evenly located at the surface.

Wavefield Decomposition Based on Hilbert Transform

According to the definition of Hilbert transform, the Hilbert transform of a signal $f(t)$ has the following quality:

$$\mathcal{F}_t\{\mathcal{H}_t[f(t)]\} = -isgn(\omega)\mathcal{F}_t[f(t)] \tag{6}$$

where $\mathcal{H}_t$ and $\mathcal{F}_t$ represent the Hilbert transform and Fourier transform along the time axis, respectively. i is the imaginary unit, ω is the frequency, and $sgn(\omega)$ is the sign function. With Hilbert transform, the downgoing and upgoing wavefields can be computed by (Zheng et al., 2018):

$$\begin{aligned} S_d(\boldsymbol{x},t) &= \frac{1}{2}\{S(\boldsymbol{x},t) + \mathcal{H}_z\mathcal{H}_t[S(\boldsymbol{x},t)]\}, \\ R_u(\boldsymbol{x},t) &= \frac{1}{2}\{R(\boldsymbol{x},t) - \mathcal{H}_z\mathcal{H}_t[R(\boldsymbol{x},t)]\} \end{aligned} \tag{7}$$

where $\mathcal{H}_z$ and $\mathcal{H}_t$ represent the Hilbert transform in depth and time, respectively. As the wavefield modeling and Hilbert transform are both linear operators, the $\mathcal{H}_t(S(\boldsymbol{x},t))$ and $\mathcal{H}_t(R(\boldsymbol{x},t))$ in **Eq. 7** is calculated by the forward modeling of the Hilbert transformed wavelet and data to avoid the wavefield storage. At each time step, Hilbert transform in depth is applied to the two wavefields, $\mathcal{H}_t(S(\boldsymbol{x},t))$ and $\mathcal{H}_t(R(\boldsymbol{x},t))$ to get the final image.

The workflow for VSP imaging using free-surface related multiples with inverse scattering imaging condition and wavefield decomposition consists of the following steps: 1) separate the upgoing and downgoing components by f-k filter and resort the shotgathers to common receiver gathers; 2) forward propagate the downgoing data from the source locations and store the boundary values; 3) apply Hilbert transform to the downgoing data and forward propagate it to construct $\mathcal{H}_t(S(\boldsymbol{x},t))$; 4) use the boundary value to reconstruct the wavefield $S(\boldsymbol{x},t)$ and $\mathcal{H}_t(S(\boldsymbol{x},t))$; 5) back propagate the downgoing data from the source locations to construct $R(\boldsymbol{x},t)$; 6) apply Hilbert transform to the downgoing data and back propagate it to construct $\mathcal{H}_t(R(\boldsymbol{x},t))$; 7) apply imaging condition in **Eq. 5** and stack all the images at all time steps.

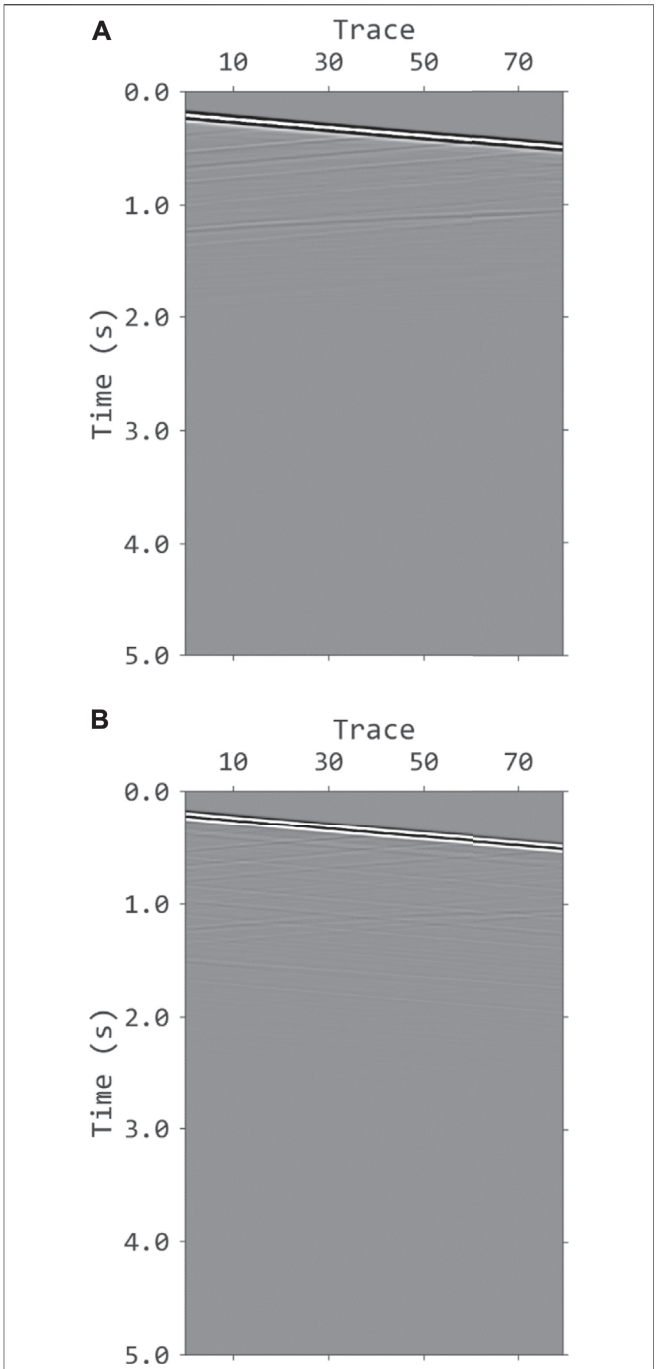

FIGURE 3 | The common shot gathers generated from the Sigsbee 2A model. **(A)** The generated data without free-surface–related multiples, which contains downgoing direct waves and upgoing primaries. **(B)** The gathers generated with free surface, which contains direct waves, primaries and free-surface related multiples.

SYNTHETIC EXAMPLES

To better illustrate the advantages of VSP imaging using the proposed method, we applied it on a part of the Sigsbee 2A

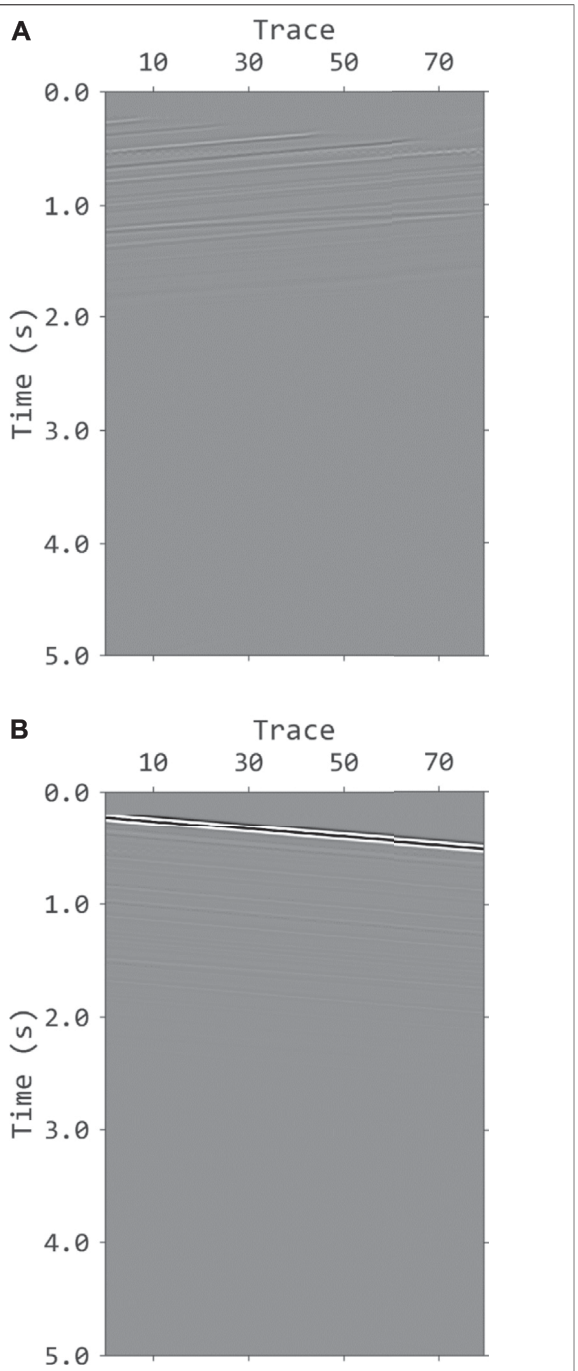

FIGURE 4 | The separated components of the data shown in **Panel 3** after f-k filtering. **(A)** The upgoing components of the data generated without free surface, it is the primaries in the original data. **(B)** The downgoing components of the data modeled with free surface, containing direct waves and free-surface–related multiples.

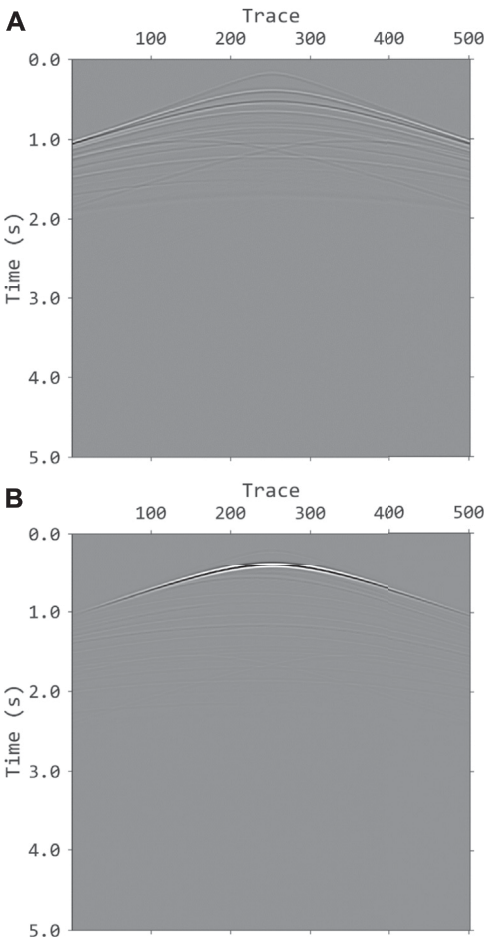

FIGURE 5 | The generated input data using Sigsbee 2A model for VSP imaging. **(A)** a common receiver gathers of VSP data containing primaries only. **(B)** Common receiver gathers of VSP data containing direct waves and free-surface–related multiples.

model. **Figure 2** shows the velocity model. 500 shots are deployed on the surface and 80 geophones are placed evenly in the observation well located at the center of the model. The time sampling interval is 1 ms and the grid spacing of the model is 10 m. A Ricker wavelet with peak frequency of 15 Hz is used as the source wavelet. **Figure 3** shows the synthetic data generated without and with free-surface related multiples. **Figure 4** shows the data for VSP imaging after f-k filtering. The upgoing components are used for conventional imaging with primaries only while the downgoing components are used for VSP imaging using free-surface related multiples. **Figure 5** shows the input common receiver gathers for VSP imaging. **Figures 6A,B** shows the conventional cross-correlation imaging (**Eq. 2**) results using primaries and free-surface related multiples, respectively. The comparison clearly demonstrates the benefits of VSP imaging using multiples. **Figure 6B** has much wider imaging area and the reflectors above the geophones are also imaged. The results using cross-correlation imaging condition with wavefield decomposition (**Eq. 4**) are shown in **Figure 7**. **Figure 7A** is the result using primaries only and **Figure 7B** is the result using multiples. The noised are suppressed but the amplitudes decrease with the depth. We apply the inverse scattering imaging condition with wavefield decomposition (**Eq. 5**) to the data and the results are shown in **Figure 8**. **Figures 8A,B** are the results using primaries only and multiples, respectively. Compared to **Figure 7**, the proposed

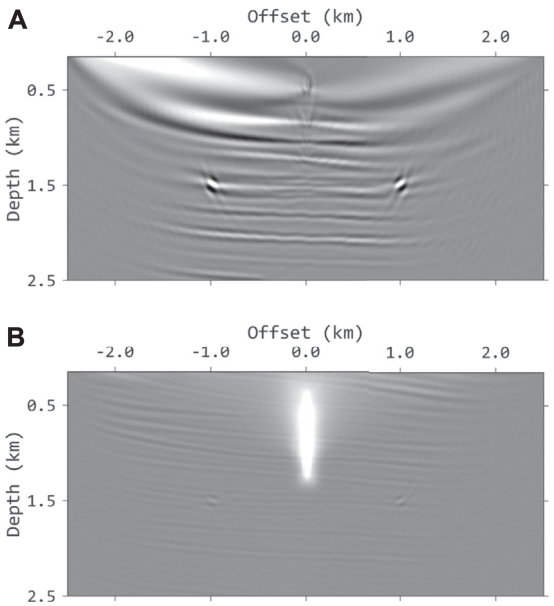

FIGURE 6 | The images generated by conventional cross-correlation imaging condition. **(A)** The image using primaries only. **(B)** The image using DDM. **(B)** has wider coverage by involving multiples in the migration. They both have noises introduced by the two-way wave-equation used in RTM.

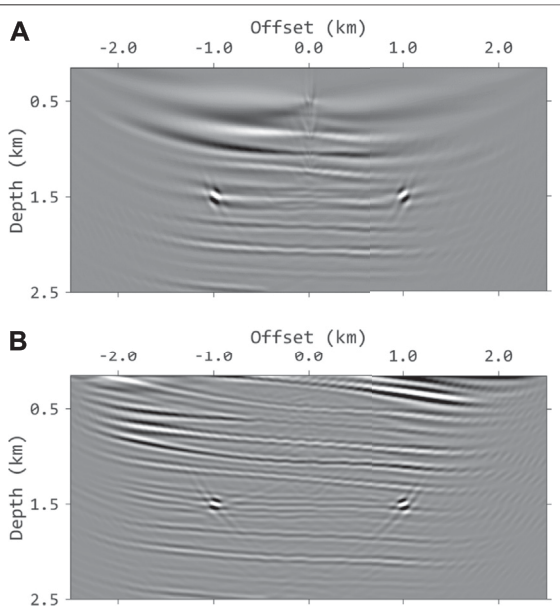

FIGURE 7 | The results using cross-correlation imaging condition with wavefield decomposition. **(A)** The image using primaries only. **(B)** The image using DDM. The noises in **Panel 6** are suppressed. There is no obvious artifacts in **(B)**.

approach yields a better estimation of the true subsurface reflectivity with improved resolution and amplitude recovery. And there are no obvious artifacts shown in **Figure 8B**, as the true images has stronger contribution to the final image.

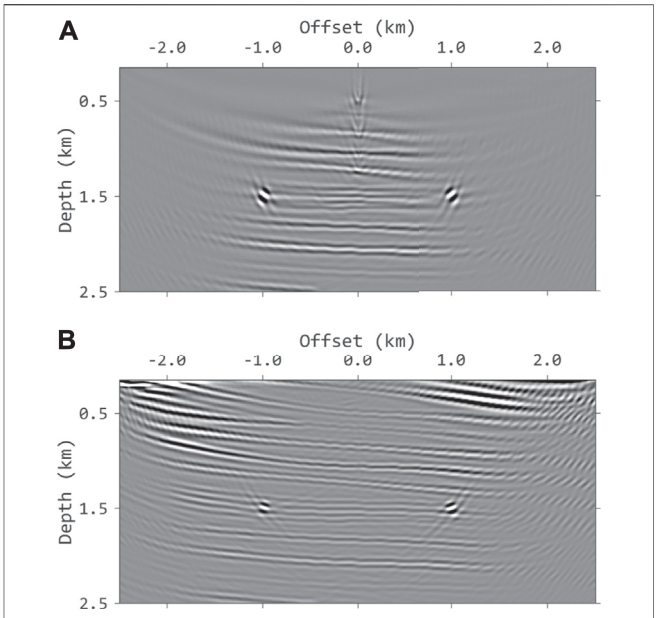

FIGURE 8 | The results using inverse-scattering imaging condition with wavefield decomposition. **(A)** The image using primaries only. **(B)** The image using DDM. Compared to **Panel 7**, the resolution is well improved.

FIELD DATA APPLICATION

To verify the adaptability of the proposed method to field data, we use a walkaway field data for further test. The walkaway VSP data is collected to monitoring the reservoir changes during the CO2 injection in northwestern China. **Figure 9A** shows the migration velocity and seismic geometry in the walkaway VSP survey. The data are recorded by 40 receivers equally spaced from the depth of 390–1,170 m.

The time sampling interval is 1 ms and the grid spacing of the model is 10 m. **Figure 9B** shows a common receiver gather for imaging using multiples. Several shots near the wellbore are missing, which can lead to the lack of multiples with small reflection angles in the generated data.

Figures 10A,B shows the images obtained from conventional cross-correlation imaging condition with wavefield decomposition using primaries only and free surface related multiples, respectively. **Figures 11A,B** shows the results of the proposed method. The inverse-scattering imaging condition with wavefield decomposition improves the resolution and balances the amplitudes.

As we can see from the results, migration with multiples can effectively image the reflector in the shallow zone and enlarge the image range. But the illumination near the borehole is influenced by the reflection angle and missing near-offset traces in the data. Note that it also contains the crosstalk generated from undesired cross-correlation of different seismic events. **Figure 12** illustrates the migration result that combines the contribution of primaries and multiples. Compared to the conventional images, the joint migration enhances the illumination and achieves the high-quality seismic images for monitoring the CO_2 injection.

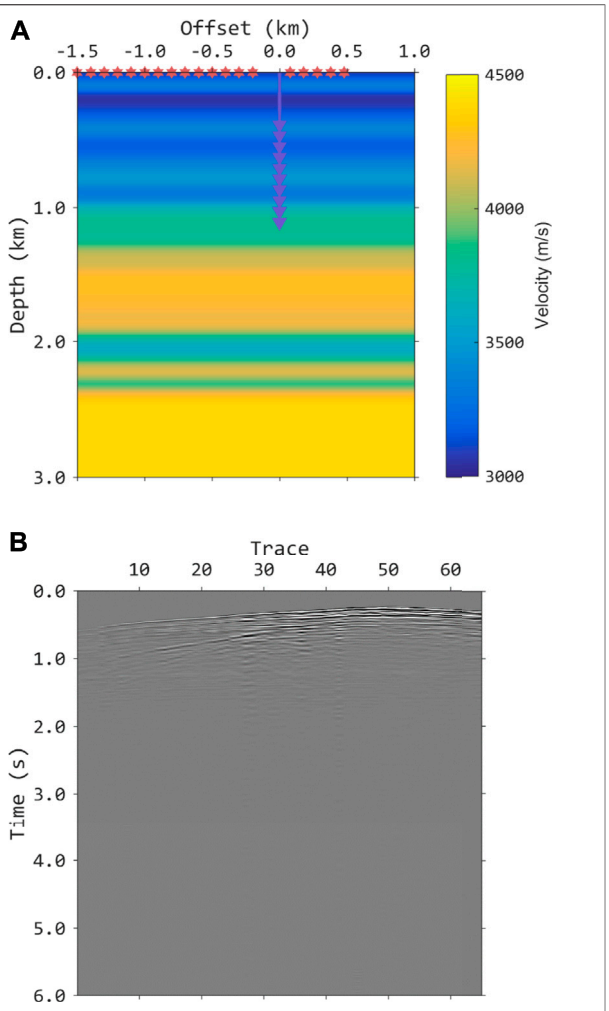

FIGURE 9 | (A) The migration velocity and walkaway VSP acquisition used in field application. **(B)** The common receiver gathers obtained from the data containing multiples. Note that several near-offset traces are missing.

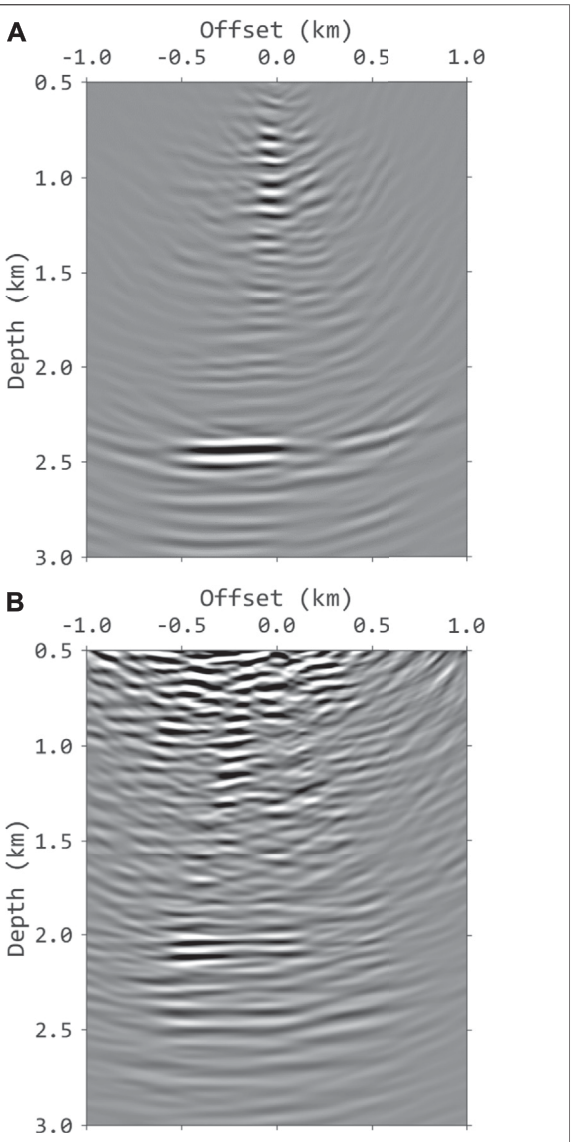

FIGURE 10 | Imaging results of the walkaway VSP field data using cross-correlation imaging condition with wavefield decomposition: **(A)** The image using primaries only. **(B)** The image using DDM. Compared to **(A, B)** has enhanced illumination away from the well and images the shallow reflectors. Due to the lack of near-offset traces, the zone near the well is not accurately imaged in **(B)**.

Overall, we see that VSP imaging using inverse-scattering imaging condition with wavefield decomposition is capable of handling real datasets.

DISCUSSION

In the proposed workflow, the downgoing components of VSP data are included in the imaging process. Combined with the conventional VSP imaging using upgoing waves, we can have improved imaging results. An important advantage of DDM is that it can image the subsurface without any knowledge of the source information. Thus, the reflector in DDM images can be used to calibrate the conventional images when the source wavelet is inaccurate. The matching filter used in the multiple subtraction (Verschuur et al., 1992; Wang, 2003; Fomel, 2009) can be modified to find the correct combination of the two kinds of imaging results. In the application of DDM to VSP walkway data, the imaging quality is contaminated by the large-amplitude, low frequency noises around the well. By using wavefield decomposition based on Hilbert transform, this kind of noises can be suppressed effectively.

In the wavefield separation using Poynting vectors, the reflection angle between the source wavefield and receiver wavefield is calculated, and the components with the opening angle more than certain values are excluded to obtain the final imaging results. Compared to the approach using Hilbert transform, the method using Poynting vectors can not remove the false images, which are generated by the second term on the right side of **Eq. 3**. But it is able to generate angle domain common image gathers. The proposed approach is only

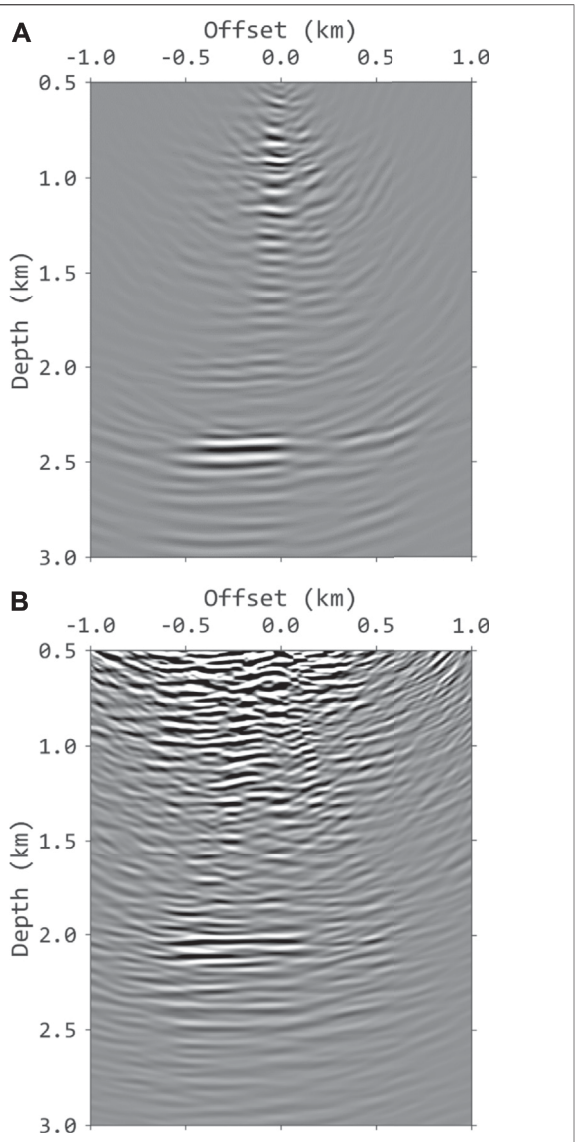

FIGURE 11 | Imaging results of the walkaway VSP field data using inverse-scattering imaging condition with wavefield decomposition: **(A)** The image using primaries only. **(B)** The image using DDM. Compared to **Panel 10**, the reflection amplitudes are well preserved, and the resolution is improved.

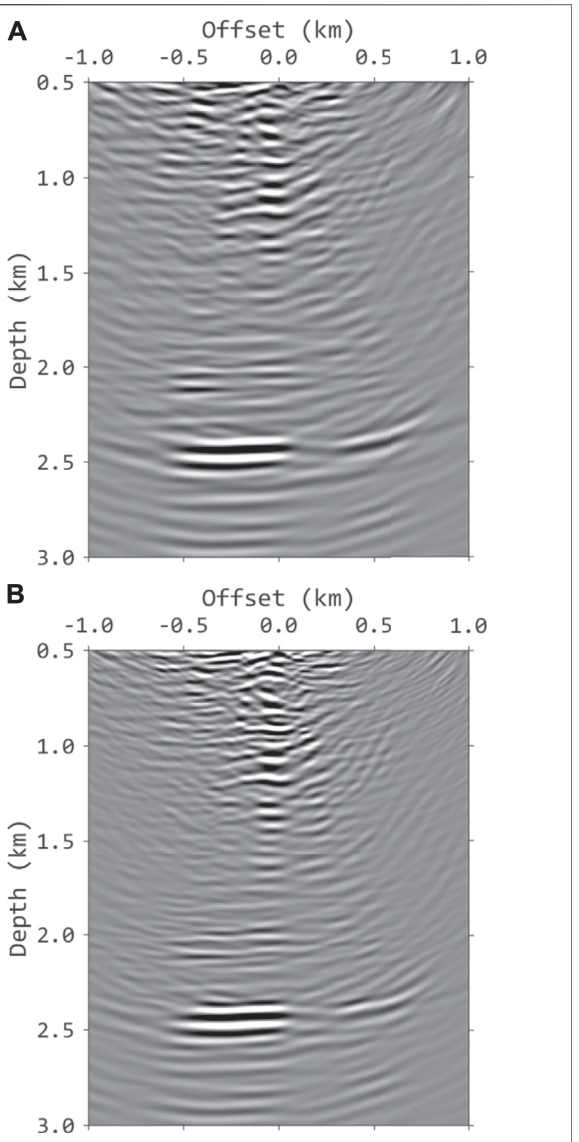

FIGURE 12 | The joint migration images using primaries and multiples. **(A)** The result using cross-correlation imaging condition with wavefield decomposition, **(B)** the result using inverse-scattering imaging condition with wavefield decomposition. **(B)** provides the best result in resolution and frequency content.

designed to separate upgoing and downgoing components in the propagated wavefields, and to provide imaging results without low-frequency noise and false images. If the finite-difference time-domain method and staggered grid are used in RTM, the extra computation cost is negligible for the wavefield separation using Poynting vectors. The computation cost in the proposed approach is doubled compared to traditional RTM, thus some high-performance computation techniques, such as MPI or GPU, are necessary to increase the efficiency of the method.

The images generated from conventional cross-correlation imaging condition may suffer from poor resolution and incorrect amplitude responses while inverse-scattering imaging condition partly overcomes the drawbacks. To make the results obtained from inverse-scattering imaging condition become suitable estimation of the slowness perturbation, wavefield decomposition is necessary to avoid the noises introduced by the two-way wave equation when strong velocity gradients exist. It is an approximated solution for true amplitude RTM. The final workflow can generate subsurface images with balanced amplitude and high resolution, which is important for amplitude variation with offset analysis.

As we have demonstrated with numerical examples, the final images obtained from DDM can be superior to conventional imaging results. However, it relies on the designed geometry. The sparse shot array and shallow receiver locations may lead to limited free-surface related multiples in the recorded data. In

practice, the results of DDM can be used as import complement of conventional imaging, as shown in the field example.

In the theory of DDM, because we have to cross-correlate all orders of multiples to avoid multiple prediction, the results of DDM contains undesirable artifacts. Assume that the amplitude of the true image is one, then the strongest artifact has the strength of the reflectivity. The final imaging result of DDM is still acceptable in most cases. The noise that leaks into the images can be further suppressed in image domain to improve the imaging quality. Least-squares migration (Nemeth et al., 1999; Dai et al., 2011) can be applied to remove the artifacts (Zhang and Schuster, 2014; Liu et al., 2018; Zheng et al., 2019; Li et al., 2020). Another option is high-resolution parabolic Radon filtering in angle domain common image gathers (Wang et al., 2014b; Zheng et al., 2016) or using 3D wide-azimuth acquisition (VerWest and Lin, 2007).

CONCLUSION

We present an effective method to imaging free-surface related multiples in VSP data. The downgoing components, which are muted in conventional VSP imaging, are used to image the subsurface. The separated downgoing components are resorted into common receiver gathers and then DDM method is used to image the subsurface. The inverse-scattering imaging condition with wavefield decomposition is applied to generate a better approximation of the subsurface reflectivity. We have illustrated the explicit workflow to apply the proposed approach with Hilbert transform in RTM. Results with synthetic VSP data and field data validate the effectiveness of the proposed approach. Compared to VSP imaging using primaries only, the results have significantly enhanced coverage and shallow reflectors with improved resolution. The algorithm handles free-surface related multiples without the need of multiple prediction in preprocessing. The method has the potential to improve the results using primaries only and offer better estimation of the geological structures.

DATA AVAILABILITY STATEMENT

The field data analyzed in this study was obtained from National Institute of Clean-and-Low-Carbon Energy and used for research purposes only. Requests to access these datasets should be directed to NICE (nice_contact@chnenergy.com.cn).

AUTHOR CONTRIBUTIONS

YZ and YW developed the theory and performed the applications. XC supervised the findings of this work. All authors discussed the results and contributed to the final manuscript.

FUNDING

This study was funded by the CAS Project for Young Scientists in Basic Research (Grant No. YSBR-020), the National Natural Science Foundation of China (Grant No. 42025403) and the Youth Innovation Promotion Association CAS (Grant No. Y201917).

ACKNOWLEDGMENTS

The authors thank National Institute of Clean-and-Low-Carbon Energy for providing research data. We thank the reviewers for their valuable comments that greatly improved the quality of this paper.

REFERENCES

Artman, B. (2006). Imaging Passive Seismic Data. *Geophysics* 71 (4), SI177–SI187. doi:10.1190/1.2209748

Baysal, E., Kosloff, D. D., and Sherwood, J. W. C. (1983). Reverse Time Migration. *Geophysics* 48, 1514–1524. doi:10.1190/1.1441434

Bevc, D. (1997). Imaging Complex Structures with Semirecursive Kirchhoff Migration. *Geophysics* 62, 577–588. doi:10.1190/1.1444167

Burch, T., Hornby, B., Sugianto, H., and Nolte, B. (2010). Subsalt 3D VSP Imaging at Deimos Field in the deepwater Gulf of Mexico. *The Leading Edge* 29, 680–685. doi:10.1190/1.3447781

Chang, W. F., and McMechan, G. A. (1986). Reverse-time Migration of Offset Vertical Seismic Profiling Data Using the Excitation-time Imaging Condition. *Geophysics* 51, 67–84. doi:10.1190/1.1442041

Dai, W., Wang, X., and Schuster, G. T. (2011). Least-squares Migration of Multisource Data with a Deblurring Filter. *Geophysics* 76 (5), R135–R146. doi:10.1190/geo2010-0159.1

Fei, T. W., Yang, J., Liu, H., Qin, F., and Luo, Y. (2015). Removing False Images in Reverse Time Migration: The Concept of De-primary. *Geophysics* 80 (6), S237–S244. doi:10.1190/geo2015-0289.1

Fletcher, R. F., Fowler, P., Kitchenside, P., and Albertin, U. (2005). *Suppressing Artifacts in Prestack Reverse Time Migration: 75th Annual International Meeting*. Houston: SEG, 2049–2051.

Fomel, S. (2009). Adaptive Multiple Subtraction Using Regularized Nonstationary Regression. *Geophysics* 74 (1), V25–V33. doi:10.1190/1.3043447

Gazdag, J. (1978). Wave Equation Migration with the Phase-shift Method. *Geophysics* 43, 1342–1351. doi:10.1190/1.1440899

Gray, S. H., and May, W. P. (1994). Kirchhoff Migration Using Eikonal Equation Traveltimes. *Geophysics* 59, 810–817. doi:10.1190/1.1443639

Guitton, A. (2002). *Shot-profile Migration of Multiple Reflections: 72nd Annual International Meeting*. Salt Lake City: SEG, 1296–1299.

Guitton, A., Valenciano, A., Bevc, D., and Claerbout, J. (2007). Smoothing Imaging Condition for Shot-Profile Migration. *Geophysics* 72 (3), S149–S154. doi:10.1190/1.2712113

Hardage, B. A. (1985). Vertical Seismic Profiling. *The Leading Edge* 4, 59. doi:10.1190/1.1487141

He, R., Hornby, B., and Schuster, G. (2007). 3D Wave-Equation Interferometric Migration of VSP Free-Surface Multiples. *Geophysics* 72 (5), S195–S203. doi:10.1190/1.2743375

Hinds, R. C., Anderson, N. L., and Kuzmiski, R. D. (1996). *VSP Interpretive Processing: Theory and Practice*. Tulsa: Society of Exploration Geophysicists.

Hua, B., and McMechan, G. A. (2003). Parsimonious 2D Prestack Kirchhoff Depth Migration. *Geophysics* 68, 1043–1051. doi:10.1190/1.1581075

Jiang, Z., Sheng, J., Yu, J., Schuster, G. T., and Hornby, B. E. (2007). Migration Methods for Imaging Different-Order Multiples. *Geophys. Prospect* 55, 1–19. doi:10.1111/j.1365-2478.2006.00598.x

Jiang, Z., Yu, J., Schuster, G. T., and Hornby, B. E. (2005). Migration of Multiples. *The Leading Edge* 24, 315–318. doi:10.1190/1.1895318

Keho, T. H., and Beydoun, W. B. (1988). Paraxial ray Kirchhoff Migration. *Geophysics* 53, 1540–1546. doi:10.1190/1.1442435

Kiyashchenko, D., Plessix, R.-E., Kashtan, B., and Troyan, V. (2007). A Modified Imaging Principle for True-Amplitude Wave-Equation Migration. *Geophys. J. Int.* 168, 1093–1104. doi:10.1111/j.1365-246x.2006.03187.x

Li, Z., Li, Z., Li, Q., Li, Q., Sun, M., Hu, P., et al. (2020). Least-squares Reverse Time Migration of Multiples in Viscoacoustic media. *Geophysics* 85 (5), S285–S297. doi:10.1190/geo2019-0464.1

Li, Z., Li, Z., Wang, P., and Zhang, M. (2017). Reverse Time Migration of Multiples Based on Different-Order Multiple Separation. *Geophysics* 82 (1), S19–S29. doi:10.1190/geo2015-0710.1

Liu, F., Zhang, G., Morton, S. A., and Leveille, J. P. (2011). An Effective Imaging Condition for Reverse-Time Migration Using Wavefield Decomposition. *Geophysics* 76 (1), S29–S39. doi:10.1190/1.3533914

Liu, X., Liu, Y., and Khan, M. (2018). Fast Least-Squares Reverse Time Migration of VSP Free-Surface Multiples with Dynamic Phase-Encoding Schemes. *Geophysics* 83 (4), S321–S332. doi:10.1190/geo2017-0419.1

Lomas, A., Singh, S., and Curtis, A. (2018). *Marchenko Imaging of Both Vertical and Horizontal Interfaces Using VSP Data: 88th Annual International Meeting*. Anaheim: SEG, 5027.

Lu, S., Whitmore, D. N., Valenciano, A. A., and Chemingui, N. (2015). Separated-wavefield Imaging Using Primary and Multiple Energy. *The Leading Edge* 34, 770–778. doi:10.1190/tle34070770.1

McMechan, G. A. (1983). Migration by Extrapolation of Time-dependent Boundary Values*. *Geophys. Prospect* 31, 413–420. doi:10.1111/j.1365-2478.1983.tb01060.x

Muijs, R., Robertsson, J. O., and Holliger, K. (2007). Prestack Depth Migration of Primary and Surface-Related Multiple Reflections: Part I - Imaging. *Geophysics* 72 (2), S59–S69. doi:10.1190/1.2422796

Nemeth, T., Wu, C., and Schuster, G. T. (1999). Least-squares Migration of Incomplete Reflection Data. *Geophysics* 64, 208–221. doi:10.1190/1.1444517

O'Brien, J., Farmani, B., and Atkinson, B. (2013). VSP Imaging Using Free-Surface Multiples: A Case Study from the Gulf of Mexico. *The Leading Edge* 32, 1258–1266. doi:10.1190/tle32101258.1

Pestana, R. C., dos Santos, A. W., and Araujo, E. S. (2014). *RTM Imaging Condition Using Impedance Sensitivity Kernel Combined with Poynting Vector: 84th Annual International Meeting*. Denver: SEG, 3763–3768.

Ristow, D., and Rühl, T. (1994). Fourier Finite-difference Migration. *Geophysics* 59, 1882–1893. doi:10.1190/1.1443575

Sava, P., and Vasconcelos, I. (2011). Extended Imaging Conditions for Wave-Equation Migration. *Geophys. Prospecting* 59, 35–55. doi:10.1111/j.1365-2478.2010.00888.x

Schuster, G. T. (2009). *Seismic Interferometry*. Cambridge: Cambridge University Press.

Shan, G. (2003). *Source-receiver Migration of Multiple Reflections: 73rd Annual International Meeting*. Dallas: SEG, 1008–1011.

Singh, S., Snieder, R., Behura, J., van der Neut, J., Wapenaar, K., and Slob, E. (2015). Marchenko Imaging: Imaging with Primaries, Internal Multiples, and Free-Surface Multiples. *Geophysics* 80 (5), S165–S174. doi:10.1190/geo2014-0494.1

Soni, A. K., and Verschuur, D. J. (2015). Imaging Blended Vertical Seismic Profiling Data Using Full-Wavefield Migration in the Common-Receiver Domain. *Geophysics* 80 (3), R123–R138. doi:10.1190/geo2014-0193.1

Stewart, R. R., Huddleston, P. D., and Kan, T. K. (1984). Seismic versus Sonic Velocities: A Vertical Seismic Profiling Study. *Geophysics* 49, 1153–1168. doi:10.1190/1.1441745

Stoffa, P. L., Fokkema, J. T., de Luna Freire, R. M., and Kessinger, W. P. (1990). Split-step Fourier Migration. *Geophysics* 55, 410–421. doi:10.1190/1.1442850

Suh, S., and Wang, B. (2013). *Improving Salt Boundary Imaging Using an RTM Inverse Scattering Imaging Condition: 83rd Annual International Meeting*. Houston: SEG, 3953–3957.

Valenciano, A. A., and Biondi, B. (2003). *2-D Deconvolution Imaging Condition for Shot-Profile Migration: 72nd Annual International Meeting*. Dallas: SEG, 1059–1062.

Verschuur, D., and Berkhout, A. (2005). *Transforming Multiples into Primaries: Experience with Field Data: 75th Annual International Meeting*. Houston: SEG, 2103–2106.

Verschuur, D. J., Berkhout, A. J., and Wapenaar, C. P. A. (1992). Adaptive Surface-related Multiple Elimination. *Geophysics* 57, 1166–1177. doi:10.1190/1.1443330

VerWest, B. J., and Lin, D. (2007). Modeling the Impact of Wide-Azimuth Acquisition on Subsalt Imaging. *Geophysics* 72 (5), SM241–SM250. doi:10.1190/1.2736516

Wang, Y., Chang, X., and Hu, H. (2014a). Simultaneous Reverse Time Migration of Primaries and Free-Surface Related Multiples without Multiple Prediction. *Geophysics* 79 (1), S1–S9. doi:10.1190/geo2012-0450.1

Wang, Y. (2003). Multiple Subtraction Using an Expanded Multichannel Matching Filter. *Geophysics* 68, 346–354. doi:10.1190/1.1543220

Wang, Y., Zheng, Y., Xue, Q., Chang, X., Fei, T. W., and Luo, Y. (2017). Reverse Time Migration of Multiples: Reducing Migration Artifacts Using the Wavefield Decomposition Imaging Condition. *Geophysics* 82 (4), S307–S314. doi:10.1190/geo2016-0354.1

Wang, Y., Zheng, Y., Xue, Q., Chang, X., Fei, T. W., and Luo, Y. (2016). Reverse Time Migration with Hilbert Transform Based Full Wavefield Decomposition. *Chin. J. Geophys.* 59, 4200–4211.

Wang, Y., Zheng, Y., Zhang, L., Chang, X., and Yao, Z. (2014b). Reverse Time Migration of Multiples: Eliminating Migration Artifacts in Angle Domain Common Image Gathers. *Geophysics* 79 (6), S263–S270. doi:10.1190/geo2013-0441.1

Wapenaar, K., and Fokkema, J. (2006). Green's Function Representations for Seismic Interferometry. *Geophysics* 71 (4), SI33–SI46. doi:10.1190/1.2213955

Wapenaar, K., van der Neut, J., and Slob, E. (2017). On the Role of Multiples in Marchenko Imaging. *Geophysics* 82, A1–A5. doi:10.1190/geo2016-0323.1

Whitmore, N. D., and Crawley, S. (2012). *Applications of RTM Inverse Scattering Imaging Conditions: 82nd Annual International Meeting*. Las Vegas: SEG, 1–6. doi:10.1190/segam2012-0779.1

Yoon, K., and Marfurt, K. J. (2006). Reverse-time Migration Using the Poynting Vector. *Exploration Geophys.* 37, 102–107. doi:10.1071/eg06102

Yu, J., and Schuster, G. T. (2001). *Crosscorrelogram Migration of IVSPWD Data: 71st Annual International Meeting*. San Antonio: SEG, 456–459.

Yu, J., and Schuster, G. T. (2002). *Joint Migration of Primary and Multiple Reflections in RVSP Data: 72nd Annual International Meeting*. Salt Lake City: SEG, 2373–2376.

Zhang, D., and Schuster, G. T. (2014). Least-squares Reverse Time Migration of Multiples. *Geophysics* 79 (1), S11–S21. doi:10.1190/geo2013-0156.1

Zhang, L., and Slob, E. (2019). Free-surface and Internal Multiple Elimination in One Step without Adaptive Subtraction. *Geophysics* 84 (1), A7–A11. doi:10.1190/geo2018-0548.1

Zhang, Y., Liu, Y., Liu, X., and Zhou, X. (2020). Reverse Time Migration Using Water-bottom-related Multiples. *Geophys. Prospecting* 68, 446–465. doi:10.1111/1365-2478.12851

Zhang, Y., and Sun, J. (2009). Practical Issues in Reverse Time Migration: True Amplitude Gathers, Noise Removal and Harmonic Source Encoding. *First break* 27, 53–59. doi:10.3997/1365-2397.2009002

Zheng, Y., Wang, Y., and Chang, X. (2018). 3D Forward Modeling of Upgoing and Downgoing Wavefields Using Hilbert Transform. *Geophysics* 83 (1), F1–F8. doi:10.1190/geo2016-0637.1

Zheng, Y., Wang, Y., and Chang, X. (2016). Eliminating Artifacts in Migration of Surface-Related Multiples: An Application to marine Data. *Interpretation* 4 (4), SQ51–SQ57. doi:10.1190/int-2016-0020.1

Zheng, Y., Wang, Y., and Chang, X. (2019). Least-squares Data-To-Data Migration: An Approach for Migrating Free-Surface-Related Multiples. *Geophysics* 84 (2), S83–S94. doi:10.1190/geo2018-0080.1

Conflict of Interest: The authors declare that the research was conducted in the absence of any commercial or financial relationships that could be construed as a potential conflict of interest.

frontiers in Earth Science

ORIGINAL RESEARCH
published: 21 October 2021
doi: 10.3389/feart.2021.690513

Reverse Time Migration Based on the Pseudo-Space-Domain First-Order Velocity-Stress Acoustic Wave Equation

Xiaobo Zhang[1,2,3,4], Xiutian Wang[3], Baohua Liu[2,4], Peng Song[3], Jun Tan[3] and Chuang Xie[3]*

[1]College of Ocean Science and Engineering, Shandong University of Science and Technology, Qingdao, China, [2]Laboratory for Marine Geology and Environment, Pilot National Laboratory for Marine Science and Technology, Qingdao, China, [3]College of Marine Geosciences, Ocean University of China, Qingdao, China, [4]National Deep Sea Center, Ministry of Natural Resources, Qingdao, China

Reverse time migration (RTM) is an ideal seismic imaging method for complex structures. However, in conventional RTM based on rectangular mesh discretization, the medium interfaces are usually distorted. Besides, reflected waves generated by the two-way wave equation can cause artifacts during imaging. To overcome these problems, a high-order finite-difference (FD) scheme and stability condition for the pseudo-space-domain first-order velocity-stress acoustic wave equation were derived, and based on the staggered-grid FD scheme, the RTM of the pseudo-space-domain acoustic wave equation was implemented. Model experiments showed that the proposed RTM of the pseudo-space-domain acoustic wave equation could systematically avoid the interface distortion problem when the velocity interfaces were considered to compute the pseudo-space-domain intervals. Moreover, this method could effectively suppress the false scattering of dipping interfaces and reflections during wavefield extrapolation, thereby reducing migration artifacts on the profile and significantly improving the quality of migration imaging.

Keywords: pseudo-space-domain, staggered-grid, acoustic wave equation, high-order finite-difference, reverse time migration

OPEN ACCESS

Edited by:
Qinya Liu,
University of Toronto, Canada

Reviewed by:
Bin He,
University College, University of Toronto, Canada
Youshan Liu,
Institute of Geology and Geophysics (CAS), China

****Correspondence:***
Xiutian Wang
xtwang@ouc.edu.cn

Specialty section:
This article was submitted to Solid Earth Geophysics, a section of the journal Frontiers in Earth Science

Received: *03 April 2021*
Accepted: *08 September 2021*
Published: *21 October 2021*

Citation:
Zhang X, Wang X, Liu B, Song P, Tan J and Xie C (2021) Reverse Time Migration Based on the Pseudo-Space-Domain First-Order Velocity-Stress Acoustic Wave Equation. Front. Earth Sci. 9:690513. doi: 10.3389/feart.2021.690513

INTRODUCTION

Based on the theory of the two-way wave equation, the reverse time migration (RTM) algorithm was conceived in the early 1980s (McMechan, 1983; Whitmore, 1983). Since the wave equation does not need to be decomposed, there is no strata dip angle limitation caused by the wave equation approximation. The RTM is recognized as an ideal imaging method for complex structures and has been a popular topic in the field of geophysics (Moradpouri et al., 2017; Li et al., 2018; Zhou et al., 2018; Li et al., 2020). Chang and McMechan (1987) generalized the two-dimensional RTM to the elastic wavefield and then extended it to three dimensions (Chang and McMechan, 1990, 1994). Zhang and Ning (2002) proposed multi-wave and multi-component RTM based on the eikonal equation. Sun and McMechan (2001) implemented elastic wave RTM based on the separation of P- and S-waves. Yan (2012) studied the viscoelastic tilted transversely isotropic medium wave equation RTM algorithm based on rotating staggered grids. Liu et al. (2013) achieved RTM of elastic waves in porous media based on Biot's theory. Song et al. (2015) proposed the RTM of divided-order multiples to solve the problem of imaging difficulty in the regions of low illumination based on primaries. In terms of computational efficiency and storage consumption, Liu et al. (2010) applied the graphics

processing unit (GPU) for algorithmic acceleration, which greatly improved the computational efficiency of RTM. Clapp (2009) and Wang et al. (2012) used the random boundary and absorbing boundary storage strategies to reduce the consumption of storage capacity. Shi et al. (2015) analyzed the effect of random boundaries and an absorbing boundary in RTM and summarized the calculation cost and storage requirement for different boundaries and storage strategies.

After a few decades of development, the RTM technology has become increasingly mature, but it still suffers from the following problems: First, the RTM is usually achieved by using the finite-difference (FD) method with regular rectangular grids. When the underground interface model is meshed by grids, dipping interfaces and undulating surfaces only can be replaced by staircase curves, which may result in false scattering and interfacial distortion during RTM. In this respect, some scholars used variable space grids (Zhu and Wei, 2005, 2007; Huang and Dong, 2009), in which fine grids were adopted at regions with severe variation of medium parameters. However, this method still doesn't eliminate the limitations of rectangular grids, and it increases computational cost. Chu and Wang (2005) proposed an FD simulation method based on an irregular triangular mesh used in the finite-element method. Compared with the traditional rectangular mesh FD scheme, this method can describe undulating interfaces better, but the computational complexity increased. Besides, now there are many studies on RTM from rugged topography using curvilinear meshing or unstructured triangular meshing to get rid of the staircase approximation (Lan et al., 2014; Shragge, 2014; Liu et al., 2016; Qu et al., 2019; Liu and Zhang, 2020). Second, in the conventional RTM wavefield extrapolation based on the two-way wave equation, it produces a large number of reflection waves (back-propagating waves) at the interfaces. On the migration profile, it forms strong low-frequency noises and artifacts generated by wavepath cross-correlation with forward- and back-propagating waves, which result in low-profile imaging quality (Du et al., 2013). To reduce the influence of reflection waves, Baysal et al. (1984) deduced that the non-reflection acoustic equation can suppress the reflection waves well in the case of small incident angle under the assumption of constant impedance of the underlying medium. On the basis of the non-reflection acoustic equation proposed by Baysal, Song (2005) realized a recursive method to calculate the non-reflection scalar wave equation by introducing a wave impedance function. Willacy and Kryvohuz (2019) tried to image steep boundaries between a salt body and surrounding sediments based on the RTM using transmitted waves. He et al. (2008) developed RTM of arbitrarily wide-angle wave equations, but the imaging effect of this method is poor in shallow regions. Yoon and Marfurt (2006) introduced Poynting vector imaging conditions into RTM to realize cross-correlation of different direction wavefields, but it has a big numerical error in the regions of complex tectonics. Liu et al. (2011) proposed an imaging condition of RTM based on wavefield decomposition that separated up-going and down-going waves by using the F-K transform; however, the method of separating wavefields required a large amount of extra calculation and storage.

The effective solution of above two problems is of great significance to improve the imaging quality of RTM. Wang et al. (2005) deduced a pseudo-space-domain scalar acoustic equation by transforming the traditional wave equation from the time-space domain to time-traveltime domain (or "traveltime domain"). This scheme not only overcomes the problem of seismic velocity interface distortion but also effectively suppresses false scattering and reflections. However, based on the second-order partial differential acoustic wave equation, Wang et al. (2005) had realized a second-order FD solution in pseudo-space domain using regular grid, which cannot meet the needs of calculation accuracy. Based on the detailed discussion of the principle of the pseudo-space-domain wave equation, this thesis derives the high-order staggered-grid FD scheme and stability condition for the pseudo-space-domain first-order velocity-stress wave equation and achieves high-precision RTM with them.

PSEUDO-SPACE-DOMAIN FIRST-ORDER VELOCITY-STRESS ACOUSTIC WAVE EQUATION

At present, the most of FD wavefield extrapolations of the acoustic wave are based on the first-order velocity-stress acoustic wave equation. It can be written as follows:

$$\begin{cases} \rho \dfrac{\partial \tilde{v}_x}{\partial t} = -\dfrac{\partial \tilde{P}}{\partial x}, \\ \rho \dfrac{\partial \tilde{v}_z}{\partial t} = -\dfrac{\partial \tilde{P}}{\partial z}, \\ \dfrac{\partial \tilde{P}}{\partial t} = -\rho c_p^2 \left(\dfrac{\partial \tilde{v}_x}{\partial x} + \dfrac{\partial \tilde{v}_z}{\partial z} \right) + s(t), \end{cases} \tag{1}$$

where x and z represent the horizontal and vertical coordinates of the space domain, respectively, c_p is the primary velocity at point (x, z), ρ is the density at point (x, z), $\tilde{P}$ represents the pressure, $\tilde{v}_x$ and $\tilde{v}_z$ represent the velocity components in the x and z directions, respectively, $s(t)$ is the source function, with t being time. To obtain the numerical solution of **Eq. 1**, we usually use differences instead of differentials to approximate derivatives based on the staggered-grid technique (Vireux, 1984).

The conventional FD method, which is applied to the acoustic equation, is based on rectangular grid. When the subsurface interface model is meshed, the dipping interface can only be described by using a staircase curve. It can cause false scattering in the process of wavefield extrapolation and interface distortion at the migration profile. At the same time, the two-way wave equation can generate reflected waves at the interfaces between different velocity layers. Furthermore, strong low-frequency noises and artifacts are formed on the migration profile, which lead to low profile imaging quality.

To solve above problems, a pseudo-space-domain first-order velocity-stress acoustic wave equation is proposed in this article. In RTM of acoustic wave equation, imaging about the pressure $\tilde{P}$ is usually used. Therefore, under the condition that the $\tilde{P}$ is not

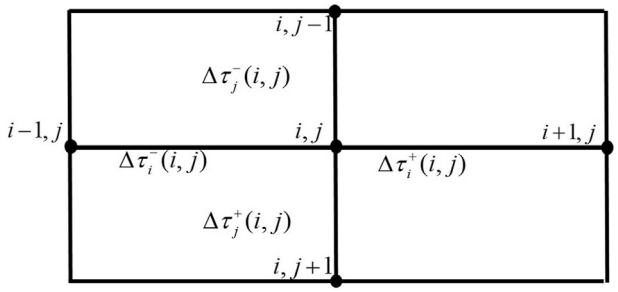

FIGURE 1 | Four pseudo-space-domain intervals at the point $P(i,j)$.

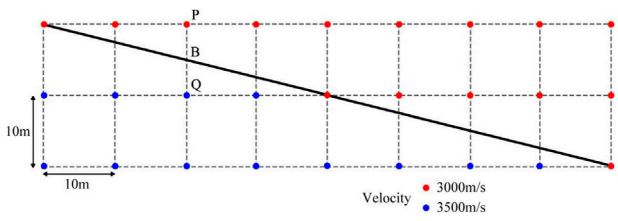

FIGURE 2 | Partial schematic illustration of a mesh model after the regular meshing of a velocity interface model including a dipping interface.

affected, assuming$v_x = c_p\tilde{v}_x$, $v_z = c_p\tilde{v}_z$, $P = \tilde{P}$, **Eq. 1** can be transformed into

$$\begin{cases} \dfrac{\partial v_x}{\partial t} = -\dfrac{c_p}{\rho}\dfrac{\partial P}{\partial x}, \\ \dfrac{\partial v_z}{\partial t} = -\dfrac{c_p}{\rho}\dfrac{\partial P}{\partial z}, \\ \dfrac{\partial P}{\partial t} = -\rho c_p\left(\dfrac{\partial v_x}{\partial x} + \dfrac{\partial v_z}{\partial z}\right) + s(t). \end{cases} \tag{2}$$

After discretizing the continuous model into a grid model, we set the spatial unit grid length as $\Delta\xi$ (where ξ can represent x or z) and that the traveltime between a grid length $\Delta\xi$ as $\Delta\tau_\xi$. Then, the space grid $\Delta\xi$ and traveltime $\Delta\tau_\xi$ satisfy the relationship $\Delta\xi = c_p\Delta\tau_\xi$, where c_p is the acoustic wave velocity in the grid point. The derivative of the pressure and velocity components with respect to space can be rewritten as:

$$\begin{cases} \dfrac{\partial P}{\partial \tau_\xi} = c_p\dfrac{\partial P}{\partial \xi}, \\ \dfrac{\partial v_x}{\partial \tau_\xi} = c_p\dfrac{\partial v_x}{\partial \xi}, \\ \dfrac{\partial v_z}{\partial \tau_\xi} = c_p\dfrac{\partial v_z}{\partial \xi}. \end{cases} \tag{3}$$

Then, substituting **Eq. 3** into **Eq. 1** yields **Eq. 4**, which is the pseudo-space-domain first-order velocity-stress acoustic wave equation.

$$\begin{cases} \dfrac{\partial v_x}{\partial t} = -\dfrac{1}{\rho}\dfrac{\partial P}{\partial \tau_x}, \\ \dfrac{\partial v_z}{\partial t} = -\dfrac{1}{\rho}\dfrac{\partial P}{\partial \tau_z}, \\ \dfrac{\partial P}{\partial t} = -\rho\left(\dfrac{\partial v_x}{\partial \tau_x} + \dfrac{\partial v_z}{\partial \tau_z}\right) + s(t). \end{cases} \tag{4}$$

NUMERICAL SIMULATION OF THE PSEUDO-SPACE-DOMAIN FIRST-ORDER VELOCITY-STRESS ACOUSTIC EQUATION

Sampling Interval Calculation in the Pseudo-Space-Domain

Usually, to solve **Eq. 4** by the FD method, first we should discretize the continuous model into a grid model and then compute the "traveltime" $\Delta\tau_\xi$ along with the grid point interval $\Delta\xi$. For simplicity, $\Delta\tau_\xi$ is called the "pseudo-space-domain interval".

In the two-dimensional case, there are four pseudo-space-domain intervals at a point $P(i, j)$, where i and $j$represent grid coordinates in the x and z directions, respectively. In the following discussion, a pseudo-space-domain interval is denoted as $\Delta\tau_l^{\pm}(i, j)$, where l represents i or j, "–" and "+" represent the side of the smaller coordinate grid number and the side of the larger coordinate grid number, respectively. As shown in **Figure 1**, $\Delta\tau_i^-(i, j)$ represents the pseudo-space-domain interval between points $P(i-1, j)$ and $P(i, j)$, $\Delta\tau_j^-(i, j)$ represents the pseudo-space-domain interval between points $P(i, j-1)$ and $P(i, j)$, $\Delta\tau_i^+(i, j)$ represents the pseudo-space-domain interval between points $P(i+1, j)$ and $P(i, j)$, and $\Delta\tau_j^+(i, j)$ represents the pseudo-space-domain interval between points $P(i, j+1)$ and $P(i, j)$.

Obviously, there are no velocity parameter items in **Eq. 4**. When the wave equation is transformed into pseudo-space domain, the original discrete space grid point velocity information is assigned to a grid line. At the same time, additional velocity information of the interfaces intersected on grid lines can be provided for computing the pseudo-space-domain intervals. **Figure 2** shows a partial schematic illustration of a mesh model after the regular meshing of a velocity interface model including a dipping interface (as shown by the black solid line in **Figure 2**). The primary velocities at the upper and lower sides of the interface are 3,000 and 3,500 m/s, respectively, and the grid interval is 10 m. It can be seen that, after meshing the velocity interface model according to a regular rectangular grid, the dipping interface is distorted to an obvious staircase fold line. However, in the pseudo-space-domain, the "propagation time" on both sides of the velocity interface is calculated according to its actual velocity and propagation distance, and the time sampling interval corresponding to the grid line is the sum of different "time of propagation" segments. Points P and Q in **Figure 2** are two adjacent spatial grid points after the velocity model is divided according to a rectangular grid, and the velocity interface as shown by the black solid line intersects segment PQ at point B. In this case, the pseudo-space-domain interval between P and Q may be calculated as $\Delta\tau = \Delta\tau_{PB} + \Delta\tau_{BQ}$, where $\Delta\tau_{PB}$ is the traveltime along with segment PB, and$\Delta\tau_{BQ}$ is the traveltime along segment BQ.

Theoretically, there is no longer a distortion of the velocity interface in the pseudo-space-domain, and even the mutation of the model parameters between adjacent grid points are weakened, so it is expected that false scattering and interface reflection in the migration calculation can be reduced.

A 2*N*th-Order-Accuracy Staggered-Grid FD Scheme of the Pseudo-Space-Domain First-Order Velocity-Stress Acoustic Wave Equation

In the implementation of FD numerical simulations based on the pseudo-space-domain acoustic wave equation, as well as to improve the accuracy of the simulation and suppress the impact of numerical dispersion, we need to improve the accuracy of the differences. Therefore, in this study, we deduce the 2*N*th-order-accuracy staggered-grid FD expression for the acoustic wave equation in the pseudo-space-domain.

In the two-dimensional case, the coordinates are denoted as (i, j) in the space-domain model discretized by sampling interval $(\Delta x, \Delta z)$. The corresponding coordinates of the pseudo-space-domain are (τ_i, τ_j). We take $\frac{\partial P}{\partial \tau_x}$ and $\frac{\partial v_x}{\partial \tau_x}$ as examples to give the propagation time interval calculation formula in pseudo-space-domain.

When calculating $\frac{\partial P}{\partial \tau_x}$ at $\tau_x = \tau_{i+1/2}$, P is located at point (τ_{i+m}, τ_j) and $(\tau_{i-(m-1)}, \tau_j)(m = 1, 2, 3, \ldots)$. In the τ_x direction, the pseudo-space-domain propagation time intervals centered on $(\tau_{i+1/2}, \tau_j)$ are shown as follows:

$$\Delta\tau_{i+1/2}^{+m} = \begin{cases} 0.5\Delta\tau_i^+(i,j) & (m=1), \\ 0.5\Delta\tau_i^+(i,j) + \sum_{k=1}^{m-1}\Delta\tau_i^+(i+k,j) & (m>1), \end{cases} \tag{5}$$

where $\Delta\tau_i^+(i+k, j)$ represents the pseudo-space-domain interval between points $(i+k, j)$ and $(i+1+k, j)$, $\Delta\tau_{i+1/2}^{+m}$ represents the propagation time interval between $(\tau_{i+1/2}, \tau_j)$ and the grid point (τ_{i+m}, τ_j) where P is located.

$$\Delta\tau_{i+1/2}^{-(m-1)} = \begin{cases} 0.5\Delta\tau_i^+(i,j) & (m=1), \\ 0.5\Delta\tau_i^+(i,j) + \sum_{k=0}^{m-2}\Delta\tau_i^-(i-k,j) & (m>1), \end{cases} \tag{6}$$

where $\Delta\tau_i^-(i-k, j)$ represents the pseudo-space-domain interval between points $(i-1-k, j)$ and $(i-k, j)$, $\Delta\tau_{i+1/2}^{-(m-1)}$ represents the propagation time interval between $(\tau_{i+1/2}, \tau_j)$ and the grid point $(\tau_{i-(m-1)}, \tau_j)$ where P is located. It notes that here and hereinafter $(\tau_{i+1/2}, \tau_j)$ indicates the center point of the propagation time between (i, j) and $(i+1, j)$.

When calculating $\frac{\partial v_x}{\partial \tau_x}$ at $\tau_x = \tau_i$, velocity v_x is located at point $(\tau_{i+(m-1/2)}, \tau_j)$ and $(\tau_{i-(m-1/2)}, \tau_j)(m = 1, 2, 3, \ldots)$. In the τ_x direction, the pseudo-space-domain propagation time intervals centered on (τ_i, τ_j) are shown as follows.

$$\Delta\tau_i^{+(m-1/2)} = \begin{cases} 0.5\Delta\tau_i^+(i,j) & (m=1), \\ 0.5\Delta\tau_i^+(i+m-1,j) + \sum_{k=0}^{m-2}\Delta\tau_i^+(i+k,j) & (m>1), \end{cases} \tag{7}$$

where $\Delta\tau_i^+(i+k, j)$ represents the pseudo-space-domain interval between points $(i+k, j)$ and $(i+1+k, j)$, and $\Delta\tau_i^{+(m-1/2)}$ represents the propagation time interval between (τ_i, τ_j) and the grid point $(\tau_{i+(m-1/2)}, \tau_j)$ where v_x is located.

$$\Delta\tau_i^{-(m-1/2)} = \begin{cases} 0.5\Delta\tau_i^-(i,j) & (m=1), \\ 0.5\Delta\tau_i^-(i-m+1,j) + \sum_{k=0}^{m-2}\Delta\tau_i^-(i-k,j) & (m>1), \end{cases} \tag{8}$$

where $\Delta\tau_i^-(i-k, j)$ represents the pseudo-space-domain interval between points $(i-1-k, j)$ and $(i-k, j)$, and $\Delta\tau_i^{-(m-1/2)}$ represents the propagation time interval between (τ_i, τ_j) and the grid point $(\tau_{i-(m-1/2)}, \tau_j)$ where v_x is located. Similarly, the pseudo-space-domain propagation time interval of P and v_z in the direction τ_z can be calculated separately in a similar manner as described above.

Using the propagation time interval shown in **Eqs 5**, **6**, the 2*N*th-order-accuracy expansion of the first-order derivative of the P with respect to the variable τ_x can be obtained. The P in the pseudo-space-domain is assumed to have a 2*N*th-order derivative. For different P_{τ_x} values, satisfying $\tau_x = \tau_{i+1/2} + \Delta\tau_{i+1/2}^{+m}$ and $\tau_x = \tau_{i+1/2} - \Delta\tau_{i+1/2}^{-(m-1)}$ corresponding to $\tau_x = \tau_{i+m}$ and $\tau_x = \tau_{i-(m-1)}$ (m=1, 2, …, $N-1$, N), respectively, the 2*N*th-order Taylor series expansions at $\tau_x = \tau_{i+1/2}$ are

$$P_{\tau_{i+1/2}+\Delta\tau_{i+1/2}^{+m}} = P_{\tau_{i+1/2}} + \sum_{n=1}^{2N-1}\frac{\left(+\Delta\tau_{i+1/2}^{+m}\right)^n}{n!}P_{\tau_{i+1/2}}^{(n)} + O\left(\left(+\Delta\tau_{i+1/2}^{+m}\right)^{2N}\right), \tag{9}$$

$$P_{\tau_{i+1/2}-\Delta\tau_{i+1/2}^{-(m-1)}} = P_{\tau_{i+1/2}} + \sum_{n=1}^{2N-1}\frac{\left(-\Delta\tau_{i+1/2}^{-(m-1)}\right)^n}{n!}P_{\tau_{i+1/2}}^{(n)} + O\left(\left(-\Delta\tau_{i+1/2}^{-(m-1)}\right)^{2N}\right), \tag{10}$$

where $P^{(n)}$ represents the nth-order derivative of P. The above 2*N* equations are multiplied by c_1^x, c_2^x, …, c_{2N-1}^x, c_{2N}^x, respectively, and then added and simplified as

$$\begin{aligned} \sum_{m=1}^{N}\left(c_{2m-1}^x P_{\tau_{i+1/2}+\Delta\tau_{i+1/2}^{+m}} + c_{2m}^x P_{\tau_{i+1/2}-\Delta\tau_{i+1/2}^{-(m-1)}}\right) &= \sum_{m=1}^{N}\left(c_{2m-1}^x + c_{2m}^x\right)P_{\tau_{i+1/2}} \\ &+ \sum_{m=1}^{N}\left(\frac{\left(\Delta\tau_{i+1/2}^{+m}\right)}{1!}c_{2m-1}^x + \frac{\left(-\Delta\tau_{i+1/2}^{-(m-1)}\right)}{1!}c_{2m}^x\right)P_{\tau_{i+1/2}}^{(1)} + \sum_{n=2}^{2N-1} \\ &\sum_{m=1}^{N}\left(\frac{\left(\Delta\tau_{i+1/2}^{+m}\right)^n}{n!}c_{2m-1}^x + \frac{\left(-\Delta\tau_{i+1/2}^{-(m-1)}\right)^n}{n!}c_{2m}^x\right)P_{\tau_{i+1/2}}^{(n)} \\ &+ O\left(\left(+\Delta\tau_{i+1/2}^{+m}\right)^{2N}\right) + O\left(\left(-\Delta\tau_{i+1/2}^{-(m-1)}\right)^{2N}\right). \end{aligned} \tag{11}$$

To resolve the first-order derivative FD scheme of P at $\tau_x = \tau_{i+1/2}$, **Eq. 11** needs to satisfy the algebraic relationship that the coefficient of the first derivative is one and the other derivative is 0 except at the first order. Therefore, according to the coefficient relationship between derivatives, we can get the FD coefficients c_m^x(m=1, 2, …, 2N−1, 2N).

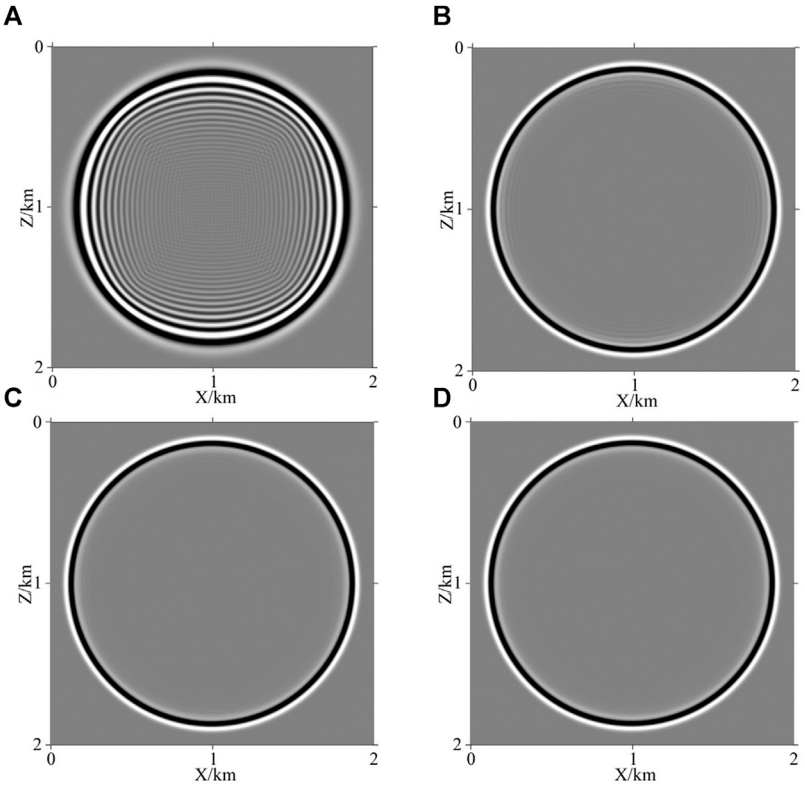

FIGURE 3 | Snapshots of wavefield extrapolation based on different orders of finite-difference operator in a pseudo-space-domain difference expression **(A)**, **(B)**, **(C)**, and **(D)** correspond, respectively, to second-order, eighth-order, twelfth-order, and sixteenth-order.

From **Eq. 11**, we can see that the solutions for the FD coefficients depend on the pseudo-space-domain propagation time intervals $\Delta\tau_{i+1/2}^{+m}$ and $\Delta\tau_{i+1/2}^{-(m-1)}(m=1, 2, \ldots, N-1, N)$. While the velocity on each grid remains constant, there exists the relationships $\Delta\tau_{i+1/2}^{+m} = \Delta\tau_{i+1/2}^{-(m-1)}$ and $c_{2k-1}^{x} = -c_{2k}^{x}(k = 1, 2, \ldots, N-1, N)$. While the velocity is not constant, there exist the relationships $\Delta\tau_{i+1/2}^{+m} \neq \Delta\tau_{i+1/2}^{-(m-1)}$ and $c_{2k-1}^{x} \neq -c_{2k}^{x}(k = 1, 2, \ldots, N-1, N)$. From the above analysis, it can be seen that the FD coefficients of the numerical simulation in the pseudo-space-domain are related to the grid velocity and the size of the grid. Even with the same difference order, the FD coefficients are different corresponding to various grid velocity and sizes.

By substituting the FD coefficients into **Eq. 11**, a 2*N*th-order difference expression for the first derivative of P at $\tau_x = \tau_{i+1/2}$ can be written as:

$$\left.\frac{dP}{d\tau_x}\right|_{\tau_x=\tau_{i+1/2}} = \sum_{m=1}^{N}\left(c_{2m-1}^{x}P_{\tau_{i+1/2}+\Delta\tau_{i+1/2}^{+m}} + c_{2m}^{x}P_{\tau_{i+1/2}-\Delta\tau_{i+1/2}^{-(m-1)}}\right). \quad (12)$$

Similarly, we have a 2*N*th-order difference expression and FD coefficients $c_m^z(m=1, 2, \ldots, 2N-1, 2N)$ for the first-order derivative of P at $\tau_z = \tau_{j+1/2}$, a 2*N*th-order difference expression, and FD coefficients $c_{vm}^{x}(m=1, 2, \ldots, 2N-1, 2N)$ for the first-order derivative of v_x at $\tau_x = \tau_i$, and a 2*N*th-order difference expression and FD coefficients $c_{vm}^{z}(m=1, 2, \ldots, 2N-1, 2N)$ for the first-order derivative of v_z at $\tau_z = \tau_j$.

Substituting the above difference expressions for P, v_x, and v_z at τ_x or τ_z and the second-order difference expressions for the first-order derivative of P, v_x, and v_z at time into **Eq. 4**, we can obtain

$$\begin{cases} v_{x\tau_{i+1/2},\tau_j}^{k+1/2} = v_{x\tau_{i+1/2},\tau_j}^{k-1/2} \\ \quad -\frac{\Delta t}{\rho}\sum_{m=1}^{N}\left(c_{2m-1}^{x}P_{\tau_{i+1/2}+\Delta\tau_{i+1/2}^{+m},\tau_j}^{k} + c_{2m}^{x}P_{\tau_{i+1/2}-\Delta\tau_{i+1/2}^{-(m-1)},\tau_j}^{k}\right), \\ v_{z\tau_i,\tau_{j+1/2}}^{k+1/2} = v_{z\tau_i,\tau_{j+1/2}}^{k-1/2} \\ \quad -\frac{\Delta t}{\rho}\sum_{m=1}^{N}\left(c_{2m-1}^{z}P_{\tau_i,\tau_{j+1/2}+\Delta\tau_{i+1/2}^{+m}}^{k} + c_{2m}^{z}P_{\tau_i,\tau_{j+1/2}-\Delta\tau_{j+1/2}^{-(m-1)}}^{k}\right), \\ P_{\tau_i,\tau_j}^{k+1} = P_{\tau_i,\tau_j}^{k} \\ \quad -\rho\Delta t\sum_{m=1}^{N}\left(c_{v2m-1}^{x}v_{x\tau_i+\Delta\tau_i^{+(m-1/2)},\tau_j}^{k+1/2} + c_{v2m}^{x}v_{x\tau_i-\Delta\tau_i^{-(m-1/2)},\tau_j}^{k+1/2}\right) \\ \quad -\rho\Delta t\sum_{m=1}^{N}\left(c_{v2m-1}^{z}v_{x\tau_i,\tau_j+\Delta\tau_j^{+(m-1/2)}}^{k+1/2} + c_{v2m}^{z}v_{x\tau_i,\tau_j-\Delta\tau_j^{-(m-1/2)}}^{k+1/2}\right) + s(t), \end{cases} \quad (13)$$

where k represents discrete time points, which satisfy $t = k\Delta t$ (where Δt represents a discrete time interval).

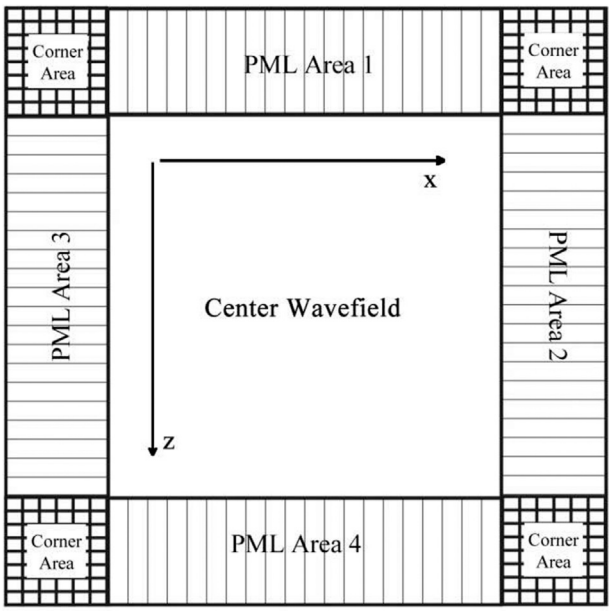

FIGURE 4 | PML layer distribution diagram (Zhang et al., 2016).

In the following, a homogeneous model is used to show the effect of the pseudo-space-domain high-order FD scheme on dispersion suppression. The size of the model is 2000 × 2000 m. The spatial sampling interval is 10 × 10 m, and the primary wave velocity is 2,500 m/s. The source location is 1,000 m, 1,000 m. As a source wavelet, we adopt the Ricker wavelet whose dominant frequency is 35 Hz, and the time sampling interval is 0.25 ms. Snapshots based on simulations of the pseudo-space-domain with different orders of FD operator are shown in **Figure 3**.

It can be seen from the snapshot shown in **Figure 3** that, for the pseudo-space-domain FD scheme with different orders of FD operator, when the spatial grid interval, model velocity, and wavelet dominant frequency are the same, the higher the order of FD operator is, the weaker the dispersion is.

Stability Condition for the Pseudo-Space-Domain First-Order Velocity-Stress Acoustic Wave Equation

First, we define the pseudo-space-domain plane harmonic variables u

$$u = u_0\, e^{i\omega n\Delta t} e^{ik_{\tau_x} j\Delta\tau_x} e^{ik_{\tau_z} k\Delta\tau_z}, \tag{14}$$

where u_0 represents the initial wavefield, ω represents the circular frequency, k_{τ_x} and k_{τ_z} represent wave numbers in the τ_x and τ_z directions, respectively; n, j, and k represent coordinates of discrete grid points in the t, τ_x, and τ_z directions, respectively; $\Delta\tau_x$ and $\Delta\tau_z$represent pseudo-space-domain intervals in the τ_x and τ_z directions, respectively; e stands for the base of the natural logarithms, and i represents the imaginary unit in this section.

According to the above equation, one can get the following relationships:

$$\begin{cases} u_{\tau_x+\Delta\tau_x^{+m}} = u_{\tau_x} e^{ik_{\tau_x}\Delta\tau_x^{+m}}, \\ u_{\tau_x-\Delta\tau_x^{-m}} = u_{\tau_x} e^{-ik_{\tau_x}\Delta\tau_x^{-m}}. \end{cases} \tag{15}$$

Substituting the above formulas into the first-derivative difference expression gives

$$\frac{du}{d\tau_x} = u\sum_{m=1}^{N}\left(c_{2m-1}^{x} e^{ik_{\tau_x}\Delta\tau_x^{+m}} + c_{2m}^{x} e^{-ik_{\tau_x}\Delta\tau_x^{-m}}\right). \tag{16}$$

Furthermore, the second-derivative expression for τ_x can be obtained as

$$\frac{d^2u}{d\tau_x^2} = u\left\{\sum_{m=1}^{N}\left(c_{2m-1}^{x} e^{ik_{\tau_x}\Delta\tau_x^{+m}} + c_{2m}^{x} e^{-ik_{\tau_x}\Delta\tau_x^{-m}}\right)\right\}^2. \tag{17}$$

According to the definition of the propagation time in the pseudo-space-domain and the sampling theorem, when the maximum wave number for τ_x is obtained, the following relationships hold: $\Delta\tau_x^{+m}k_{\tau_x} = (m-1/2)\pi$ and $\Delta\tau_x^{-m}k_{\tau_x} = (m-1/2)\pi$. Therefore, the above equation can be converted into

$$\frac{d^2u}{d\tau_x^2} = -u\left\{\sum_{m=1}^{N}\left((-1)^{m-1}c_{2m-1}^{x} + (-1)^{m}c_{2m}^{x}\right)\right\}^2. \tag{18}$$

Similarly, the second-derivative expression for τ_z can be obtained as

$$\frac{d^2u}{d\tau_z^2} = -u\left\{\sum_{m=1}^{N}\left((-1)^{m-1}c_{2m-1}^{z} + (-1)^{m}c_{2m}^{z}\right)\right\},^2 \tag{19}$$

and the second-derivative expression for t can be obtained as

$$\frac{\partial^2u}{\partial t^2} = -u\left(\frac{2\sin(\omega\Delta t/2)}{\Delta t}\right)^2 \tag{20}$$

Eq. (4) is reduced to the form of a pseudo-space-domain second-order scalar acoustic wave equation, and **Eqs. (18)**, **(19)**, and **(20)** are substituted to yield

$$\left(\frac{2\sin(\omega\Delta t/2)}{\Delta t}\right)^2 = \left\{\sum_{m=1}^{N}\left((-1)^{m-1}c_{2m-1}^{x} + (-1)^{m}c_{2m}^{x}\right)\right\}^2 + \left\{\sum_{m=1}^{N}\left((-1)^{m-1}c_{2m-1}^{z} + (-1)^{m}c_{2m}^{z}\right)\right\}^2. \tag{21}$$

Because the left side of the equation above satisfies $0 \le \sin^2\omega\frac{\Delta t}{2} \le 1$, and under the assumption that the differential coefficients in the τ_x and τ_z directions are equal, the following relation holds:

$$\Delta t \le \frac{\sqrt{2}}{\left|\sum_{m=1}^{N}\left((-1)^{m-1}c_{2m-1} + (-1)^{m}c_{2m}\right)\right|}, \tag{22}$$

where $c_m = c_m^x = c_m^z$ $(m = 1, 2, \ldots, 2N-1, 2N)$.

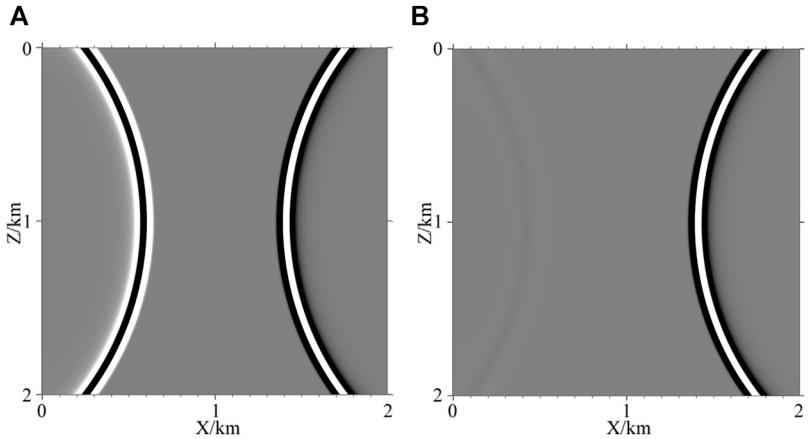

FIGURE 5 | Snapshot of the pseudo-space-domain acoustic wave equation at 0.82 s: **(A)** left boundary without PML boundary conditions; **(B)** left boundary with PML boundary conditions.

Perfectly Matched Layer Boundary Conditions of the Pseudo-Space-Domain First-Order Velocity-Stress Acoustic Wave Equation

In the central wavefield calculation region, FD numerical simulation of the pseudo-space-domain first-order velocity-stress acoustic wave equation with 2*N*th order in pseudo-space and second-order in time can be realized by applying **Eq. 13**. In the artificial boundary region, to effectively suppress the artificial boundary reflection, absorbing boundary processing is required. The perfectly matched layer (PML) boundary conditions for the first-order velocity-stress acoustic wave equation in the pseudo-space-domain are given below.

Because the PML attenuation term is independent of the partial derivative of wave equation, the space domain partial derivative in the equation is transformed into a pseudo-space-domain partial derivative; meanwhile, the space domain attenuation factors d_x and d_z are transformed into pseudo-space-domain attenuation factors d_{τ_x} and d_{τ_z}. The PML boundary conditions for the pseudo-space-domain acoustic wave equation are as follows:

$$\begin{cases} \dfrac{\partial v_x}{\partial t} + d_{\tau_x} v_x = -\dfrac{1}{\rho}\dfrac{\partial P}{\partial \tau_x}, \\ \dfrac{\partial v_z}{\partial t} + d_{\tau_z} v_z = -\dfrac{1}{\rho}\dfrac{\partial P}{\partial \tau_z}, \\ \dfrac{\partial P_x}{\partial t} + d_{\tau_x} P_x = -\rho\dfrac{\partial v_x}{\partial \tau_x}, \\ \dfrac{\partial P_z}{\partial t} + d_{\tau_z} P_z = -\rho\dfrac{\partial v_z}{\partial \tau_z}, \\ P = P_x + P_z, \end{cases} \tag{23}$$

where P_x and P_z represent the components of P in the τ_x and τ_z directions. d_{τ_x} and d_{τ_z} represent the attenuation factors in the τ_x and τ_z directions, which are given by

$$d(\tau_m) = \log\left(\frac{1}{R}\right)\cdot\frac{3}{2\tau_L}\left(\frac{\tau_m}{\tau_L}\right)^2, \tag{24}$$

where τ_m represents the normal pseudo-space-domain propagation time interval from the point in the PML layer to the outer edge of the center wavefield, R represents the theoretical reflection coefficient for the PML layer (ranging from 10^{-5} to 10^{-7}), and τ_L represents the pseudo-space-domain PML layer thickness. As is shown in **Figure 4**, when wavefield calculations are performed, $d_{\tau_x} = 0$, $d_{\tau_z} = 0$ in the center wavefield area; $d_{\tau_x} = 0$, $d_{\tau_z} = d(\tau_m)$ in PML areas one and PML area 4; $d_{\tau_x} = d(\tau_m)$, $d_{\tau_z} = 0$ in PML areas two and PML area three; and $d_{\tau_x} = d(\tau_m)$, $d_{\tau_z} = d(\tau_m)$ in the corner area.

We can write the attenuation factors $d_{\tau_x} v_x$, $d_{\tau_z} v_z$, $d_{\tau_x} P_x$, and $d_{\tau_z} P_z$ in the PML boundary conditions into a differential form, and by substituting them with the difference expression of each first-order derivative into **Eq. 23**, we can derive

$$\begin{cases} v^{k+1/2}_{x\tau_{i+1/2},\tau_j} = \dfrac{1}{1+d_{\tau_x}\Delta t/2}\Big[(1-d_{\tau_x}\Delta t/2)v^{k-1/2}_{x\tau_{i+1/2},\tau_j} \\ \qquad -\dfrac{\Delta t}{\rho}\sum\limits_{m=1}^{N}\left(c^x_{2m-1}P^k_{\tau_{i+1/2}+\Delta\tau^{+m}_{i+1/2},\tau_j} + c^x_{2m}P^k_{\tau_{i+1/2}-\Delta\tau^{-(m-1)}_{i+1/2},\tau_j}\right)\Big], \\ v^{k+1/2}_{z\tau_i,\tau_{j+1/2}} = \dfrac{1}{1+d_{\tau_z}\Delta t/2}\Big[(1-d_{\tau_z}\Delta t/2)v^{k-1/2}_{z\tau_i,\tau_{j+1/2}} \\ \qquad -\dfrac{\Delta t}{\rho}\sum\limits_{m=1}^{N}\left(c^z_{2m-1}P^k_{\tau_i,\tau_{j+1/2}+\Delta\tau^{+m}_{i+1/2}} + c^z_{2m}P^k_{\tau_i,\tau_{j+1/2}-\Delta\tau^{-(m-1)}_{j+1/2}}\right)\Big], \\ P^{k+1}_{x\tau_i,\tau_j} = \dfrac{1}{1+d_{\tau_x}\Delta t/2}\Big[(1-d_{\tau_x}\Delta t/2)P^k_{x\tau_i,\tau_j} \\ \qquad -\rho\Delta t\sum\limits_{m=1}^{N}\left(c^x_{v2m-1}v^{k+1/2}_{x\tau_i+\Delta\tau^{+(m-1/2)}_i,\tau_j} + c^x_{v2m}v^{k+1/2}_{x\tau_i-\Delta\tau^{-(m-1/2)}_i,\tau_j}\right)\Big], \\ P^{k+1}_{z\tau_i,\tau_j} = \dfrac{1}{1+d_{\tau_z}\Delta t/2}\Big[(1-d_{\tau_z}\Delta t/2)P^k_{z\tau_i,\tau_j} \\ \qquad -\rho\Delta t\sum\limits_{m=1}^{N}\left(c^z_{v2m-1}v^{k+1/2}_{x\tau_i,\tau_j+\Delta\tau^{+(m-1/2)}_j} + c^z_{v2m}v^{k+1/2}_{x\tau_i,\tau_j-\Delta\tau^{-(m-1/2)}_j}\right)\Big], \\ P^{k+1}_{\tau_i,\tau_j} = P^{k+1}_{x\tau_i,\tau_j} + P^{k+1}_{z\tau_i,\tau_j}. \end{cases} \tag{25}$$

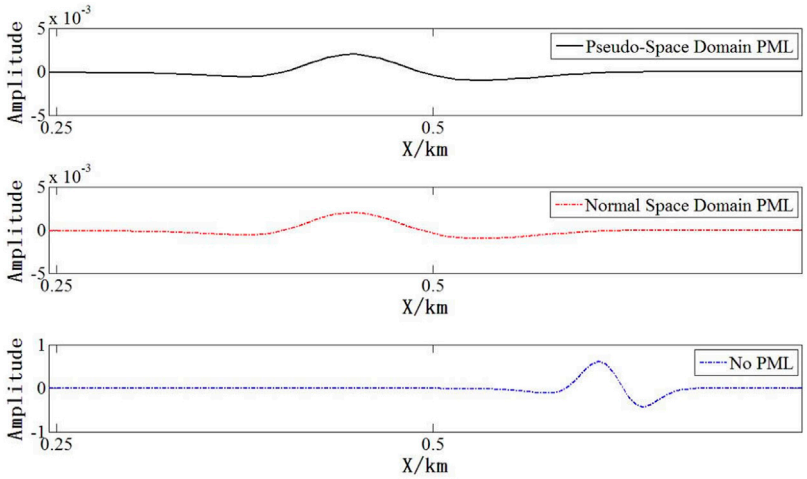

FIGURE 6 | PML boundary condition absorption effect comparison.

Equation 25 is the difference expression for PML boundary conditions of the pseudo-space-domain first-order velocity-stress acoustic wave equation.

A uniform medium model is used to verify the effectiveness of the PML boundary conditions of first-order velocity-stress acoustic wave equations in the pseudo-space-domain for eliminating artificial boundary reflections. The horizontal and vertical lengths of the model are 2000 and 2000 m, respectively, and the grid interval is 5 m. The primary wave velocity in the model is 2,500 m/s, and the density is 2000 kg/m^3. The source location is (1,000 m, 1,000 m), and the source wavelet employs Ricker wavelet with a dominant frequency of 35 Hz. To avoid the effects of numerical dispersion, the pseudo-space-domain FD order is 10th order. The snapshot of the wavefield extrapolation process at 0.82 s is shown in **Figure 5**, where **Figure 5A** shows the snapshot of the left boundary without the PML boundary conditions, and **Figure 5B** shows a snapshot of the left boundary with PML boundary conditions.

To further illustrate the boundary absorption effect of the PML boundary conditions in the pseudo-space-domain acoustic wave equation, the left boundary reflection wave corresponding to a depth of 1 km in the wavefield shown in **Figure 5** is magnified and displayed and is compared with the conventional acoustic wave equation wave based on the same simulation parameters. As shown in **Figure 6**, the black solid line is the left boundary reflection wave absorbed by the PML boundary condition of the pseudo-space-domain acoustic wave equation, the red dotted line is the left boundary reflection wave absorbed by the PML boundary condition of conventional method, and the blue dotted line is the reflected wave of left boundary without attenuation by PML boundary conditions. It can be seen that the amplitude of the boundary reflection wave after absorption by the pseudo-space-domain PML boundary condition is basically the same as that obtained by the conventional PML boundary condition, and it is obviously weaker than the amplitude of the uncompressed boundary reflection wave.

Normalized Cross-Correlation Imaging Conditions

In this study, normalized cross-correlation imaging conditions (Kaelin and Guitton, 2006) are used in the RTM. The realization process employs the zero-delay cross-correlation of the source wavefield to normalize the zero-delay cross-correlation between the forward time wavefield and the reverse time wavefield as

$$I(x,z)=\frac{\sum_{t=0}^{T}(v)^{F}(x,z,t)\cdot(v)^{R}(x,z,t)}{\sum_{t=0}^{T}(v)^{F}(x,z,t)\cdot(v)^{F}(x,z,t)}, \tag{26}$$

where T is the total recording time. $(v)^F$ is the forward time wavefield, and $(v)^R$ is the reverse time wavefield.

When using the above imaging conditions, it is usually necessary to save the forward time wavefield at each time. However, when all the wavefield values are stored on the storage medium, large amount of memory storage space is required and also a long data access time. To overcome this problem, in this study, we implement an effective boundary storage strategy (Clapp, 2008; Wang et al., 2012) based on PML boundary conditions in the pseudo-space-domain. This entails storing the wavefield value of the N-layer grid point (the FD order is 2Nth order) that is adjacent to the central wavefield on each PML boundary during the forward time source wavefield extrapolation, as well as the central wavefield value at the last moment. These boundary wavefield values are taken out as a boundary condition when extrapolating along reverse time, and then, the source wavefield can be rebuilt in the time iteration. Although this method requires the forward time source wavefield extrapolation in advance, this can effectively reduce the storage requirements for the RTM in pseudo-space-domain.

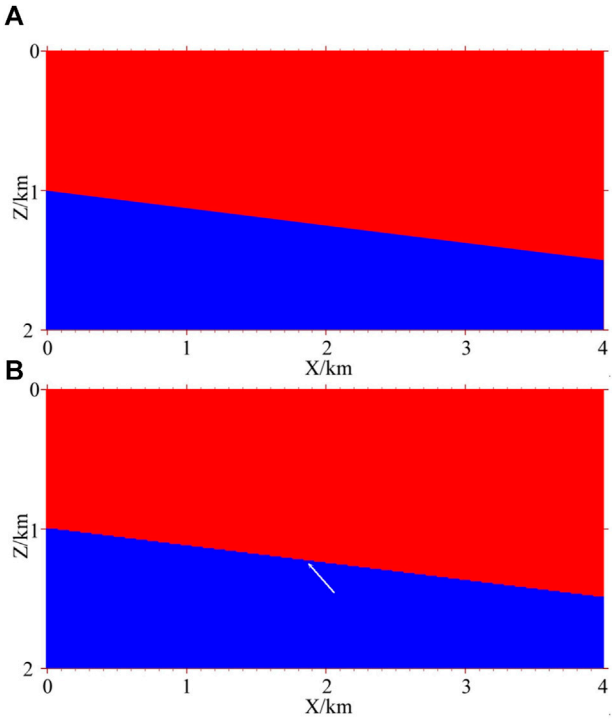

FIGURE 7 | Two-layer velocity model with a dipping interface: **(A)** original model with a smooth dipping interface; **(B)** model with 10 m grid interval.

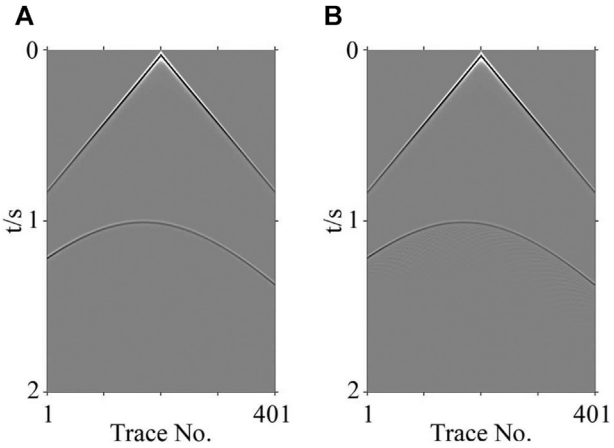

FIGURE 8 | Synthetic shot gather record (76th shot): **(A)** grid interval of 1 m; **(B)** grid interval of 10 m.

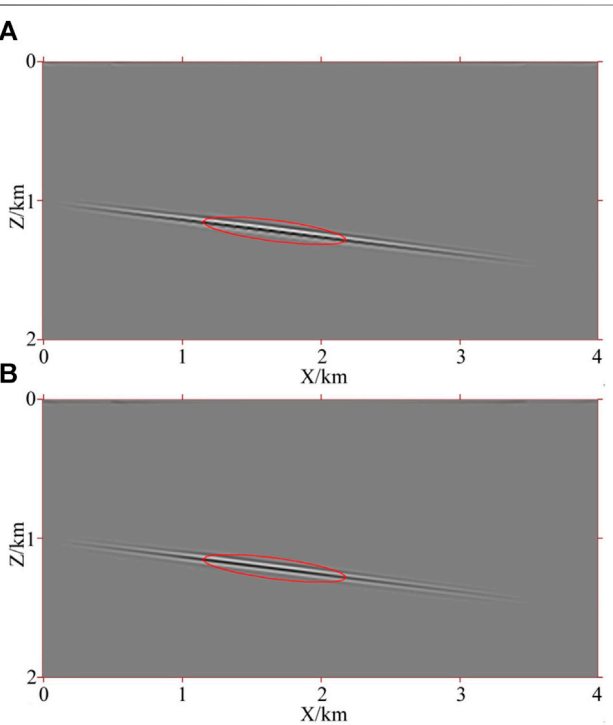

FIGURE 9 | Reverse time migration seismic profile. **(A)** based on the conventional acoustic equation and **(B)** based on the pseudo-space-domain acoustic equation.

MODEL EXPERIMENT

Reverse Time Migration of the Dipping Interface Model

The main purpose of this experiment is to test the validity of pseudo-space-domain acoustic wave equation RTM in solving velocity interface distortion and suppressing false scattering and reflected waves.

The experiment used a two-layer velocity model with a dipping interface, as shown in **Figure 7A**. The horizontal and vertical lengths were 4,000 m and 2000 m, respectively. The primary wave velocities at the upper and lower sides of the interface were 2,500 m/s and 3,500 m/s, respectively. The density was 2000 kg/m^3. The grid model obtained by meshing this interface model with vertical and horizontal grid intervals of 10 m is shown in **Figure 7B**. It can be seen that the original smooth velocity interface has become an obviously stepped interface (white arrow in the figure). In the experiment, a geometry with a fixed position of receivers and changeable source position was established. The shot point was between 500 and 3,480 m, the interval between the shots was 20 m, and a total of 150 shots was made. There were 401 receivers per shot, and each receiver was located between 0 and 4,000 m. The interval between receivers was 10 m. The depths of shots and receivers were both 10 m.

Obviously, to verify the effectiveness of a migration method in solving velocity interface distortion, it is necessary to ensure that the acquired seismic record is accurate. The shot records required for this experiment were obtained by using FD wave equation forward modeling. In theory, only by using a small enough grid spacing can ensure that the obtained shot records are relatively accurate. Therefore, in this study, we first used a model with 1 m grid intervals in both vertical and horizontal directions for forward modeling. (Note that, even if the number of grid points is only doubled, this can cause a huge increase in the amount of

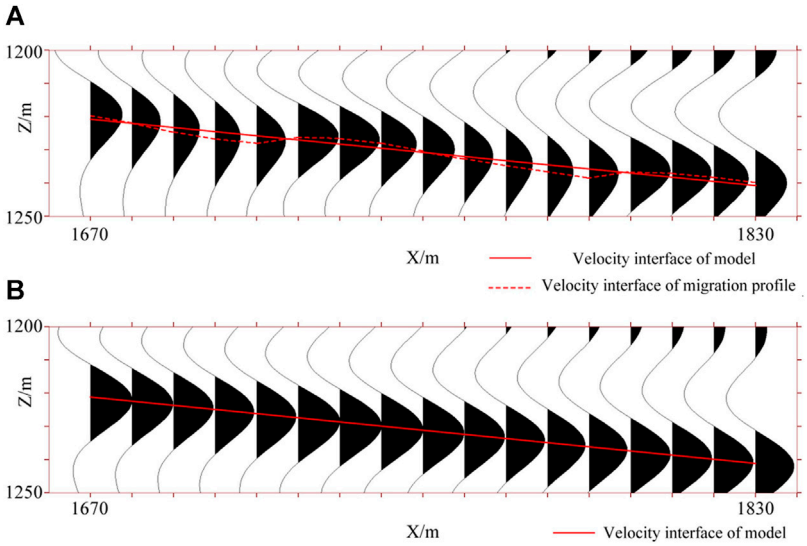

FIGURE 10 | Local magnification of a reverse time migration profile. **(A)** based on the conventional acoustic equation and **(B)** based on the pseudo-space-domain acoustic equation.

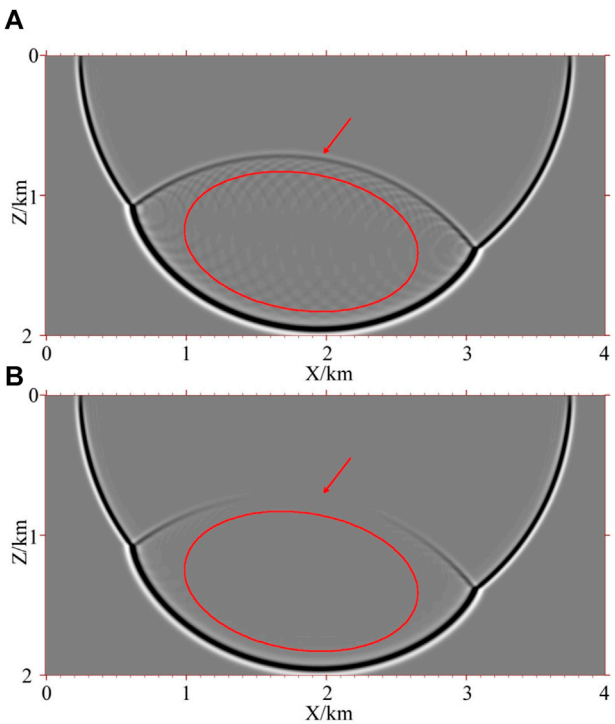

FIGURE 11 | Snapshots of forward time wavefield in reverse time migration (76th shot at 0.9 s). **(A)** based on the conventional acoustic equation and **(B)** based on the pseudo-space-domain acoustic equation.

computation. Therefore, regardless of whether one realizes forward modeling in actual processing or migration and inversion, it is generally unrealistic to use such a small grid interval.) The simulation used a Ricker wavelet with a dominant frequency of 35 Hz. The FD order was 16th order in space and second-order in time, and a total of 150 shots of seismic records was obtained. The record of the 76th shot is shown in **Figure 8A**. For comparison, a record obtained with the grid interval of 10 m is shown in **Figure 8B**, which existed strong artificial scattered waves.

Based on the model of 10 m grid interval as shown in **Figure 7B**, the FD algorithm for the conventional and pseudo-space-domain acoustic wave equations is used for RTM with second-order accuracy in time and sixteenth-order accuracy in both space and pseudo-space. (Note that the pseudo-space-domain RTM needs to add velocity interface information to calculate the traveltime between two grid points.) The migration profiles are, respectively, shown in **Figures 9A,B**.

To more intuitively compare the morphology of the dipping interface in the migration profile of the two methods, the event in the elliptical region in **Figures 9A,B** is magnified, as shown in **Figures 10A,B**. It can be seen that the shape of the dipping interface in the RTM profile of the conventional acoustic wave equation (the red dotted line in **Figure 10A**) is significantly distorted compared with the real interface morphology (the red solid line in **Figure 10A**). The interface shape in the RTM profile of the pseudo-space-domain acoustic wave equation is basically consistent with the real interface morphology (the red solid line in **Figure 10B**). This demonstrates that pseudo-space-domain acoustic wave equation RTM can effectively solve the distortion problem of the velocity interface.

Figures 11A,B show a snapshot of the forward time wavefield of the 76th shot at 0.9 s. It can be seen that there are obvious false scatterings in the wavefield of the conventional acoustic wave equation (as shown in the elliptical region in **Figure 11A**), and there are no obvious false scatterings in the wavefield of the pseudo-space-domain acoustic wave equation (as shown in the elliptical region in **Figure 11B**). By comparing the interface reflections at the arrows in **Figure 11**, we can see that the

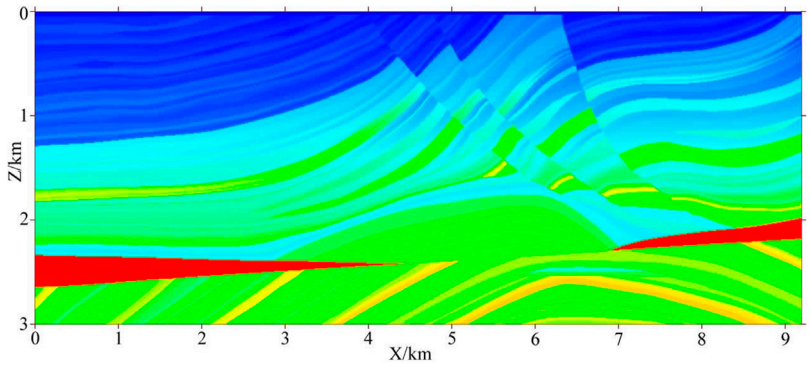

FIGURE 12 | Grid velocity model of Marmousi.

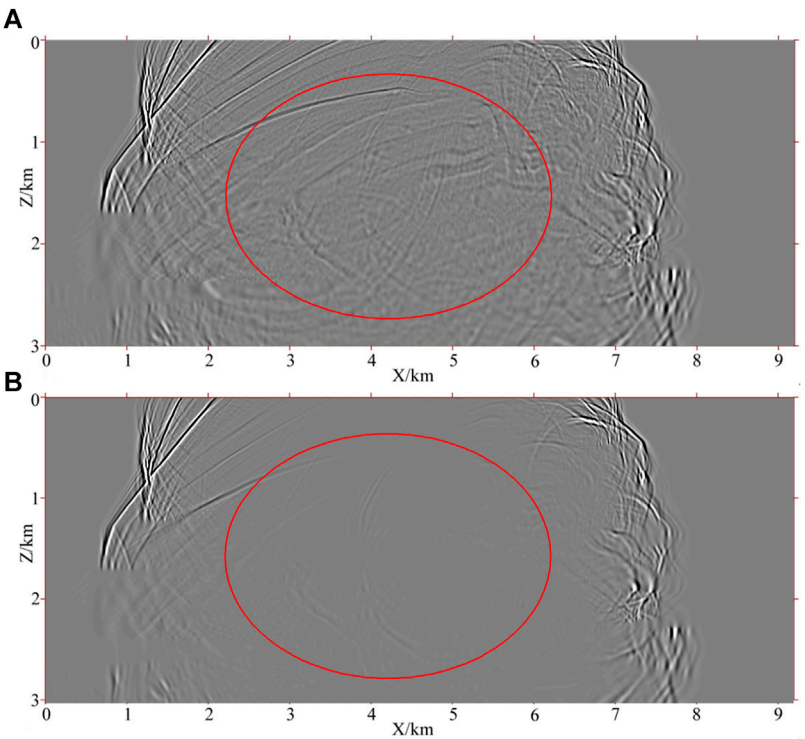

FIGURE 13 | Forward time wavefield snapshots in reverse time migration for the Marmousi model (138th shot at 1.9 s in time). **(A)** based on the conventional acoustic equation and **(B)** based on the pseudo-space-domain acoustic equation.

pseudo-space-domain acoustic wave equation significantly suppresses reflected waves (especially those of near-normal incidence). This demonstrates the effectiveness of the pseudo-space-domain acoustic wave equation in suppressing interfacial false scattering and reflected waves.

Reverse Time Migration of the Marmousi Model

The Marmousi model (shown in **Figure 12**) is a grid velocity model of complex tectonic with numerous velocity interfaces, steep dip structures, and dramatic velocity changes. The model size is 9,200 m * 3,000 m, respectively. The horizontal and vertical grid spacings are, respectively, 5 and 4 m. In the experiment, the unilateral shot geometry used was a seismic source located at the right side and receivers located at the left side. The interval between the shots was 25 m, with 426 shots in total. There were 104 receivers per shot. The depths of the shot and the receivers were both 8 m. The source wavelet used a Ricker wavelet with a dominant frequency of 35 Hz. Synthetic seismograms were simulated by the conventional acoustic wave equation FD method whose FD order was second-order in time and eighth-order in space.

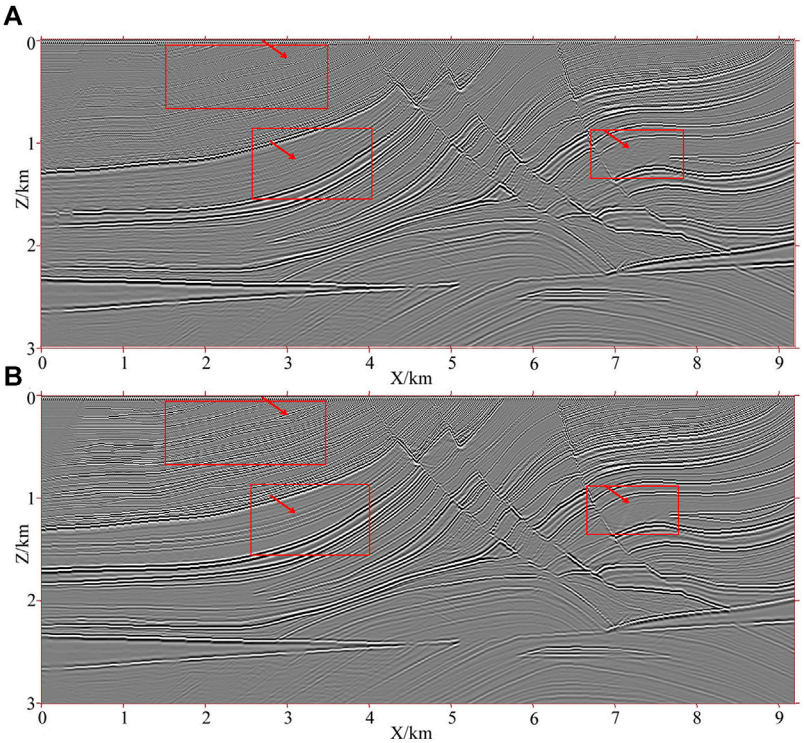

FIGURE 14 | Reverse time migration profile for the Marmousi model. **(A)** based on the conventional acoustic equation and **(B)** based on the pseudo-space-domain acoustic equation.

We applied the conventional acoustic wave equation and pseudo-space-domain acoustic wave equation FD (with FD order being second-order in time and eighth-order in space and pseudo-space) to perform RTM. **Figures 13A,B** show the snapshots of the 138th shot based on the two methods at 1.9 s. **Figures 14A,B** show the RTM profiles based on the two methods, respectively.

Figure 13 shows that the pseudo-space-domain acoustic wave equation has a significantly weakened reflection wave in the wavefield compared with the conventional acoustic wave equation. It indicates the validity of the pseudo-space-domain acoustic wave equation in suppressing reflected waves during wavefield extrapolation.

Comparing the local migration profiles in the red rectangular region in **Figure 14**, we can see that the pseudo-space-domain acoustic wave equation has a clearer structure and better continuity of the event where the arrows point the conventional acoustic wave equation. This demonstrates that the imaging quality of RTM by using the pseudo-space-domain acoustic wave equation is better than that obtained by using a conventional acoustic wave equation.

CONCLUSION AND DISCUSSION

Based on the first-order velocity-stress acoustic wave equation in the pseudo-space-domain, we derived a 2*N*th-order-accuracy staggered-grid FD expression and its PML boundary condition, deduced the stability conditions of the staggered-grid FD expression, and realized RTM in the pseudo-space-domain. At the same time, numerical experiments were carried out based on a dipping interface model and the Marmousi model. Experimental results were as follows:

1) The RTM method based on the pseudo-space-domain acoustic wave equation could solve the problem of velocity interface distortion that appears in the conventional RTM profile.
2) Wavefield extrapolation based on the pseudo-space-domain acoustic wave equation could significantly weaken interface false scattering and reflection waves, thereby further improving the quality of the migration imaging.

Of course, the high-order FD RTM method for the acoustic wave equations in the pseudo-space-domain is not ideal for reflection waves suppression under non-normal incidence. Therefore, the focus of future research work will be the further improvement of the reflection waves suppression effect of the method and accuracy of RTM imaging, along with developing it into the elastic wave equation and the RTM of the three-dimensional wave equation.

DATA AVAILABILITY STATEMENT

The raw data supporting the conclusion of this article will be made available by the authors, without undue reservation.

AUTHOR CONTRIBUTIONS

XZ: writing—original draft. XW: conceptualization, project administration. BL: suggestions. PS: formal analysis. JT: software. CX: methodology.

FUNDING

The authors are grateful for the support of the Shandong Provincial Natural Science Foundation (No. ZR2020QD071), the National Natural Science Foundation of China (No. 42106072; No. 42074138; No.U2006202), the Fundamental Research Funds for the Central Universities (No. 201964016), the Major Scientific and Technological Innovation Project of Shandong Province (No. 2019JZZY010803), and the Taishan Scholar Project Funding (No. tspd20161007).

REFERENCES

Baysal, E., Kosloff, D. D., and Sherwood, J. W. C. (1984). A Two-way Nonreflecting Wave Equation. *Geophysics.* 49 (2), 132–141. doi:10.1190/1.1441644

Chang, W. F., and McMechan, G. A. (1987). Elastic Reverse-Time Migration. *Geophysics.* 52 (10), 1365–1375. doi:10.1190/1.1442249

Chang, W.-F., and McMechan, G. A. (1990). 3D Acoustic Prestack Reverse-Time Migration1. *Geophys. Prospect.* 38 (7), 737–755. doi:10.1111/j.1365-2478.1990.tb01872.x

Chang, W. F., and McMechan, G. A. (1994). 3-D Elastic Prestack, Reverse-Time Depth Migration. *Geophysics.* 59 (4), 597–609. doi:10.1190/1.1443620

Chu, C. L., and Wang, X. T. (2005). Seismic Modeling With a Finite-Difference Method on Irregular Triangular Grids. *Periodical Ocean Univ. China.* 35 (01), 43–48. doi:10.16441/j.cnki.hdxb.2005.01.0.09

Clapp, R. G. (2008). Reverse Time Migration: Saving the Boundaries. *Stanford Exploration Project Tech. Rep.* 136, 136–144.

Clapp, R. G. (2009). Reverse Time Migration with Random Boundaries. *79th Annu. Int. Meet.* (Houston: SEG Expanded Abstract), 2809–2813. doi:10.1190/1.3255432

Du, Q. Z., Zhu, Y. T., Zhang, M. Q., and Gong, X. F. (2013). A Study on the Strategy of Low Wavenumber Noise Suppression for Prestack Reverse-Time Depth Migration. *Chin. J. Geophys.* 56 (7), 2391–2401. doi:10.6038/cjg20130725

He, B. S., Zhang, H. X., and Zhang, J. (2008). Prestack Reverse-Time Depth Migration of Arbitrarily Wide-Angle Wave Equations. *Acta Seismologica Sinica.* 30 (5), 491–499. doi:10.3321/j.issn:0253-3782.2008.05.007

Huang, C., and Dong, L. G. (2009). High-Order FD Method in Seismic Wave Simulation With Variable Grids and Local Time-Steps. *Chin. J. Geophys.* 52 (11), 176–186. doi:10.3969/j.issn.0001-5733.2009.11.022

Kaelin, B., and Guitton, A. (2006). Imaging Condition for Reverse Time Migration. *76th Annu. Int. Meet.* (New Orleans: SEG Expanded Abstract), 2594–2598. doi:10.1190/1.2370059

Lan, H., Zhang, Z., Chen, J., and Liu, Y. (2014). Reverse Time Migration from Irregular Surface by Flattening Surface Topography. *Tectonophysics.* 627, 26–37. doi:10.1016/j.tecto.2014.04.015

Li, H., Li, J., Gu, N., Gao, J., and Zhang, H. (2020). Ambient Noise Surface Wave Reverse Time Migration for Fault Imaging. *J. Geophys. Res. Solid Earth.* 125, e2020JB020381. doi:10.1029/2020JB020381

Li, Y., Choi, Y., Alkhalifah, T., Li, Z., and Zhang, K. (2018). Full-Waveform Inversion Using a Nonlinearly Smoothed Wavefield. *Geophysics.* 83 (2), R117–R127. doi:10.1190/geo2017-0312.1

Liu, F., Zhang, G., Morton, S. A., and Leveille, J. P. (2011). An Effective Imaging Condition for Reverse-Time Migration Using Wavefield Decomposition. *Geophysics.* 76 (1), S29–S39. doi:10.1190/1.3533914

Liu, H. W., Li, B., Liu, H., Tong, X. L., and Liu, Q. (2010). The Algorithm of High Order Finite Difference Pre-stack Reverse Time Migration and GPU Implementation. *Chin. J. Geophys.* 53 (7), 600–610. doi:10.1002/cjg2.1530

Liu, Q., Zhang, J., and Gao, H. (2016). Reverse-Time Migration From Rugged Topography Using Irregular, Unstructured Mesh. *Geophys. Prospecting.* 65 (2), 453–466. doi:10.1111/1365-2478.12415

Liu, Q., and Zhang, J. (2020). Topography Least-Squares Reverse-Time Migration Based on Adaptive Unstructured Mesh. *Surv. Geophys.* 41, 343–361. doi:10.1007/s10712-019-09578-0

Liu, X. X., Yin, X. Y., and Liu, B. H. (2013). Prestack Reverse Time Migration of Elastic Waves in Porous media. *Prog. Geophys.* 28 (6), 3165–3173. doi:10.6038/pg20130643

McMechan, G. A. (1983). Migration by Extrapolation of Time-dependent Boundary Values. *Geophys. Prospect.* 31 (3), 413–420. doi:10.1111/j.1365-2478.1983.tb01060.x

Moradpouri, F., Moradzadeh, A., Pestana, R., Ghaedrahmati, R., and Soleimani Monfared, M. (2017). An Improvement in Wavefield Extrapolation and Imaging Condition to Suppress Reverse Time Migration Artifacts. *Geophysics.* 82 (6), S403–S409. doi:10.1190/geo2016-0475.1

Qu, Y., Guan, Z., and Li, Z. (2019). Topographic Elastic Least-squares Reverse Time Migration Based on Vector P- and S-wave Equations in the Curvilinear Coordinates. *Geophys. Prospecting.* 67 (5), 1271–1295. doi:10.1111/1365-2478.12775

Shi, Y., Ke, X., and Zhang, Y. Y. (2015). Analyzing the Boundary Conditions and Storage Strategy for Reverse Time Migration. *Prog. Geophys.* 30 (2), 581–585. doi:10.6038/pg20150214

Shragge, J. (2014). Reverse Time Migration from Topography. *Geophysics.* 79 (4), S141–S152. doi:10.1190/GEO2013-0405.1

Song, P. (2005). *Accurate Absorbing Boundary Conditions and Reverse-Time Migration of Acoustic Wave Equation Using Non-reflecting Recursive Algorithm: [Master's Thesis]*. Qingdao: Ocean University of China.

Song, P., Zhu, B., Li, J. S., and Tan, J. (2015). Reverse Time Migration of Divided-Order Multiples. *Chin. J. Geophys.* 58 (10), 3791–3803. doi:10.6038/cjg20151029

Sun, R., and McMechan, G. A. (2001). Scalar Reverse-Time Depth Migration of Prestack Elastic Seismic Data. *Geophysics.* 66 (5), 1519–1527. doi:10.1190/1.1487098

Virieux, J. (1984). SH-Wave Propagation in Heterogeneous Media: Velocity-Stress Finite-Difference Method. *Geophysics.* 49 (11), 1933–1942. doi:10.1190/1.1441605

Wang, B. L., Gao, J. H., Chen, W. C., and Zhang, H. L. (2012). Efficient Boundary Storage Strategies for Seismic Reverse Time Migration. *Chin. J. Geophys.* 55 (07), 2412–2421. doi:10.6038/j.issn.0001-5733.2012.07.025

Wang, X., Xia, D., Li, J., Tang, Q., and Jiang, X. (2005). Model Based Processing (III): Pseudo-Space Reverse Time Migration. *75th Annu. Int. Meet.* (Houston: SEG Expanded Abstract), 1838–1841. doi:10.1190/1.2148060

Whitmore, N. D. (1983). Iterative Depth Migration by Backward Time Propagation. *53rd Annu. Int. Meet.* (Las Vegas: SEG Expanded Abstract), 382–386. doi:10.1190/1.1893867

Willacy, C., and Kryvohuz, M. (2019). Reverse Time Migration of Transmitted Wavefields for Salt Boundary Imaging. *Geophysics.* 84 (2), S71–S82. doi:10.1190/geo2018-0182.1

Yan, H. Y. (2012). *Study on Seismic Wave Field Numerical Simulation and Prestack Reverse Time Migration Method in Viscoelastic Medium: [PhD Thesis]*. Beijing: China University of Petroleum.

Yoon, K., and Marfurt, K. J. (2006). Reverse-Time Migration Using the Poynting Vector. *Exploration Geophys.* 37 (1), 102–107. doi:10.1071/EG06102

Zhang, H. X., and Ning, S. N. (2002). Pre-Stack Reverse Time Migration of Elastic Wave Equation. *J. China Univ. Mining Technology.* 31 (5), 371–375. doi:10.3321/j.issn:1000-1964.2002.05.008

Zhang, X. B., Song, P., Li, J. S., Tan, J., Liu, Z. L., and Xia, D. M. (2016). Analysis of the Impactof the Theoretical Reflection Coefficient on the Perfectly Matched Layer Absorbing Boundary. *Periodical of Ocean University of China.* 46 (06), 84–89. doi:10.16441/j.cnki.hdxb.20150190

Zhou, H. W., Hu, H., Zou, Z., Wo, Y., and Youn, O. (2018). Reverse Time Migration: a Prospect of Seismic Imaging Methodology. *Earth-Science Rev.* 179 (2018), 207–227. doi:10.1016/j.earscirev.2018.02.008

Zhu, S. W., Qu, S. L., Wei, X. C., and Liu, C. Y. (2007). Numeric Simulation by Grid-Various Finite-Difference Elastic Wave Equation. *Oil Geophys. Prospecting.* 42 (06), 634–639. doi:10.3321/j.issn:1000-7210.2007.06.006

Zhu, S. W., and Wei, X. C. (2005). Differential Forward Modeling of Wave Equation Having Irregular Grid and Any-Order Precision. *Oil Geophys. Prospecting.* 40 (02), 149–153. doi:10.3321/j.issn:1000-7210.2005.02.012

Conflict of Interest: The authors declare that the research was conducted in the absence of any commercial or financial relationships that could be construed as a potential conflict of interest.

frontiers in Earth Science

ORIGINAL RESEARCH
published: 27 October 2021
doi: 10.3389/feart.2021.732123

Angle-Weighted Reverse Time Migration With Wavefield Decomposition Based on the Optical Flow Vector

Chuang Xie[1], *Peng Song*[1,2,3]*, *Xishuang Li*[2,4], *Jun Tan*[1,2,3], *Shaowen Wang*[1] *and Bo Zhao*[1,2,3]

[1]College of Marine Geo-Sciences, Ocean University of China, Qingdao, China, [2]Laboratory for Marine Mineral Resources, Pilot National Laboratory for Marine Science and Technology, Qingdao, China, [3]Key Laboratory of Submarine Geosciences and Prospecting Techniques Ministry of Education, Qingdao, China, [4]The First Institute of Oceanography, Ministry of National Resources, Qingdao, China

Reverse time migration (RTM) is based on the two-way wave equation, so its imaging results obtained by conventional zero-lag cross-correlation imaging conditions contain a lot of low-wavenumber noises. So far, the wavefield decomposition method based on the Poynting vector has been developed to suppress these noises; however, this method also has some problems, such as unstable calculation of the Poynting vector, low accuracy of wavefield decomposition, and poor effect of large-angle migration artifacts suppression. This article introduces the optical flow vector method to RTM to realize high-precision wavefield decomposition for both the source and receiver wavefields and obtains four directions of wavefields: up-, down-, left-, and right-going. Then, the cross-correlation imaging sections of one-way propagation components of forward- and back-propagated wavefields are optimized and stacked. On this basis, the reflection angle of each imaging point is calculated based on the optical flow vector, and an attenuation factor related to the reflection angle is introduced as the weight to generate the optimal stack images. The tests of theoretical model and field marine seismic data illustrate that compared with the conventional RTM with wavefield decomposition based on the Poynting vector, the angle-weighted RTM with wavefield decomposition based on the optical flow vector proposed in this article can achieve wavefield decomposition for both the source and receiver wavefields and calculate the reflection angle of each imaging point more accurately and stably. Moreover, the proposed method adopts angle weighting processing, which can further eliminate large-angle migration artifacts and effectively improve the imaging accuracy of RTM.

Keywords: reverse time migration, low-wavenumber noise, wavefield decomposition, optical flow vector, angle weighting

OPEN ACCESS

Edited by:
Wei Zhang,
Southern University of Science and Technology, China

Reviewed by:
Changsoo Shin,
Seoul National University, South Korea
Lianjie Huang,
Los Alamos National Laboratory (DOE), United States

***Correspondence:**
Peng Song
pengs@ouc.edu.cn

Specialty section:
This article was submitted to Solid Earth Geophysics, a section of the journal Frontiers in Earth Science

Received: *28 June 2021*
Accepted: *17 September 2021*
Published: *27 October 2021*

Citation:
Xie C, Song P, Li X, Tan J, Wang S and Zhao B (2021) Angle-Weighted Reverse Time Migration With Wavefield Decomposition Based on the Optical Flow Vector. Front. Earth Sci. 9:732123. doi: 10.3389/feart.2021.732123

INTRODUCTION

Reverse time migration (RTM) was proposed in the 1980s (Baysal, 1983; McMechan, 1983; Whitmore, 1983), which is based on a two-way wave equation and applies zero-lag cross-correlation imaging conditions to realize imaging. Theoretically, RTM can adapt to any complex velocity model without dip limitations and image nearly all kinds of waves, including refractions,

prismatic waves, diffractions, and multiples, so it is considered to be the most accurate imaging algorithm and has been widely used in the field data processing (Sun et al., 2015; Oh et al., 2018; Qu et al., 2020; Fee et al., 2021). However, due to using the two-way wave equation to implement wavefield continuation, the backward reflection will occur when the seismic wave propagates to the reflection interface. The conventional zero-lag cross-correlation imaging conditions directly use all forward- and back-propagated wavefields to form subsurface images (Du et al., 2013; Chen and He, 2014; Fei et al., 2015), which could inevitably produce a lot of low-wavenumber migration artifacts.

At present, three main methods can be used to reduce the migration artifacts in RTM. The first one is a backward reflection suppression method, which usually employs the nonreflecting acoustic equation to imaging. Baysal (1984) has first proposed a nonreflecting acoustic equation based on an assumption of constant wave impedance, which can significantly suppress the backward reflection of the vertical incident seismic waves. Song (2005) has improved the nonreflecting acoustic equation to enhance the suppression effect of backward reflection. However, in general, the backward reflection suppression effect is not ideal, and it is difficult to achieve the purpose of effectively eliminating migration artifacts. The second one is the filtering method. Mulder and Plessix (2004) have directly used high-pass filtering to denoise the imaging section. Zhang and Sun (2009) have applied Laplacian filtering to filter the results of RTM. However, this kind of method has problems such as difficulty in determining the threshold, damage to the effective signal, and incomplete noises removal. The third one is to modify the imaging conditions. There are two kinds of methods used to modify the imaging conditions usually. One is the angle weighting method proposed by Yoon and Marfurt (2006), which can effectively remove the large-angle migration artifacts by introducing an attenuation factor related to the reflection angle into the imaging conditions. The other is the wavefield decomposition method, which decomposes the source and receiver wavefields into going wavefields in different directions and then extracts the effective wavefield components to form images to achieve the accurate imaging of underground structures. Some scholars (Liu et al., 2011; Fei et al., 2015; Wang et al., 2016) have successively applied the Hilbert transform to realize wavefield decomposition and obtained high-precision imaging sections. However, when the Hilbert transform is applied to wavefield decomposition, a certain amount of the computational cost is required. Chen and He (2014) have used the Poynting vector to decompose the source and receiver wavefields in the four directions of up, down, left, and right, which can greatly improve the suppression effect of low-wavenumber noises with small additional computation cost. Therefore, this method has been widely used (Wang and He, 2017; Liu, 2019; Li and He, 2020; Wang et al., 2021). However, there are also two problems in wavefield decomposition based on the Poynting vector method. First, it is not accurate enough for the Poynting vector method to indicate all directions of seismic wave propagation (Du et al., 2012; Zhang, 2014; Duan and Sava, 2015; Li and He, 2020) and the second is that there are always some singularities in the Poynting vector.

The optical flow method was first proposed to solve the motion information problem of objects between adjacent frames (Horn and Schunck, 1981; Lucas and Kanade, 1981), and then it was introduced to RTM (Hu et al., 2014; Zhang, 2014; Gong et al., 2016; Zhang et al., 2018; Wu et al., 2021). Compared with the Poynting vector, the optical flow vector is a more accurate vector that is closer to the real wavefield propagation direction. Moreover, there is no singularity in the optical flow vector. In this article, the optical flow vector method is introduced into RTM to decompose wavefields and calculate the reflection angle of each imaging point underground. Based on the optical flow vector method, both source and receiver wavefields can be decomposed accurately and the accurate reflection angle of each imaging point underground can be obtained; then, by the introduction of an attenuation factor related to the reflection angles, the angle-weighted RTM with wavefield decomposition based on the optical flow vector is implemented, which greatly improves RTM imaging.

In the next section, we review the wavefield continuation of RTM based on the acoustic wave equation. In *Wavefield Decomposition Based on the Optical Flow Vecto*r, the wavefield decomposition based on the optical flow vector method is introduced and some tests are given to compare the effects of wavefield decomposition for the Poynting vector method and the optical flow vector method. In *Angle-Weighted RTM Imaging Based on the Optical Flow Vector*, we show how to calculate the reflection angle of each imaging point underground based on the optical flow vector method and how to produce the final RTM image using an attenuation factor related to the reflection angles. In *Numerical Tests on the Marmousi Model* and *Field Marine Seismic Data Imaging*, we present some tests to show the imaging effect of the method developed in the article. We end with some concluding remarks in *Conclusion*.

WAVEFIELD CONTINUATION OF RTM

The first-order stress-velocity acoustic wave equation in a two-dimensional isotropic medium can be expressed as follows:

$$\begin{cases} \dfrac{\partial v_x}{\partial t} = \dfrac{1}{\rho}\dfrac{\partial p}{\partial x} \\ \dfrac{\partial v_z}{\partial t} = \dfrac{1}{\rho}\dfrac{\partial p}{\partial z} \\ \dfrac{\partial p}{\partial t} = \rho v^2\left(\dfrac{\partial v_x}{\partial x} + \dfrac{\partial v_z}{\partial z}\right) \end{cases}, \tag{1}$$

where x and z represent the space coordinates, respectively; v_x and v_z denote the practical vibration velocity in the x and z direction, respectively; t is the time; ρ signifies the density; v represents the velocity of the acoustic wave; p denotes the stress.

We use staggered grids to discretize **Eq. 1** by finite-difference for realizing forward wavefield continuation and reverse time wavefield continuation. Taking forward continuation as an example, the high-order difference schemes of **Eq. 1** can be written as follows:

$$\begin{cases} v_x^k(i+1/2,j) = v_x^{k-1}(i+1/2,j) + \dfrac{\Delta t}{\rho(i,j)\Delta x}\sum\limits_{m=1}^{N} C_m\left[p^{k-1/2}(i+m,j) - p^{k-1/2}(i-m+1,j)\right] \\ v_z^k(i,j+1/2) = v_z^{k-1}(i,j+1/2) + \dfrac{\Delta t}{\rho(i,j)\Delta z}\sum\limits_{m=1}^{N} C_m\left[p^{k-1/2}(i,j+m) - p^{k-1/2}(i,j-m+1)\right] \\ p^{k+1/2}(i,j) = p^{k-1/2}(i,j) + \rho(i,j)v^2(i,j)\dfrac{\Delta t}{\Delta x}\sum\limits_{m=1}^{N} C_m\left[v_x^k(i+m-1/2,j) - v_x^k(i-m+1/2,j)\right] \\ +\rho(i,j)v^2(i,j)\dfrac{\Delta t}{\Delta z}\sum\limits_{m=1}^{N} C_m\left[v_z^k(i,j+m-1/2) - v_z^k(i,j-m+1/2)\right], \end{cases} \tag{2}$$

where k represents the temporal discrete point number, i and j denote the spatial discrete point numbers in the x and z direction, respectively. Δt is the time discrete step; Δx and Δz are the spatial discrete steps in the x and z directions, respectively. N denotes half of the accuracy of spatial difference, and C_m is the difference coefficients.

In wavefield continuation based on the finite-difference method, artificial boundaries have been used in practice to suppress boundary reflection. To eliminate the boundary reflection, the perfectly matched layer (PML) method is used here. PML boundary algorithm has been widely studied (Berenger, 1994; Collino and Tsogka, 2001; Zhang and Shen, 2010), so we do not discuss it in detail.

WAVEFIELD DECOMPOSITION BASED ON THE OPTICAL FLOW VECTOR

The Poynting vector, also known as the energy flux density vector, was first applied in the field of electromagnetic computing (Poynting, 1884). Now, it has become a common algorithm used to indicate the propagation direction of wavefields in seismic wavefield calculation (Yoon and Marfurt, 2006; Tang et al., 2017).

The Poynting vector of the first-order stress-velocity acoustic wave equation can be expressed as follows:

$$\mathbf{P}^y = -\nabla u\frac{\partial u}{\partial t} = \left(-pv_x, -pv_z\right) = \left(P_x^y, P_z^y\right), \tag{3}$$

where u represents the wavefields, P_z^y and P_z^y are the horizontal and vertical components of the Poynting vector, respectively, and ∇ denotes the gradient operator. We can obtain, using the Poynting vector, the up-, down-, left-, and right-going wavefields after wavefield decomposition. Taking the wavefield decomposition of source wavefields as an example, the specific expression can be represented as follows:

$$\begin{aligned} S_u(x,z,t) &= \begin{cases} S(x,z,t) & if\ P_z^y < 0 \\ 0 \end{cases} \\ S_d(x,z,t) &= \begin{cases} S(x,z,t) & if\ P_z^y \geq 0 \\ 0 \end{cases} \\ S_l(x,z,t) &= \begin{cases} S(x,z,t) & if\ P_x^y < 0 \\ 0 \end{cases} \\ S_r(x,z,t) &= \begin{cases} S(x,z,t) & if\ P_x^y \geq 0 \\ 0 \end{cases} \end{aligned}, \tag{4}$$

where $S_u(x, z, t)$, $S_d(x, z, t)$, $S_l(x, z, t)$, and $S_r(x, z, t)$ are the up-, down-, left- and right-going source wavefields, respectively. It can be seen from **Eq. 3** that the calculation of the Poynting vector is composed of the product of the time derivative and the space derivative of the wavefield. When the time derivative or the space derivative is zero, the Poynting vector must be zero too, which causes instability. Furthermore, Zhang et al. (2014) have pointed out that the Poynting vector itself is difficult to indicate the propagation direction of the wavefield with high accuracy.

The optical flow vector is a vector that is obtained by several iterations and can indicate the propagation direction of the wavefield stably and accurately. Therefore, we introduce the optical flow vector into the wavefield decomposition process of RTM. In the two-dimensional RTM, the fundamental assumption for the optical flow problem is that the wavefield u at a spatial point (x, z) is continuous for very small variations in space (dx and dz) and time (dt), and its expression is as follows:

$$u(x+dx, z+dz, t+dt) = u(x,z,t), \tag{5}$$

where u denotes the wavefields, x and z represent the space coordinates, respectively, and t is time. We use the Taylor formula to expand $u(x + dx, z + dz, t + dt)$ and discard higher-order terms above the second order and obtain

$$u_x P_x^o + u_z P_z^o + u_t = 0, \tag{6}$$

where u_x and u_z are the spatial derivatives of wavefields, u_t is the time derivatives of wavefields, and P_x^o and P_z^o are the orthogonal (x and z) components of the optical flow vector, respectively. With two unknowns (P_x^o and P_z^o) and only one **Eq. 6**, the problem is ill-posed and the solution is nonunique. To address this underdetermined problem (**Eq. 6**), the regularization terms of global smooth constraints are introduced by requiring that neighboring points have similar flow directions as that at a central target point. Therefore, we construct the following misfit function:

$$E = \iint\left[\left(u_x P_x^o + u_z P_z^o + u_t\right)^2 + \alpha^2 C\right]dxdz, \tag{7}$$

where C is the regularization terms, which can be written as follows:

$$C = \nabla^2 P_x^o + \nabla^2 P_z^o, \tag{8}$$

where ∇^2 is the Laplacian operator and α is a weighting factor of the regularization term, generally taken as 1. **Equation 7** can be solved using an iterative least-squares approach, in which the update parameters are computed as follows:

$$\begin{cases} \left(P_x^o\right)^{n+1} = \left(\bar{P}_x^o\right)^n - \dfrac{u_x\left[u_x\left(\bar{P}_x^o\right)^n + u_z\left(\bar{P}_z^o\right)^n + u_t\right]}{\alpha^2 + u_x^2 + u_z^2} \\ \left(P_z^o\right)^{n+1} = \left(\bar{P}_z^o\right)^n - \dfrac{u_z\left[u_x\left(\bar{P}_x^o\right)^n + u_z\left(\bar{P}_z^o\right)^n + u_t\right]}{\alpha^2 + u_x^2 + u_z^2} \end{cases}, \tag{9}$$

where $\bar{P}_x^o$ and $\bar{P}_z^o$ are the local average values of the horizontal and vertical components of the optical flow vector, respectively, and n is the number of iterations. From **Eqs 7**, **8**, and **9**, it can be seen that the optical flow vector is no longer a simple vector generated by multiplying the time derivative and the spatial

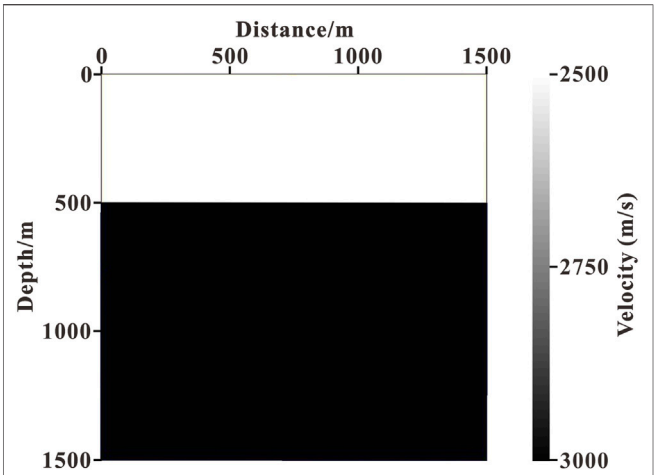

FIGURE 1 | A two-layer velocity model.

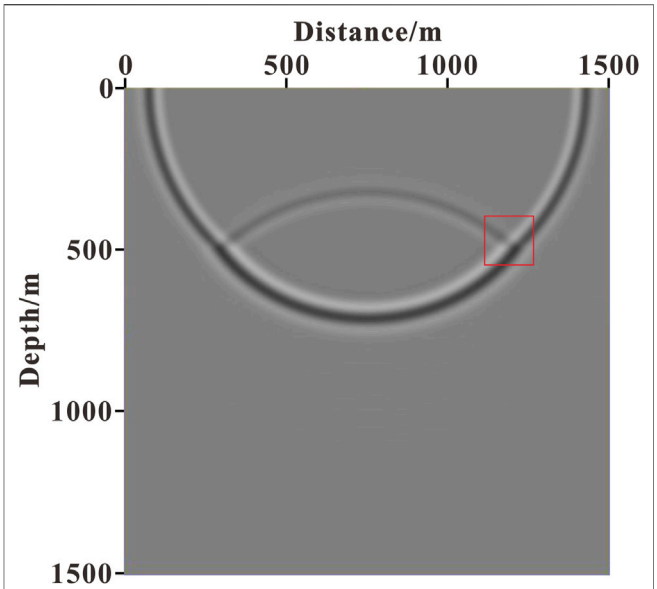

FIGURE 2 | The source wavefield snapshot at 0.3 s.

derivative of the wavefield directly, but an accurate vector obtained by several iterative operations based on an initial optical flow vector, so it is closer to the real propagation direction information of the wavefield. Besides, because of the addition of the regularization term in the calculation process of the optical flow vector, only when the time derivative and space derivative are both zero, the optical flow vector is zero, which avoids the instability effectively in the calculation process of the optical flow vector.

The feasibility and accuracy of the method are first evaluated using a two-layer velocity model (as shown in **Figure 1**). The size of the homogeneous medium model is 1,500 m in length and 1,500 m in depth. The velocity of the first layer is 2,500 m/s and the second layer is 3,000 m/s. A Ricker wavelet with a dominant frequency of 30 Hz is used as the source, which is excited at (750 m, 0 m). The grid interval in the x and z directions is 5 m. The finite-difference accuracy of wavefield continuation is tenth order in space. The time sampling step is 0.5 ms and the maximum recording time is 0.8 s. **Figure 2** illustrates the source wavefield snapshot at 0.3 s. **Figures 3A,B**, respectively, show the wavefield direction near the reflection interface (indicated by the red box in **Figure 2**) calculated using the Poynting vector and the optical flow vector. **Figures 4A,B** contain the horizontal components of the Poynting vector and the optical flow vector at this time, respectively. The left-going wavefield obtained by wavefield decomposition based on the Poynting vector and the optical flow vector are plotted in **Figures 5A,B**.

From **Figures 3A,B** (indicated by the red circle) and **Figures 4A,B** (indicated by the red arrow), it can be seen that accurately indicating the propagation direction of the wavefield using the Poynting vector is challenging and singular values are prone to appear, whereas the optical flow vector is smoother and the instability phenomenon is avoided effectively. Comparing **Figures 5A,B**, we can see that for the wavefield decomposition achieved based on the Poynting vector, some other wavefield components as indicated by the arrow appear because the Poynting vector calculation is inaccurate and unstable, whereas the optical flow vector does not generate other wavefield components, so the decomposed wavefield is more accurate.

ANGLE-WEIGHTED RTM IMAGING BASED ON THE OPTICAL FLOW VECTOR

Based on the optical flow vector, we use **Eq. 10** to decompose the source and receiver wavefields in the four directions of up, down, left, and right:

$$
\begin{aligned}
S_u(x,z,t) &= \begin{cases} S(x,z,t) & if\ P_z^o < 0 \\ 0 \end{cases} \\
S_d(x,z,t) &= \begin{cases} S(x,z,t) & if\ P_z^o \geq 0 \\ 0 \end{cases} \\
S_l(x,z,t) &= \begin{cases} S(x,z,t) & if\ P_x^o < 0 \\ 0 \end{cases} \\
S_r(x,z,t) &= \begin{cases} S(x,z,t) & if\ P_x^o \geq 0 \\ 0 \end{cases} \\
R_u(x,z,t) &= \begin{cases} R(x,z,t) & if\ P_z^o < 0 \\ 0 \end{cases} \\
R_d(x,z,t) &= \begin{cases} R(x,z,t) & if\ P_z^o \geq 0 \\ 0 \end{cases} \\
R_l(x,z,t) &= \begin{cases} R(x,z,t) & if\ P_x^o < 0 \\ 0 \end{cases} \\
R_r(x,z,t) &= \begin{cases} R(x,z,t) & if\ P_x^o \geq 0 \\ 0 \end{cases}
\end{aligned}
, \tag{10}
$$

where $S_u(x,z,t)$, $S_d(x,z,t)$, $S_l(x,z,t)$, and $S_r(x,z,t)$ denote the up-, down-, left-, and right-going source wavefields, respectively, and $R_u(x,z,t)$, $R_d(x,z,t)$, $R_l(x,z,t)$, and $R_r(x,z,t)$ represent the up-, down-, left-, and right-going wavefields of receivers, respectively.

The decomposed wavefields of both sources and receivers in the opposite direction are selected for imaging separately to avoid migration artifacts (Chen and He, 2014), using the following:

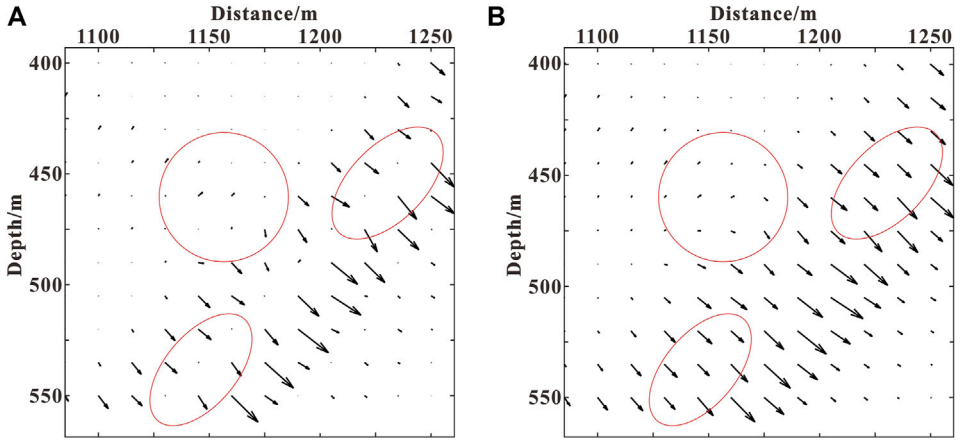

FIGURE 3 | The wavefield direction near the reflection interface calculated: **(A)** based on the Poynting vector; **(B)** based on the optical flow vector.

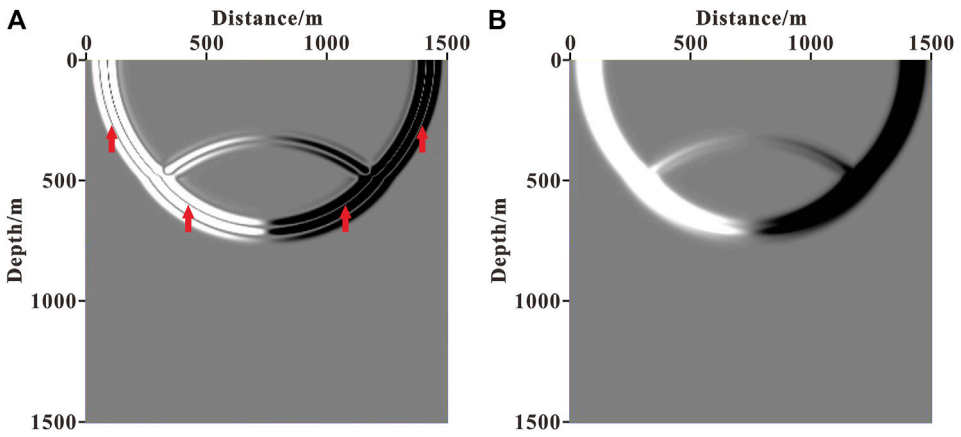

FIGURE 4 | Horizontal components: **(A)** the Poynting vector; **(B)** the optical flow vector.

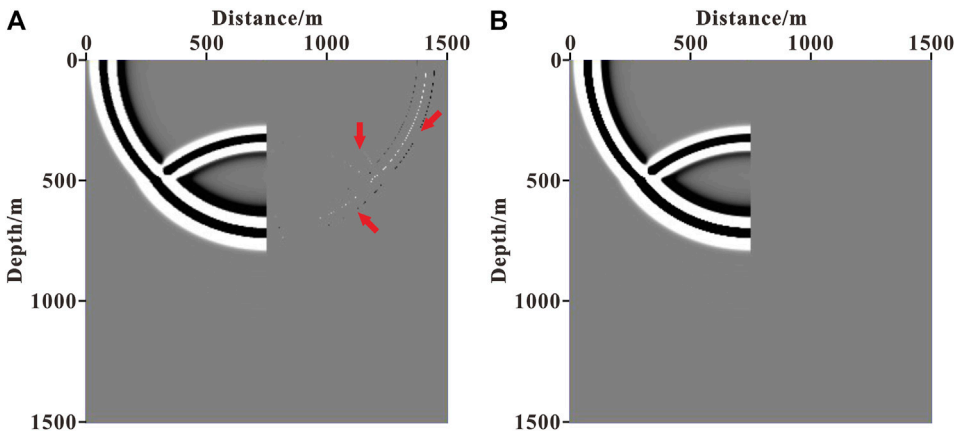

FIGURE 5 | Left-going wavefield after decomposition: **(A)** based on the Poynting vector; **(B)** based on optical flow vector.

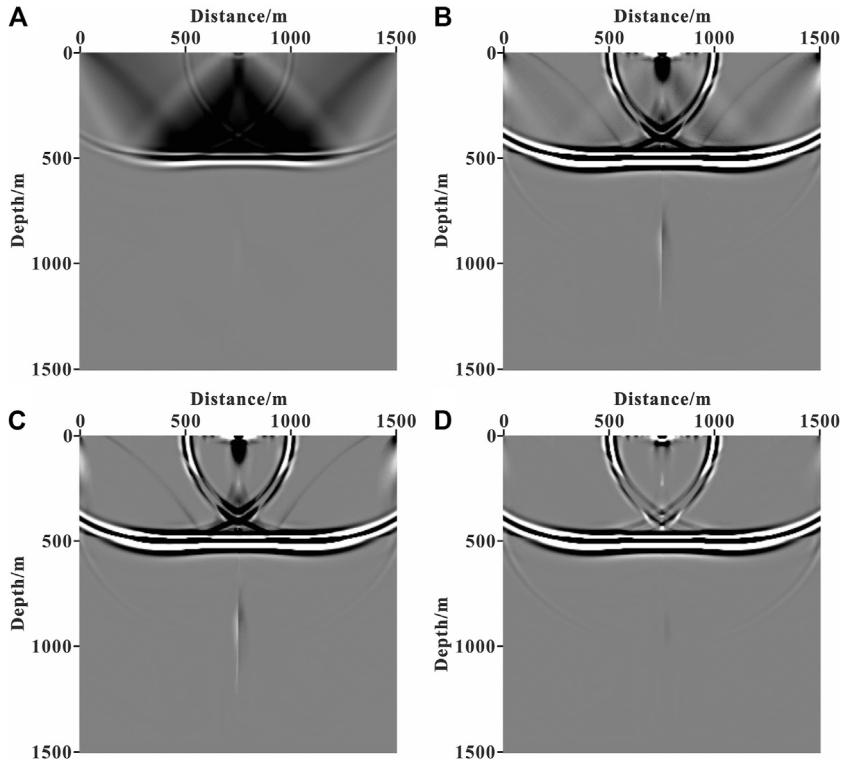

FIGURE 6 | The imaging result of RTM: **(A)** conventional RTM; **(B)** RTM with wavefield decomposition based on the Poynting vector; **(C)** RTM with wavefield decomposition based on the optical flow vector; **(D)** angle-weighted RTM with wavefield decomposition based on the optical flow vector.

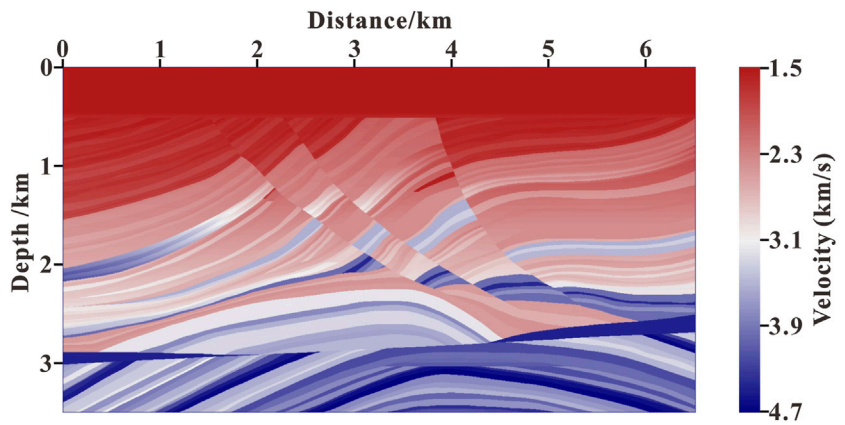

FIGURE 7 | The local velocity model of the Marmousi-II model.

$$I_{op}(x,z) = \frac{\sum_t S_u(x,z,t)R_d(x,z,t) + \sum_t S_d(x,z,t)R_u(x,z,t)}{\sum_t S^2(x,z,t)} + \frac{\sum_t S_l(x,z,t)R_r(x,z,t) + \sum_t S_r(x,z,t)R_l(x,z,t)}{\sum_t S^2(x,z,t)}, \quad (11)$$

where I_{op} (x, z) is the optimal stack section. However, in fact, the migration artifacts are mainly distributed in the large-angle region (Yoon and Marfurt, 2006; Zhang et al., 2014; Zhang et al., 2020). Although the method of selecting the wavefields in the opposite direction for imaging can reduce the migration artifacts of 180° or close to 180°, the suppression effect on the migration artifacts coming from other large-angle regions is

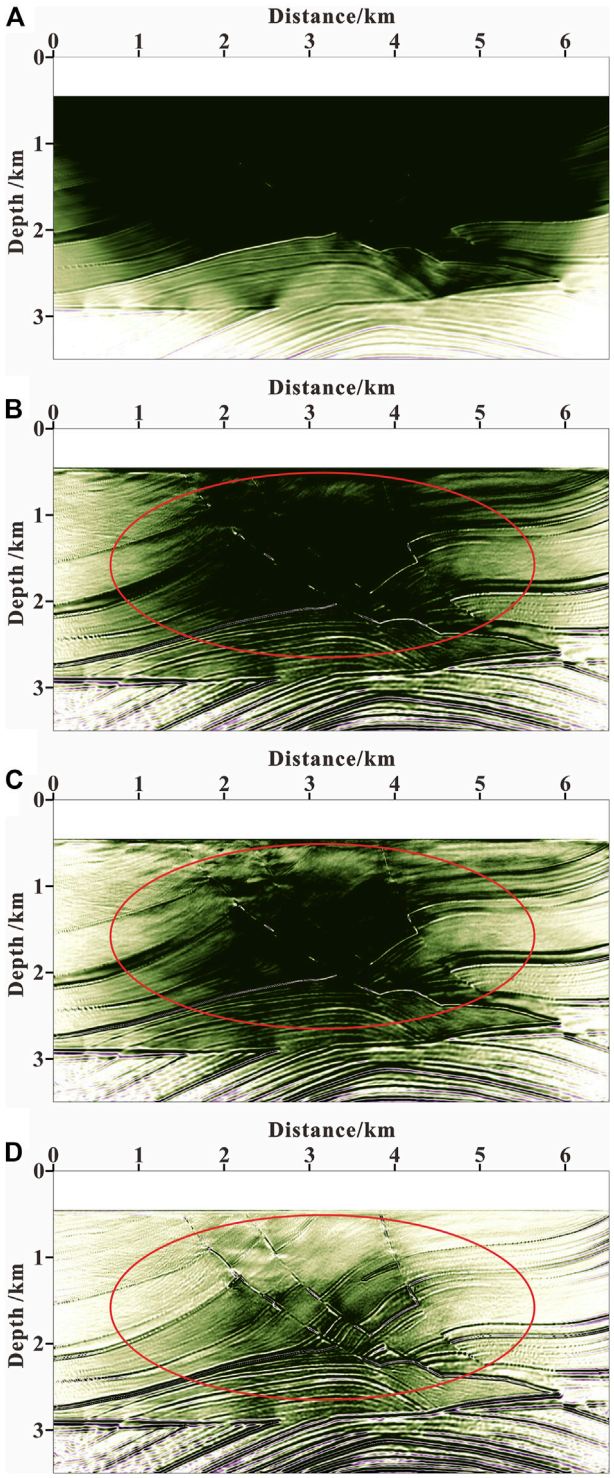

FIGURE 8 | RTM section for Marmousi-II model: **(A)** conventional RTM; **(B)** RTM with wavefield decomposition based on the Poynting vector; **(C)** RTM with wavefield decomposition based on the optical flow vector; **(D)** angle-weighted RTM with wavefield decomposition based on the optical flow vector.

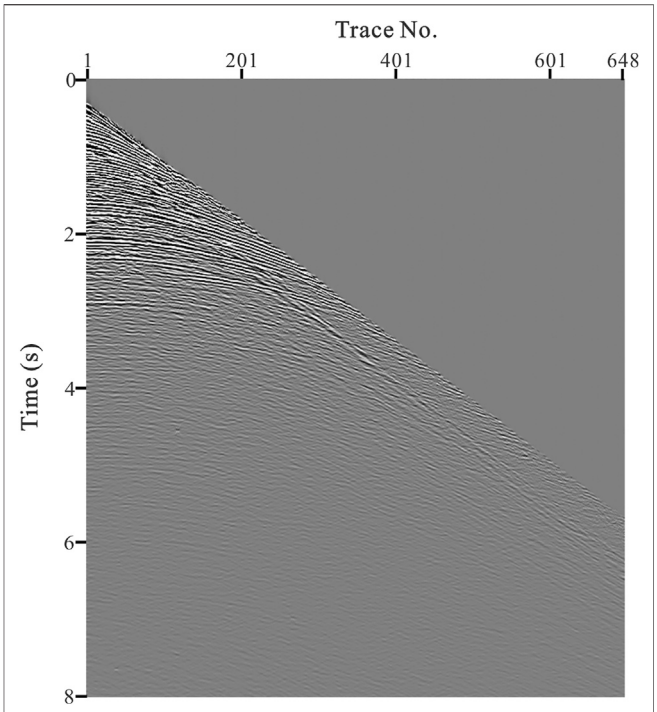

FIGURE 9 | The seismic record of the 601st shot.

weak. Moreover, there is also a risk of losing effective information if only the wavefields in the opposite direction are selected for imaging. To address this problem, the reflection angle of each imaging point underground is first calculated based on the optical flow vector. The calculation formula can be defined as follows:

$$\theta = \pi - \arccos\left(\frac{\mathbf{P}_{\mathbf{S}}^{\mathbf{o}}(x,z,t)\cdot\mathbf{P}_{\mathbf{R}}^{\mathbf{o}}(x,z,t)}{\left|\mathbf{P}_{\mathbf{S}}^{\mathbf{o}}(x,z,t)\right|*\left|\mathbf{P}_{\mathbf{R}}^{\mathbf{o}}(x,z,t)\right|}\right), \tag{12}$$

where θ is the reflection angle of each imaging point and $\mathbf{P}_{\mathbf{S}}^{\mathbf{o}}$ and $\mathbf{P}_{\mathbf{R}}^{\mathbf{o}}$ are the optical flow vectors of the source and receiver wavefields, respectively. Then, an attenuation factor related to the reflection angle is introduced as a weight to generate the optimal stack section, and the final imaging result is obtained according to **Eq. 13**:

$$I(x,z) = \left(\begin{array}{c}\dfrac{\sum_t S_u(x,z,t)R_d(x,z,t) + \sum_t S_d(x,z,t)R_u(x,z,t)}{\sum_t S^2(x,z,t)} \\ + \dfrac{\sum_t S_l(x,z,t)R_r(x,z,t) + \sum_t S_r(x,z,t)R_l(x,z,t)}{\sum_t S^2(x,z,t)}\end{array}\right) w(\theta), \tag{13}$$

where $I(x, z)$ is the final imaging result of angle-weighted RTM with wavefield decomposition based on the optical flow vector and $w(\theta)$ is the attenuation function, and we choose a cosine-type function as the attenuation function.

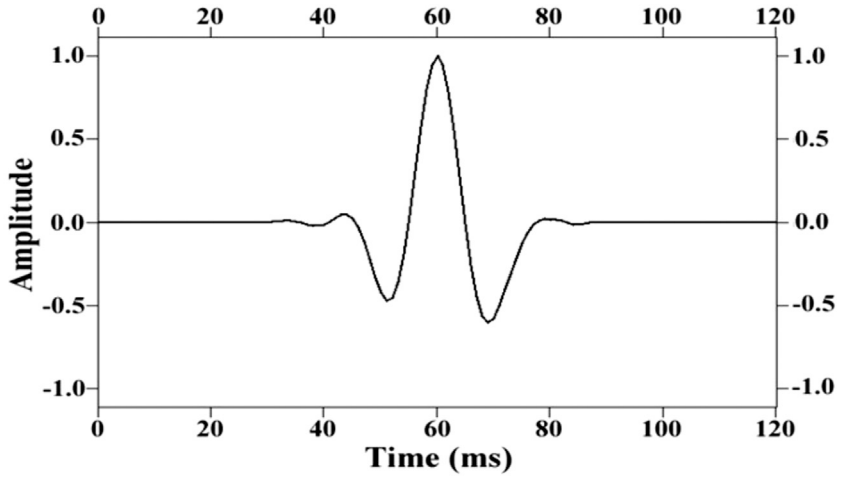

FIGURE 10 | Source wavelet.

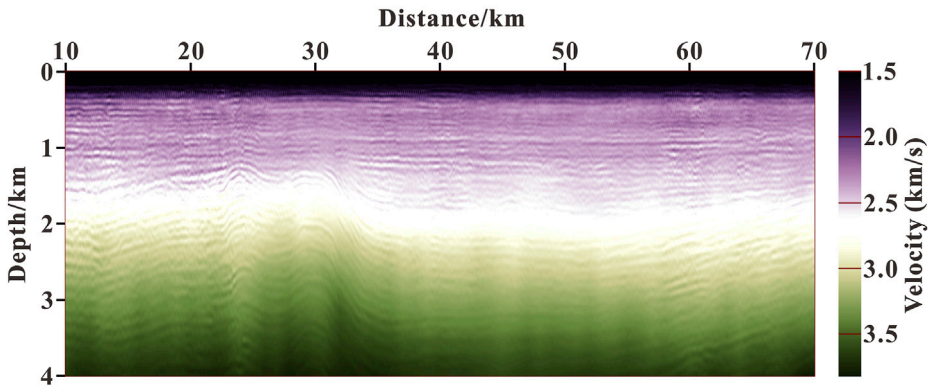

FIGURE 11 | Velocity model of field data.

The two-layer velocity model in *Wavefield Decomposition Based on the Optical Flow Vector* is used to test the effect of the angle-weighted imaging method. **Figure 6A** shows the result of conventional RTM, **Figure 6B** illustrates the result of RTM with wavefield decomposition based on the Poynting vector, **Figure 6C** contains the result of RTM with wavefield decomposition based on the optical flow vector, and **Figure 6D** is the result of angle-weighted RTM with wavefield decomposition based on the optical flow vector.

There are obvious migration artifacts in the conventional RTM imaging result in **Figure 6A**. As shown in **Figures 6B–D**, we can see that most of the migration artifacts are eliminated in the result of RTM with wavefield decomposition based on the Poynting vector. However, due to inaccurate wavefield decomposition, there are still some noises remaining, and as a result of RTM with wavefield decomposition based on the optical flow vector, the migration artifacts are further suppressed. Moreover, the migration artifacts are basically completely suppressed, and the effective structural imaging is highlighted by performing angle weighting processing on the optimal stack section. Therefore, the angle-weighted RTM with wavefield decomposition based on the optical flow vector can produce the accurate imaging of underground structures.

NUMERICAL TEST ON THE MARMOUSI MODEL

A region of the Marmousi-II model (as shown in **Figure 7**) is used to test the imaging accuracy of our method. The size of the model is 6,500 m in length and 3,500 m in depth. The grid spacing is 5 m. There are a total of 101 shots and each shot contains 1,300 receivers. The sampling intervals for the shots and receivers are 65 m and 5 m, respectively. The depths of shots and receivers are both 0 m. A Ricker wavelet with a dominant frequency of 30 Hz is used as the source. The time sampling interval is 0.4 ms and the

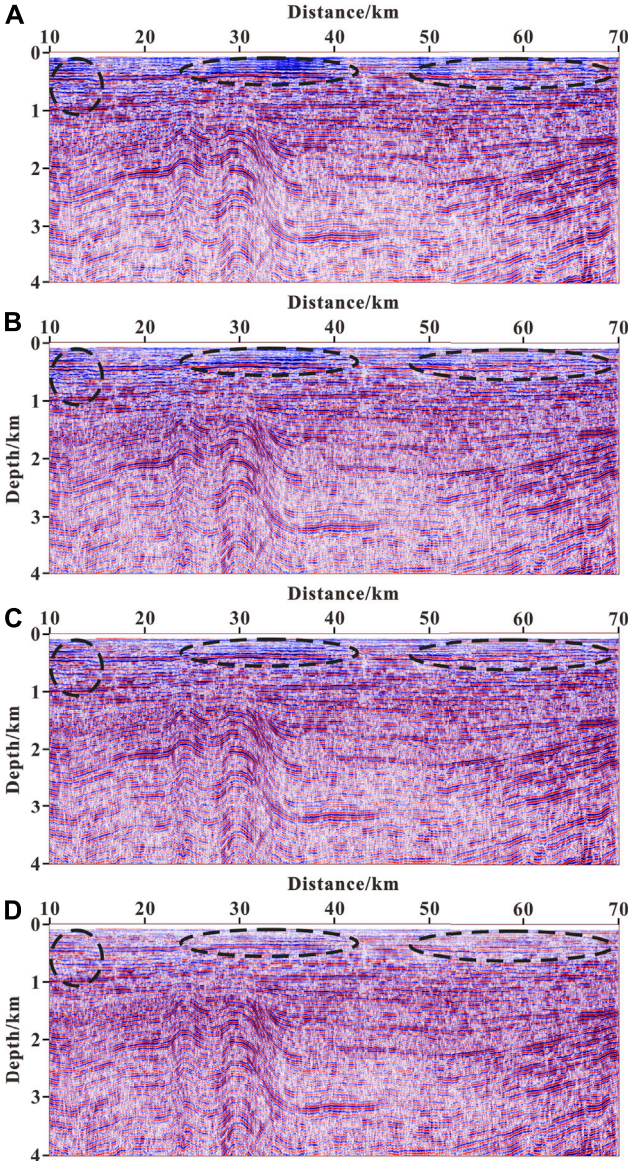

FIGURE 12 | RTM section for field marine seismic data: **(A)** conventional RTM; **(B)** RTM with wavefield decomposition based on the Poynting vector; **(C)** RTM with wavefield decomposition based on the optical flow vector; **(D)** angle-weighted RTM with wavefield decomposition based on the optical flow vector.

total recording time is 4 s. The finite-difference accuracy of wavefield continuation is eighth order in space. **Figure 8A** contains the result of conventional RTM, **Figure 8B** illustrates the result of RTM with wavefield decomposition based on the Poynting vector, **Figure 8C** shows the result of RTM with wavefield decomposition based on the optical flow vector, and **Figure 8D** is the result of angle-weighted RTM with wavefield decomposition based on the optical flow vector.

As shown in **Figure 8A**, the image suffers from low-wavenumber noises. The migration artifacts seriously affect the imaging quality and the real imaging structure is completely concealed. It can be seen from **Figures 8B–D** that all three methods can significantly suppress migration image noises. However, as shown by the red circle in **Figure 8**, there are still lots of image noises in **Figure 8B**, and although the migration artifacts in **Figure 8C** are further eliminated, a few noises are still left. The noises suppression effect in **Figure 8D** is the best, the underground structure is the clearest, and the quality of the migration section is greatly improved. Moreover, our attenuation factor puts more weight on the RTM result in the deep part because the reflections generated in the deep part usually have a smaller reflection angle than those in the shallow part for a fixed offset. Therefore, the deep imaging accuracy is further enhanced using our attenuation factor.

FIELD MARINE SEISMIC DATA IMAGING

A field marine seismic line in the East China sea is selected for the RTM test. The line involves 1,637 shots, among which shots are arranged on the right side, while receivers are on the left side. A total of 648 receivers are allotted for each shot. The interval between shots is 37.5 m and the interval between receivers is 12.5 m. The depths of shots and receivers are both 12.5 m. The minimum offset is 187.5 m and the maximum recording time of shot gather is 8 s. The finite-difference difference accuracy of wavefield continuation is eighth order in space and second order in time. Meanwhile, the time sampling step is 1 ms. **Figure 9** shows the seismic record of the 601st shot. **Figure 10** illustrates a source wavelet that is extracted from the original data.

Figure 11 shows the velocity model of field data, which is obtained by full waveform inversion. **Figure 12** illustrates the RTM sections for field marine seismic data (the part ranging from 10 to 70 km is displayed). Among them, **Figure 12A** is the result of conventional RTM; **Figure 12B** illustrates the result of RTM with wavefield decomposition based on the Poynting vector; **Figure 12C** is the result of RTM with wavefield decomposition based on the optical flow vector; **Figure 12D** shows the result of angle-weighted RTM with wavefield decomposition based on the optical flow vector. From **Figure 12A**, we can see that there are lots of low-wavenumber noises in the shallow part, as shown by the black dotted circle, which seriously reduces the imaging quality. It can be seen from **Figure 12B** that low-wavenumber noises are reduced a lot. In **Figure 12C**, there are fewer noises than in **Figure 12B**, and in **Figure 12D**, there are no obvious noises. Therefore, we can conclude that the method in this article can more effectively eliminate low-wavenumber noises compared to other methods and it is suitable for RTM of real data.

CONCLUSION

The decomposition of source and receiver wavefields can be accurately implemented using the optical flow vector. Then,

the cross-correlation imaging sections of one-way propagation components of the forward- and back-propagated wavefields are optimized and stacked. Furthermore, the reflection angle of each imaging point is calculated based on the optical flow vector, and an attenuation factor related to the reflection angle is used as the weight to give the optimal stack images. The numerical experimental results demonstrate the following:

1) The optical flow vector can be used to decompose the wavefield accurately and stably, and RTM with wavefield decomposition based on the optical flow vector can alleviate the effect of low-wavenumber noises effectively.
2) Angle weighting processing can further eliminate large-angle migration artifacts and highlight effective underground structure imaging, thereby significantly improving the imaging accuracy of RTM.
3) The angle-weighted RTM with wavefield decomposition based on the optical flow vector can more effectively eliminate low-wavenumber noises than other methods and it is suitable for RTM of real data.

The proposed method can be applied to elastic-wave RTM and can be further extended to least-squares RTM.

DATA AVAILABILITY STATEMENT

The original contributions presented in the study are included in the article/Supplementary Material; further inquiries can be directed to the corresponding author.

AUTHOR CONTRIBUTIONS

CX contributed to the writing of the original draft. PS was responsible for conceptualization and project administration. XL was responsible for formal analysis. JT was responsible for software application. SW contributed to the methodology. BZ offered suggestions.

FUNDING

This research is jointly funded by the National Natural Science Foundation of China (No. 42074138), Fundamental Research Funds for the Central Universities (201964016), and the Major Scientific and Technological Innovation Project of Shandong Province (2019JZZY010803).

REFERENCES

Baysal, E., Kosloff, D. D., and Sherwood, J. W. C. (1984). A Two-way Nonreflecting Wave Equation. *Geophysics* 49, 132–141. doi:10.1190/1.1441644

Baysal, E., Kosloff, D. D., and Sherwood, J. W. C. (1983). Reverse Time Migration. *Geophysics* 48, 1514–1524. doi:10.1190/1.1441434

Berenger, J.-P. (1994). A Perfectly Matched Layer for the Absorption of Electromagnetic Waves. *J. Comput. Phys.* 114, 185–200. doi:10.1006/jcph.1994.1159

Chen, T., and He, B.-S. (2014). A Normalized Wavefield Separation Cross-Correlation Imaging Condition for Reverse Time Migration Based on Poynting Vector. *Appl. Geophys.* 11, 158–166. doi:10.1007/s11770-014-0441-5

Collino, F., and Tsogka, C. (2001). Application of the Perfectly Matched Absorbing Layer Model to the Linear Elastodynamic Problem in Anisotropic Heterogeneous media. *Geophysics* 66, 294–307. doi:10.1190/1.1444908

Du, Q., Zhu, Y., and Ba, J. (2012). Polarity Reversal Correction for Elastic Reverse Time Migration. *Geophysics* 77, S31–S41. doi:10.1190/GEO2011-0348.1

Du, Q. Z., Zhu, Y. T., Zhang, M. Q., and Gong, X. F. (2013). A Study on the Strategy of Low Wavenumber Noise Suppression for Prestack Reverse-Time Depth Migration. *Chin. J. Geophys.* 56, 2391–2401. doi:10.6038/cjg20130725

Duan, Y., and Sava, P. (2015). Scalar Imaging Condition for Elastic Reverse Time Migration. *Geophysics* 80, S127–S136. doi:10.1190/GEO2014-0453.1

Fee, D., Toney, L., Kim, K., Sanderson, R. W., Iezzi, A. M., Matoza, R. S., et al. (2021). Local Explosion Detection and Infrasound Localization by Reverse Time Migration Using 3-D Finite-Difference Wave Propagation. *Front. Earth Sci.* 9, 620813. doi:10.3389/feart.2021.620813

Fei, T. W., Luo, Y., Yang, J., Liu, H., and Qin, F. (2015). Removing False Images in Reverse Time Migration: The Concept of De-primary. *Geophysics* 80, S237–S244. doi:10.1190/GEO2015-0289.1

Gong, T., Nguyen, B. D., and McMechan, G. A. (2016). Polarized Wavefield Magnitudes with Optical Flow for Elastic Angle-Domain Common-Image Gathers. *Geophysics* 81, S239–S251. doi:10.1190/GEO2015-0518.1

Horn, B. K. P., and Schunck, B. G. (1981). Determining Optical Flow. *Artif. intelligence* 17, 185–203. doi:10.1016/0004-3702(81)90024-2

Hu, C., Albertin, U., and Johnsen, T. (2014). Optical Flow Equation Based Imaging Condition for Elastic Reverse Time Migration. *Ann. Internat Mtg.Soc. Expi. Geophys. Expanded Abstr.* 84, 3877–3881. doi:10.1190/segam2014-0140.1

Li, K.-R., and He, B.-S. (2020). Extraction of P- and S-Wave Angle-Domain Common-Image Gathers Based on First-Order Velocity-Dilatation-Rotation Equations. *Appl. Geophys.* 17, 92–102. doi:10.1007/s11770-019-0799-5

Liu, F., Zhang, G., Morton, S. A., and Leveille, J. P. (2011). An Effective Imaging Condition for Reverse-Time Migration Using Wavefield Decomposition. *Geophysics* 76, S29–S39. doi:10.1190/1.3533914

Liu, Q. (2019). Dip-angle Image Gather Computation Using the Poynting Vector in Elastic Reverse Time Migration and Their Application for Noise Suppression. *Geophysics* 84, S159–S169. doi:10.1190/GEO2018-0229.1

Lucas, B. D., and Kanade, T. (1981). "An Iterative Image Registration Technique with an Application to Stereo Vision," in Proceedings of the 7th International Joint Conference on Artificial Intelligence, San Francisco, CA, United States (San Mateo, CA: Morgan Kaufmann Publishers Inc.), 674–679.

McMechan, G. A. (1983). Migration by Extrapolation of Time-dependent Boundary Values. *Geophys. Prospect* 31, 413–420. doi:10.1111/j.1365-2478.1983.tb01060.x

Mulder, W. A., and Plessix, R. E. (2004). A Comparison between One-way and Two-way Wave-equation Migration. *Geophysics* 69, 1491–1504. doi:10.1190/1.1836822

Oh, J.-W., Kalita, M., and Alkhalifah, T. (2018). 3D Elastic Full-Waveform Inversion Using P-Wave Excitation Amplitude: Application to Ocean Bottom cable Field Data. *Geophysics* 83, R129–R140. doi:10.1190/GEO2017-0236.1

Poynting, J. H. (1884). XV. On the Transfer of Energy in the Electromagnetic Field. *Phil. Trans. R. Soc.* 175, 343–361. doi:10.1098/rspl.1883.009610.1098/rstl.1884.0016

Qu, Y., Guan, Z., Li, J., and Li, Z. (2020). Fluid-solid Coupled Full-Waveform Inversion in the Curvilinear Coordinates for Ocean-Bottom cable Data. *Geophysics* 85, R113–R133. doi:10.1190/GEO2018-0743.1

Song, P. (2005). *Accurate Absorbing Boundary Conditions and Reverse-Time Migration of Acoustic Wave Equation Using Non-reflecting Recursive Algorithm: [Master's Thesis]*. Qingdao: Ocean University of China.

Sun, D., Jiao, K., Cheng, X., and Vigh, D. (2015). Compensating for Source and Receiver Ghost Effects in Full Waveform Inversion and Reverse Time Migration for marine Streamer Data. *Geophys. J. Int.* 201, 1507–1521. doi:10.1093/gji/ggv089

Tang, C., McMechan, G. A., and Wang, D. (2017). Two Algorithms to Stabilize Multidirectional Poynting Vectors for Calculating Angle Gathers from Reverse Time Migration. *Geophysics* 82, S129–S141. doi:10.1190/GEO2016-0101.1

Wang, P. F., and He, B. S. (2017). Vector Field Dot Product Cross-Correlation Imaging Based on 3D Elastic Wave Separation. *Oil Geophys. Prospecting* 52, 477–483. doi:10.1380/j.cnki.issn.1000-7210.2017.03.009

Wang, X. Y., Zhang, J. J., Xu, H. Q., and Tian, B. Q. (2021). Least-squares Reverse Time Migration with Wavefield Decomposition Based on the Poynting Vector. *Chin. J. Geophys.* 64, 645–655. doi:10.06038/cjg2021O0120

Wang, Y. B., Zheng, Y. K., Xue, Q. F., Chang, X., Fei, W., and Luo, Y. (2016). Reverse Time Migration with Hilbert Transform Based Full Wavefield Decomposition. *Chin. J. Geophys.* 59, 4200–4211. doi:10.6038/cjg20161122

Whitmore, N. D. (1983). Iterative Depth Migration by Backward Time Propagation. *Ann. Internat Mtg.Soc. Expi. Geophys. Expanded Abstr.* 53, 382–385. doi:10.1190/1.1893867

Wu, C. L., Wang, H. Z., Feng, B., and Sheng, S. (2021). RTM Angle Gathers Based on the Combining Local and Global (CLG) Optical Flow Method and Wavefield Decomposition Method. *Chin. J. Geophys.* 64, 1375–1388. doi:10.6038/cjg2021O0088Yoon

Yoon, K., and Marfurt, K. J. (2006). Reverse-time Migration Using the Poynting Vector. *Exploration Geophys.* 37, 102–107. doi:10.1071/EG06102

Zhang, D., Fei, T. W., and Luo, Y. (2018). Improving Reverse Time Migration Angle Gathers by Efficient Wavefield Separation. *Geophysics* 83, S187–S195. doi:10.1190/GEO2017-0348.1

Zhang, L., Liu, Y., Jia, W., and Wang, J. (2020). Suppressing Residual Low-Frequency Noise in VSP Reverse Time Migration by Combining Wavefield Decomposition Imaging Condition with Poynting Vector Filtering. *Exploration Geophys.* 52, 235–244. doi:10.1080/08123985.2020.1804298

Zhang, W., and Shen, Y. (2010). Unsplit Complex Frequency-Shifted PML Implementation Using Auxiliary Differential Equations for Seismic Wave Modeling. *Geophysics* 75, T141–T154. doi:10.1190/1.3463431

Zhang, Y., and Sun, J. (2009). Practical Issues in Reverse Time Migration: True Amplitude Gathers, Noise Removal and Harmonic Source Encodingnoise Removal and Harmonic-Source Encoding. *First Break* 27, 53–59. doi:10.3997/1365-2397.2009002

Zhang, Q. (2014). RTM Angle Gathers and Specular Filter (SF) RTM Using Optical Flow. *Ann. Internat Mtg.Soc. Expi. Geophys. Expanded Abstr.* 84, 3816–3820. doi:10.1190/segam2014-0792.1

Conflict of Interest: The authors declare that the research was conducted in the absence of any commercial or financial relationships that could be construed as a potential conflict of interest.

Publisher's Note: All claims expressed in this article are solely those of the authors and do not necessarily represent those of their affiliated organizations, or those of the publisher, the editors and the reviewers. Any product that may be evaluated in this article, or claim that may be made by its manufacturer, is not guaranteed or endorsed by the publisher.

frontiers in Earth Science

ORIGINAL RESEARCH
published: 23 November 2021
doi: 10.3389/feart.2021.751202

Reverse Time Migration of Vertical Cable Seismic Data to Image Hydrate-Bearing Sediments With High Resolution

Linfei Wang[1,2], *Huaishan Liu*[1,2]*, *Zhong Wang*[3], *Jin Zhang*[1,2], *Lei Xing*[1,2]* and *Yanxin Yin*[1,2]

[1]Key Lab of Submarine Geosciences and Prospecting Techniques, College of Marine Geo Sciences, Ocean University of China, Qingdao, China, [2]Laboratory for Marine Mineral Resources, Qingdao National Laboratory for Marine Science and Technology, Qingdao, China, [3]College of Marine Geosciences, Ocean University of China, Qingdao, China

Marine vertical cable seismic (VCS) is a promising survey technique for submarine complex structure imaging and reservoir monitoring, which uses vertical arrays of hydrophones deployed near the seafloor to record seismic wavefields in a quiet environment. Recently, we developed a new type of distributed VCS system for exploration and development of natural gas hydrates preserved in shallow sediments under the seafloor. Using this system and air-gun sources, we accomplished a 3D VCS yield data acquisition for gas hydrates exploration in the Shenhu area, South China Sea. In view of the characteristics of VCS geometry, we implement reverse time migration (RTM) on a common receiver gather to obtain high-resolution images of marine sediments. Due to the unique acquisition method, it is asymmetrical for the reflection path between the sources and the receivers in the VCS survey. Therefore, we apply accurate velocity analysis to common scatter point (CSP) gathers generated from common receiver gathers instead of the conventional velocity analysis based on common depth point gathers. RTM with this reliable velocity model results in high-resolution images of submarine hydrate-bearing sediments in deep water conditions. The RTM imaging section clearly shows the bottom simulating reflector (BSR) and also the reflection characteristics of the hydrate-bearing sediments filled with consolidated hydrates. Moreover, its resolution is relative to that of acoustic logging curves from the nearby borehole, and this imaging section is well consistent with the synthetic seismogram trace generated by the logging data. All these results reveal that VCS is a great potential technology for exploration and production of marine natural gas hydrates.

Keywords: vertical cable seismic (VCS), natural gas hydrate, common scatter point gathers, seismic imaging, bottom simulating reflector (BSR)

OPEN ACCESS

Edited by:
Hao Hu,
University of Houston, United States

Reviewed by:
Kelly Liu,
Missouri University of Science and Technology, United States
Wu Shiguo,
Institute of Deep-Sea Science and Engineering (CAS), China

***Correspondence:**
Huaishan Liu
lhs@ouc.edu.cn
Lei Xing
xingleiouc@ouc.edu.cn

Specialty section:
This article was submitted to Solid Earth Geophysics, a section of the journal Frontiers in Earth Science

Received: *31 July 2021*
Accepted: *11 October 2021*
Published: *23 November 2021*

Citation:
Wang L, Liu H, Wang Z, Zhang J, Xing L and Yin Y (2021) Reverse Time Migration of Vertical Cable Seismic Data to Image Hydrate-Bearing Sediments With High Resolution. Front. Earth Sci. 9:751202. doi: 10.3389/feart.2021.751202

INTRODUCTION

Vertical cable seismic (VCS) is a potential prospective technology for target imaging in geologically complex areas (Krail, 1991; 1993), especially for offshore acquisition (Ikelle and Wilson, 1999). This technology is based on antisubmarine warfare from the US Navy (Krail, 1994). It uses vertical hydrophone array (VHA) to record seismic wavefield, which is moored near the seafloor with a heavyweight anchor. Then, the source can be air-gun or other sources such as sparker, towed by a

seismic survey vessel. Higher resolution seismic data can be acquired using vertical cables with no more than 500 m in length at 500 m intervals (Wilson, 2002), compared with conventional marine seismic survey.

From the late 1980s to the early 1990s, Texaco Inc. constructed vertical cables and conducted vertical cable acquisition experiments in the Gulf of Mexico (Krail, 1994; 1997). They obtained high-quality 3D seismic volume with this special method. The edge of the salt dome and the reflectors below salt are clearly imaged using the VCS volume. It is difficult for conventional seismic exploration to overcome this problem. In the summers of 1995 and 1996, the Strathspey Field Group performed the VCS survey in the North Sea (Leach, 1997). The processed dataset shows dramatic improvement over the conventional 3D dataset. Moreover, it provides the partners with an effective assessment of the remaining exploration potential in the Strathspey block. However, VCS has not been widespread used for resource survey owing to its expensive acquisition system and unique processing method. In 2009, JGI Inc. started to develop an integrated VCS acquisition system for hydrothermal deposit exploration and research on corresponding data processing and analysis technique (Asakawa et al., 2012). They carried out the VCS experiment in Lake Biwa and obtained high-resolution 3D images which are better than the conventional surface seismic. Based on this experiment, they manufactured autonomous VCS recording systems in 2010. Using these VCS acquisition systems, they conducted seafloor massive sulphide (SMS) survey in Izena Cauldron in 2011 and 2013, respectively (Asakawa et al., 2014a; 2014b; 2015; 2016). The first survey gives the large-scale and deeper structure of hydrothermal system and the second survey gives the clear structure of SMS deposit. Since 2013, the Guangzhou Marine Geological Survey Bureau of Chinese Geological Survey Bureau and Ocean University of China (OUC) have been developing VCS technology for Natural Gas Hydrates exploration, financially supported with National High-Technology Research and Development Program of China. In 2015, the Guangzhou Marine Geological Survey Bureau of Chinese Geological Survey Bureau manufactured a VCS system composed of multiple ocean bottom seismometers (OBS) and carried out a test with "Fendou4" vessel in the South China Sea (Huang et al., 2016). In the same year, OUC developed a distributed VCS recording system with eight hydrophones and performed an experiment with "Nahai502" vessel in Southeast Hainan Basin (Xing et al., 2016). In 2017, a multi-OBS VCS acquisition system (Wang et al., 2019) and a distributed VCS acquisition system were developed, respectively. Then, the Guangzhou Marine Geological Survey Bureau of Chinese Geological Survey Bureau conducted the first 3D VCS survey for natural gas hydrates in the Shenhu area, South China Sea.

In this study, we review the concept of the VCS survey and present the construction of the distributed VCS acquisition system for exploring the hydrates resources beneath the seafloor, and we process and analyze the VCS dataset recorded by this system in deep water in the South China Sea. In view of the dramatic advantages of reverse time migration (RTM) method, we confirm that RTM helps to better image hydrate-bearing sediments than the other migration method. In order to obtain a reliable velocity model for RTM, we rebuild the common scatter point (CSP) gathers from each common receiver gather of VCS dataset and then perform accurate velocity analysis on these CSP gathers. With this velocity model, we implement RTM on the common receiver point gather of the first receiver and obtain high-quality images of the shallow sediments layers. In comparison with synthetic seismogram made by the P-wave velocity from log data in nearby well, the imaging result presents high resolution relative to acoustic logging curves and provides a better understanding of the characteristic of hydrate-bearing sediments.

MARINE VERTICAL CABLE SEISMIC EXPLORATION

General Concept

VCS technology was first applied in the marine setting (Wilson, 2002). As is illustrated in **Figure 1**, vertical seismic cable is deployed at the sea bottom which is close to the subsurface target. Multihydrophones compose vertical array, attached to the cable with regular intervals. A set of buoyant spheres is moored on the top of the cable and the heavy anchor is moored at the sea bottom, in order to maintain vertical tension on the cable. Generally speaking, the recording units are arranged in an instrument of buoy, which can record seismic signals continuously. As vertical cable is fixed near the seafloor, the source vessel could shoot along the surveying lines in any azimuth. In addition, VCS acquisition can use various marine sources, such as sparkers and air-gun (Asakawa et al., 2012). In fact, VCS exploration can be considered a multi-offset vertical seismic profiling (VSP). The main difference is that all hydrophones are suspended in sea water for VCS and receiver sensors are arranged in the borehole for VSP. Therefore, VCS has no expensive standby rig time. It also has several advantages over conventional marine seismic exploration (Krail, 1991; Wang, 2003):

1) VCS can provide high-resolution 3D images around submarine targets. Compared with the conventional towed-streamers survey, it does not suffer from the swell at greater depths in seawater. Hence, the VCS data with high signal-to-noise ratio (SNR) is effective for reservoir characterization.
2) Vertical cable is fixed for all shot points, so a true 3D shot record is obtainable. Yield acquisition geometry can be designed to suit exploration and production needs, because it allows complete flexibility in azimuth and offset distribution for survey planning.
3) VCS exploration costs are considerably less than conventional 3D seismic surveys. With no towed-streamers, the seismic vessel can navigate easily and quickly over the survey area. Thus, it greatly reduces the time of data acquisition in yield. In addition, it more economically performs 3D pre-stack depth migration on VCS dataset compared with conventional surface data.

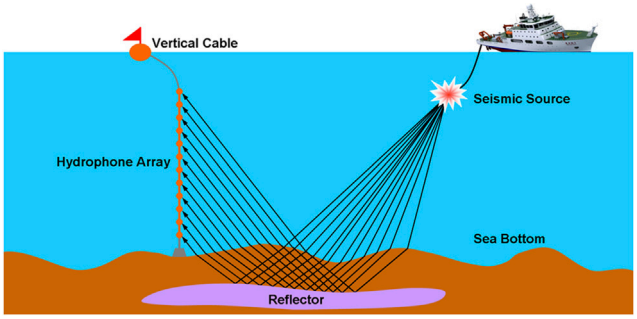

FIGURE 1 | Sketch of vertical cable seismic exploration.

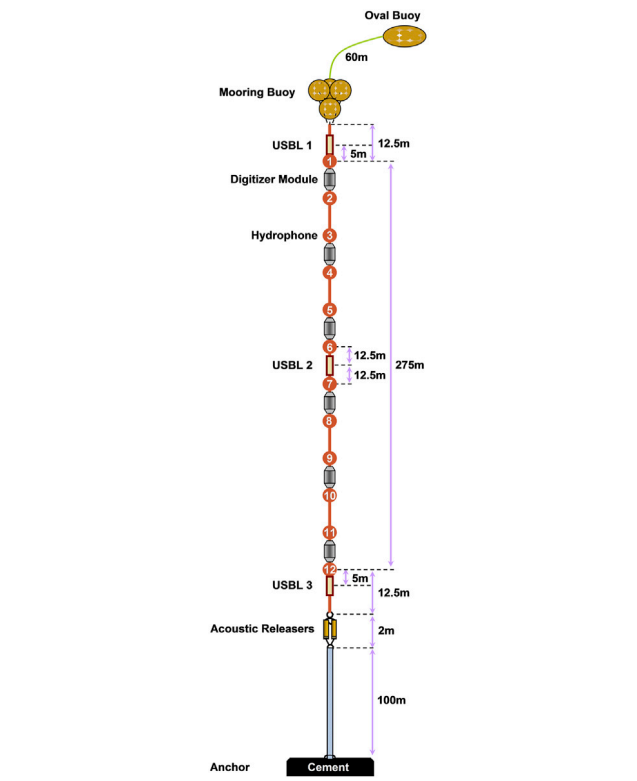

FIGURE 2 | Distributed vertical cable seismic acquisition system.

Distributed Vertical Cable Seismic Acquisition System

It is becoming increasingly more difficult for exploration and production of natural gas hydrates in geologically complex area. During gas hydrates drilling or production operations, it is unavoidable for hydrate-bearing sediments to destabilize spontaneously as part of geologic processes (Wang et al., 2012). Therefore, the fine structure of hydrate-bearing sediments is indispensable in exploration and development of gas hydrates. It is extremely difficult to achieve this goal for the conventional 3D multi-channel seismic with long streamers. Considering the advantages of VCS, we propose that it is an effective technology to obtain high-resolution 3D images of hydrate-bearing sediments.

After years of painstaking research, we have completed development of a distributed vertical cable seismic (DVCS) acquisition system for natural gas hydrates exploration and production in 2017. Its construction is shown in **Figure 2**. The DVCS acquisition system uses a high-strength Kevlar stress member in order to satisfy marine engineering requirements. This Kevlar cable length is about 300 m. Twelve hydrophone arrays are attached to outside of the Kevlar cable with 25 m interval and each array is composed of two parallel hydrophones. Six digitizer modules are arranged in the cable and each of them can record seismic data from two hydrophone arrays, respectively. The sampling rate of these digitizer modules is up to 8,000 Hz. With this sampling rate, it can record the data continuously for about 2 weeks in the water depth of about 2,000 m. An accurate atomic clock is assembled in every module in order to correct the recording time. It should be synchronized with the GPS time before deploying this acquisition system. In order to obtain the positions of the vertical cable, three ultra-short base line (USBL) acoustic position systems are deployed on the top, in the middle, and at the end of the cable, respectively. In the beginning of the VCS survey, we can throw the vertical cable into the water from the vessel. Then, it can be autonomously moored on the seabed by a cement anchor at the bottom. By this heavy anchor (about 300 kg) and the buoyancy with several buoys on the top, the seismic vertical cable is being tensioned vertically in the sea water. When retrieving this vertical cable at the end of the survey, we can transmit a release command to the two parallel acoustic releasers by the acoustic communication system. Then, we can download the yield data from those digitizer modules onboard, conveniently.

REVERSE TIME MIGRATION

High-resolution seismic exploration has been widespread used in resources exploration and development in recent years (Li, 2017). Seismic imaging is the most effective approach to map the subsurface structures and locate the target in the geologically complex area (Zhou et al., 2018). Reverse time migration (RTM) has proved to be one of the most vigorous seismic imaging methods. With no limitation on the variations in velocity, reflector dip, and wave type, RTM can achieve the best accuracy among all seismic migration methods (Bednar, 2005). It computes forward-in-time propagation of the source field and the reverse time propagation of the receiver field, without any simplification assumption (Baysal et al., 1983; McMechan, 1983), and the migrated section (or reflectivity estimate) can be obtained by crosscorrelation of these two fields at equal times.

Image fidelity including resolution limitations, position errors, and artifacts are the main challenges for seismic imaging (Zhou, 2014). In practice of exploration geophysics, velocity model building and seismic migration such as RTM are applied jointly and interactively under variety of geology and data conditions. Therefore, an accurate velocity model is essential to implement RTM effectively. Conventional velocity analysis method is not being applied to the VCS data, due to the irregular yield geometry of the VCS survey. Alternatively, an imaging technique based on common scatter point (CSP) gathers has been developed for VCS

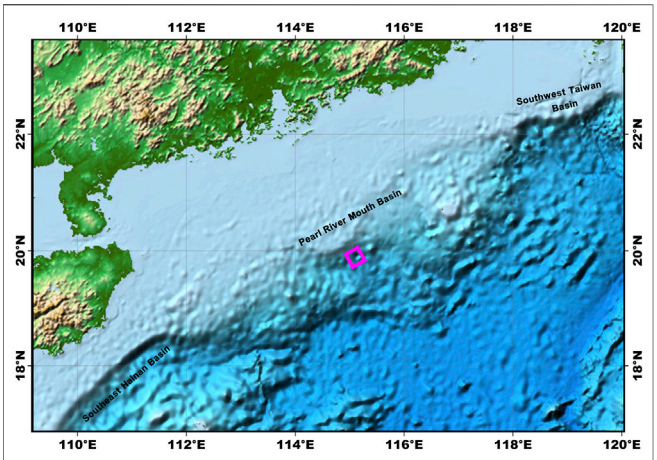

FIGURE 3 | Location map of VCS acquisition in the study area. The pink square frame indicates the area of VCS operation.

data processing (Wang, 2003). Based on this method, accurate velocity analysis can be implemented at each imaging position in different depths. Consequently, we can build a reference velocity model with previous processes. What's more, conventional processing methods are able to implement on the CSP gathers. Another effective approach to obtain the velocity wavefield is to perform velocity analysis on virtual shot gathers produced by seismic interferometry of multiples in the VCS data (Hondori et al., 2019). In this paper, we apply the CSP-based processing method to build the velocity wavefield used for RTM.

DATA ACQUISITION EXPERIMENT

The 3D VCS acquisition for natural gas hydrates exploration was carried out by the Guangzhou Marine Geological Survey Bureau in April 2017 to obtain the fine structure of hydrate-bearing sediments in the Shenhu area, South China Sea (**Figure 3**). Two vertical cables are deployed at the central part of the survey area in this experiment. One is the multi-OBS vertical cable, the other one is the DVCS acquisition system. GI gun array (540 cu. in) is used as the source for this experiment. The shooting area (pink dashed frame in **Figure 4**) is about 6 km × 6 km with 25 m shot point interval. In total, 60 shot lines spread over this area with 100 m shot line interval, and they are numbered from L13 to L72, respectively. The DVCS acquisition system (12-channel) recorded seismic waves with 0.25 msec sampling rate, continuously. Several days later, a high-quality vertical cable dataset is obtained for hydrate-bearing sediments imaging.

Surveying Line 39 is the closest to VC among all the shot lines, through Site SH7. The vertical cable is approximately 13 m away from the L39 line. Hence, we mainly focus on hydrate-bearing sediments imaging across this surveying line in this paper. **Figure 5A** shows a common receiver point gather (just like shot record in conventional surface seismic), sorted by the first channel from the field data in Line 39. It is band-pass filtered to remove low (less than 12 Hz) and high (more than 512 Hz) frequencies. This gather clearly shows the direct wave, seafloor refection, and multiple reflection. In addition, enhanced reflections (ER) with greater amplitudes seem to be present above the weakness reflection zones. Their energy is comparable to that of the direct wave and the seafloor reflection.

DATA PROCESSING

Similar to the 3D Walkaway VSP technique, VCS can use VSP processing and imaging workflows for data processing (Bailey et al., 2017). However, there is no universal processing method for VCS dataset up to now. Aiming at primary waves imaging in this paper, we mainly apply the CSP-based approach (Wang, 2003) to process the VCS data. As shown in **Figure 6A**, the reflection time can be expressed as follows:

$$t = t_s + t_r = \frac{1}{v_0}\sqrt{(x_s + x_r)^2 + (2h - h_r)^2} = \frac{1}{v_0}\sqrt{x^2 + (2h - h_r)^2} = \sqrt{\frac{x^2}{v_0^2} + \left(t_0 - \frac{h_r}{v_0}\right)^2} \tag{1}$$

where t_s is the traveltime from the source to the reflection point, t_r is the traveltime from the reflection point to the receiver point, v_0 is the acoustic velocity of the seawater, x_s is the horizontal distance from the source to the reflection point, x_r is the horizontal distance from the receiver to the reflection point, h is the depth of the reflector, h_r is the depth of the receiver, $t_0 = 2h/v$ is the two-way vertical traveltime at the reflection point and x is the offset. We perform initial velocity analysis using **Equation 1** on the common receiver gather. Before this work, the direct wave should be removed by the median filter or differential equation based filter. Due to the

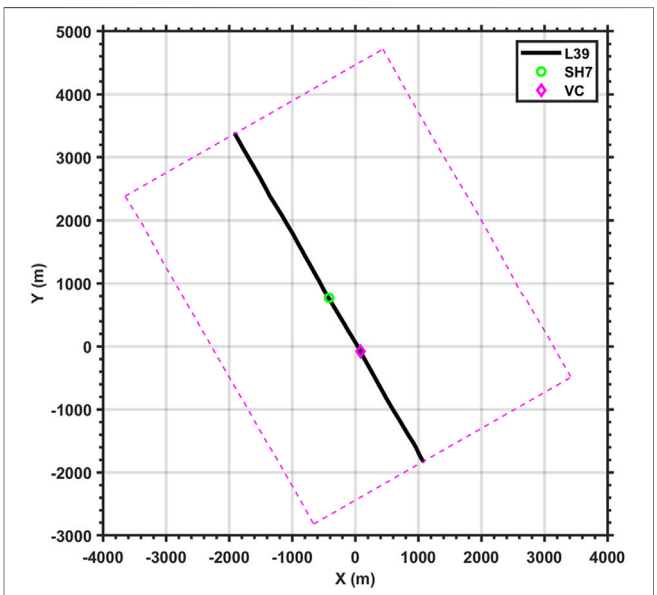

FIGURE 4 | Location of Line 39 (black line) in the 3D survey area (pink dashed frame). Blue circle shape indicates the position of Well SH7 and the pink diamond shape indicates the position of the vertical cable.

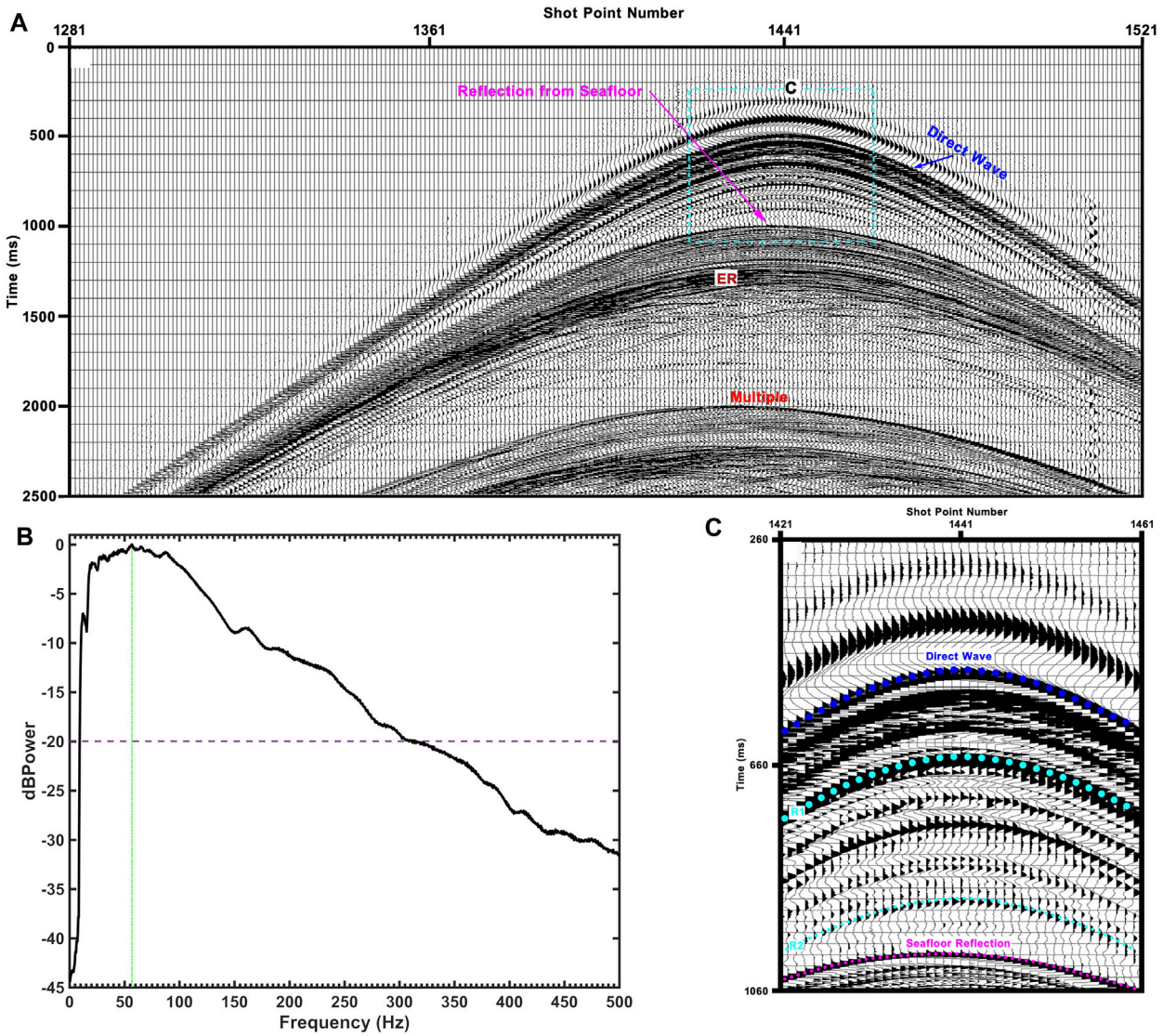

FIGURE 5 | (A) Common receiver gather from the first receiver after band-pass filtered. **(B)** The spectrum of this common receiver gather. **(C)** The seismic reflections from the seawater layers. The water body reflections occur between dashed line R1 and R2.

irregular coverage of VCS geometry, it is not sufficient to implement VCS imaging with the above-mentioned single velocity function. However, we can update the initial velocity model by means of performing the residual velocity analysis on the common scatter point (CSP) gathers. A CSP gather can be built from a common receiver gather, by binning all the traces with offset and transmitting to the new traveltime t_{CSP} and offset x_{CSP}, which is given by

$$\begin{cases} t_{CSP} = 2t_s = \sqrt{t_0^2 + \dfrac{x_{CSP}}{v_0^2}} \\ x_{CSP} = 2x_s \end{cases} \tag{2}$$

As illustrated in **Figure 6B**, it can be described as a process of time shift ($t_s = t - t_r$) with coordinate scaling ($t_{CSP} = 2t_s$ and $x_{CSP} = 2x_s$) for this mapping procedure. Consequently, we can map each input trace into many CSP gathers by this procedure and the new traveltime equation for the CSP gather is turned into the standard hyperbolic equation for velocity analysis. In addition, we can create CSP gathers at any arbitrary location within VCS dataset so that the high fold and large offsets enable appropriate velocity analysis at every imaging point.

In this paper, we select one common receiver gather from the first channel (**Figure 5A**) along the source line L39 to perform seismic imaging process. After initial velocity analysis, we produce a lot of CSP gathers with 6.25 m interval. In fact, the interval of CSP gather can be defined as arbitrary value (for example, 1 m) according to the imaging accuracy. **Figure 7** shows three CSP gathers (the direct wave is muted) generated from the first channel, respectively. Among them, CSP 180 is nearly located at the same surface position as the vertical seismic cable. Seafloor reflection and

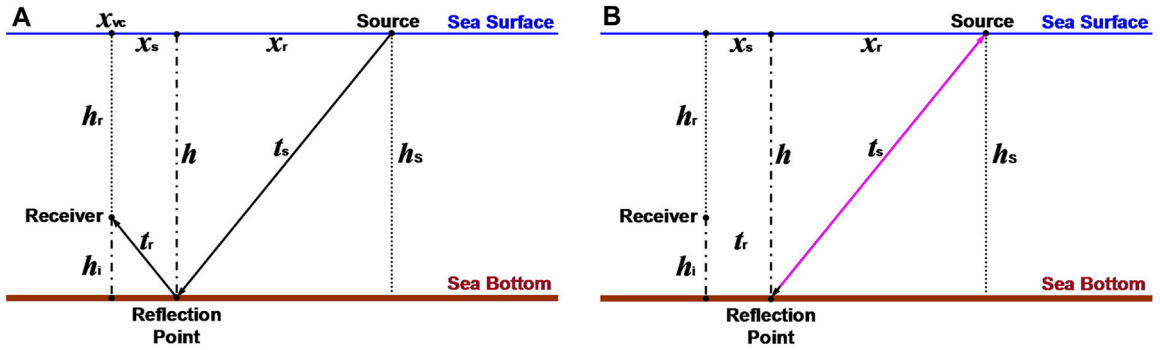

FIGURE 6 | The schematic diagram showing generation of CSP gathers from a common receiver gather. **(A)** The ray path in VCS geometry. **(B)** The sketch of common scatter point.

enhanced reflection are clearly recognized in these CSP gathers and their events are continuous. After applying the residual velocity analysis to these CSP gathers, we obtain the more accurate velocity model which is used for RTM (**Figure 8**). Finally, we implement reverse time migration of the common receiver gather from the first channel with this velocity wavefield and the imaging result is shown in **Figure 9A**. In this RTM section, we can clearly recognize seafloor reflection and reflections related to marine sediments beneath the seafloor. This imaging section gives useful information to hydrates exploration.

RESULTS AND DISCUSSION

RTM Is Suitable for VCS Imaging

In principle, RTM offers the best accuracy than that of the other seismic migration methods (Bednar, 2005; Zhou et al., 2018). According to its advantages, RTM can provide depth imaging with better quality in complex geologic structure such as hydrate-bearing sediments. VCS uses vertical arrays of hydrophones to acquire seismic data in marine environment so that the sources and receivers locate at significantly different depths. Consequently, the large elevation difference makes it invalid to process VCS data with conventional method based common midpoint (CMP) theory such as velocity analysis, normal move-out (NMO), common depth point (CDP) stack, and seismic imaging (Wang, 2003). RTM is a shot-based processing, independent of acquisition irregularity. Hence, it can address the large elevation changes by assuming the concept of seismic reciprocity to exchange sources and receivers locations for imaging (Guimarães et al., 1998; Shen et al., 2000). According to reciprocal principle, the common receiver gather would be equivalent to a shot gather where the single receiver would be the source in seawater and the receivers would be the shots generated close to the sea surface. Thus, RTM as a pre-stack shot record migration was applied on this common receiver gather. As a result, it is convenient to implement RTM for VCS dataset, especially for complex geological area.

Seismic migration is the most effective way to image the subsurface, based on seismic reflected waves including scattered and diffracted waves (Zhou et al., 2018). In order to obtain better imaging results, it is essential to build an accurate velocity modeling for seismic migration such as RTM. VCS uses vertical hydrophone array suspended in seawater environment to record seismic wave, compared with horizontal arrays in towed-streamer. As a result, single hydrophone can be used at each receiver point, which provides complete seismic data used for accurate data analysis. Hence, it is possible to build accurate velocity model from VCS dataset. In addition, we establish the reference velocity model by accurate velocity analysis on common scatter point (CSP) gathers. In practice, constructing CSP gathers from common receiver gathers is an initial process of Kirchhoff pre-stack migration (Bancroft and Xu, 1999). By this processing, we can address large elevation changes and the travel times for the source and receiver ray paths can be computed to the actual locations. In particular, CSP gathers can be created at any arbitrary location with VCS dataset for velocity analysis so that the high fold and large offsets enable accurate velocity analysis at each imaging point position (Wang, 2003). If we form a common depth gather in a VCS dataset, it will be sparsely populated in offset and low in fold, since there are only a few receivers for a source in the VCS geometry. Thus, we can obtain more accurate velocity model for RTM based on the idea of CSP gathers, compared with conventional process method. With this reference velocity model, we can obtain better seismic imaging section by performing RTM on VCS dataset. As mentioned above, RTM is an effective way to better image subsurface geologic structure for VCS dataset.

Resolution for VCS Dataset

High-resolution seismic prospecting is profound system engineering, consisting of many links (such as field acquisition, data processing, and interpretation). A weakness in any link may result in the failure of the entire system (Li, 2017). Improving seismic resolution has been a primary issue to be debated in exploration seismology, especially in petroleum exploration.

Compared with conventional seismic exploration, VCS can obtain high-resolution seismic data with high signal-to-noise ratio (SNR). First of all, vertical cable is suspended within the

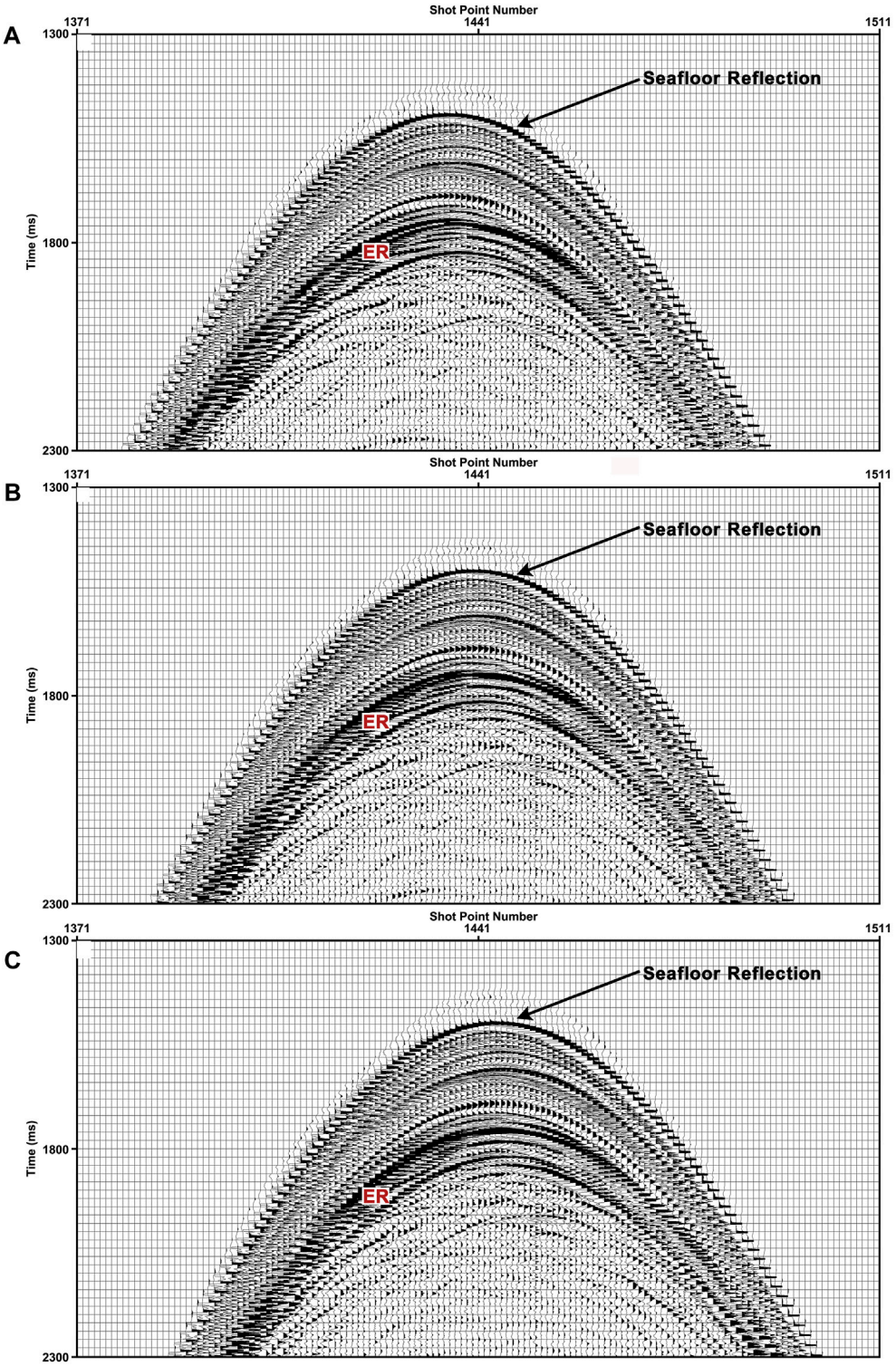

FIGURE 7 | The CSP gathers. **(A)** CSP 165. **(B)** CSP 180. **(C)** CSP 195.

seawater so that the seismic vessel is only towing the source (Wilson, 2002). As a result, we can obtain adequate resolution only by evaluating the interval between the source lines. Secondly, hydrophones are suspended in a quiet environment compared with surface seismic prospecting so that single hydrophone can be used at each receiver point in different

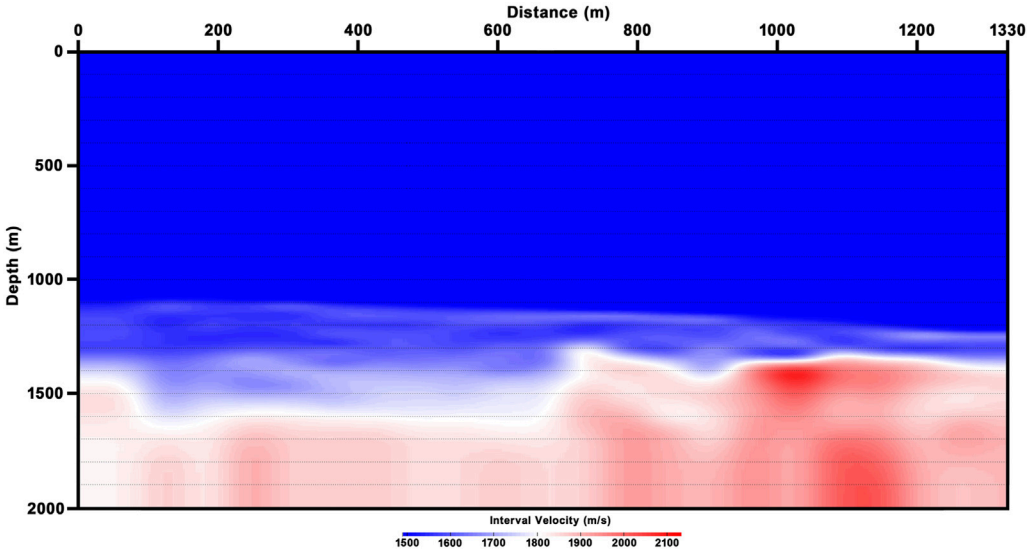

FIGURE 8 | Velocity model used for RTM.

water depths (Wang, 2003). It provides adequate bandwidth of the field VCS dataset, which seismic resolution is dependent upon. Thirdly, vertical cables are moored near the seafloor and the hydrophones are close to the target underneath the seabed. Thus, the Fresnel zone is smaller than surface seismic and better imaging results can be obtained from the VCS dataset. Finally, all the hydrophone sensors are suspended within the water column, overcoming receiver coupling problems and avoiding lots of noises such as mechanical cable noise, swell noise, and tail buoy noise. Consequently, the SNR of field VCS dataset is significantly improved and the high-quality data are effective for reservoir characterization. In a word, the seismic resolution of VCS dataset is superior to the surface seismic method.

Figure 5A shows a common receiver point gather from the first channel in Line 39, which is band-pass filtered. By spectrum analysis, we obtain the peak frequency is about 56 Hz (vertical solid line) and the dominant bandwidth is about 10–300 Hz (dashed line). Li (2017) points out seismic resolution is dependent upon the relative bandwidth. For a band-pass filtered wavelet, its low-frequency limit can be defined as f_1 and its high-frequency limit as f_2. Then, the relative bandwidth is $R = f_2/f_1$. According to this equation, the relative bandwidth of the common receiver point gather (**Figure 5A**) is $R = 30$. There is an alternative expression of this relative bandwidth, using octaves $2^4 < R < 2^5$. It demonstrates that the relative bandwidth is more than one octave (4–5 octaves) and the number of the consecutive phase legs decreases rapidly. Thus, we can tell that its resolution is very high compared with that of conventional seismic prospecting using GI gun array source. Besides, **Figure 5C** shows reflections from the water body layers between direct wave and seafloor reflection. There are several reflection events between R1 and R2. Among them, event R1 is the one with the strongest energy which is comparable to that of direct wave and seafloor reflection. Generally speaking, it is different to image seawater interface using convention seismic prospecting method, because the wave impedance of seawater interface is weaker than that of strata beneath the seafloor. Thus, high-resolution seismic prospecting is beneficial to imaging seawater layers. As shown in **Figure 5C**, distinct reflections from the seawater interface between R1 and R2 reveal that the field dataset recorded by DVCS is of high resolution.

The imaging resolution of vertical cables is superior to surface seismic methods for an image point, horizontal reflector, and dipping reflector (Wilson, 2002). For the sake of preserving the resolution, we perform RTM on the primary reflections in the common receiver gather sorted from original VCS dataset, with accurate velocity model (**Figure 8**). As shown in **Figure 9A**, we obtained the imaging section with high resolution and high SNR. Seafloor reflection and sediments waves beneath the seafloor can be clearly recognized from this imaging section. In order to illustrate the high resolution of the imaging section with RTM, the P-wave velocity (the red curve in **Figure 10A**) from logging data at Site SH7 is superimposed to highlight on the imaging section. It shows that the resolution of the imaging section is relative to that of the P-wave velocity curve, especially around depth of 1249 m. In addition, we calculated the synthetic seismogram (the red curve in **Figure 10B**) using the extracted source wavelet with the logging data at Site 7. In **Figure 10B**, seismic traces around Site SH7 agree well with the synthetic seismogram (the red curve). Consequently, this RTM result has adequate resolution to figure out the structure of hydrate-bearing sediments.

Characterization of Hydrate-Bearing Sediments

Bottom simulating reflectors (BSRs) are phase reversed polarity reflections with respect to the seafloor reflection, parallel to the

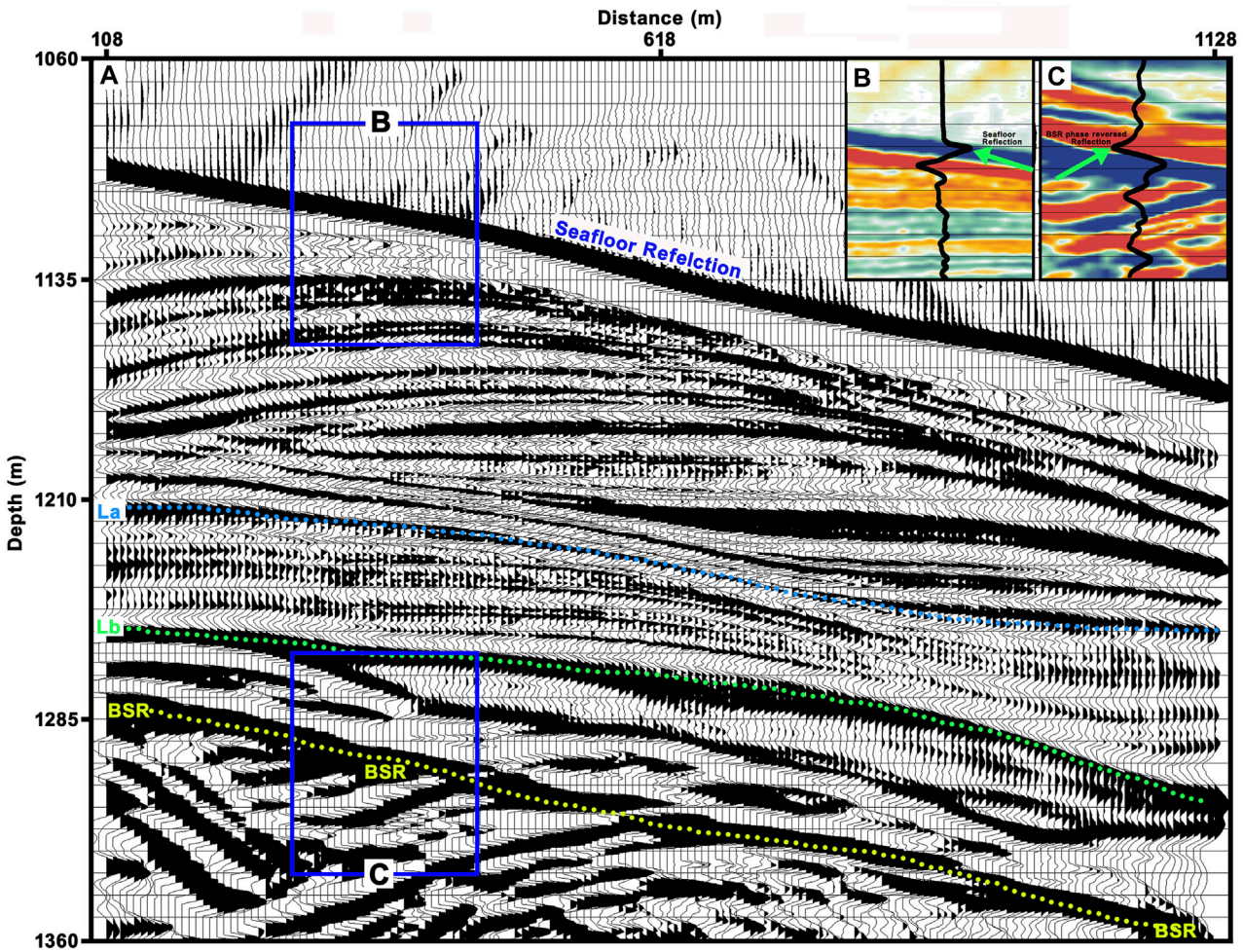

FIGURE 9 | (A) The RTM imaging section with velocity model shown in **Figure 8**. The yellow dotted line shows the BSR. **(B)** Closeup view shows the signature of seafloor reflection. **(C)** Closeup view shows the signature of bottom simulating reflector (BSR) which is phase reversed reflection.

seafloor. In general, the occurrence of the BSRs is used to indicate the presence of gas hydrate on seismic sections (Wang et al., 2014). BSRs coincide with the base of gas hydrate stability zone (BGHSZ) so that it can be used to infer the presence of free gas below the BSRs. Consequently, BSRs are considered as a prominent indication between overlying hydrate-bearing sediments and underlying free gas zone. A high amplitude continuous BSR with reversed polarity was identified on the RTM imaging section through Site SH7, indicated by the yellow dotted line in **Figure 9A**. This regional BSR cross-cuts the reflection from the normal strata, approximately located at the depth of 1292 m under the sea surface around Site SH7.

The Site SH7 was drilled in water depths of 1,105 m. In the conventional surface seismic section crossing Site SH7, the continuous, prominent BSR was identified at a depth of 181 m below the seafloor (mbsf) and the depth to the BGHSZ at 184 mbsf was calculated from core temperature measurement at this site (Wang et al., 2014). Compared with this depth of BSR inferred by surface seismic, the depth of BSR on the RTM section from VCS dataset is about 187 mbsf. The difference between the two depth values may be caused by different resolution of seismic dataset, so we consider the depth of BSR on VCS RTM section is relatively reliable. High P-wave velocity and resistivity was measured from 155 to 180 mbsf at Site SH7 (**Figure 11**) and it shows the gas hydrate-bearing sediments layer is about 25 m thick just above the predicted BGHSZ (Wang et al., 2011). Corresponding to this thick layer, these enhanced reflections appear in **Figure 9A**, between the green dotted line Lb and the yellow dotted line BSR. Free gas is believed to be trapped in unconsolidated sediments, underneath the hydrate-bearing sediments. **Figure 11** shows P-wave velocity elevates at depths ranging from 125 to 150 mbsf, and it indicates the lithological changes (Wang et al., 2014). Reflections with respect to these lithological changes appear between the blue dotted line La and the green dotted line Lb in **Figure 9A**. These reflections reveal the fine structure of hydrate-bearing sediments, which is difficult to obtain this structure by conventional seismic surveys. The variation of these reflections indicates heterogeneous nature of

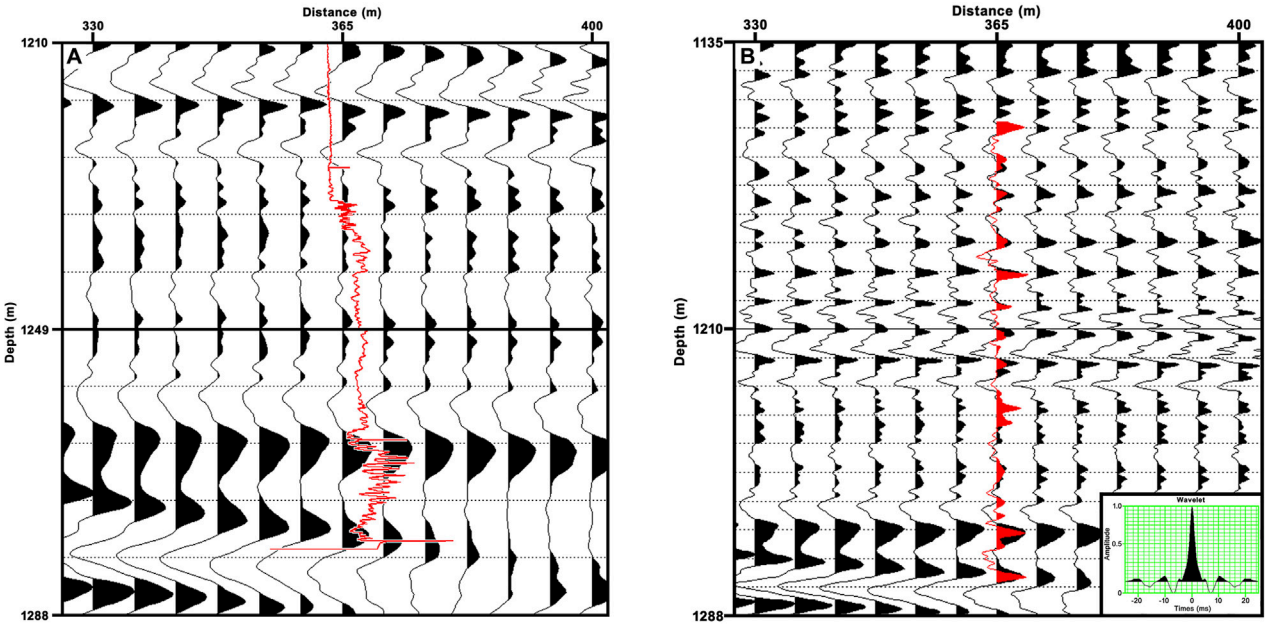

FIGURE 10 | (A) The comparison of VCS imaging section through Site SH7. The red curve is the P-wave velocity from the logging data at Site SH7. **(B)** Synthetic seismogram (the red curve) intersects the imaging section.

the hydrate-bearing sediments. Considering the characteristics of gas hydrate formation and accumulation, we infer that these hydrate-bearing sediments are partially filled with consolidated hydrates and it leads to lithological changes in sediments layers. As a result, reflections from these hydrate-bearing sediments vary considerably in amplitudes, frequencies, and phases. In summary, RTM section from VCS dataset provides fine structure of hydrate-bearing sediments with high resolution and high SNR.

CONCLUSION

High-quality 3D VCS data were acquired for natural gas hydrates exploration in deep water, South China Sea. However, it is difficult to image these datasets with conventional seismic processing method due to the irregular acquisition characteristics of VCS. We make use of CSP-based technique to perform accurate velocity analysis to obtain a reliable velocity model. Then, we perform RTM on common receiver gather from VCS dataset with this velocity wavefield and obtain the high-resolution image of hydrate-bearing sediments. The imaging section clearly shows BSR and the reflections from sediments partially filled with the consolidated hydrates. It is well in agreement with the synthetic seismogram trace generated by the P-wave velocity from log data at Site SH7, and it illustrates that the imaging result of VCS dataset is of higher resolution and higher SNR than that of the conventional surface seismic exploration. In conclusion, the results clearly show a great improvement in seismic imaging of hydrate-bearing sediments with high resolution which cannot be achieved by conventional seismic survey for hydrates. The VCS survey will become an

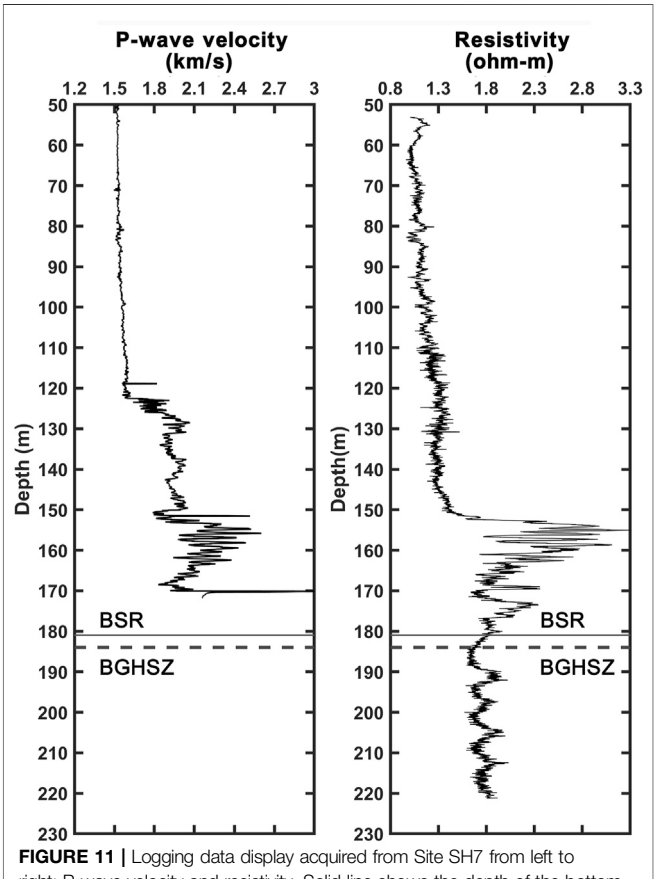

FIGURE 11 | Logging data display acquired from Site SH7 from left to right: P-wave velocity and resistivity. Solid line shows the depth of the bottom simulating reflector (BSR) and the dashed line shows the base of gas hydrate stability zone (BGHSZ).

effective approach to explore and develop natural gas hydrates in the future.

DATA AVAILABILITY STATEMENT

The raw data supporting the conclusions of this article will be made available by the authors, without undue reservation.

AUTHOR CONTRIBUTIONS

HL and LW contributed to design of the study. ZW debugged the programs of RTM. JZ made synthetic seismogram. LX and YY organized the database. LW wrote the first draft of the manuscript. All authors contributed to manuscript revision, read, and approved the submitted version.

FUNDING

This work was financially supported by the National Natural Science Foundation of China (No. 91958206), the Fundamental Research Funds for the Central Universities (201964016), the National Key R&D Program of China (No. 2017YFC0307401), the National High-Tech R&D Program (No. 2013AA092501), and the China Scholarship Council.

ACKNOWLEDGMENTS

The authors would like to thank the Guangzhou Marine Geological Survey Bureau of Chinese Geological Survey Bureau for conducting the vertical cable seismic acquisition experiment. They also thank the reviewers for their constructive comments and suggestions, which significantly improved the quality of this paper.

REFERENCES

Asakawa, E., Murakami, F., Sekino, Y., Okamoto, T., Ishikawa, K., Tsukahara, H., et al. (2012). "Development of Vertical Cable Seismic System, "74th EAGE Conference and Exhibition, *Extended Abstr.* P008. doi:10.3997/2214-4609.20148328

Asakawa, E., Murakami, F., Tsukahara, H., and Mizohata, S. (2014a). "Vertical Cable Seismic (VCS) Survey for Seafloor Massive Sulphide (SMS) Exploration," in 76th EAGE Conference and Exhibition. *Extended Abstr.* TH ELI2 14. doi:10.3997/2214-4609.20141468

Asakawa, E., Murakami, F., Tsukahara, H., and Mizohata, S. (2014b). "Development of Vertical cable Seismic (VCS) System for Seafloor Massive Sulfide (SMS)," in Proceedings of 2014 Oceans 76th EAGE Conference and Exhibition (St. John's, NL: IEEE), 1–7. doi:10.1109/OCEANS.2014.7003171

Asakawa, E., Murakami, F., Tsukahara, H., Mizohata, S., and Tara, K. (2015). "Vertical Cable Seismic (VCS) Survey for SMS Exploration in Izena Cauldron, Okinawa-Trough," in Vertical Cable Seismic Surveys for SMS exploration in Izena Cauldron, Okinawa-Trough: Offshore Technology Conference. doi:10.4043/25680-MS

Asakawa, E., Tara, K., Murakami, F., Tsukaraha, H., and Mizohata, S. (2016). "Vertical Cable Seismic (VCS) Survey for Buried Hydrothermal Sulfide Deposit," in Vertical Cable Seismic (VCS) Survey for Buried Hydrothermal Sulfide Deposit: Offshore Technology Conference. doi:10.4043/26583-MS

Bancroft, J. C., and Xu, Y. (1999). "Equivalent Offset Migration for Vertical Receiver Arrays," in Equivalent offset migration for vertical receiver arrays: SEG Annual Meeting, P1279–P1282. Expanded Abstracts. doi:10.1190/1.1820742

Baysal, E., Kosloff, D. D., and Sherwood, J. W. C. (1983). Reverse Time Migration. *Geophysics* 48, 1514–1524. doi:10.1190/1.1441434

Bednar, J. B. (2005). A Brief History of Seismic Migration. *Geophysics* 70 (3), 3mj–20mj. doi:10.1190/1.1926579

Guimarães, M. G., Sekharan, K. K., Sukup, D., and Krail, P. (1998). "3-D Pre-stack Depth Migration of Vertical cable Data over SEG/EAGE Physical Model," in 3-D Pre-stack Depth Migration of Vertical Cable Data Over SEG/EAGE Physical Model: SEG Annual Meeting. SEG-1998-1182. doi:10.1190/1.1820104

Huang, J-Y., Wu, Z-L., Wang, W-W., and Cheng-liang, X. (2016). Key Techniques and Experimental Study of Vertical cable Seismic System for Gas Hydrate. *Adv. New Renew. Energ.* 4 (3), 219–224. doi:10.3969/j.issn.2095-560X.2016.03.009

Ikelle, L. T., and Wilson, R. J. (1999). Potential Impacts of Vertical cable (VC). *The Leading Edge* 18 (10), 1154–1157. doi:10.1190/1.1438172

Jamali H., E., Katou, M., Tara, K., Asakawa, E., and Mikada, H. (2019). Mirror Reverse Time Migration Using Vertical cable Seismic Data for Methane Hydrate Exploration. *Geophysics* 84 (6), B447–B460. doi:10.1190/geo2018-0422.1

Krail, P. M. (1993). Sub-salt Acquisiton with a marine Vertical cable. *Extended Abstr.*, 1376. doi:10.1190/1.1822401

Krail, P. M. (1994). Vertical cable as a Subsalt Imaging Tool. *The Leading Edge* 13 (8), 885–887. doi:10.1190/1.1437049

Krail, P. M. (1997). "Vertical cable marine Seismic Acquisition," in Offshore Technology Conference. doi:10.4043/8315-MS

Leach, P. (1997). Strathspey Vertical-Cable Seismic Survey: A North Sea First. *SPE, Abstr.*, 333–347. doi:10.2118/38508-MS

Li, Qing-Zhong. (2017). *High-resolution Seismic Exploration*. Tulsa: Society of Exploration Geophysicists.

McMechan, G. A. (1983). Migration by Extrapolation of Time-dependent Boundary Values*. *Geophys. Prospect.* 31 (3), 413–420. doi:10.1111/j.1365-2478.1983.tb01060.x

M. Krail, P. (1991). Case History Vertical cable 3D Acquisition. *Extended Abstr.*, B052. doi:10.3997/2214-4609.201410933

Shen, Y. Q., Valasek, P. A., Kelly, K. R., Whitmore, N. D., and Wyatt, K. D. (2000). *3-D Prestack Reverse-Time Depth Migration Applied to Vertical Cable Seismic Data*. SEG Tech. Progr. Expand. Abstr. 762–766. doi:10.1190/1.1816181

Wang, H. J. (2003). *Seismic Imaging and Anisotropic Inversion Using Vertical cable Data*. [doctor's thesis] (Edinburgh]: University of Edinburgh).

Wang, X., Collett, T. S., Lee, M. W., Yang, S., Guo, Y., and Wu, S. (2014). Geological Controls on the Occurrence of Gas Hydrate from Core, Downhole Log, and Seismic Data in the Shenhu Area, South China Sea. *Mar. Geology.* 357, 272–292. doi:10.1016/j.margeo.2014.09.040

Wang, X., Lee, M., Wu, S., and Yang, S. (2012). Identification of Gas Hydrate Dissociation from Wireline-Log Data in the Shenhu Area, South China Sea. *Geophysics* 77 (3), B125–B134. doi:10.1190/GEO2011-0324.1

Wang, X., Wu, S., Lee, M., Guo, Y., Yang, S., and Liang, J. (2011). Gas Hydrate Saturation from Acoustic Impedance and Resistivity Logs in the Shenhu Area, South China Sea. *Mar. Pet. Geology.* 28, 1625–1633. doi:10.1016/j.marpetgeo.2011.07.002

Wang, X., Zhao, Q., Wu, Z., Liu, B., and Huang, T. (2019). Research on Vertical cable Seismic Multiples Imaging Processing. *Arab J. Geosci.* 12, 129. doi:10.1007/s12517-019-4322-3

Wilson, R. J. (2002). *Potential Impacts of Vertical cable Seismic: Modeling, Resolution and Multiple Attenuation*. [master's thesis] ([College Station (TX): Texas A&M University).

Xing, L., Liu, H., Zheng, X., Liu, X., Zhang, J., Wang, L., et al. (2016). Phase Characteristic Analysis of Continuous Depth Air-Gun Source Wavelet. *J. Ocean Univ. China* 15 (5), 815–824. doi:10.1007/s11802-016-3167-6

Zhou, H.-W., Hu, H., Zou, Z., Wo, Y., and Youn, O. (2018). Reverse Time Migration: A prospect of Seismic Imaging Methodology. *Earth-Science Rev.* 179, 207–227. doi:10.1016/j.earscirev.2018.02.008

Zhou, H. (2014). *Practical Seismic Data Analysis*. New York: Cambridge University Press.

Conflict of Interest: The authors declare that the research was conducted in the absence of any commercial or financial relationships that could be construed as a potential conflict of interest.

Publisher's Note: All claims expressed in this article are solely those of the authors and do not necessarily represent those of their affiliated organizations, or those of the publisher, the editors, and the reviewers. Any product that may be evaluated in this article, or claim that may be made by its manufacturer, is not guaranteed or endorsed by the publisher.

frontiers in Earth Science

ORIGINAL RESEARCH
published: 25 November 2021
doi: 10.3389/feart.2021.782901

Imaging Complex Subsurface Structures for Geothermal Exploration at Pirouette Mountain and Eleven-Mile Canyon in Nevada

Yunsong Huang[1], *Miao Zhang*[1], *Kai Gao*[1], *Andrew Sabin*[2] *and Lianjie Huang*[1]*

[1]*Los Alamos National Laboratory, Geophysics Group, Los Alamos, NM, United States,* [2]*Navy Geothermal Program Office, China Lake, CA, United States*

OPEN ACCESS

Edited by:
Zhihui Zou,
Ocean University of China, China

Reviewed by:
Yike Liu,
Key Laboratory of Oil and Gas Resources Research, Institute of Geology and Geophysics (CAS), China
Bin He,
University of Toronto, Canada

***Correspondence:**
Lianjie Huang
ljh@lanl.gov

Specialty section:
This article was submitted to Solid Earth Geophysics, a section of the journal Frontiers in Earth Science

Received: *24 September 2021*
Accepted: *02 November 2021*
Published: *25 November 2021*

Citation:
Huang Y, Zhang M, Gao K, Sabin A and Huang L (2021) Imaging Complex Subsurface Structures for Geothermal Exploration at Pirouette Mountain and Eleven-Mile Canyon in Nevada. Front. Earth Sci. 9:782901. doi: 10.3389/feart.2021.782901

Accurate imaging of subsurface complex structures with faults is crucial for geothermal exploration because faults are generally the primary conduit of hydrothermal flow. It is very challenging to image geothermal exploration areas because of complex geologic structures with various faults and noisy surface seismic data with strong and coherent ground-roll noise. In addition, fracture zones and most geologic formations behave as anisotropic media for seismic-wave propagation. Properly suppressing ground-roll noise and accounting for subsurface anisotropic properties are essential for high-resolution imaging of subsurface structures and faults for geothermal exploration. We develop a novel wavenumber-adaptive bandpass filter to suppress the ground-roll noise without affecting useful seismic signals. This filter adaptively exploits both characteristics of the lower frequency and the smaller velocity of the ground-roll noise than those of the signals. Consequently, this filter can effectively differentiate the ground-roll noise from the signal. We use our novel filter to attenuate the ground-roll noise in seismic data along five survey lines acquired by the U.S. Navy Geothermal Program Office at Pirouette Mountain and Eleven-Mile Canyon in Nevada, United States. We then apply our novel anisotropic least-squares reverse-time migration algorithm to the resulting data for imaging subsurface structures at the Pirouette Mountain and Eleven-Mile Canyon geothermal exploration areas. The migration method employs an efficient implicit wavefield-separation scheme to reduce image artifacts and improve the image quality. Our results demonstrate that our wavenumber-adaptive bandpass filtering method successfully suppresses the strong and coherent ground-roll noise in the land seismic data, and our anisotropic least-squares reverse-time migration produces high-resolution subsurface images of Pirouette Mountain and Eleven-Mile Canyon, facilitating accurate fault interpretation for geothermal exploration.

Keywords: anisotropic least-squares reverse-time migration, imaging, geothermal exploration, ground-roll suppression, fault, complex structure

INTRODUCTION

The geothermal exploration areas at Pirouette Mountain and Eleven-Mile Canyon are located near the margins of Dixie Valley in Nevada, United States. Eleven-Mile Canyon lies next to the surface rupture terminations of 1954 Fairview Peak—Dixie Valley earthquake sequence (Caskey et al., 1996). The area contains a complex network of steeply-dipping faults and fractures, which creates the highly permeable fractures for the potential production zone at 2–3 km in depth (Unruh et al., 2016). It is crucial to accurately image and delineate subsurface fracture/fault zones for geothermal exploration and optimizing well placement, because faults/fracture zones provide paths for hydrothermal flow, but they may also be effective barriers to geothermal flow in some situations (Ba et al., 2015). It is particularly challenging to accurately image the subsurface structures at Pirouette Mountain and Eleven-Mile Canyon because of complex heterogeneities and possible anisotropies in both fracture zones and geologic formations.

In 2013, the U.S. Navy Geothermal Program Office carried out a seismic reflection survey (Alm et al., 2016) along five lines to evaluate the geothermal potential at Pirouette Mountain and Eleven-Mile Canyon, NV. Lines 1, 2, 3, and 4 were aligned west-east to cross the valley, while Line 5 was placed along a north-south trend to intersect Lines 1–3 (**Figure 1**). Lines 1, 2, 3, and 5 are located at Pirouette Mountain, and Line 4 is at Eleven-Mile Canyon. Such a geometry of the survey aimed to allow enhanced horizon and fault interpretations.

For imaging complex subsurface structures at Pirouette Mountain and Eleven-Mile Canyon, we first need to properly suppressing ground-roll noise in the acquired seismic data.

Ground-roll noise refers to high-amplitude and coherent surface waves (Sheriff, 2002), which not only provide little information regarding deeper reflectors of interest, but also contaminate subsequent geophysical imaging, particularly for waveform inversion and least-squares reverse-time migration that are based on waveform fitting. Although Rayleigh waves dominate ground-roll noise, the latter may also include Love waves, reverberated refractions, and waves scattered by near-surface heterogeneities. Ground-roll noise often masks shallow reflections at near offsets and deep reflections at far offsets. This problem is acute for land

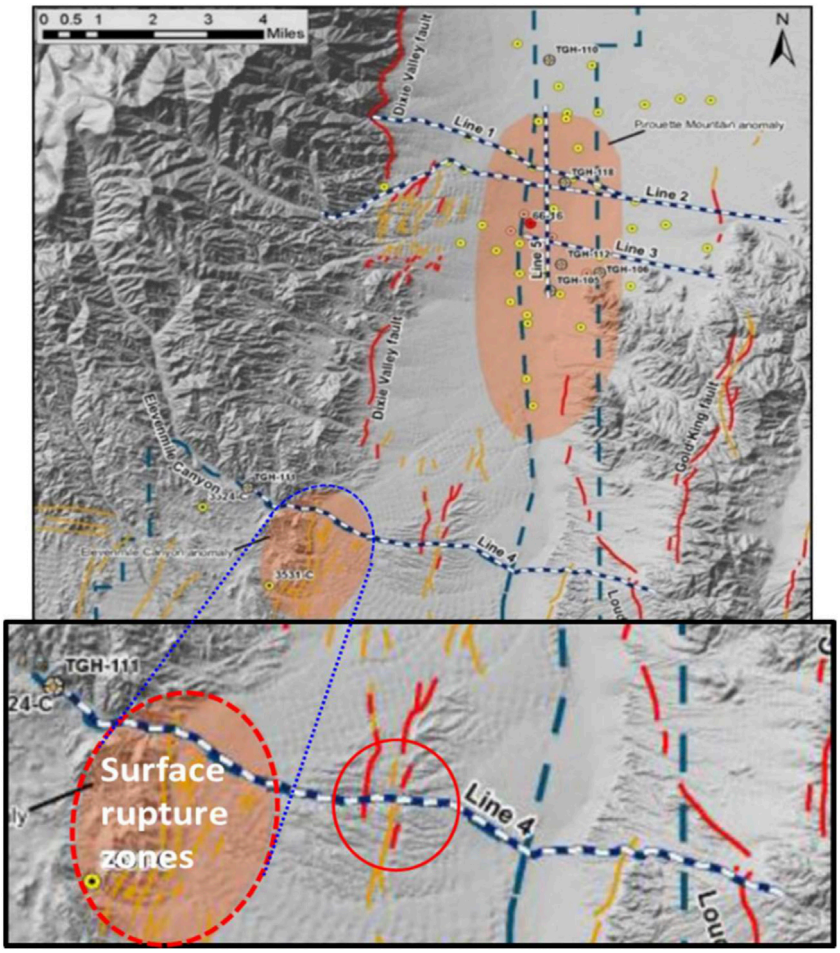

FIGURE 1 | Location map of the geothermal exploration areas at Pirouette Mountain and Eleven-Mile Canyon in southern Dixie Valley, Nevada, with five lines of seismic survey depicted in rails. The faults shown are from the U.S. Geological Survey Quaternary fault and fold database. Surface rupture zones correspond to the 1954 earthquake sequence (Unruh et al., 2016). The northern shaded region is at Pirouette Mountain, and the southern shaded region is at Eleven-Mile Canyon.

surface seismic data acquired at Pirouette Mountain and Eleven-Mile Canyon for geothermal exploration.

Because of near-surface layers and unconsolidated weathering zones, ground-roll noise propagates more slowly and exhibits lower frequency than do seismic reflections. A simple method to reduce ground-roll noise is therefore to apply a low-cut filter.

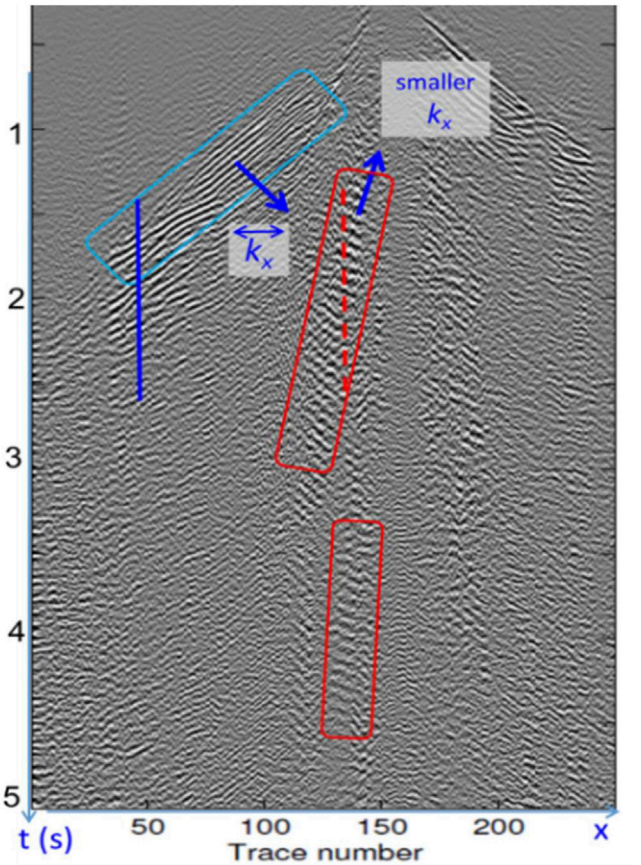

FIGURE 2 | A representative common-shot gather of surface seismic data. Red rectangles enclose the ground-roll noise. The cyan rectangle encloses reflection signals. The vertical red dashed line and blue solid line stride across the ground-roll noise and reflection signals, respectively. The single-barbed arrows indicate the wavenumber directions.

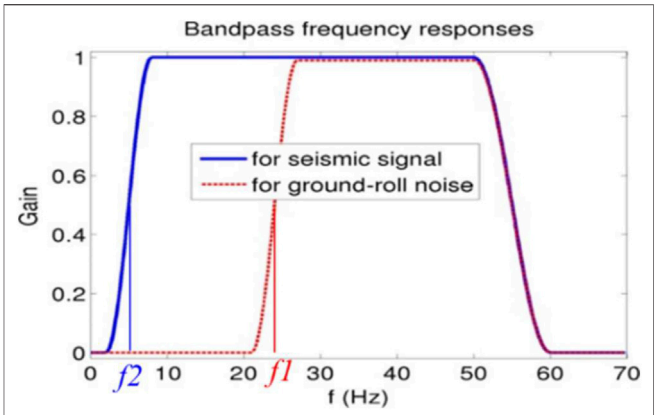

FIGURE 4 | If the input data are likely seismic signals, a bandpass filter with low cut-off frequency f_2 is preferable. Otherwise, a bandpass filter with a relatively high cut-off frequency f_1 is used to reject the ground-roll noise, of which the spectrum lies below f_1.

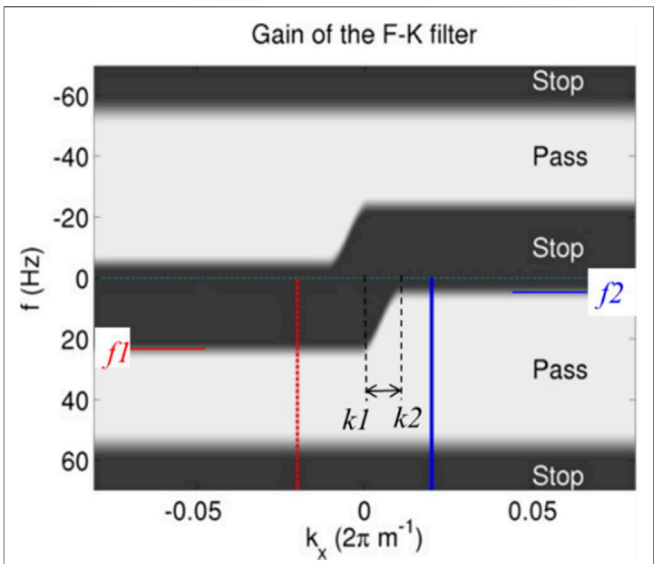

FIGURE 5 | Illustration of the new wavenumber-adaptive bandpass filter for seismic traces on the left side of the shot in a common-shot gather. The vertical slices along the blue and red lines yield the bandpass profiles in **Figure 4**. The cut-off frequencies f_1 and f_2 take the same values as in **Figure 4**.

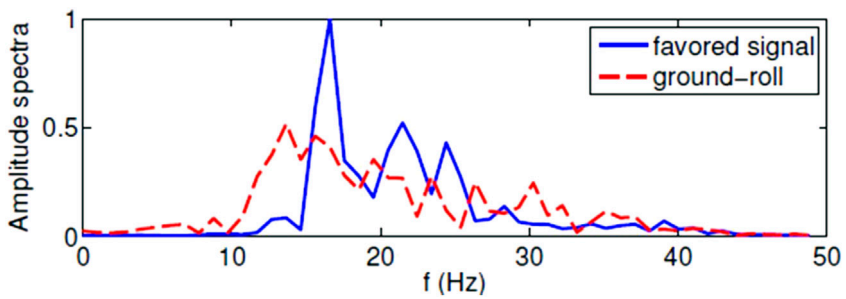

FIGURE 3 | The spectra of the ground-roll noise (red) and the reflection signal (blue).

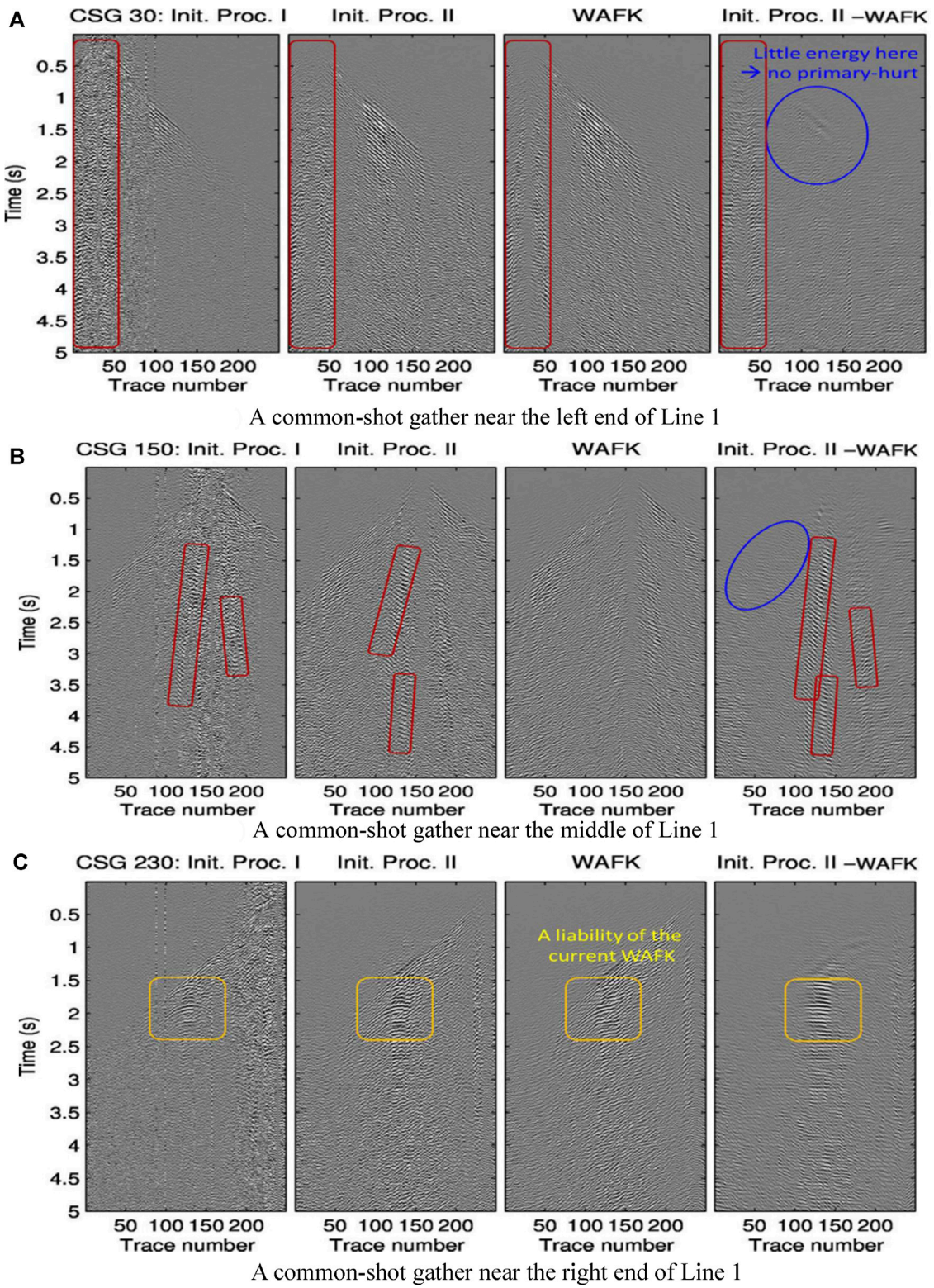

FIGURE 6 | Three common-shot gathers (CSGs 30, 150, and 230) corresponding to the three shots along Line 1: **(A)** CSG near the left end, **(B)** CSG around the middle, and **(C)** CSG near the right end of Line 1. The leftmost column shows an industry-processed data. The column titled "Init. Proc. II" presents the other industry-processed data. Our wavenumber-adaptive F-K filter (WAFK) operates upon this column, yielding results shown in column "WAFK." The rightmost column shows the difference between the inputs and outputs of WAFK. **(A)** A common-shot gather near the left end of Line 1. **(B)** A common-shot gather near the middle of Line 1. **(C)** A common-shot gather near the right end of Line 1.

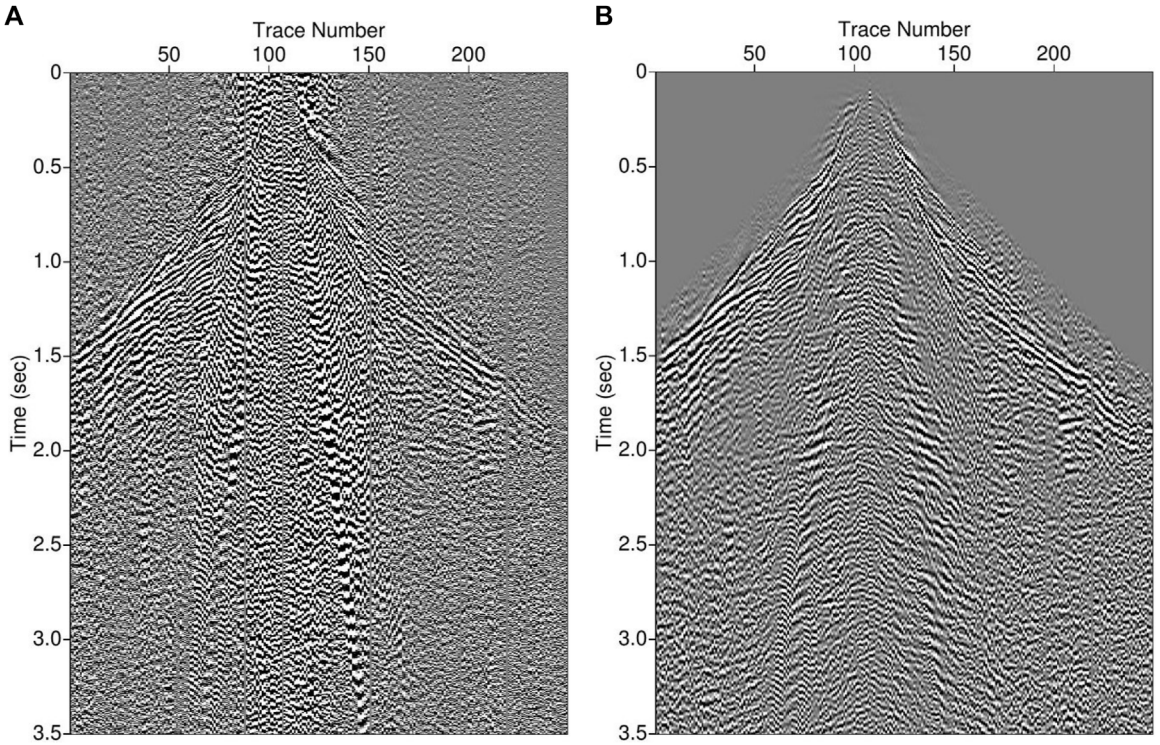

FIGURE 7 | Another example of a common-shot gather from Pirouette Mountain and Eleven-Mile Canyon before **(A)** and after **(B)** wavenumber-adaptive bandpass filtering. Waveforms before first arrivals in the right panel are muted with a cosine taper near the first arrivals. Coherent subsurface reflections become visible after filtering.

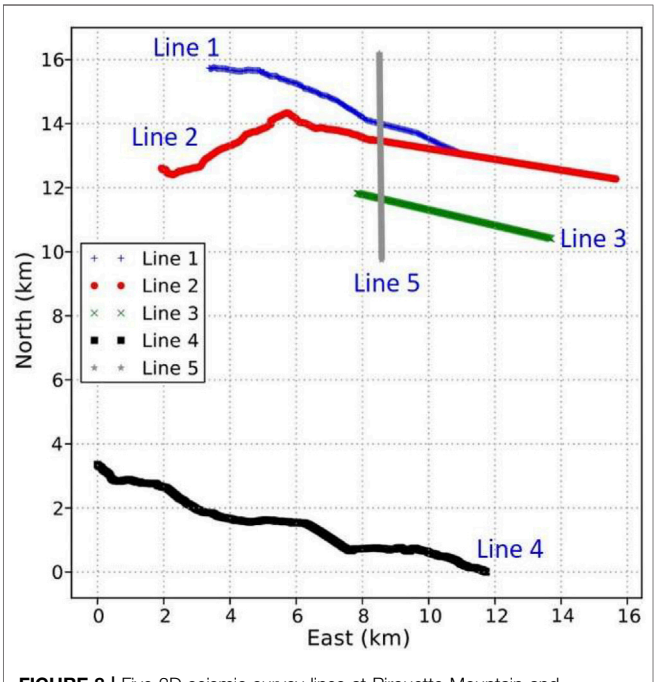

FIGURE 8 | Five 2D seismic survey lines at Pirouette Mountain and Eleven-Mile Canyon, Nevada, United States.

Unfortunately, this method also eliminates the low-frequency part of seismic reflection data, which is critical to waveform inversion and least-squares reverse-time migration.

Several methods were developed to suppress the ground-roll noise over the past several decades. A common motivation is to express the signal and the noise in a certain transform domain that helps separate the signal from the noise. A number of filtering methods were designed (Shieh and Herrmann, 1990), but the reflection data within the frequency bands overlapping with those of the noise could be filtered out (Coruh and Costain, 1983). One of techniques in the transform domain uses *f-k* filtering (Embree et al., 1963; Treitel et al., 1967; Yilmaz, 2001). Radon, or τ-p, transform was also applied to ground-roll noise suppression (Brysk and McCowan, 1986; Henley, 2003). Sparse Radon transforms (Trad et al., 2003) produce sparse representations of the signal and noise in the transform domain, thereby facilitating signal and noise separation. Challenges exist, however, when the moveout of seismic signals in a common-shot gather is irregular because of irregularities in the surface topography and weathering zones. Other techniques for suppressing the ground-roll noise include interferometry (Halliday, 2011), Karhunen–Loève (K–L) transform (Liu, 1999), singular value decomposition (SVD) (Jin and Ronen, 2005), wavelet transform (Deighan and Watts, 1997), and Wiener filtering (Karsli and Bayrak, 2008).

We develop a novel method to suppress the ground-roll noise without affecting reflection data. To distinguish the ground-roll noise from the signal, we exploit the information of the frequency content, wavenumber, and the relative offset in seismic data. Ground-roll noise exhibits dispersion, resulting in shingled events. The dip of each individual event lies opposite to those of reflections. This observation allows us to design a bandpass filter that is adaptive to wavenumber to fulfill our aim of ground-roll noise suppression.

After suppressing ground-roll noise in the seismic data acquired at Pirouette Mountain and Eleven-Mile Canyon using our novel wavenumber-adaptive bandpass filter, we can use the data to image subsurface structures and faults for geothermal exploration.

Reverse-time migration (RTM) is a powerful tool for imaging complex subsurface structures. In essence, RTM relocates the wave energy in seismic data to subsurface reflectors where the seismic waves are reflected before reaching seismic receivers at the surface for a surface seismic survey. Such a relocation of seismic-wave energy relies on numerical simulations of seismic-wave forward and backward propagation. When the subsurface media are anisotropic, as are typical in complex geothermal exploration fields (Gao and Huang, 2015), it is crucial to properly account for the subsurface anisotropic properties to allow accurate simulations of seismic wavefields. Anisotropic RTM can account for anisotropy for high-resolution subsurface imaging of complex structures with faults.

While RTM performs wave-energy relocation non-iteratively, an extension of RTM is termed least-squares RTM (LSRTM) (Nemeth et al., 1999), which iteratively adjusts the subsurface reflectors so that synthetic seismic data would maximally resemble (in the sense of least-squares residue) real seismic data. Because of ambiguity in the velocity model and limited numbers of sources and receivers, the non-iterative RTM suffers from migration artifacts. By contrast, because of the feedback control mechanism in the iterative LSRTM, the discrepancy between the imaged reflectors and the physical reflectors is restrained.

We apply our anisotropic least-squares reverse-time migration algorithm to the seismic data acquired at the Pirouette Mountain and Eleven-Mile Canyon geothermal exploration areas for reliable imaging of the complex subsurface structures with faults. First, we use our wavenumber-adaptive bandpass filter to suppress the ground-roll noise of the five 2D lines of surface seismic data acquired at Pirouette Mountain and Eleven-Mile Canyon. Then we apply our anisotropic LSRTM to the resulting data to obtain high-resolution subsurface images, and compare the images with industrial images and those obtained using anisotropic RTM.

We organize our paper as follows. We first introduce the methodology of our wavenumber-adaptive bandpass filter and anisotropic least-squares reverse-time migration, present results of ground-roll suppression using our wavenumber-adaptive bandpass filter, give anisotropic LSRTM images with comparison with industrial images and those obtained using anisotropic RTM images, and draw our findings in the Conclusion section.

METHODOLOGY

We present the methodology of our novel wavenumber-adaptive bandpass filter for suppressing the ground-roll noise, and our anisotropic least-squares reverse-time migration below.

Wavenumber-Adaptive Bandpass Filter

In a typical common-shot gather of surface seismic data, the ground-roll noise appears to be coherent and energetic (**Figure 2**). **Figure 3** shows spectra of two temporal slices of the reflection signals (blue line in **Figure 2**) and the ground-roll noise (red dashed line in **Figure 2**). Although the ground-roll noise is of lower frequency compared with the signal, it is evident that there is much overlap between the frequency bands of the signal and the noise. Note

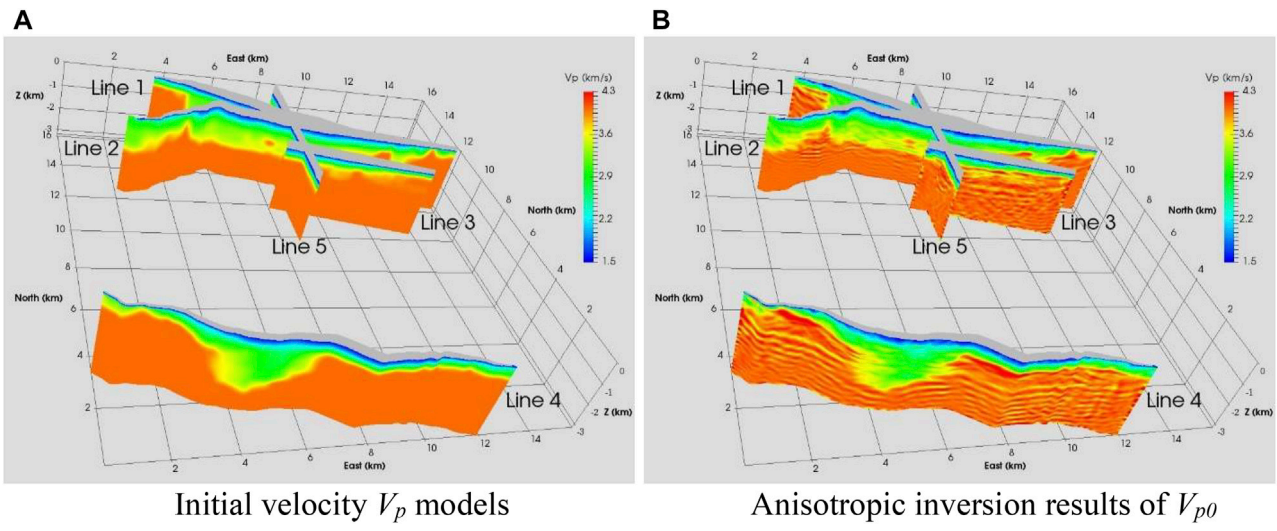

FIGURE 9 | Initial velocity models V_p and anisotropic waveform inversion results of V_{p0} along five 2D lines at Pirouette Mountain and Eleven-Mile Canyon. **(A)** Initial velocity V_p models. **(B)** Anisotropic waveform inversion results of V_{p0}.

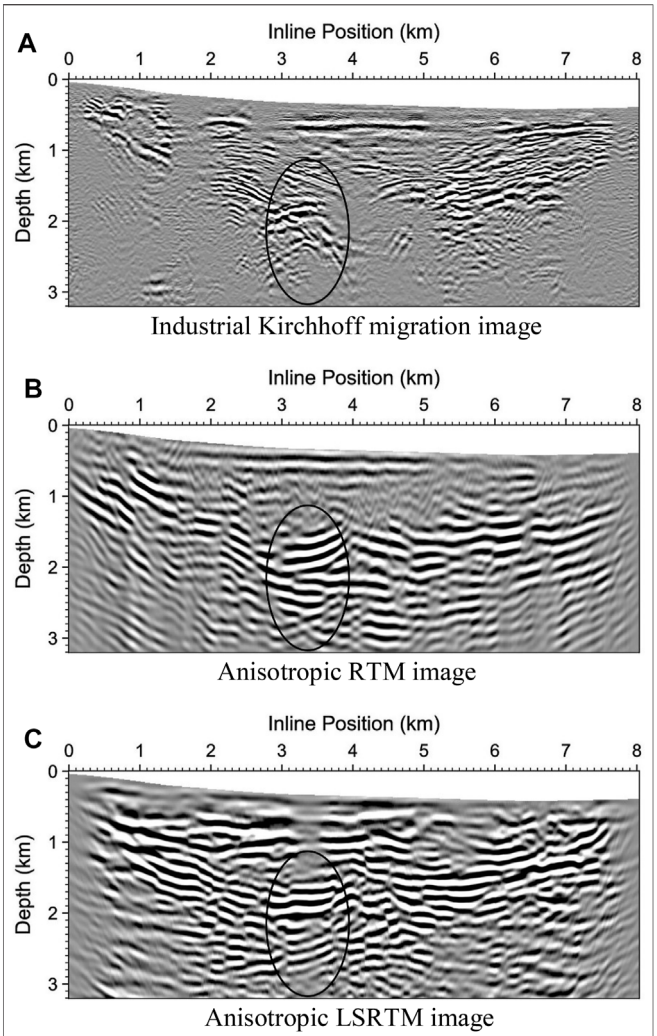

FIGURE 10 | Subsurface migration images of Line 1 at Pirouette Mountain produced using various migration methods: **(A)** Industrial Kirchhoff migration, **(B)** Anisotropic RTM, **(C)** Anisotropic LSRTM. Two nearly-vertical faults can be clearly identified within the ellipse region in **(C)**.

that the slice for the ground-roll noise (red dashed line in **Figure 2**) may also contain signals. This explains the existence of the high-frequency component (above 15 Hz) in the red dashed curve in **Figure 3**. In the low-frequency band, the signal spectrum (blue curve) encroaches on the spectrum of the ground-roll noise. Therefore, a simple low-cut filtering to suppress the ground-roll noise would also filter out some low-frequency component of the signal, while low-frequency data are crucial for full-waveform inversion.

If an input trace is the signal (e.g., of the blue spectral profile in **Figure 3**), we would enforce a wide bandpass filter, e.g., of the blue filtering profile in **Figure 4**. This filter is wide because the low cut-off frequency f_2 is small. On the other hand, if an input trace is the ground-roll noise, we would enforce a narrow bandpass filter, e.g., of the red filtering profile in **Figure 3**. This filter is narrow because the low cut-off frequency f_1 is large. In reality, however, we do not know whether an input trace is signal or ground-roll noise a priori. Fortunately, the wavenumbers in common-shot gathers can indicate the likelihood whether an input trace is the ground-roll noise.

Figure 2 shows that the wavenumber-magnitude $|k_x|$ of the ground-roll noise is smaller than that of the reflection signal, because the apparent horizontal wavelength λ_x of the ground-roll noise is larger than that of the reflection signal. Furthermore, the dipping angles of the narrow 'wavefronts' of the ground-roll noise within the red rectangles are opposite to those of the signal within the cyan rectangle. One can infer whether an input is the ground-roll noise using this wavenumber information. We use this information to design an *f-k* filter as shown in **Figure 5** for suppressing the ground-roll noise.

For seismic traces on the left side of the shot in a common-shot gather, any vertical cross-section of **Figure 5** is a bandpass filter, similar to the profiles in **Figure 4**. When k_x is large, the input should be signal, and therefore, the bandpass filter would have a small low-cut frequency f_2 value. On the other hand, when signed k_x is small, the input should be the ground-roll noise, and therefore, the bandpass filter would have a large low-cut frequency f_1. The k_1 and k_2 values in **Figure 5** define a transition zone between those two bandpass filters. Since the bandpass filter's parameterization changes with respect to wavenumber k_x, we name our filter "the wavenumber-adaptive bandpass filter." For seismic traces on the right side of a shot in a common-shot gather, **Figure 5** is mirror-reflected with respect to the k_x axis.

We use the following procedure to determine parameters of the wavenumber-adaptive bandpass filter:

1) Pick f_2, e.g., 5 Hz, and f_1, e.g., 24 Hz (**Figure 4**).
2) Work on a few common-shot gathers. Enclose regions of ground-roll (G) and reflections (R), e.g., **Figure 2**. Let the objective function $J = e(\mathrm{R}) - e(\mathrm{G})$, where e is average energy.
3) Pick initial values of $k_1 = 0$, $k_2 = 2\pi/\lambda_2$ where $\lambda_2 = 578$ m. Update k_1 and k_2 by maximizing J (**Figure 5**).
4) Construct the F-K filter (**Figure 5**).

Then we use the following procedure to attenuate the ground-roll noise:

1) For a common-shot gather (CSG) with shot s_x, pick the left part where traces $g_x < s_x + margin$.
2) Apply the F-K filter (**Figure 5**) on this left part, to yield AGN1.
3) For this same CSG, pick the right part where traces $g_x > s_x - margin$.
4) Mirror-reflect the F-K filter in **Figure 5**; namely $k_x \leftarrow -k_x$.
5) Apply this mirror-reflected F-K on the right part, to yield AGN2.
6) Merge AGN1 and AGN2; use a cosine interpolation weight in their overlapping regions.

Anisotropic Least-Squares Reverse-Time Migration

Least-squares reverse-time migration (LSRTM) seeks to improve a reflectivity model m over iterations, by minimizing a least-squares data residue J defined as

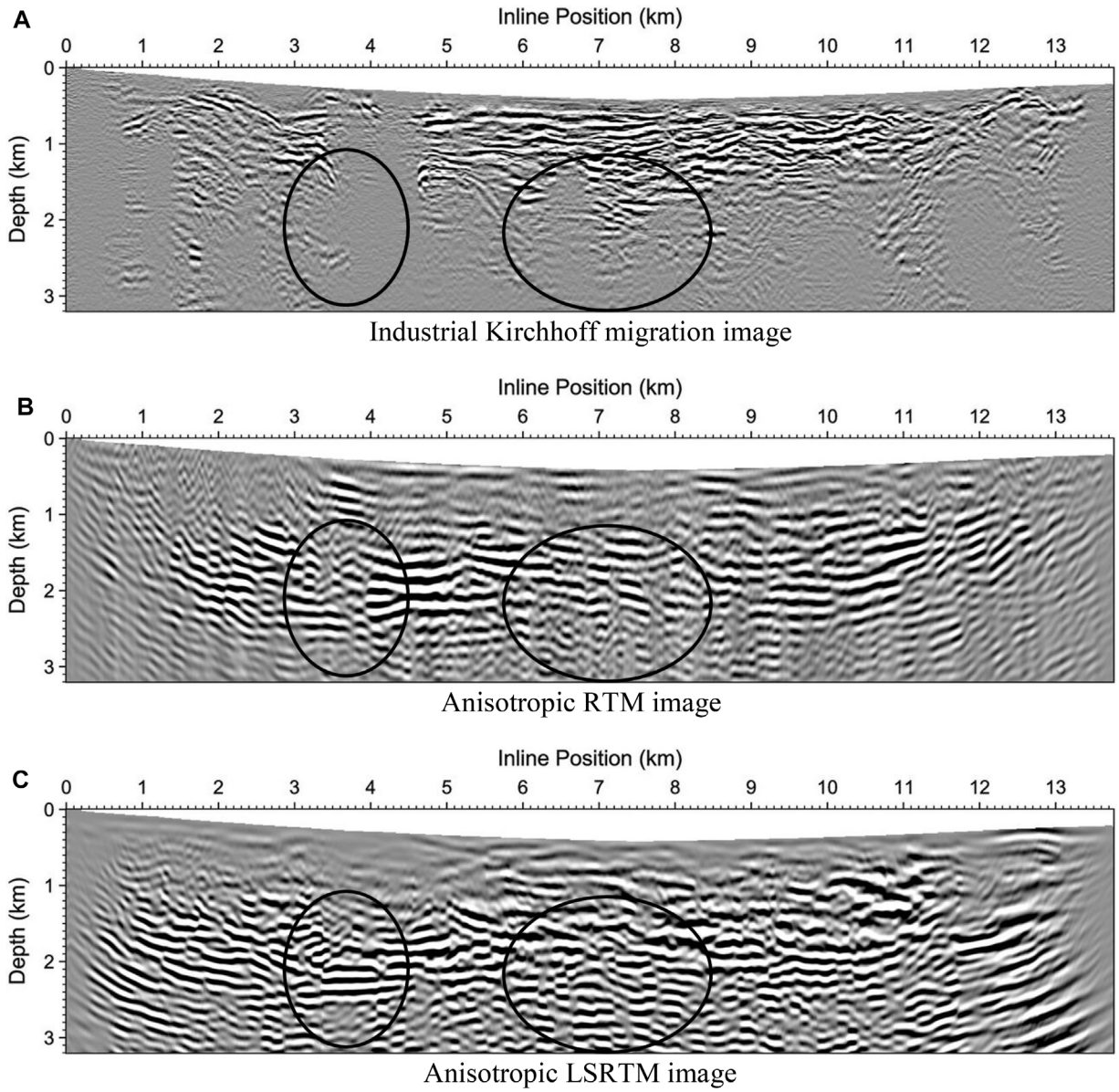

FIGURE 11 | Subsurface migration images of Line 2 at Pirouette Mountain produced using various migration methods: **(A)** Industrial Kirchhoff migration, **(B)** Anisotropic RTM, **(C)** Anisotropic LSRTM. The images within the ellipse regions in **(C)** are much better than those in **(B)**, and are not imaged in **(A)**.

$$J = \frac{1}{2} \| \mathbf{d} - \mathbf{Lm} \|_2^2, \tag{1}$$

where **d** represents observed seismic data, and operator **L** is the Born modeling operator. The Born modeling operator is based on the full-wavefield propagator. For 2D tilted transversely isotropic (TTI) media, we adopt a decoupled qP-wave equation to describe the qP-wave propagation (Zhan et al., 2012):

$$\frac{1}{V_{p0}^2} \frac{\partial^2 P}{\partial t^2} = \nabla_{\text{aniso}}^2 P, \tag{2}$$

where the spatial Laplacian ∇_{aniso}^2 for acoustic TTI media is

$$\nabla_{\text{aniso}}^2 = -\left\{ \begin{array}{l} k_x^2 + k_z^2 \\ + \left(2\varepsilon \cos^4\theta + 2\delta \sin^2\theta \cos^2\theta\right) \frac{k_x^4}{k_x^2 + k_z^2} + \left(2\varepsilon \sin^4\theta + 2\delta \sin^2\theta \cos^2\theta\right) \frac{k_z^4}{k_x^2 + k_z^2} \\ + \left(-4\varepsilon \sin 2\theta \cos^2\theta + \delta \sin 4\theta\right) \frac{k_x^3 k_z}{k_x^2 + k_z^2} + \left(3\varepsilon \sin^2 2\theta - \delta \sin^2 2\theta + 2\delta \cos^2 2\theta\right) \frac{k_x^2 k_z^2}{k_x^2 + k_z^2} \end{array} \right\} \tag{3}$$

where V_{p0} is the qP-wave velocity along the TTI symmetry axis; k_x and k_z are the spatial wavenumbers in the x and z directions, respectively; ε and δ are the Thomsen parameters (Thomsen, 1986), where ε describes the difference between the qP-wave velocities perpendicular to and parallel with the TTI symmetry

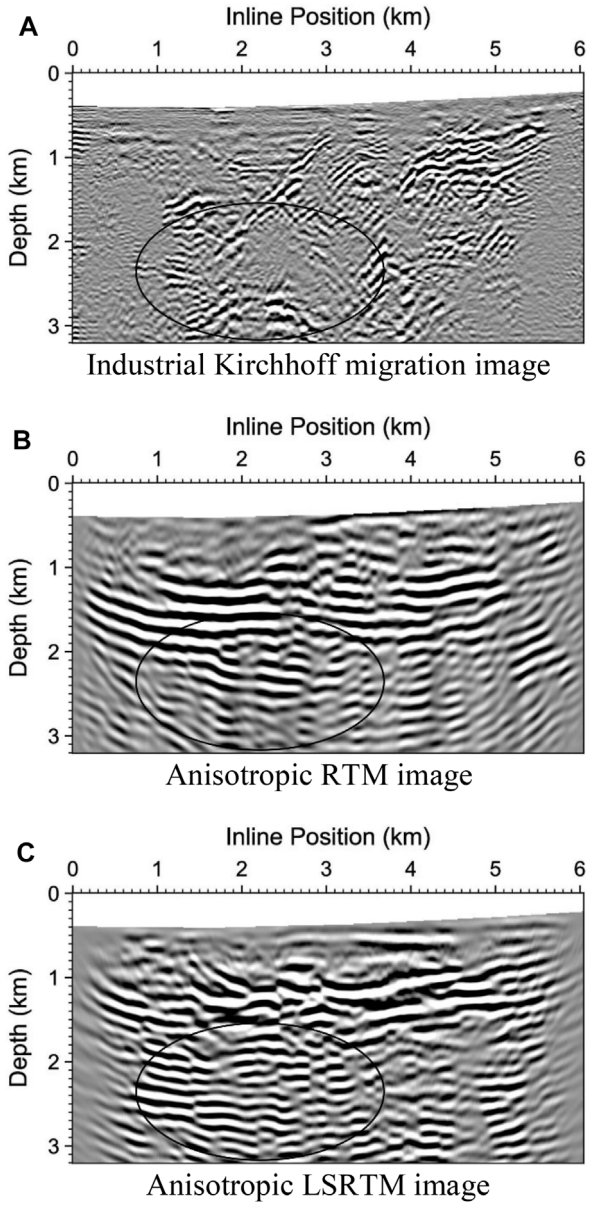

FIGURE 12 | Subsurface migration images of Line 3 at Pirouette Mountain produced using various migration methods: **(A)** Industrial Kirchhoff migration, **(B)** Anisotropic RTM, **(C)** Anisotropic LSRTM. The image within the ellipse region in **(C)** has higher resolution than that in **(B)**, and is imaged very poorly in **(A)**.

axis (i.e., the long offset effect), δ describes the near-symmetry-axis qP-wave velocity variation (i.e., the short offset effect), and θ is the tilt angle of the TTI symmetry axis.

To minimize the misfit functional J, $\mathbf{m}$ is updated iteratively through

$$\begin{aligned}\mathbf{m}^{(k+1)} &= \mathbf{m}^{(k)} - \alpha^{(k)}\nabla_{\mathbf{m}}J \\ &= \mathbf{m}^{(k)} + \alpha^{(k)}\mathbf{L}^{\mathrm{T}}\left(\mathbf{d} - \mathbf{L}\mathbf{m}^{(k)}\right),\end{aligned} \tag{4}$$

where the superscripts (k) and $(k+1)$ denote the k^{th} and $(k+1)^{\mathrm{th}}$ iteration, respectively, and $\alpha^{(k)}$ denotes the step length at the k^{th} iteration. Note that when $m^{(k)} = 0$ at the second line of **Eq. (4)**, the line is proportional to $L^{\mathrm{T}}0$, which is considered as the image of RTM. Therefore, RTM is merely the first iteration of LSRTM when starting from $m^{(0)} = 0$.

The gradient term $\mathbf{L}^{\mathrm{T}}(\mathbf{d} - \mathbf{L}\mathbf{m})$ is equivalent to computing an imaging condition as in reverse-time migration by migrating the data residue $(\mathbf{d} - \mathbf{L}\mathbf{m})$. To more accurately form this imaging condition free of low-wavenumber artifacts, we implement this step as below:

$$\begin{aligned}G_{\mathrm{pp,down}}(\mathbf{x}) &= \sum_{N_s,N_r}\int_0^T [P_sP_r - H_z(P_s)H_z(P_r) - P_sH_z(H_t(P_r)) \\ &\quad - H_z(P_s)H_t(P_r)]dt, \\ G_{\mathrm{pp,left}}(\mathbf{x}) &= \sum_{N_s,N_r}\int_0^T [P_sP_r - H_x(P_s)H_x(P_r) + P_sH_x(H_t(P_r)) \\ &\quad + H_x(P_s)H_t(P_r)]dt, \\ G_{\mathrm{pp,right}}(\mathbf{x}) &= \sum_{N_s,N_r}\int_0^T [P_sP_r - H_x(P_s)H_x(P_r) - P_sH_x(H_t(P_r)) \\ &\quad - H_x(P_s)H_t(P_r)]dt,\end{aligned} \tag{5}$$

where $G_{pp,\bullet}$'s are gradients associated with the directional PP images; P is the pure qP-wavefield, and subscripts $s$and r represent the source and receiver, respectively; and H_x, H_z and H_t represent the Hilbert transforms in the horizontal direction, vertical direction, and time domain, respectively.

To produce more reliable and high-resolution images when the observed data are noisy, irregular, and sparse, we employ a modified total-variation regularization scheme (Gao et al., 2015; Lin and Huang, 2015) to improve the convergence and imaging fidelity. The misfit function in **Eq. (1)** becomes

$$J(\mathbf{m},\mathbf{u}) = \min_{\mathbf{m}}\left\{\min_{\mathbf{u}}\left\{\frac{1}{2}\|\mathbf{d} - \mathbf{L}\mathbf{m}\|_2^2 + \lambda_1\|\mathbf{m} - \mathbf{u}\|_2^2 + \lambda_2\|\mathbf{u}\|_1^1\right\}\right\}, \tag{6}$$

where λ_1 and λ_2 are regularization parameters. We solve this regularized minimization problem using an alternating-direction minimization scheme (Lin and Huang, 2015).

Suppressing the Ground-Roll Noise of Land Surface Seismic Data From Pirouette Mountain and Eleven-Mile Canyon

We apply our novel wavenumber-adaptive bandpass filter to five lines of 2-D seismic data acquired at Pirouette Mountain and Eleven-Mile Canyon for geothermal exploration (**Figure 1**) to suppress the ground-roll noise. As an example of ground-roll noise suppression for the seismic data on Line 1, we depict the results of three common-shot gathers in **Figure 6**. Comparing the second and third columns in **Figure 6**, we find that the ground-roll noise is mostly suppressed in the third column. The

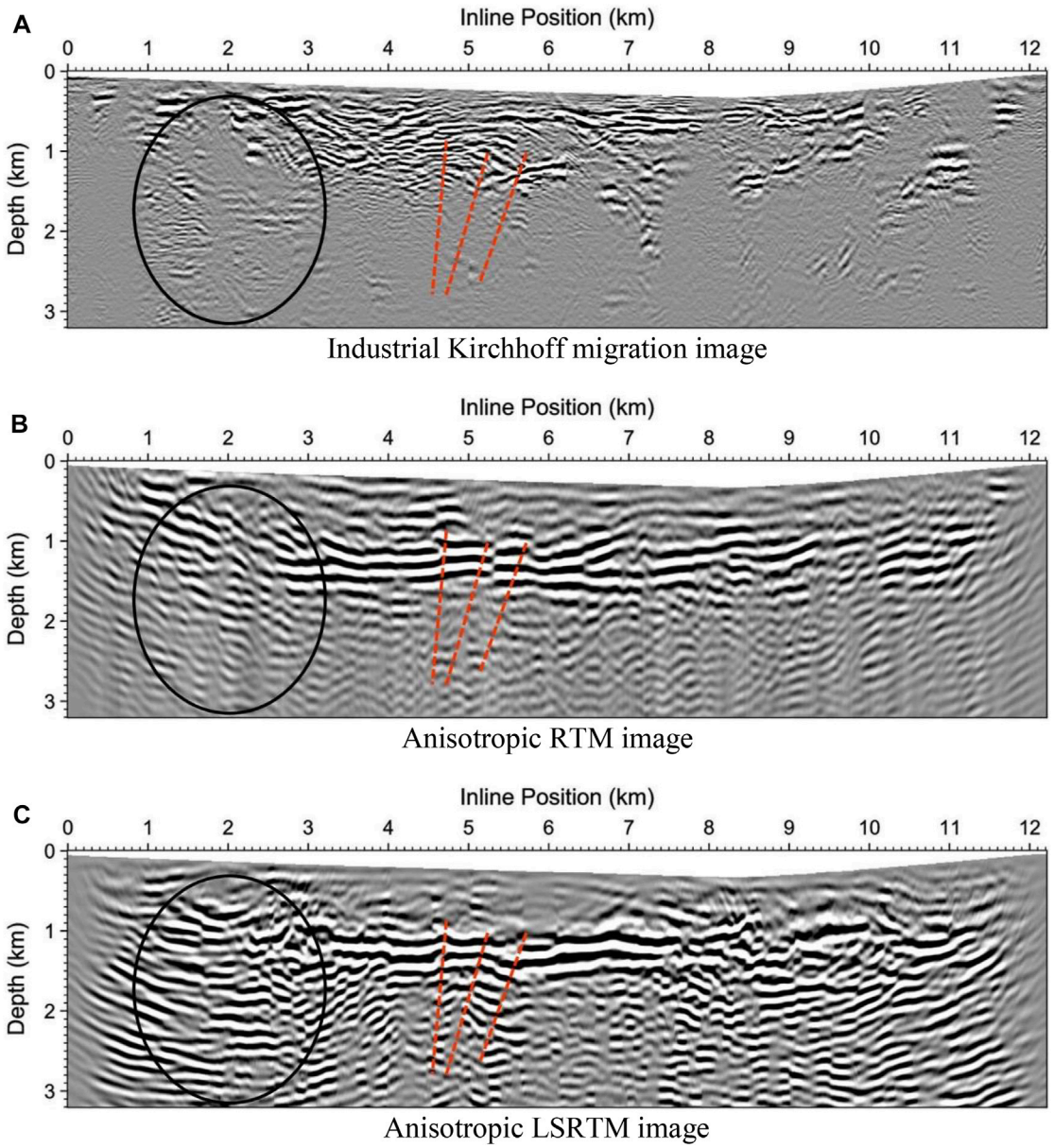

FIGURE 13 | Subsurface migration images of Line 4 at Eleven-Mile Canyon produced using various migration methods: **(A)** Industrial Kirchhoff migration, **(B)** Anisotropic RTM, **(C)** Anisotropic LSRTM. The image within the ellipse region in **(C)** corresponds to the rupture region as shown in **Figure 1**. The image in this region has higher resolution than that in **(B)**, and is almost invisible in **(A)**. The delineated faults in **(C)** may correspond to the faults identified in the U.S. Geological Survey Quaternary fault and fold database as shown in **Figure 1**.

signals within the blue ellipses preserve the low-frequency component.

Figure 7 shows a common-shot gather before and after wavenumber-adaptive bandpass filtering. Some coherent subsurface reflections can be identified on the processed common-shot gather displayed on the right panel of **Figure 7**.

Note that the wavenumber-adaptive bandpass filters used are the same for all common-shot gathers. However, in case the nature of common-shot gathers differs a lot, then it is necessary to determine different values for parameters f_1, f_2, and k_2.

We use the processed data with the ground-roll noise removed to produce subsurface complex structural images using anisotropic RTM and anisotropic LSRTM.

Anisotropic Least-Squares Reverse-Time Migration of Seismic Data From Pirouette Mountain and Eleven-Mile Canyon

After suppressing the ground-roll noise in the surface seismic data along five 2D lines (**Figure 8**) acquired at Pirouette

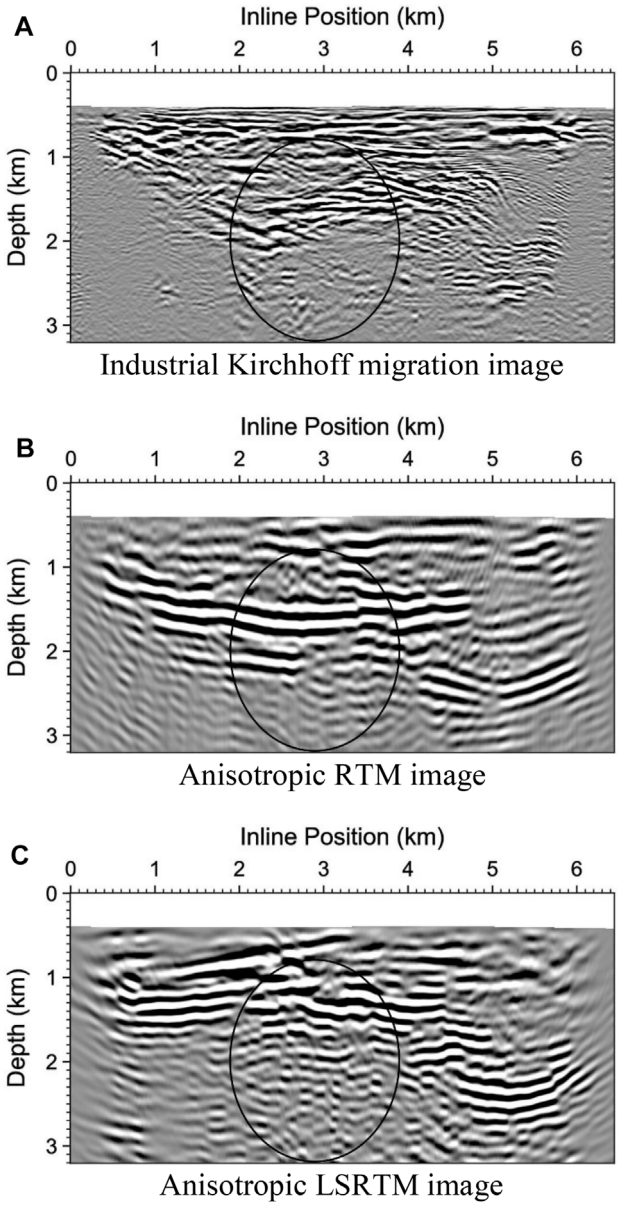

FIGURE 14 | Subsurface migration images of Line 5 at Pirouette Mountain produced using various migration methods: **(A)** Industrial Kirchhoff migration, **(B)** Anisotropic RTM, **(C)** Anisotropic LSRTM. The image within the ellipse region in **(C)** shows high-resolution structures in the deep region that are not well imaged in **(B)** and **(A)**.

Mountain and Eleven-Mile Canyon, we apply anisotropic LSRTM to the resulting data, and compare our imaging results with industrial Kirchhoff migration images and those of anisotropic RTM. We carry out necessary preprocessing steps, such as converting the phase of the seismic data from 3D to 2D because we perform migration imaging in 2D, in addition to the ground-roll noise removal. For anisotropic RTM and anisotropic LSRTM, we first obtain a velocity model and anisotropic parameters $(V_{P0}, \varepsilon, \delta, \theta)$ using multi-scale anisotropic full-waveform inversion with total generalized p-variation regularization (Gao and Huang 2019). Our full-waveform inversion starts from a low-frequency band and an initial velocity model obtained using refraction traveltime tomography to produce reliable models of anisotropic parameters. **Figure 9** shows the initial velocity V_p models along the five seismic survey lines at Pirouette Mountain and Eleven-Mile Canyon obtained using refraction tomography, and our anisotropic waveform inversion results of V_{p0}.

Figures 10–14 show images of the industrial Kirchnoff migration, anisotropic RTM, and anisotropic LSRTM, for seismic survey Lines 1–5. Both anisotropic RTM and anisotropic LSRTM images outperform the industrial images, and anisotropic LSRTM outperforms anisotropic RTM. Kirchhoff migration generates poor images, and particularly in the deep regions. Anisotropic LSRTM produces images with higher resolution, particularly in the deep region and the regions near both end of each line, than anisotropic RTM.

As shown within the ellipse regions in **Figure 10** for Line 1, two steeply-dipping faults can be clearly identified on the anisotropic LSRTM image, which cannot be easily recognized on the anisotropic RTM image, and are invisible on the Kirchhoff migration image.

Figure 11 shows that anisotropic LSRTM reveals more structures in the deep region along Line 2. For example, the images within the ellipse regions in the anisotropic LSRTM image depicted in **Figure 11C** are much better than those of anisotropic RTM in **Figure 11B**, and are not imaged by Kirchhoff migration in **Figure 11A**.

Along Line 3 as shown in **Figure 12**, the image within the ellipse region of the anisotropic LSRTM result in **Figure 12C** has higher resolution than that of anisotropic RTM in **Figure 12B**, and is imaged very poorly by Kirchhoff migration in **Figure 12A**.

The image within the ellipse region in **Figure 13C** along Line 4 obtained using anisotropic LSRTM corresponds to the rupture region as shown in **Figure 1**. The image in this region has higher resolution than that of anisotropic RTM in **Figure 13B**, and is almost invisible in the industrial Kirchhoff migration image in **Figure 13A**. The delineated faults in **Figure 13C** may correspond to the faults identified in the U.S. Geological Survey Quaternary fault and fold database as shown in **Figure 1**.

Line 5 cuts through Lines 1-3 along the North-South direction. The image within the ellipse region of the anisotropic LSRTM image in **Figure 14C** shows high-resolution structures in the deep region that are not well imaged in the other two methods shown in **Figures 14A,B**.

Figure 15 displays a comparison between 3D views of industrial Kirchhoff migration (left) and our anisotropic LSRTM migration (right) for the five seismic survey lines at Pirouette Mountain and Eleven-Mile Canyon. Anisotropic LSRTM reveals high-resolution subsurface images along five seismic survey lines that can be used to identify faults for geothermal exploration.

The final data misfit of anisotropic LSRTM reduces to approximately 50–60% of the initial data misfit after eight iterations. Anisotropic RTM is the first iteration of anisotropic LSRTM. Therefore, our anisotropic LSRTM images are more reliable than those of anisotropic RTM for geothermal exploration.

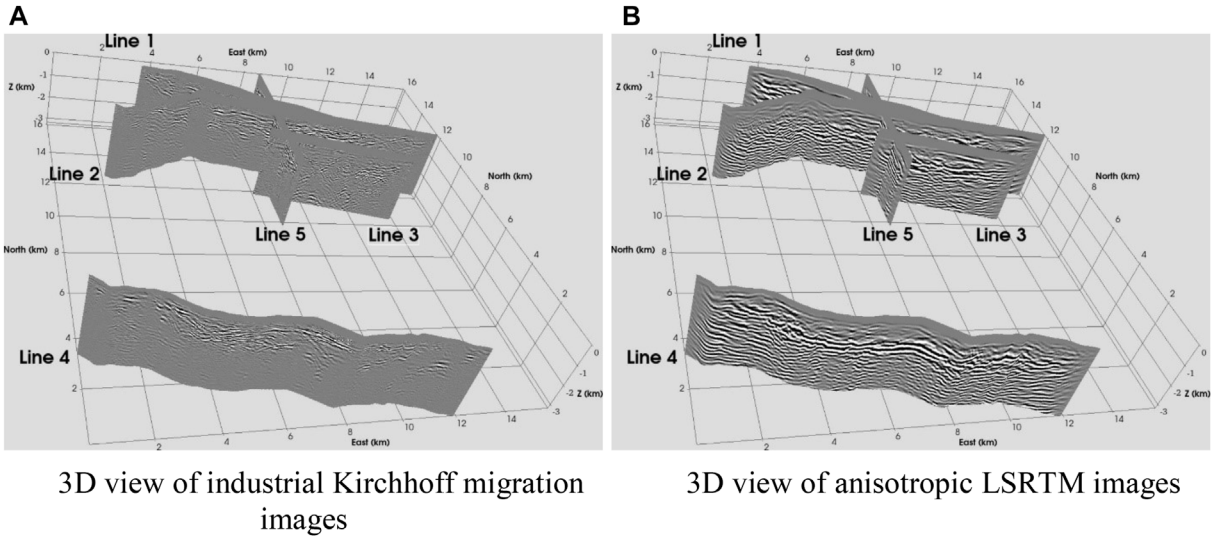

FIGURE 15 | Comparison between 3D views of industrial Kirchhoff migration **(left)** and our anisotropic LSRTM migration **(right)**. Anisotropic LSRTM reveals high-resolution subsurface images along five seismic survey lines at Pirouette Mountain and Eleven-Mile Canyon that can be used to identify faults for geothermal exploration. **(A)** 3D view of industrial Kirchhoff migration images. **(B)** 3D view of anisotropic LSRTM images.

CONCLUSION

We have developed a novel wavenumber-adaptive bandpass filtering method for suppressing the ground-roll noise in land seismic data without filtering out seismic signals. This method employs the fact that the frequency-wavenumber information of the ground-roll noise differs from that of the signal. We have applied our new method to five 2D lines of seismic data acquired at Pirouette Mountain and Eleven-Mile Canyon in Nevada for geothermal exploration, and have successfully suppressed the strong and coherent ground-roll noise. We have applied our anisotropic least-squares reverse-time migration method to the processed seismic data and produced high-resolution subsurface images. Compared with both industrial Kirchhoff migration and anisotropic reverse-time migration, our anisotropic least-squares reverse-time migration improves the subsurface images significantly, both in image resolution and image quality, particularly in the deep region. Our images reveal faults more clearly, some of which are invisible on the other images. This improvement is particularly evidenced by the subsurface images of Line 4, where our image manifests faults consistent with the geology. These results demonstrate that anisotropic least-squares reverse-time migration is an advantageous addition to the state-of-the-art anisotropic reverse-time migration for imaging complex subsurface structures with various faults. Our high-resolution subsurface images at Pirouette Mountain and Eleven-Mile Canyon facilitate accurate fault interpretation for reliable geothermal exploration.

DATA AVAILABILITY STATEMENT

The data analyzed in this study are subject to the following licenses/restrictions: Data are available through the US Navy Geothermal Program Office by contacting co-author AS. Requests to access these datasets should be directed to AS.

AUTHOR CONTRIBUTIONS

YH performed ground-roll suppression and imaging. MZ performed data analyses and anisotropic waveform inversion. KG developed the inversion and imaging codes. AS provided the field seismic data, and performed geologic interpretation. LH was the principal investigator of the research project, obtained funding, provided the research ideas, wrote the paper.

FUNDING

This work was supported by the Geothermal Technologies Office of the U.S. Department of Energy (DOE) through the Los Alamos National Laboratory (LANL), which is operated by Triad National Security, LLC, for the National Nuclear Security Administration (NNSA) of U.S. DOE under Contract No. 89233218CNA000001. This research used resources provided by the LANL Institutional Computing Program, which is supported by the U.S. DOE NNSA under Contract No. 89233218CNA000001.

ACKNOWLEDGMENTS

We thank reviewers YL and BH for their valuable comments.

REFERENCES

Alm, S., Walker, J. D., and Blake, K. (2016). Structural Complexity of the Pirouette Mountain and Elevenmile Canyon Geothermal Systems. *Trans. Geothermal Resour. Counc.* 40, 433–438.

Ba, J., Du, Q., Carcione, J. M., Zhang, H., and Muller, T. M. (2015). *Seismic Exploration of Hydrocarbons in Heterogeneous Reservoirs*. Amsterdam, Netherlands: Elsevier.

Brysk, H., and McCowan, D. W. (1986). A Slant-stack Procedure for point-source Data. *Geophysics* 51 (7), 1370–1386. doi:10.1190/1.1442187

Caskey, S. J., Wesnousky, S. G., Zhang, P., and Slemmons, D. B. (1996). Surface Faulting of the 1954 Fairview Peak (MS 7.2) and Dixie Valley (MS 6.8) Earthquakes, Central Nevada. *Bull. Seismological Soc. America* 86, 761–787. doi:10.1785/BSSA0860030761

Coruh, C., and Costain, J. K. (1983). Noise Attenuation by Vibroseis Whitening (VSW) Processing. *Geophysics* 48 (5), 543–554. doi:10.1190/1.1441485

Deighan, A. J., and Watts, D. R. (1997). Ground-roll Suppression Using the Wavelet Transform. *Geophysics* 62 (6), 1896–1903. doi:10.1190/1.1444290

Embree, P., Burg, J. P., and Backus, M. M. (1963). Wide-band Velocity Filtering-The Pie-slice Process. *Geophysics* 28 (6), 948–974. doi:10.1190/1.1439310

Gao, K., and Huang, L. (2019). Acoustic- and Elastic-Waveform Inversion with Total Generalized P-Variation Regularization. *Geophys. J. Int.* 218, 933–957. doi:10.1093/gji/ggz203

Gao, K., and Huang, L. (2015).Anisotropic Elastic-Waveform Modeling for Fracture Characterization in EGS Reservoirs. Proceedings of the 40th Workshop on Geothermal Reservoir Engineering, CA (United States), 26-28 Jan 2015. Stanford, CA: Stanford University. doi:10.2172/1168705

Halliday, D. (2011). Adaptive Interferometry for Ground-Roll Suppression. *The Leading Edge* 30 (5), 532–537. doi:10.1190/1.3589110

Henley, D. C. (2003). Coherent Noise Attenuation in the Radial Trace Domain. *Geophysics* 68 (4), 1408–1416. doi:10.1190/1.1598134

Jin, S., and Ronen, S. (2005).Ground Roll Detection and Attenuation by 3C Polarization Analysis. Proceedings of the 67th Annual Conference and Exhibition, Madrid, Spain, Jun 2005. Extended Abstracts (Houten, The Netherlands: European Association of Geoscientists & Engineers). doi:10.3997/2214-4609-pdb.1.b020

Karsli, H., and Bayrak, Y. (2008). Ground-Roll Attenuation Based on Wiener Filtering and Benefits of Time-Frequency Imaging. *The Leading Edge* 27 (2), 206–209. doi:10.1190/1.2840368

Lin, Y., and Huang, L. (2015). Acoustic- and Elastic-Waveform Inversion Using a Modified Total-Variation Regularization Scheme. *Geophys. J. Int.* 200, 489–502. doi:10.1093/gji/ggu393

Liu, X. (1999). Ground Roll Supression Using the Karhunen-Loeve Transform. *Geophysics* 64 (2), 564–566. doi:10.1190/1.1444562

Nemeth, T., Wu, C., and Schuster, G. T. (1999). Least-squares Migration of Incomplete Reflection Data. *Geophysics* 64, 208–221. doi:10.1190/1.1444517

Sheriff, R. E. (2002). Encyclopedic Dictionary of Applied Geophysics. *Soc. exploration geophysicists*, 442. doi:10.1190/1.9781560802969

Shieh, C. F., and Herrmann, R. B. (1990). Ground Roll: Rejection Using Polarization Filters. *Geophysics* 55 (9), 1216–1222. doi:10.1190/1.1442937

Thomsen, L. (1986). Weak Elastic Anisotropy. *Geophysics* 51, 1954–1966. doi:10.1190/1.1442051

Trad, D., Ulrych, T., and Sacchi, M. (2003). Latest Views of the Sparse Radon Transform. *Geophysics* 68 (1), 386–399. doi:10.1190/1.1543224

Treitel, S., Shanks, J. L., and Frasier, C. W. (1967). Some Aspects of Fan Filtering. *Geophysics* 32 (5), 789–800. doi:10.1190/1.1439889

Unruh, J., Gray, B., Christopherson, K., Pullammanappallil, S., Alm, S., and Blake, K. (2016). Seismic Reflection and Magnetotelluric Imaging of Southwestern Dixie Valley Basin, Nevada. *Trans. Geothermal Resour. Counc.* 40, 455–461.

Yilmaz, Ö. (2001). Seismic Data Analysis: Processing, Inversion, and Interpretation of Seismic Data. *Soc. exploration geophysicists* 10, 837–1000. doi:10.1190/1.9781560801580

Zhan, G., Pestana, R. C., and Stoffa, P. L. (2012). Decoupled Equations for Reverse Time Migration in Tilted Transversely Isotropic media. *Geophysics* 77, T37–T45. doi:10.1190/geo2011-0175.1

Conflict of Interest: The authors declare that the research was conducted in the absence of any commercial or financial relationships that could be construed as a potential conflict of interest.

frontiers in Earth Science

ORIGINAL RESEARCH
published: 29 November 2021
doi: 10.3389/feart.2021.732425

Least-Squares Reverse Time Migration Using the Gradient Preconditioning Based on Transmitted Wave Energy

Chuang Xie[1], *Peng Song*[1,2,3]*, *Xishuang Li*[2,4], *Jun Tan*[1,2,3], *Shaowen Wang*[1] *and Bo Zhao*[1,2,3]

[1]College of Marine Geo-sciences, Ocean University of China, Qingdao, China, [2]Laboratory for Marine Mineral Resources, Pilot National Laboratory for Marine Science and Technology (Qingdao), Qingdao, China, [3]Key Laboratory of Submarine Geosciences and Prospecting Techniques Ministry of Education, Qingdao, China, [4]The First Institute of Oceanography, Ministry of National Resources, Qingdao, China

A gradient preconditioning approach based on transmitted wave energy for least-squares reverse time migration (LSRTM) is proposed in this study. The gradient is preconditioned by using the energy of "approximate transmission wavefield," which is calculated based on the non-reflecting acoustic equation. The proposed method can effectively avoid a huge amount of calculation and storage required by the Hessian matrix or approximated Hessian matrix and can overcome the influence of reflected waves, multiples, and other wavefields on the gradient in gradient preconditioning based on seismic wave energy (GPSWE). The numerical experiments, compared with that using GPSWE, show that LSRTM using the gradient preconditioning based on transmitted wave energy (GPTWE) can significantly improve the imaging accuracy of deep target and accelerate the convergence rate without trivial increased calculation.

Keywords: least-squares reverse time migration, gradient preconditioning, transmitted wave, non-reflecting acoustic wave equation, disproportioned illumination

OPEN ACCESS

Edited by:
Hao Hu,
University of Houston, United States

Reviewed by:
Shohei Minato,
Delft University of Technology, Netherlands
Gang Yao,
China University of Petroleum, China
Jidong Yang,
China University of Petroleum (Huadong), China

***Correspondence:**
Peng Song
pengs@ouc.edu.cn

Specialty section:
This article was submitted to Solid Earth Geophysics, a section of the journal Frontiers in Earth Science

Received: *29 June 2021*
Accepted: *25 October 2021*
Published: *29 November 2021*

Citation:
Xie C, Song P, Li X, Tan J, Wang S and Zhao B (2021) Least-Squares Reverse Time Migration Using the Gradient Preconditioning Based on Transmitted Wave Energy. Front. Earth Sci. 9:732425. doi: 10.3389/feart.2021.732425

INTRODUCTION

Compared with traditional migration techniques such as Kirchhoff integral migration, reverse time migration (RTM) based on the two-way wave equation is widely favored by researchers (Baysal et al., 1983; McMechan, 1983; Yoon and Marfurt, 2006; Symes, 2007; Fletcher et al., 2009; Liu et al., 2011; Sun et al., 2016) because of its obvious advantages in accurate imaging of complex media (especially high-steep structure and subsalt structure). However, RTM still belongs to the category of conventional migration, and its migration operator is the conjugate transposition of the forward-modeling operator, rather than the exact inverse operator (Claerbout, 1992). Therefore, conventional RTM produces blurring imaging of underground media under the influence of factors such as a complex structure, limited bandwidth, and under-sampled acquisition system, which is difficult to satisfy the current needs of oil and gas exploration and development (Nemeth et al., 1999).

Dai et al. (2010) regarded the conventional RTM as an inversion problem under the framework of least squares, used the iterative method to obtain the reflection coefficient model, and developed a least-squares reverse time migration (LSRTM) method. Since the LSRTM can obtain the imaging results with high precision, high-amplitude preservation, and high resolution, it has become a research hotspot in the field of geophysics (Dai et al., 2012; Guo and Li, 2014; Huang et al., 2014; Yao and Jakubowicz, 2016; Ren et al., 2017; Rocha and Sava, 2018; Gong et al., 2019; Yang et al., 2019;

Yang and Zhu, 2019; Li et al., 2020). Dai et al. (2012) proposed multisource LSRTM based on phase encoding, which improved the computational efficiency of the algorithm. Guo and Li (2014) implemented the true-amplitude imaging based on LSRTM and obtained the imaging with high resolution and true amplitude. Huang et al. (2014) achieved high-precision imaging of near surfaces based on LSRTM. Wong et al. (2015) proposed a joint LSRTM method by using primary and free-surface multiples and attenuated crosstalk artifacts in the image. Yao and Jakubowicz (2016) developed the LSRTM in a matrix-based formulation, which could obtain the high-precision section on the basis of effectively suppressing artifacts. Ren et al. (2017) developed elastic LSRTM, which provided more abundant and effective information for accurate imaging of complex media. Rocha and Sava (2018) proposed elastic LSRTM using the energy norm to improve imaging accuracy and speed up the convergence. Gong et al. (2019) applied a sparsity-promoting constraint to the LSRTM and obtained better imaging, especially for the metallogenetic geological model containing small-scale scatters. Yang et al. (2019) used a high-order Born approximation algorithm to supplement the information of prismatic waves in conventional LSRTM and further enhanced the ability to finely characterize the steeply dipping structure. Yang and Zhu (2019) implemented a viscoacoustic LSRTM based on a time-domain complex-valued wave equation, which could improve imaging resolution and compensate attenuation effects effectively. Moreover, there were also some researchers focusing on computational efficiency (Dai and Schuster, 2013; Huang et al., 2015; Zhang et al., 2015; Hu et al., 2016; Liu et al., 2016; Li et al., 2018; Zhao and Sen, 2018; Gao et al., 2020) and extended applications (Wu et al., 2016; Zhang et al., 2016; Gu et al., 2017; Guo and McMechan, 2018; Fang et al., 2019; Liu and Liu, 2019; Qu et al., 2019; Yang et al., 2020).

As the gradient of traditional LSRTM is affected by geometric spreading and disproportioned illumination, the update of reflection coefficient model in the shallow depth has always been dominant, resulting in low imaging accuracy and slow convergence rate. At present, the gradient preconditioning algorithms such as the methods on the Hessian matrix (Hessian matrix, approximated Hessian matrix, and pseudo-Hessian) and gradient preconditioning based on seismic wave energy (GPSWE) are usually applied to improve the imaging accuracy of deep part. The algorithms based on the Hessian matrix (Pratt et al., 1998) usually require explicit calculation and storage of the Hessian matrix, which will inevitably bring huge computation and memory consumption. The algorithms based on the approximated Hessian matrix are also necessary to approximate the diagonal Hessian matrix to correct the energy of amplitude, which are still difficult to be applied to field data processing. The algorithms based on the pseudo-Hessian matrix (Shin et al., 2001; Choi et al., 2008) are popular preconditioning methods, and they are less computationally expensive, but these approaches only account for the geometrical spreading effect from the sources. GPSWE had been first proposed by Zhang et al. (2012) in full waveform inversion, which takes seismic wave energy as the correction factor and effectively eliminates the impact on gradient caused by geometric spreading and disproportioned illumination. Tan and Huang (2014), Zhang et al. (2016), and Gao et al. (2017) have applied this method to the LSRTM, which have significantly improved the imaging accuracy and convergence efficiency, especially for deep strata. However, GPSWE used in LSRTM still has the following problem. Seismic wavefield is divided into "transmitted wavefield" and "reflected wavefield." Theoretically, it is more accurate to characterize the geometric spreading and illumination effects of the gradient by the information of "transmitted wavefield." However, when adopting the operator of gradient preconditioning based on seismic wave energy (GPSWE), we discovered that the wavefield used to calculate the operator is simulated by the acoustic wave equation, which contains a lot of reflected waves besides transmitted waves. Therefore, the operator of GPSWE will be considerably influenced by the strong reflected wave energy and not accurate enough to estimate geometric spreading or illumination distribution (Song et al., 2019).

To solve the previous problem, we developed an LSRTM algorithm using the gradient preconditioning based on transmitted wave energy (GPTWE), which obtains the forward- and back-propagated "approximate transmission wavefield" based on the non-reflecting acoustic equation and applies the energy of "approximate transmission wavefield" to precondition the original gradient. This method requires neither the calculation nor storage of the Hessian matrix or the approximated Hessian matrix but can effectively improve the imaging accuracy without significantly increasing the amount of calculation.

In *Principles of LSRTM*, we introduce the principles and processing steps of LSRTM. In *LSRTM Using the GPTWE*, we expound the principles and procedures of LSRTM using GPTWE. In *Marmousi Model Test* and *Pluto Data Example*, we display the results of numerical simulation of the complex model. Finally, in *Conclusion and Prospect*, we present a summary of conclusions and the future research.

PRINCIPLES OF LSRTM

The two-dimensional scalar constant density acoustic wave equation is expressed as follows:

$$\left(\frac{1}{v^2}\frac{\partial^2}{\partial t^2} - \nabla^2\right)P = S, \tag{1}$$

where v represents the velocity model, P signifies the stress, S represents the source, t denotes the time, and ∇^2 stands for the Laplacian operator. According to the perturbation theory and principle of Born approximation, we can obtain the following equation:

$$\left(\frac{1}{v_0^2}\frac{\partial^2}{\partial t^2} - \nabla^2\right)P_s = \frac{2v_s}{v_0^3}\frac{\partial^2 P_0}{\partial t^2}, \tag{2}$$

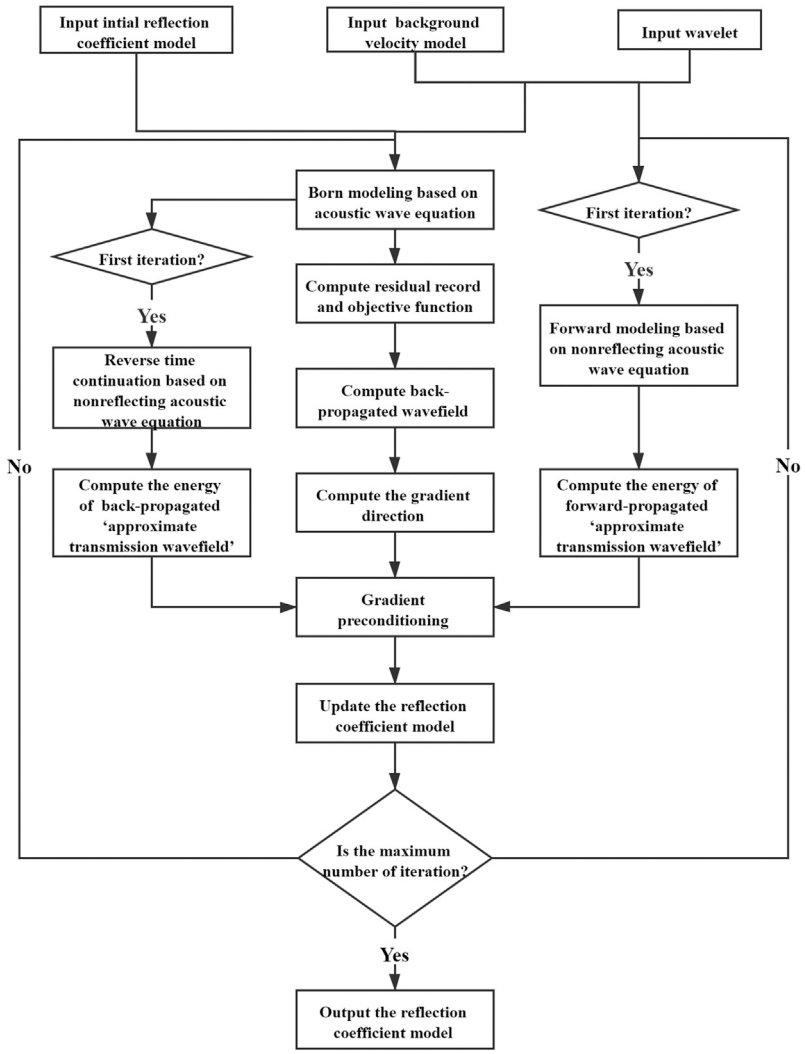

FIGURE 1 | Flowchart of the LSRTM using GPTWE.

where v_0 is a background velocity model, v_s is the perturbation in the velocity model, P_0 represents the background wavefield, and P_s represents the perturbed wavefield. Here, reflection coefficient model can be defined as follows (Dai and Schuster, 2013):

$$m = \frac{2v_s}{v_0}, \tag{3}$$

where m is the reflection coefficient model. Therefore, the Born modeling of acoustic LSRTM can be expressed as follows:

$$\begin{cases} \left(\frac{1}{v_0^2}\frac{\partial^2}{\partial t^2} - \nabla^2\right)P_0 = S \\ \left(\frac{1}{v_0^2}\frac{\partial^2}{\partial t^2} - \nabla^2\right)P_s = \frac{m}{v_0^2}\frac{\partial^2 P_0}{\partial t^2} \end{cases}. \tag{4}$$

It can be seen from **Eq. 4** that Born modeling can be calculated in two steps. At the background velocity, the background wavefield is calculated by using the seismic wavelet as the source first and then the perturbed wavefield is calculated by using the background wavefield and the reflection coefficient model as the perturbed term. **Eq. 4** is also written as the matrix form as follows:

$$\mathbf{d} = \mathbf{Lm}, \tag{5}$$

where $\mathbf{d}$ refers to the matrix form of seismic record (P_0+P_s) obtained by Born modeling, $\mathbf{m}$ denotes the matrix form of the reflection coefficient model, and $\mathbf{L}$ represents the Born modeling operator. Since the Born modeling operator $\mathbf{L}$ is independent of the reflection coefficient model $\mathbf{m}$, the Born modeling can also be described as linearized modeling.

The L2 norm is used to construct the objective function of LSRTM, which can be defined as follows:

$$\mathrm{J}(\mathbf{m}) = \frac{1}{2}||\mathbf{Lm} - \mathbf{d}_{\mathrm{obs}}||_2^{\,2}, \tag{6}$$

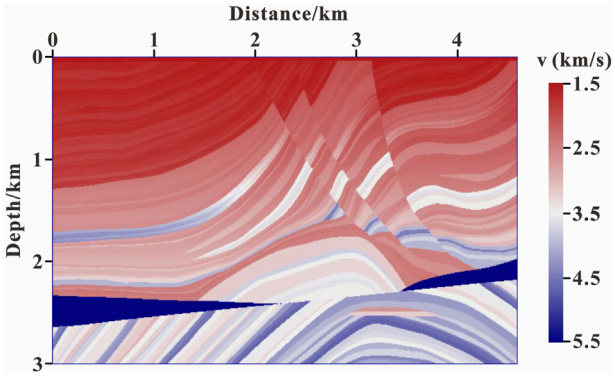

FIGURE 2 | Marmousi velocity model.

where $\mathbf{d}_{\text{obs}}$ is the matrix form of observation seismic record. We usually apply the gradient algorithms to implement the iterative of the reflection coefficient model.

Here, we used the adjoint state method (Plessix, 2006) to calculate the gradient and can obtain the following equation:

$$g = \int_t \frac{\lambda}{v_0^2} \frac{\partial^2 P_0}{\partial t^2} \, dt, \tag{7}$$

where g represents the gradient, and λ represents the adjoint wavefield, which satisfies the adjoint equation as follows:

$$\left(\frac{1}{v_0^2} \frac{\partial^2}{\partial t^2} - \nabla^2 \right) \lambda = d, \tag{8}$$

where d refers to the difference between the simulated seismic records obtained by Born modeling and observed seismic records. Similarly, **Eq. 7** can be described in the matrix form, which is simplified as follows:

$$\mathbf{g} = \mathbf{L}^{\mathrm{T}} (\mathbf{Lm} - \mathbf{d}_{\text{obs}}), \tag{9}$$

where $\mathbf{g}$ denotes the matrix form of the gradient and the superscript "T" represents the transpose of a matrix. The conjugate gradient algorithm based on gradient preconditioning is used to update the reflection coefficient model; the model update process can be expressed as follows:

$$\begin{cases} \beta_k = \dfrac{(\mathbf{Qg}_k)^{\mathrm{T}} (\mathbf{Qg}_k - \mathbf{Qg}_{k-1})}{\left\| \mathbf{Qg}_{k-1} \right\|^2} \\ \mathbf{y}_k = \begin{cases} -\mathbf{Qg}_k & k = 1 \\ -\mathbf{Qg}_k + \beta_k \mathbf{y}_{k-1} & k \geq 2 \end{cases}, \\ \alpha_k = \dfrac{(\mathbf{Ly}_k)^{\mathrm{T}} (\mathbf{Lm}_k - \mathbf{d}_{\text{obs}})}{(\mathbf{Ly}_k)^{\mathrm{T}} (\mathbf{Ly}_k)} \\ \mathbf{m}_{k+1} = \mathbf{m}_k + \alpha_k \mathbf{y}_k \end{cases} \tag{10}$$

where k represents the number of iterations, β is the correction factor of conjugate gradient, $\mathbf{y}$ is the matrix form of conjugate gradient, α denotes the step length, and $\mathbf{Q}$ stands for the gradient preconditioning operator. And as we all know, an accurate and easy-to-calculate gradient preconditioning operator can significantly improve the imaging accuracy and accelerate the convergence rate of LSRTM.

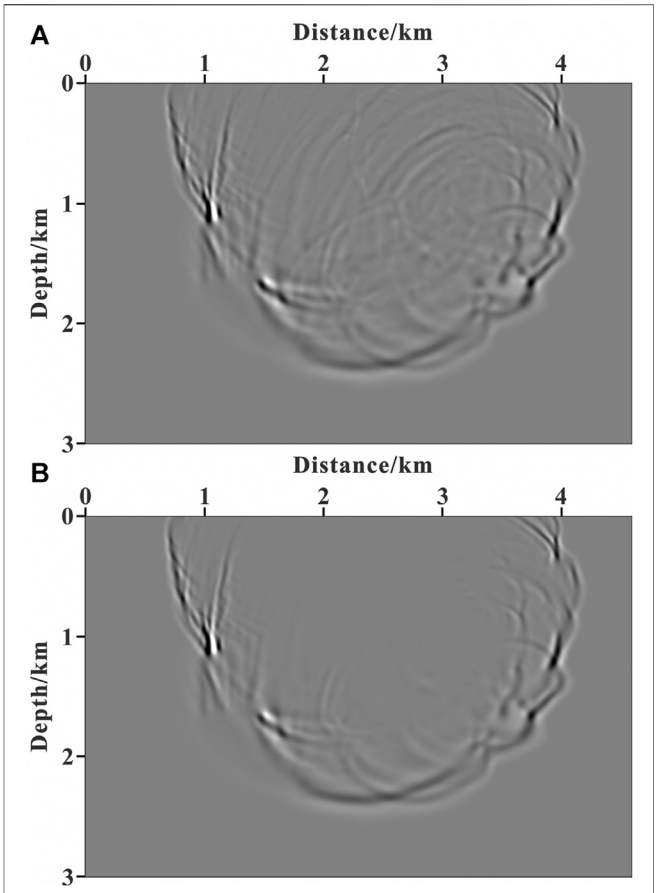

FIGURE 3 | Wavefront snapshots of numeric modeling at 1.05 s: **(A)** based on the acoustic wave equation; **(B)** based on the non-reflecting acoustic wave equation.

LSRTM USING THE GPTWE

The Hessian matrix can accurately reflect the geometric spreading of wavefield and the degree of illumination (Pratt et al., 1998). Theoretically, applying the Hessian matrix to precondition, the original gradient is able to eliminate the impact caused by geometric spreading and disproportioned illumination on gradient. Therefore, the imaging accuracy and convergence rate of LSRTM are greatly improved. However, the storage and calculation required by the method of conventional gradient preconditioning based on the Hessian matrix are usually unbearable for the LSRTM of massive data. GPSWE (Zhang et al., 2012) can directly avoid the calculation and storage of the Hessian matrix or approximated Hessian matrix, which has received extensive attention from

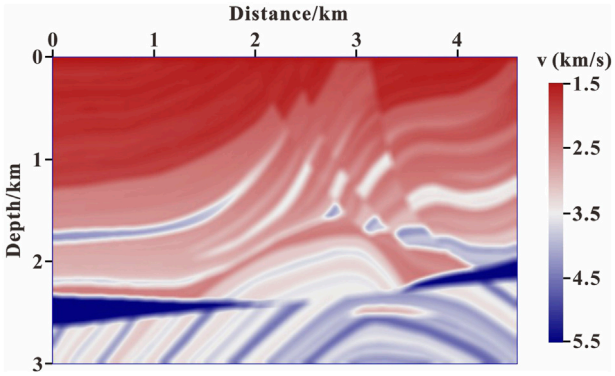

FIGURE 4 | Background velocity model.

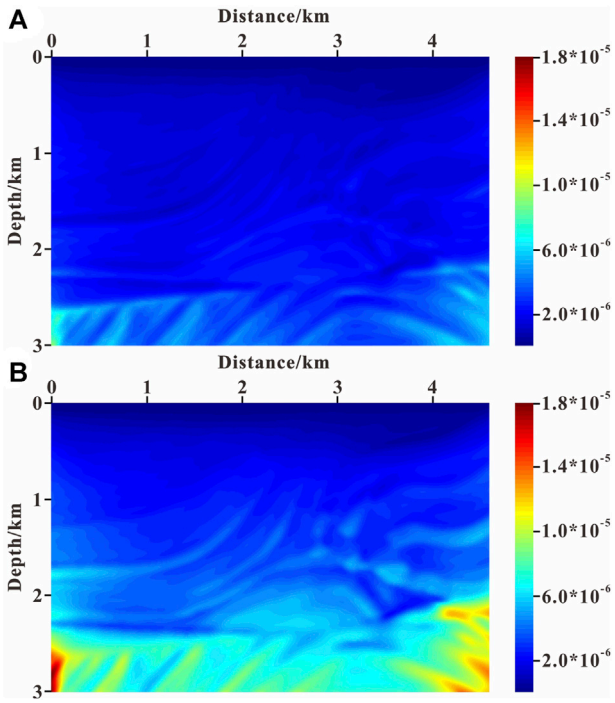

FIGURE 5 | Schematic description of the gradient preconditioning operator: **(A)** GPSWE; **(B)** GPTWE.

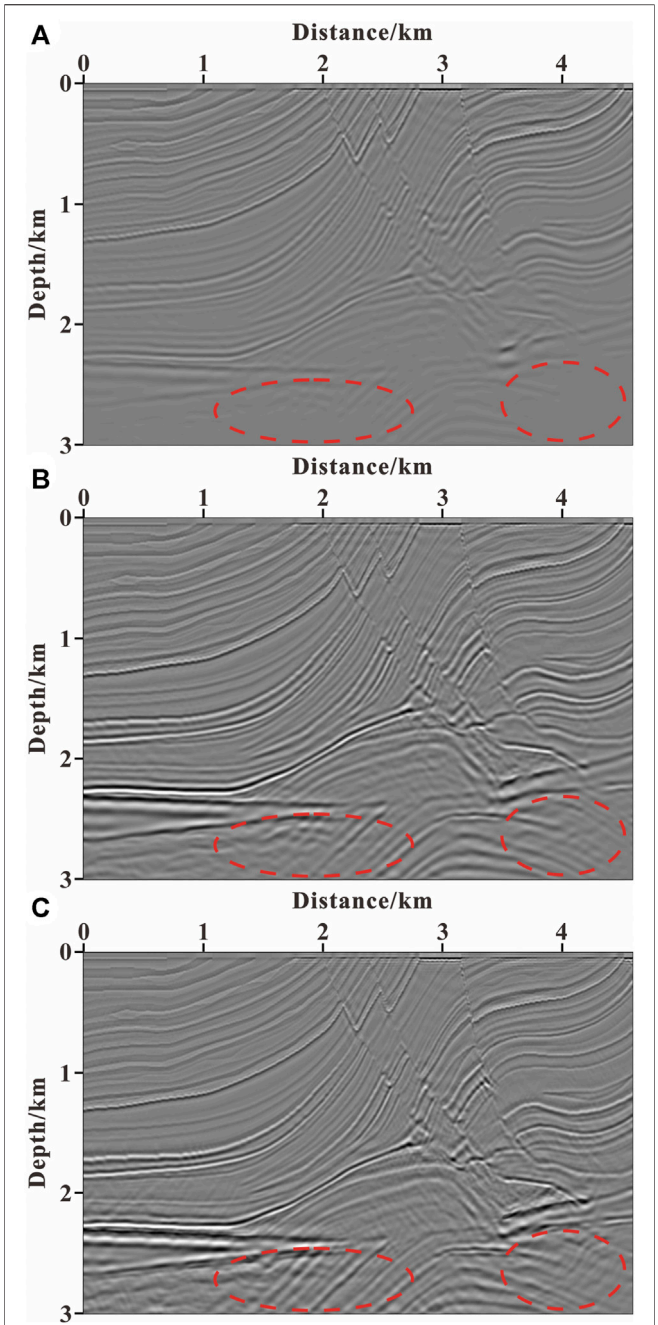

FIGURE 6 | Imaging results of LSRTM after 60 iterations: **(A)** without gradient preconditioning; **(B)** using GPSWE; and **(C)** using GPTWE.

scholars. $\mathbf{W_s}(\boldsymbol{x})$ is the energy of forward-propagated wavefield and is represented as follows:

$$\mathbf{W_s}(\boldsymbol{x}) = \sum_{(s,t)} \mathbf{P_s^2}(\boldsymbol{x}, t, \boldsymbol{x_s}), \tag{11}$$

where $\mathbf{P_s}(\boldsymbol{x}, t, \boldsymbol{x_s})$ is the forward-propagated wavefield value at $\boldsymbol{x}$, which is obtained by the forward modeling based on the acoustic wave equation (as shown in **Eq. 1**) with the source disturbance at $\boldsymbol{x_s}$. $\boldsymbol{x}$ represents the one-dimensional space vector. Analogously, $\mathbf{W_r}(\boldsymbol{x})$ is the energy of back-propagated wavefield and is defined as follows:

$$\mathbf{W_r}(\boldsymbol{x}) = \sum_{(s,r,t)} \mathbf{P_r^2}(\boldsymbol{x}, t, \boldsymbol{x_r}), \tag{12}$$

where $\mathbf{P_r}(\boldsymbol{x}, t, \boldsymbol{x_r})$ stands for the back-propagated wavefield value at $\boldsymbol{x}$, which is obtained by the reverse time extrapolation based on the acoustic wave equation (inverse process of **Eq. 1**) with the impulse disturbance at $\boldsymbol{x_r}$. Then we used the energy of forward- and back-propagated wavefields to precondition the original gradient and obtain the following equation:

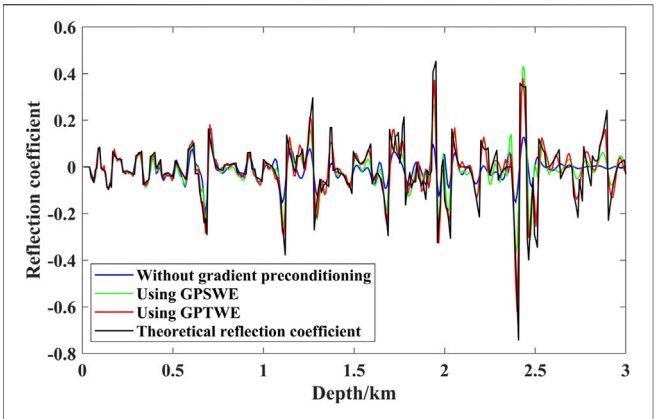

FIGURE 7 | Single-trace display of imaging results after 60 iterations.

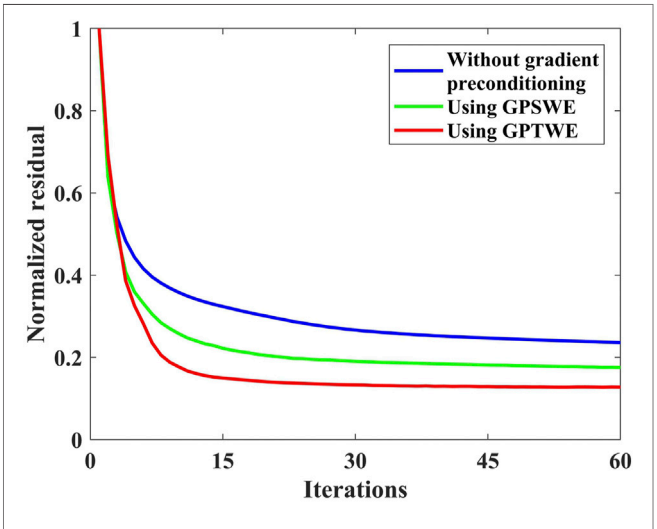

FIGURE 8 | Normalized residual curves.

$$\mathbf{g}_{\mathbf{p}}(\boldsymbol{x}) = \frac{\mathbf{g}(\boldsymbol{x})}{\sqrt{\mathbf{W}_{\mathbf{s}}(\boldsymbol{x})\mathbf{W}_{\mathbf{r}}(\boldsymbol{x})}}, \tag{13}$$

where $\mathbf{g}_{\mathbf{p}}$ is the operator of GPSWE.

In essence, this method is not a direct approximation of the Hessian matrix but uses the distribution of the energy of seismic wavefield to correct the geometric spreading and proportioned illumination, which avoids the storage and calculation of large matrix. The research of Song et al. (2019) in full waveform inversion shows that only the transmission wavefield contains accurate information of geometric spreading and illumination. However, the conventional seismic wavefield also contains a large number of reflected waves, multiples, and other wavefields in addition to the transmission wavefield, which makes the operator of GPSWE not accurate enough. For this reason, this study develops a highly efficient LSRTM algorithm using GPTWE. The implementation steps of this method are described in detail later, which are similar to the one of GPSWE.

TABLE 1 | Calculation time of LSRTM with 60 iterations.

	Without gradient preconditioning	GPSWE	GPTWE
Time/s	24,275	24,335	24,407

First, the forward modeling based on the non-reflecting acoustic wave equation (Baysal et al., 1984) (as shown in **Eq. 14**) is used to obtain the forward-propagated "approximate transmission wavefield" with the seismic wavelet as the source.

$$\left(\frac{1}{v^2}\frac{\partial^2}{\partial t^2} - \nabla^2\right)U = \frac{1}{v}\left(\frac{\partial U}{\partial x}\frac{\partial v}{\partial x} + \frac{\partial U}{\partial z}\frac{\partial v}{\partial z}\right) + S, \tag{14}$$

where x and z denote the space coordinates, respectively, and U stands for the "approximate transmission wavefield." $\mathbf{E}_{\mathbf{s}}(\boldsymbol{x})$ is the energy of forward-propagated "approximate transmission wavefield" and is represented as follows:

$$\mathbf{E}_{\mathbf{s}}(\boldsymbol{x}) = \sum_{(s,t)} \mathbf{U}_{\mathbf{s}}^2(\boldsymbol{x}, t, \boldsymbol{x}_s), \tag{15}$$

where $\mathbf{U}_{\mathbf{s}}(\boldsymbol{x}, t, \boldsymbol{x}_s)$ is the forward-propagated "approximate transmission wavefield" value at $\boldsymbol{x}$, which is obtained by the forward modeling based on the non-reflecting acoustic wave equation (as shown in **Eq. 14**) with the source disturbance at $\boldsymbol{x}_s$. Similarly, $\mathbf{E}_{\mathbf{r}}(\boldsymbol{x})$ is the energy of back-propagated "approximate transmission wavefield" and is defined as follows:

$$\mathbf{E}_{\mathbf{r}}(\boldsymbol{x}) = \sum_{(s,r,t)} \mathbf{U}_{\mathbf{r}}^2(\boldsymbol{x}, t, \boldsymbol{x}_r), \tag{16}$$

where $\mathbf{U}_{\mathbf{r}}(\boldsymbol{x}, t, \boldsymbol{x}_r)$ stands for the backward-propagated wavefield value at $\boldsymbol{x}$, which is obtained by the reverse time extrapolation based on the non-reflecting acoustic wave equation (inverse process of **Eq. 14**) with the impulse disturbance at $\boldsymbol{x}_r$. Then we used the energy of forward- and back-propagated "approximate transmission wavefield" to precondition the original gradient and can obtain the following:

$$\mathbf{g}_{\mathbf{t}}(\boldsymbol{x}) = \frac{\mathbf{g}(\boldsymbol{x})}{\sqrt{\mathbf{E}_{\mathbf{s}}(\boldsymbol{x})\mathbf{E}_{\mathbf{r}}(\boldsymbol{x})}}, \tag{17}$$

where $\mathbf{g}_{\mathbf{t}}$ is the operator of GPTWE. The flowchart of the LSRTM using GPTWE is shown in **Figure 1**.

It should be noted that in the implementation process of the LSRTM using GPTWE, all the steps are the same as the LSRTM using GPSWE, except that the acoustic wave equation in calculating preconditioning operator is replaced with the non-reflecting acoustic wave equation, so the calculation of the LSRTM using GPTWE is essentially in agreement with the one using GPSWE. The LSRTM using GPSWE only needs to add one additional forward modeling and one additional reverse time continuation in the first iteration in comparison with the conventional LSRTM without gradient preconditioning. And the additional calculation is negligible compared with the LSRTM itself, which often needs hundreds of wavefield continuation. Therefore, theoretically, the computational efficiency of the three

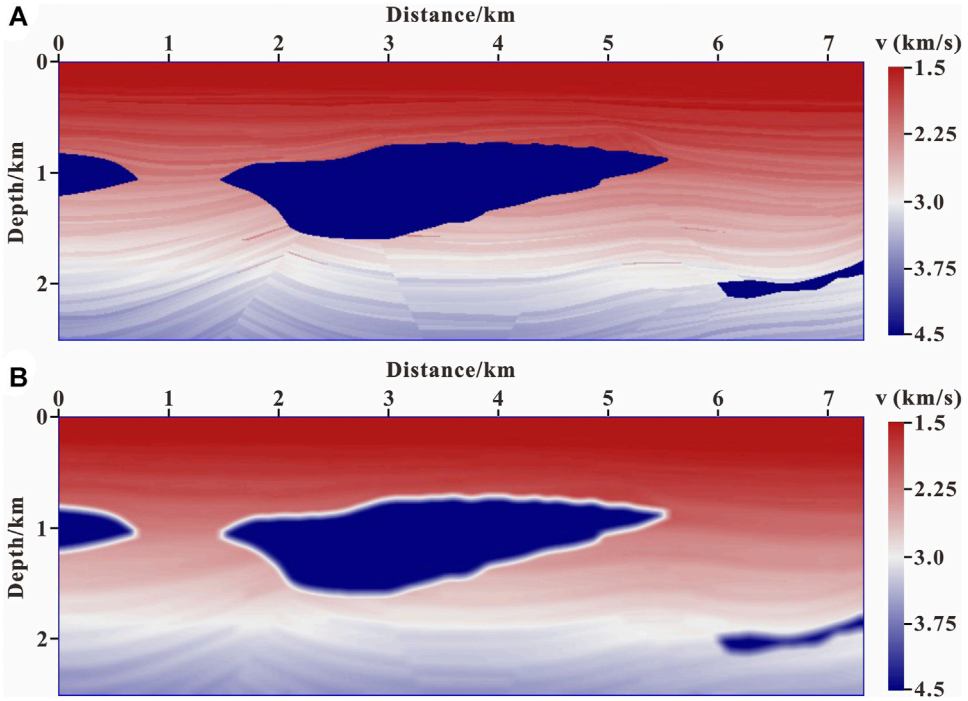

FIGURE 9 | Pluto velocity model: **(A)** real velocity model; **(B)** background velocity model.

methods including the conventional LSRTM without gradient preconditioning, the LSRTM using GPSWE, and the LSRTM using GPTWE are basically equivalent.

To test the suppressing effect of the non-reflecting acoustic wave equation on reflected waves, the forward modeling experiment was carried out based on the Marmousi model. The size of model is 4,600 m in length and 3,000 m in depth (as shown in **Figure 2**). The grid interval in the x and z directions is 8 m. A Ricker wavelet with a dominant frequency of 20 Hz is used as the source, which is excited at (2,300 m, 0 m). The accuracy in finite difference wavefield modeling is eighth order in space and second order in time. The time sampling step is 0.5 ms, and the maximum recording time is 3 s. The hybrid absorbing boundary condition (Xie et al., 2020) is used for boundary processing. **Figure 3** illustrates the wavefront snapshots at 1.05 s simulated by the acoustic wave equation and the non-reflecting acoustic wave equation.

From **Figure 3**, we can observe that the reflected waves in the wavefield simulated by the non-reflecting acoustic wave equation have been suppressed effectively, and the simulated wavefield is closer to a pure transmitted wavefield than that simulated by the acoustic wave equation. Therefore, in theory, it is more accurate to precondition the gradient using "approximate transmission wavefield" information simulated by the non-reflecting acoustic wave equation.

MARMOUSI MODEL TEST

The Marmousi model in *LSRTM Using the GPTWE* is used to test the feasibility and accuracy of the algorithm in complex media conditions. The background velocity model used for LSRTM imaging is shown in **Figure 4**, which is the result of Gaussian smoothing of the original velocity model in **Figure 2**. A total of 116 shots are considered for imaging, and the shots are evenly distributed on the surface with the interval of 40 m. A total of 451 receivers are allotted for each shot, and the receivers are evenly distributed on both sides of each shot with 8-m interval. The observation data are generated by the full-waveform modeling (**Eq. 1**). The remaining experimental parameters are the same as those in *LSRTM Using the GPTWE*.

Figure 5 shows the preconditioners using GPSWE and GPTWE. In **Figures 5A,B**, we can observe that the preconditioning operator of GPTWE is more related to the model, and the deep illumination compensation is stronger. **Figure 6** illustrates the imaging result of LSRTM after 60 iterations. Through the compassion between **Figures 6A–C** (marked by the dashed red circle), it can be seen that the imaging results of LSRTM based on gradient preconditioning are better than those without gradient preconditioning. Specifically, after 60 iterations, the LSRTM using GPTWE has the best amplitude preservation, the highest spatial resolution, and the highest imaging accuracy of deep part, followed by the LSRTM using GPSWE, and the LSRTM without gradient preconditioning has the worst imaging result.

In order to compare the imaging effects of the previous three methods more clearly, we extract the imaging curves at x = 1960 m from the sections in **Figure 6** and compare them with theoretical reflection coefficient curve, which is calculated using **Eq. 3**; **Figure 7** is the single-trace display of imaging results

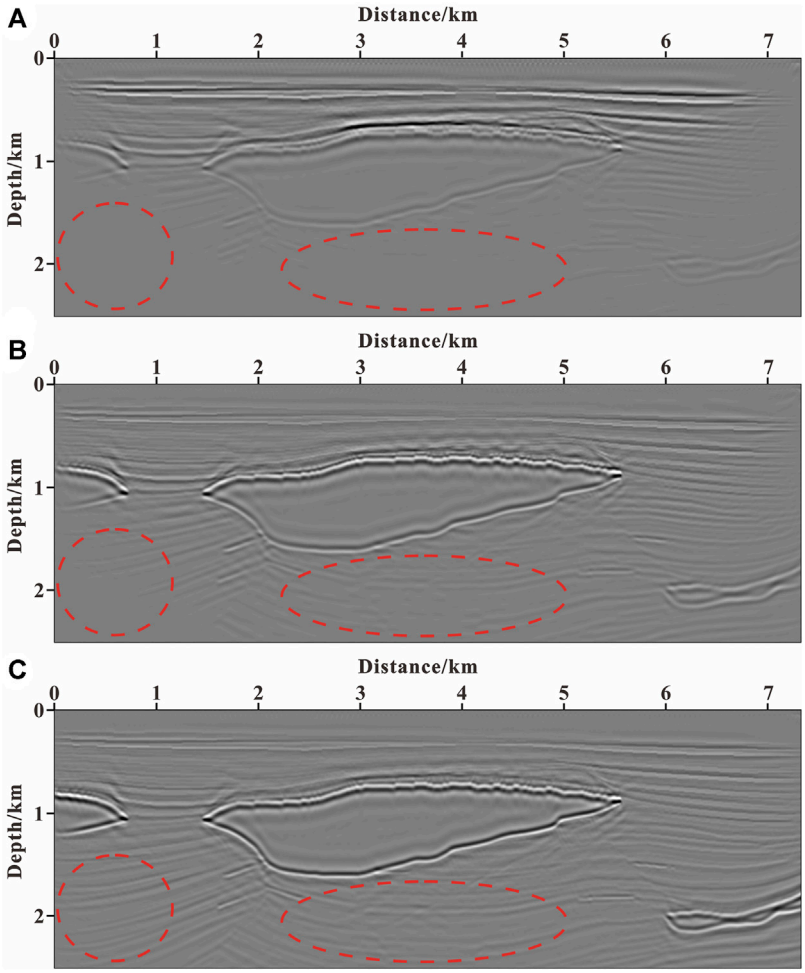

FIGURE 10 | Imaging results of LSRTM after 60 iterations: **(A)** without gradient preconditioning; **(B)** using GPSWE; and **(C)** using GPTWE.

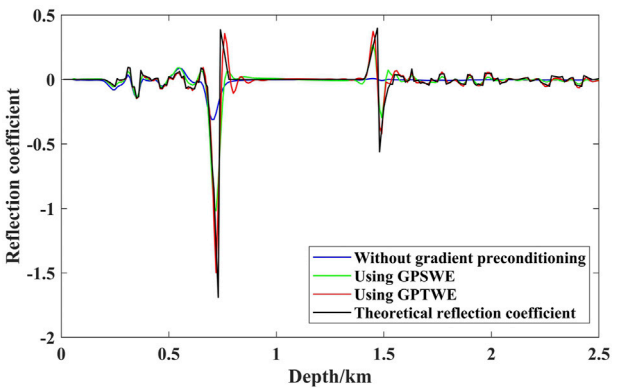

FIGURE 11 | Single-trace display of imaging results after 60 iterations.

after 60 iterations, where blue, green, red, and black are the single-trace curves of LSRTM without gradient preconditioning, using GPSWE, using GPTWE, and theoretical reflection coefficient, respectively. As observed from **Figure 7**, the imaging result of LSRTM using GPTWE is closest to the theoretical reflection coefficient curve, while the imaging result of LSRTM without gradient preconditioning is the different from the theoretical reflection coefficient curve at different imaging positions. Therefore, the amplitude preservation of the LSRTM using GPTWE is the highest, followed by the LSRTM using GPSWE, and the lowest without gradient preconditioning.

The convergence curves are shown in **Figure 8** for this example, where blue, green, and red are the convergence curves of LSRTM without gradient preconditioning, using GPSWE, and using GPTWE, respectively. In **Figure 8**, it can be seen that the LSRTM using GPTWE has the fastest convergence rate and the smallest residual error, followed by the LSRTM using GPSWE, while the LSRTM without gradient preconditioning has the slowest convergence rate and converges to the largest value after 60 iterations.

Furthermore, the computational efficiency of the previous three methods is analyzed, as shown in **Table 1**. (The GPU used in this experiment is GeForce RTX 2080 Ti.) **Table 1** shows that computational efficiency of those methods is basically the

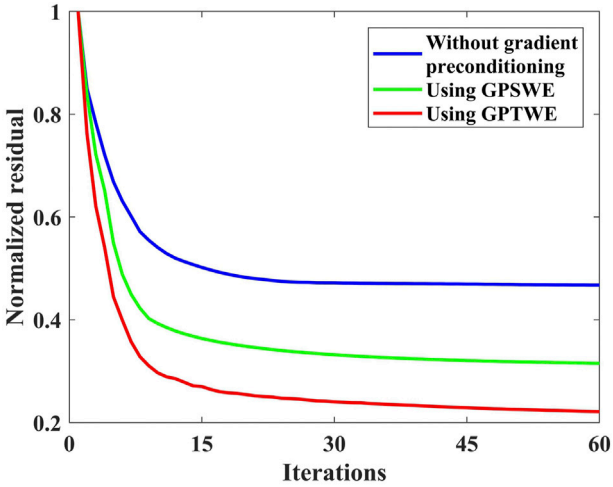

FIGURE 12 | Normalized residual curves.

same. It is also consistent with the result of theoretical analysis in *LSRTM Using the GPTWE*.

PLUTO DATA EXAMPLE

Due to the poor illumination beneath the salt bodies, the subsalt imaging problem has always been a challenging issue. So, in the second example, we performed LSRTM on the Pluto model to check the ability of LSRTM using GPTWE in recovering the weak events in the deep part and accelerating the convergence rate. **Figure 9A** shows the Pluto model, which is 7.33 km in length and 2.5 km in depth with a 10-m grid interval in the horizontal and vertical directions. And **Figure 9B** shows the smoothed background velocity model. The line involves 147 shots, and a total of 734 receivers are allotted for each shot. The observation data are generated by the full-waveform modeling (**Eq. 1**). The interval between shots is 50 m, and the interval between receivers is 10 m. The depth of shots and receivers are both 0 m. A Ricker wavelet with a 20 Hz dominant frequency is used to generate the data. The time sampling step is 1 ms, and the maximum recording time is 6 s. The accuracy in finite difference wavefield modeling is tenth order in space and second order in time. The hybrid absorbing boundary condition (Xie et al., 2020) is used for boundary processing.

The inverted images after 60 iterations with three different methods for the Pluto model are shown in **Figure 10**. As shown in **Figure 10** (marked by the dashed red circle), the LSRTM without gradient preconditioning is difficult to image the structure below the salt bodies because of the poor illumination; the LSRTM using GPSWE is helpful for imaging the subsalt structures, but the event is weak and the horizontal balance is poor; the LSRTM using GPTWE can effectively improve the imaging accuracy of deep target, and the subsalt structures are clearer and more continuous than those of other images.

Analogously, the imaging curves and theoretical reflection coefficient curve at x = 3,500 m are displayed in **Figure 11**. As observed from **Figure 11**, the imaging result of LSRTM using GPTWE is closest to the theoretical reflection coefficient curve, especially in the deep part.

The convergence curves are plotted in **Figure 12**. It can be seen that after 60 iterations, the red curve for LSRTM using GPTWE has the fastest convergence rate and converges to the smallest value.

CONCLUSION AND PROSPECT

Based on the calculation characteristics of LSRTM, this study proposes a gradient preconditioning approach using transmitted wave energy for LSRTM. In comparison with conventional methods, the imaging results of theoretical model tests show that the LSRTM using GPTWE can improve the imaging accuracy of deep target and speed up the convergence rate without significantly increasing the amount of calculation. In addition, this study only implements the two-dimensional LSRTM using GPTWE, and further extending the algorithm to three-dimensional migration will be the focus of subsequent research.

DATA AVAILABILITY STATEMENT

The original contributions presented in the study are included in the article/Supplementary Material; further inquiries can be directed to the corresponding author.

AUTHOR CONTRIBUTIONS

CX contributed to writing—original draft. PS helped with conceptualization and project administration. XL assisted with formal analysis. JT helped with software. SW framed the methodology. BZ provided suggestions.

FUNDING

This research is jointly funded by the National Natural Science Foundation of China (No. 42074138), Fundamental Research Funds for the Central Universities (201964016), and the Major Scientific and Technological Innovation Project of Shandong Province (2019JZZY010803).

REFERENCES

Baysal, E., Kosloff, D. D., and Sherwood, J. W. C. (1984). A Two-way Nonreflecting Wave Equation. *Geophysics* 49, 132–141. doi:10.1190/1.1441644

Baysal, E., Kosloff, D. D., and Sherwood, J. W. C. (1983). Reverse Time Migration. *Geophysics* 48, 1514–1524. doi:10.1190/1.1441434

Choi, Y., Min, D.-J., and Shin, C. (2008). Frequency-domain Elastic Full Waveform Inversion Using the New Pseudo-hessian Matrix: Experience of Elastic Marmousi-2 Synthetic Data. *Bull. Seismological Soc. America* 98 (5), 2402–2415. doi:10.1785/0120070179

Claerbout, J. F. (1992). *Earth Soundings Analysis: Processing versus Inversion*. Blackwell Scientific Publications.

Dai, W., Boonyasiriwat, C., and Schuster, G. T. (2010). 3D Multi-Source Least-Squares Reverse Time Migration. *80th Annu. Int. Meet. SEG. Denver*, 3120–3124. doi:10.1190/1.3513494

Dai, W., Fowler, P., and Schuster, G. T. (2012). Multi-source Least-Squares Reverse Time Migration. *Geophys. Prospecting* 60, 681–695. doi:10.1111/j.1365-2478.2012.01092.x

Dai, W., and Schuster, G. T. (2013). Plane-wave Least-Squares Reverse-Time Migration. *Geophysics* 78, S165–S177. doi:10.1190/GEO2012-0377.1

Fang, J., Zhou, H., Chen, H., Wang, N., Wang, Y., Sun, P., et al. (2019). Source-independent Elastic Least-Squares Reverse Time Migration. *Geophysics* 84, S1–S16. doi:10.1190/GEO2017-0847.1

Fletcher, R. P., Du, X., and Fowler, P. J. (2009). Reverse Time Migration in Tilted Transversely Isotropic (TTI) media. *Geophysics* 74, WCA179–WCA187. doi:10.1190/1.3269902

Gao, K., Chi, B. X., and Huang, L. J. (2017). "Elastic Least-Squares Reverse-Time Migration with Implicit Wavefield Separation," in 87th Annual International Meeting, September 23, 2017 to September 29, 2017 (Houston: SEG), 4389–4394.

Gao, W., Matharu, G., and Sacchi, M. D. (2020). Fast Least-Squares Reverse Time Migration via a Superposition of Kronecker Products. *Geophysics* 85, S115–S134. doi:10.1190/GEO2019-0254.1

Gerhard Pratt, R. G., Shin, C., and Hicks, G. J. (1998). Gauss-Newton and Full Newton Methods in Frequency-Space Seismic Waveform Inversion. *Geophys. J. Int.* 133, 341–362. doi:10.1046/j.1365-246x.1998.00498.x

Gong, X. B., Wang, S. C., and Han, L. G. (2019). Sparse Least-Squares Reverse Time Migration of Small Scatters in Seismic Exploration. *Chin. J. Geophys.* 62, 4028–4038. doi:10.6038/cjg2019M0420

Gu, B., Li, Z., Yang, P., Xu, W., and Han, J. (2017). Elastic Least-Squares Reverse Time Migration with Hybrid L1/l2 Misfit Function. *Geophysics* 82, S271–S291. doi:10.1190/GEO2016-0235.1

Guo, P., and McMechan, G. A. (2018). Compensating Q Effects in Viscoelastic media by Adjoint-Based Least-Squares Reverse Time Migration. *Geophysics* 83, S151–S172. doi:10.1190/GEO2017-0235.1

Guo, Z. B., and Li, Z. C. (2014). True-amplitude Imaging Based on Least-Squares Reverse Time Migration. *Oil Geophys. Prospecting* 49, 113–120. doi:10.13810/j.cnki.issn.1000-7210.2014.01.014

Hu, J., Wang, H., Fang, Z., Li, T., and Zhang, J. (2016). Efficient Amplitude Encoding Least-Squares Reverse Time Migration Using Cosine Basis. *Geophys. Prospecting* 64, 1483–1497. doi:10.1111/1365-2478.12356

Huang, J. P., Cao, X. L., Li, Z. C., Sun, Y. S., Li, C., and Gao, G. C. (2014). Least Square Reverse Time Migration in High Resolution Imaging of Near Surface. *Oil Geophys. Prospecting* 49, 107–112. doi:10.13810/j.cnki.issn.1000-7210.2014.01.013

Huang, J. P., Li, C., Li, Q. Y., Guo, S. J., Duan, X. B., Li, J. G., et al. (2015). Least-squares Reverse Time Migration with Static Plane-Wave Encoding. *Chin. J. Geophys.* 58, 2046–2056. doi:10.6038/cjg20150619

Li, C., Huang, J., Li, Z., and Wang, R. (2018). Plane-wave Least-Squares Reverse Time Migration with a Preconditioned Stochastic Conjugate Gradient Method. *Geophysics* 83, S33–S46. doi:10.1190/GEO2017-0339.1

Li, F., Gao, J., Gao, Z., Jiang, X., and Sun, W. (2020). Least-squares Reverse Time Migration with Sparse Regularization in the 2D Wavelet Domain. *Geophysics* 85, S313–S325. doi:10.1190/GEO2018-0763.1

Liu, F., Zhang, G., Morton, S. A., and Leveille, J. P. (2011). An Effective Imaging Condition for Reverse-Time Migration Using Wavefield Decomposition. *Geophysics* 76, S29–S39. doi:10.1190/1.3533914

Liu, X., and Liu, Y. (2019). Deghosting-based Reverse Time Migration with Free-Surface Multiples. *Geophys. J. Int.* 216, 1191–1200. doi:10.1093/gji/ggy486

Liu, X., Liu, Y., Huang, X., and Li, P. (2016). Least-squares Reverse-Time Migration with Cost-Effective Computation and Memory Storage. *J. Appl. Geophys.* 129, 200–208. doi:10.1016/j.jappgeo.2016.03.009

McMechan, G. A. (1983). Migration by Extrapolation of Time-dependent Boundary Values*. *Geophys. Prospect* 31, 413–420. doi:10.1111/j.1365-2478.1983.tb01060.x

Nemeth, T., Wu, C., and Schuster, G. T. (1999). Least-squares Migration of Incomplete Reflection Data. *Geophysics* 64, 208–221. doi:10.1190/1.144455710.1190/1.1444517

Plessix, R.-E. (2006). A Review of the Adjoint-State Method for Computing the Gradient of a Functional with Geophysical Applications. *Geophys. J. Int.* 167, 495–503. doi:10.1111/j.1365-246X.2006.02978.x

Qu, Y. M., Li, J. L., Wang, Y. C., Li, Z. C., Sun, W. Z., and Sun, J. Z. (2019). Correction of Viscoelasticity and Anisotropy in Least-Squares Reverse Time Migration: a Bohai Bay Seismic Case Study. *Chin. J. Geophys.* 62, 2203–2216. doi:10.6038/cjg2019M0597

Ren, Z., Liu, Y., and Sen, M. K. (2017). Least-squares Reverse Time Migration in Elastic media. *Geophys. J. Int.* 208, 1103–1125. doi:10.1093/gji/ggw443

Rocha, D., and Sava, P. (2018). Elastic Least-Squares Reverse Time Migration Using the Energy Norm. *Geophysics* 83, S237–S248. doi:10.1190/GEO2017-0465.1

Shin, C., Jang, S., and Min, D.-J. (2001). Improved Amplitude Preservation for Prestack Depth Migration by Inverse Scattering Theory. *Geophys. prospecting* 49 (5), 592–606. doi:10.1046/j.1365-2478.2001.00279.x

Song, P., Tan, J., Liu, Z., Zhang, X., Liu, B., Yu, K., et al. (2019). Time-domain Full Waveform Inversion Using the Gradient Preconditioning Based on Transmitted Wave Energy. *J. Ocean Univ. China* 18, 859–867. doi:10.1007/s11802-019-3783-z

Sun, J., Fomel, S., and Ying, L. (2016). Low-rank One-step Wave Extrapolation for Reverse Time Migration. *Geophysics* 81, S39–S54. doi:10.1190/GEO2015-0183.1

Symes, W. W. (2007). Reverse Time Migration with Optimal Checkpointing. *Geophysics* 72, SM213–SM221. doi:10.1190/1.2742686

Tan, S., and Huang, L. (2014). Least-squares Reverse-Time Migration with a Wavefield-Separation Imaging Condition and Updated Source Wavefields. *Geophysics* 79, S195–S205. doi:10.1190/GEO2014-0020.1

Wong, M., Biondi, B. L., and Ronen, S. (2015). Imaging with Primaries and Free-Surface Multiples by Joint Least-Squares Reverse Time Migration. *Geophysics* 80, S223–S235. doi:10.1190/GEO2015-0093.1

Wu, D., Yao, G., Cao, J., and Wang, Y. (2016). Least-squares RTM with L1 Norm Regularisation. *J. Geophys. Eng.* 13, 666–673. doi:10.1088/1742-2132/13/5/666

Xie, C., Song, P., Tan, J., Liu, B., Li, J., Yu, K., et al. (2020). Cosine-type Weighted Hybrid Absorbing Boundary Based on the Second-Order Higdon Boundary Condition and its GPU Implementation. *J. Geophys. Eng.* 17, 231–248. doi:10.1093/jge/gxz102

Yang, J., Li, Y. E., Liu, Y., and Zong, J. (2020). Least-squares Extended Reverse Time Migration with Randomly Sampled Space Shifts. *Geophysics* 85, S357–S369. doi:10.1190/GEO2019-0536.1

Yang, J., Liu, Y., Li, Y. E., Cheng, A., Dong, L., and Du, Y. (2019). Joint Least-Squares Reverse Time Migration of Primary and Prismatic Waves. *Geophysics* 84, S29–S40. doi:10.1190/GEO2017-0850.1

Yang, J., and Zhu, H. (2019). Viscoacoustic Least-Squares Reverse Time Migration Using a Time-Domain Complex-Valued Wave Equation. *Geophysics* 84, S479–S499. doi:10.1190/GEO2018-0804.1

Yao, G., and Jakubowicz, H. (2016). Least-squares Reverse-Time Migration in a Matrix-Based Formulation. *Geophys. Prospecting* 64, 611–621. doi:10.1111/1365-2478.12305

Yoon, K., and Marfurt, K. J. (2006). Reverse-time Migration Using the Poynting Vector. *Exploration Geophys.* 37, 102–107. doi:10.1071/EG06102

Zhang, Q., Zhou, H., Chen, H., and Wang, J. (2016). Least-squares Reverse Time Migration with and without Source Wavelet Estimation. *J. Appl. Geophys.* 134, 1–10. doi:10.1016/j.jappgeo.2016.08.003

Zhang, Y., Duan, L., and Xie, Y. (2015). A Stable and Practical Implementation of Least-Squares Reverse Time Migration. *Geophysics* 80, V23–V31. doi:10.1190/GEO2013-0461.1

Zhang, Z., Huang, L., and Lin, Y. (2012). "A Wave-Energy-Based Precondition Approach to Full-Waveform Inversion in the Time Domain," in 82nd Annual International Meeting, November 4 to November 9, 2012 (Las Vegas: SEG), 1–5. doi:10.1190/segam2012-1555.1

Zhao, Z., and Sen, M. K. (2018). Fast Image-Domain Target-Oriented Least-Squares Reverse Time Migration. *Geophysics* 83, A81–A86. doi:10.1190/GEO2018-0033.1

Conflict of Interest: The authors declare that the research was conducted in the absence of any commercial or financial relationships that could be construed as a potential conflict of interest.

Publisher's Note: All claims expressed in this article are solely those of the authors and do not necessarily represent those of their affiliated organizations, or those of the publisher, the editors, and the reviewers. Any product that may be evaluated in this article, or claim that may be made by its manufacturer, is not guaranteed or endorsed by the publisher.

frontiers in Earth Science

ORIGINAL RESEARCH
published: 27 January 2022
doi: 10.3389/feart.2022.749462

Source-Free P-SV Converted-Wave Reverse-Time Migration Using First-Order Velocity-Dilatation-Rotation Equations

Bingshou He[1,2]*, *Xinru Yao*[1,2] *and Xiangqi Shao*[1,2]

[1]Key Lab of Submarine Geoscience and Prospecting Techniques, Ministry of Education, Ocean University of China, Qingdao, China, [2]Evaluation and Detection Technology Laboratory of Marine Mineral Resources, Qingdao National Laboratory for Marine Science and Technology, Qingdao, China

The cross-correlation imaging condition between source- and receiver-wavefields is often used in the elastic wave reverse-time migration (RTM) to utilize P- and S-waves. However, it cannot be applied in the absence of source information (e.g., source location, and source wavelet), which is quite common in passive source exploration. We employ a source-free P-SV converted-wave imaging condition, which only requires the back-propagating receiver-wavefield to utilize the P-SV converted waves in imaging the subsurface structures. The imaging condition is independent of source information, which can avoid the extrapolation and reconstruction of the source-wavefield. As a result, the computational cost is decreased to about one-third of conventional RTM that uses source-wavefield reconstruction strategies, e.g., random boundaries. The memory requirement could be also reduced by avoiding the calculation of source-wavefield. Because our imaging condition uses the vector P-wavefield and vector S-wavefield to utilize the P-SV waves, it is necessary to decouple P-wavefield and S-wavefield during the reverse-time extrapolation of receiver-wavefield. We use the first-order velocity-dilatation-rotation elastic wave equations to realize the reverse-time propagation of vector receiver-wavefield, where the vector P-wavefield and vector S-wavefield can be obtained directly. Based on the above methods, a source-free P-SV converted-wave RTM of multi-component seismic data is realized. The model tests show that this method can generate promising subsurface images and can be complementarily used when conventional cross-correlation imaging conditions are not suitable.

Keywords: P-SV converted-wave, reverse-time migration (RTM), first-order velocity-dilatation-rotation equations, source-free imaging condition, poynting vector

OPEN ACCESS

Edited by:
Hao Hu,
University of Houston, United States

Reviewed by:
Xuejian Liu,
The Pennsylvania State University (PSU), United States
Yanbao Zhang,
Institute of Geophysics, China

***Correspondence:**
Bingshou He
hebinshou@ouc.edu.cn

Specialty section:
This article was submitted to Solid Earth Geophysics, a section of the journal Frontiers in Earth Science

Received: *29 July 2021*
Accepted: *03 January 2022*
Published: *27 January 2022*

Citation:
He B, Yao X and Shao X (2022) Source-Free P-SV Converted-Wave Reverse-Time Migration Using First-Order Velocity-Dilatation-Rotation Equations. Front. Earth Sci. 10:749462. doi: 10.3389/feart.2022.749462

INTRODUCTION

Techniques based on reflected P-wave have played an important role in seismic exploration. However, with the continued improvement of seismic exploration accuracy and the increased complexity of exploration targeted structure and lithology in the oil and gas industry, seismic exploration based solely on reflected P-wave is progressively restricted by its theoretical assumptions

and single wavefield information. It has become challenging to obtain satisfactory imaging results for exploring fractured carbonate, coalbed methane, and shale gas reservoirs (Stewart et al., 2003; Yang et al., 2006; Bian et al., 2017). Multi-component seismic exploration based on the elastic wave theory can obtain more subsurface imaging information. Compared with the reflected P-wave exploration techniques, multi-component seismic imaging methods require fewer theoretical assumptions and take account of S-wave propagation in complex media. In theory, multi-component seismic exploration is more capable of fully characterizing the subsurface using both P- and S-waves, which is more conducive to improving the accuracy and resolution of imaging.

Prestack depth migration is a popular research topic of multi-component seismic exploration. At present, there are two main ways to achieve prestack migration using multi-component seismic data. One is based on scalar wave theory (Whitemore, 1983; Sun and McMechan, 2001; Sun et al., 2006; Chattopadhyay and McMechan, 2008; Liu et al., 2011) to first obtain the reflected P-wave and converted S-wave recordings by decoupling P- and S-waves from multi-component seismic data. Then, the existing acoustic RTM operator is adopted to realize the migration imaging of P- and S-waves data, respectively. It has the advantage of few calculations and high efficiency, but it also has apparent issues in that ignoring the vector properties of elastic waves and the accuracy of P-wave and S-wave decoupling can seriously affect the migration results. The other way is the elastic wave prestack depth migration based on vector wavefield (Chang and McMechan, 1994; He and Zhang, 2006), which is mainly realized by elastic reverse-time migration (ERTM) techniques. It regards multi-component seismic data as a vector wavefield for processing. Generally, the method based on the vector wavefield does not require the decoupling of P- and S-waves in the data domain. By solving the elastic wave equations and combining them with a proper imaging condition, e.g., the joint migration of multi-component, the simultaneous imaging of reflected P-wave and converted S-wave can be obtained. Therefore, the ERTM techniques have attracted extensive attention in the industry.

A large number of studies have been conducted on ERTM in recent years, and significant advancements have been made in wavefield extrapolation (Dellinger and Etgen, 1990; Dong et al., 2000b), imaging methods (He and Zhang, 2006; Du et al., 2012a; Du et al., 2014), decoupling methods of P- and S-waves in the migration process (Sun et al., 2004; Yan and Sava, 2009), migration noise suppression (Yu et al., 2018; Zhang et al., 2021), reverse-time reconstruction of the source-wavefield (Clapp, 2009; Wu and Qin, 2014), and GPU parallelism (Bao et al., 2021; Shen, 2017), respectively. These results are of great significance to promote the development of multi-component seismic RTM techniques. However, the existing ERTM techniques have two main issues. 1) The ERTM techniques assume that each component in the multi-component seismic data has the same seismic frequency spectrum. In fact, due to the different absorption mechanisms of the P-wave and S-wave in the subsurface media (Biot, 1956; Murphy, 1982; Wang et al., 2006), the attenuation of the high-frequency components of the S-wave in the actual recordings is greater than that of the P-wave, resulting in P-wave often having a higher dominant frequency and a broader bandwidth. The spectrum discrepancy of recorded P- and S-waves introduces difficulty in setting the wavelet in ERTM. 2) It is challenging to obtain accurate propagation directions of P- and S-waves for wavefield separation. In the ERTM, cross-correlation imaging condition (Claerbout, 1971) based on wavefield separation is often used to utilize the P- and S-waves, and further suppress low-wavenumber imaging artifacts. The prerequisite for accurate wavefield separation is that the propagation directions of pure P-wavefield and pure S-wavefield at all imaging grid points must be obtained for each timestep. Based on the Poynting vector (Poynting, 1884), the conventional methods for calculating wavefield propagation directions can only get the propagation directions of the coupled wavefield (Du et al., 2012b), rather than that of pure P-wavefield and pure S-wavefield. The error in propagation direction will be transferred to the migration results, reducing the accuracy of the migration.

This paper demonstrates a converted-wave RTM method that can avoid the two issues of existing traditional elastic techniques. The first-order velocity-dilatation-rotation elastic wave equations in the isotropic medium are used to implement the reverse-time extrapolation of the receiver-wavefield. The P-wavefield and S-wavefield can be automatically decoupled during the propagation which we refer to as "wavefield decomposition". Then the decoupled receiver-wavefields are separated into the pure P- and S-wavefields of different propagation directions based on the Poynting vector which we refer to as "wavefield separation". This study utilizes the up-going pure P- and S-waves derived from the Poynting vector to realize the converted-wave RTM by using the source-free P-SV converted-wave imaging condition.

The advantages of the method proposed in this study are 1) The first-order velocity-dilatation-rotation elastic wave equations explicitly provide various parameters for calculating the vector wavefield of pure P- and S-waves. Such decoupled vector wavefields can be easily used to obtain the Poynting vector of different wave types in the wavefield extrapolation. Thus, it overcomes the issue that the conventional elastic wave equations can only get the coupled wavefield propagation directions in RTM. 2) A source-free converted-wave imaging condition is applied for converted-wave imaging. The migration process does not require the forward extrapolation of the source-wavefield, which avoids the problem of wavelet setting. 3) The vector wavefield is processed, and there is no need to decompose the P- and S-waves from the measured multi-component seismic recordings in data pre-processing. 4) The algorithm in this paper is suitable for migration using both passive- and active-source multi-component data. The calculation cost is typically one-third of that of conventional ERTM techniques that use source-wavefield reconstruction strategies, e.g., random boundaries.

THE EXTRAPOLATION AND SEPARATION OF WAVEFIELD OF FIRST-ORDER VELOCITY-DILATATION-ROTATION ELASTIC WAVE EQUATIONS

The purpose of ERTM is to realize the depth-domain imaging of pure P-wavefield and pure S-wavefield. As a result, it requires that the pure P-wavefield and pure S-wavefield must be obtained

before applying the imaging condition. To suppress the low wavenumber imaging artifacts in RTM, it is necessary to separate the different propagation directions of P- and S-waves, and then only the wavefields with the opposite propagation directions are used in cross-correlation imaging. Wang and McMechan (2015) used the particle velocity and stress tensor of the traditional stress-particle velocity wave equations to calculate additional P-wave stress and obtain the P-wave particle velocity by using the divergence operator. Then, the S-wave particle velocity can be obtained by subtracting that of the P-wave from the complete particle velocity. The Poynting vector was used to obtain the propagation directions of the P-wave and S-wave. Du et al. (2017) adopted a similar method as Wang and McMechan (2015) to realize the imaging of various reflected- and converted-wavefields, but their imaging condition does not require polarity correction. Their works have improved the accuracy of ERTM, but it still requires explicitly decoupling the P-and S-waves during the migration process. In this study, we use the first-order velocity-dilatation-rotation equations to extrapolate the wavefield, which does not require explicit decoupling.

Reverse-Time Extrapolation of First-Order Velocity-Dilatation-Rotation Elastic Wave Equations

The three-dimension first-order velocity-dilatation-rotation equations in an isotropic medium are (Tang et al., 2016):

$$\begin{cases} \dfrac{\partial \boldsymbol{v_P}}{\partial t} = c_P^2 \nabla\theta \\ \dfrac{\partial \boldsymbol{v_S}}{\partial t} = -c_S^2 \nabla \times \boldsymbol{\omega} \\ \boldsymbol{v} = \boldsymbol{v_P} + \boldsymbol{v_S} \\ \dfrac{\partial \theta}{\partial t} = \nabla \cdot \boldsymbol{v} \\ \dfrac{\partial \boldsymbol{\omega}}{\partial t} = \nabla \times \boldsymbol{v} \end{cases} \tag{1}$$

where c_P and c_S are the propagation velocity of P-wave and S-wave, respectively, which are functions of the spatial coordinates. $\boldsymbol{v} = (v_x, v_y, v_z)$ is the particle vibration velocity vector, $\boldsymbol{v_P} = (v_{Px}, v_{Py}, v_{Pz})$ is the velocity vector of particle vibration caused by dilatation motion, $\boldsymbol{v_S} = (v_{Sx}, v_{Sy}, v_{Sz})$ is the velocity vector of particle vibration caused by shear motion. $\theta = \nabla \cdot \boldsymbol{u}$ is the scalar P-wave, and $\boldsymbol{\omega} = \nabla \times \boldsymbol{u}$ is the vector S-wave. ∇, $\nabla\cdot$ and $\nabla\times$ are the gradient, divergence, and curl, respectively.

The finite-difference scheme of the multi-component seismic recording for reverse-time extrapolation can be obtained by using a high-order finite-difference algorithm to discrete **Eq. 1** in staggered-grid space (Dong et al., 2000b). The derivation by Dong et al. (2000a) is used to obtain the stability condition of the finite-difference scheme, and the reverse-time extrapolation of multi-component seismic recordings can be realized by using the finite-difference scheme in combination with the stability condition. **Eq. 1** explicitly includes the scalar P-wave component and the vector S-wave component, as well as the particle vibration velocity vector caused by the dilatation and the shear motion. As an example, we compute the wavefield for a two-layer horizontal model based on **Eq. 1**. As shown in **Figure 1**, the model is of the size of 1,000 m × 600 × 1,000 m, with the spatial grid size of 5 × 5 × 5 m. The depth of the single interface is 500 m. The P source is a Ricker wavelet with a dominant frequency of 35 Hz placed at (500 m, 300 m, 0 m). The P-wave velocities for the upper and lower layers are 2,300 and 2,800 m/s, respectively. The P-wave and S-wave velocity ratio is fixed at 1.73. The perfectly-matched-layer (PML) absorbing boundaries are set to 30 layers. **Figure 1** shows the three-component wavefront snapshots of particle velocity at 0.4 s, and it can be clearly observed that the P- and S-waves can be obtained without explicit decoupling in the wavefield extrapolation by applying **Eq. 1**, and the P- and S-wave polarities are consistent with that of the mixed wavefield.

Obtaining the Poynting Vector of Pure P- and S-Waves in the Reverse-Time Extrapolation

According to the definition of the Poynting vector in seismic wavefield (Yoon and Marfurt, 2006), the following equations can be used to calculate the Poynting vector of pure P- and S-waves in the wavefield extrapolation using **Eq. 1** (Tang et al., 2016):

$$\begin{cases} \boldsymbol{E_P} = -\theta \boldsymbol{v_P} \\ \boldsymbol{E_S} = -\boldsymbol{v_S} \times \boldsymbol{\omega} \end{cases} \tag{2}$$

where $\boldsymbol{E_P}$ and $\boldsymbol{E_S}$ are P-wave and S-wave Poynting vectors, respectively.

Since **Eq. 1** explicitly contains parameters needed in **Eq. 2**, it is convenient to obtain the Poynting vector of P-wave and S-wave in the reverse-time extrapolation of the receiver-wavefield by applying **Eq. 1**, and further obtain the propagation directions of pure P- and S-waves at each imaging point for each timestep (Tang et al., 2016). The wavefield can be separated into pure P- and S-wavefields of different propagation directions simultaneously during the imaging.

To verify the advantages mentioned above, we take the three-layer model shown in **Figure 2** to calculate the forward extrapolated Poynting vector of source-wavefield based on the first-order velocity-stress equations and the first-order velocity-dilatation-rotation equations, respectively. The model is the size of 2000 × 2000 m, and the grid size is 5 × 5 m. The absorbing boundaries are implied by PML with 100 layers. The P-wave velocity model is shown in **Figure 2**, and the corresponding S-wave velocity model is computed from c_P with a ratio of $\frac{c_P}{c_S} = 1.73$. The P-wave source is a Ricker wavelet with a dominant frequency of 35 Hz located in the middle of the surface (1,000 m, 0 m). The time-stepping interval is 0.5 ms. In **Figure 3**, we show the difference of the Poynting vectors obtained from velocity-stress equations (**Figure 3A**) and velocity-dilatation-rotation equations (**Figure 3B** for P-wave and **Figure 3C** for S-wave). The first-order velocity-stress equations notably can only get the Poynting vector of the mixed P- and S-wavefields

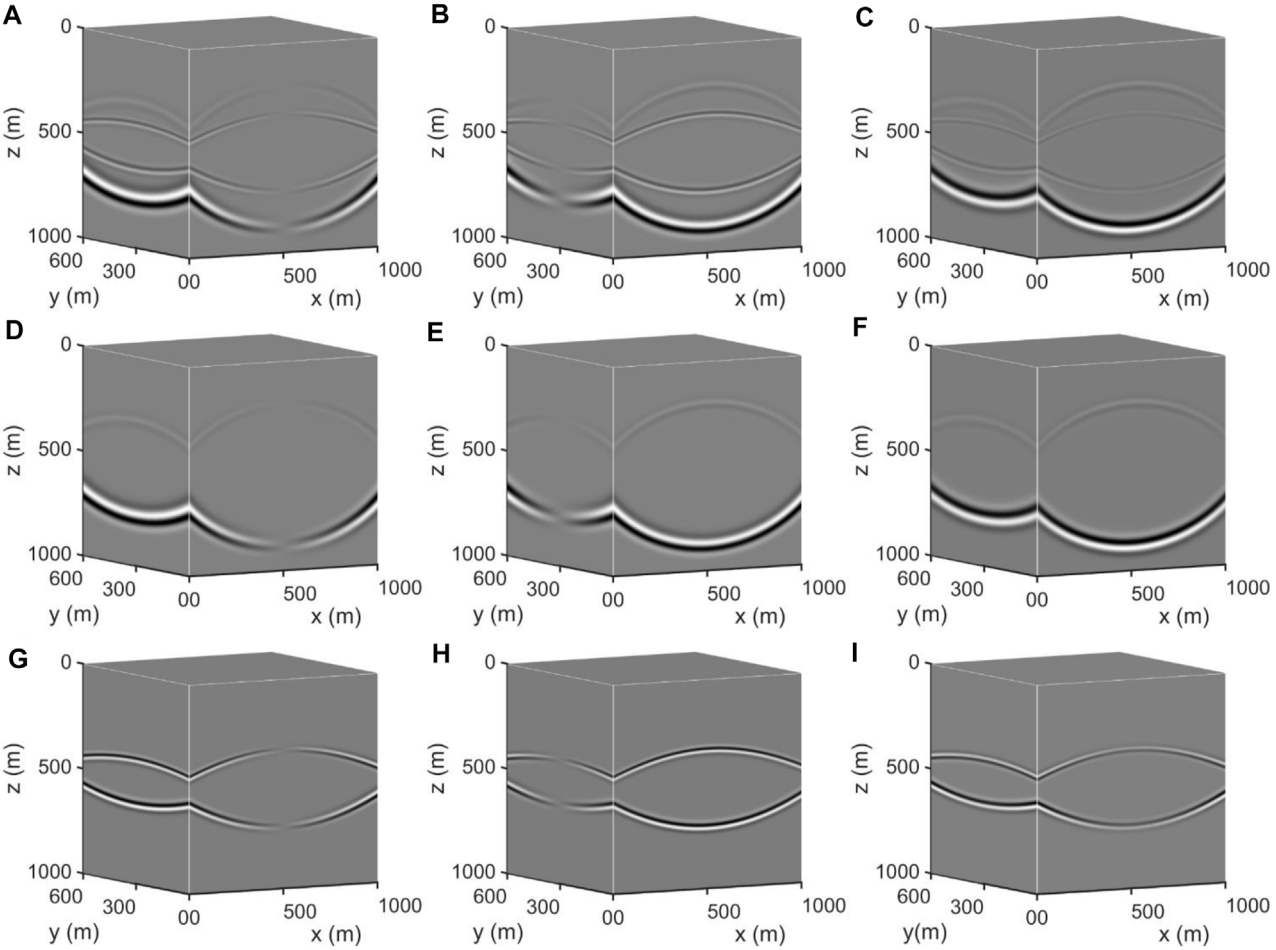

FIGURE 1 | Three-component snapshots of particle velocity at 0.4 s computed based on **Eq. 1**. **(A–C)** The joint velocity components of P- and S-waves in *x*, *y*, *z* directions, **(D–F)** The P-wave components in *x*, *y*, *z* directions computed by applying **Eq. 1**, **(G–I)** The S-wave components in *x*, *y*, *z* directions computed by applying **Eq. 1**.

as shown in **Figure 3A**. When P- and S-waves exist simultaneously at a certain imaging point, the Poynting vector is neither that of P-wave nor that of S-wave (for example, indicated by the black circle in **Figure 3A**). Apparently, it is not easy to accurately distinguish the propagation directions of pure P-wave and pure S-wave based on this vector. In contrast, the Poynting vector of pure P-wave and pure S-wave can be obtained by applying the velocity-dilatation-rotation equations (**Figure 3B,C**), which can accurately describe the propagation directions of a particular type of wave.

Once the Poynting vector of P-wave and S-wave are calculated in wavefield extrapolation, the wavefield can be separated into wavefields propagating in different directions. The formulas for separating P-wave into waves of opposite propagation directions are given by:

$$\boldsymbol{P}^{+}(x,y,z,t) = \begin{cases} 0 & E_P^i \geq 0 \\ \boldsymbol{P}(x,y,z,t) & E_P^i < 0 \end{cases}$$
$$\boldsymbol{P}^{-}(x,y,z,t) = \begin{cases} \boldsymbol{P}(x,y,z,t) & E_P^i \geq 0 \\ 0 & E_P^i < 0 \end{cases} \quad (3)$$

where $\boldsymbol{P}(x,y,z,t)$ is the vector P-wave at the position (x, y, z) at time t, which represents the $\boldsymbol{v_P}$ in the velocity-dilatation-rotation equations. $\boldsymbol{E_P} = \sum_{i=x,y,z} E_p^i$, where E_p^i is the i-component of P-wave Poynting vector, and i represents the multi-component of the P-wave. + and − represent the opposite directions of waves in the i-component, respectively. When $i = z$, $\boldsymbol{P}^{+}(x,y,z,t)$ and $\boldsymbol{P}^{-}(x,y,z,t)$ represent the up- and down-going waves in the z-component of the P-wave, respectively. The formulas for S-wave separation are analogous to **Eq. 3**, with the Poynting vector of the P-wave replaced by that of the S-wave. And the other two components are separated in the same way as the z-component.

IMAGING CONDITION

The cross-correlation of source- and receiver-wavefields is commonly used in the ERTM using P- and S-waves (Yan and Sava, 2008; Du et al., 2012b) with the following basic ideas. 1) Calculating the divergence of the source-wavefield to obtain the pure P-wave (S_P) component of the source-wavefield, and calculating the divergence and curl of the receiver-wavefield to obtain the pure P-wave (R_P) and the pure vector S-wave ($\boldsymbol{R_S}$) of

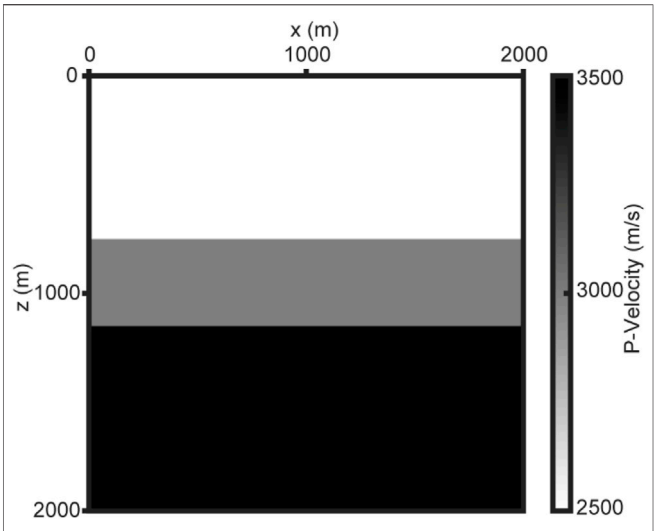

FIGURE 2 | The three-layer horizontal P-wave velocity model. The P-wave velocities of the three layers from top to bottom are 2,500, 3,000, and 3,500 m/s, respectively. The depths of the two interfaces are 750 and 1,150 m, respectively.

the receiver-wavefield (Dellinger and Etgen, 1990). 2) Applying R_P and S_P to perform zero-time-delay cross-correlation and stack to get the reflected wave migration image. 3) Realizing the scalarization of $\boldsymbol{R}_S$ (Du et al., 2014) and performing zero-time-delay cross-correlation with S_P to obtain the converted-wave migration image. The above imaging methods are robust to noise existence (Xue, 2013) and with clear physical meanings of the imaging results. However, the scalarization of the vector S-wave will lose its vector properties. In addition, many challenging problems in the vector S-wave scalarization technique are still not resolved. For example, when the structure is complex, the polarity of the S-wave is challenging to obtain accurately. The inaccurate polarity correction will cause local fragmentation in the migration image.

To overcome the above problems, Wang and He (2017) proposed the cross-correlation imaging condition of vector wavefield dot product based on the separation of traveling waves. It first calculates the gradient and curl of the scalar P-wave and the vector S-wave respectively by the divergence and curl operators to obtain the P- and S-waves of the vector potential. Then, it uses the Poynting vector to separate P- and S-waves of the vector potential to acquire waves of the different propagation directions. Finally, the cross-correlation imaging is carried out by using the source- and receiver-wavefields of the opposite propagation directions to obtain P- and S-waves migration results. Their method does not require the scalarization of the vector S-wave, and the vector properties of the S-wave remain during the imaging process. Moreover, it is not necessary to employ polarity correction for the converted-wave migration result.

Although the imaging conditions mentioned above can often achieve promising imaging results for active source multi-component seismic data, they are not suitable for passive source data that lack accurate source information and cannot enable the extrapolation of the source-wavefield. Furthermore, it is difficult for the active source data to provide an accurate source wavelet for the wavefield extrapolation when the spectra of the multi-component seismic recording are inconsistent. The incorrect source wavelet will often result in large position errors in migration results. Xiao and Schuster (2009) proposed the passive source imaging condition for VSP imaging. The source-free imaging condition helps avoid the overburden effects and results in a better image of the salt flank by the receiver data. Shang et al. (2012) and Shabelansky et al. (2015) argued that passive seismic without location information can be used to achieve the source-free subsurface image. Based on the relationship between the P-wavefield and converted S-wavefield in the receiver extrapolation, Shabelansky et al. (2017) demonstrated a source-free converted-wave RTM imaging condition, which only uses the back-propagation P- and S-waves to perform cross-correlation imaging. As a result, it does not require source extrapolation, thereby saving

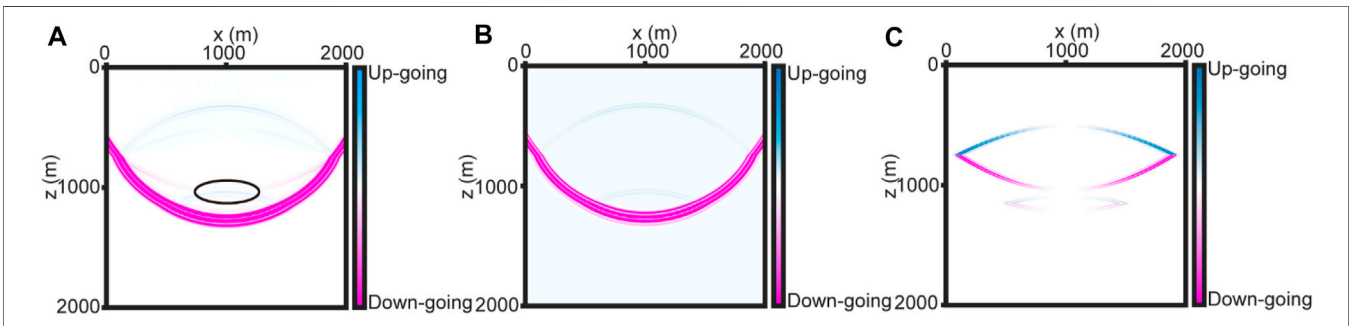

FIGURE 3 | Comparisons of Poynting vector snapshots for the velocity-stress equations and velocity-dilatation-rotation equations at 0.495 s. Blue represents the up-going wave and pink represents the down-going wave, respectively. **(A)** A snapshot of the z-component of the Poynting vector using the velocity-stress equations. The black ellipse indicates locations that P- and S-waves exist simultaneously. **(B)** A snapshot of the z-component of the Poynting vector of the P-wave using the velocity-dilatation-rotation equations. **(C)** A snapshot of the z-component of the Poynting vector of the S-wave using the velocity-dilatation-rotation equations.

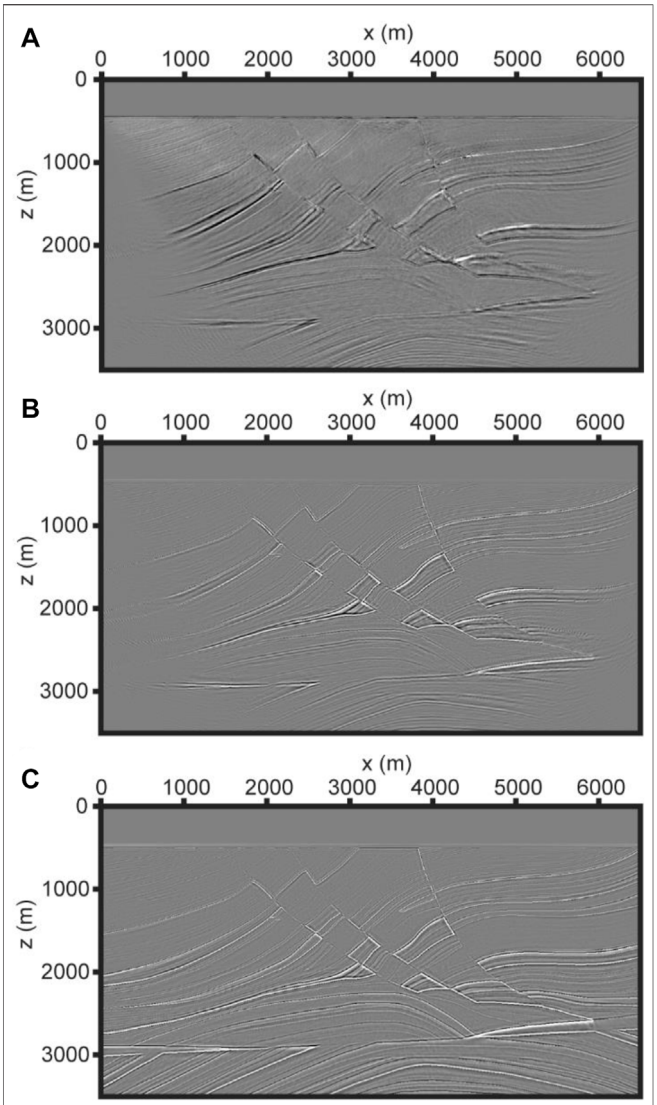

FIGURE 4 | (A) The migration image of the cross-correlation imaging conditions without wavefield decomposition and wavefield separation, using the first-order velocity-stress equations. **(B)** The migration image of the cross-correlation imaging condition with wavefield separation, using the first-order velocity-stress equations. **(C)** The migration image uses the imaging condition of **Eq. 6** and the elastic wave equations of **Eq. 1**.

calculation time and storage resources for source-wavefield reconstruction.

In this study, we apply the vector imaging condition to the RTM of the first-order velocity-dilatation-rotation elastic wave equations. First, we take advantage of velocity-dilatation-rotation equations to obtain the P-wave and S-wave with different propagation directions. There is no need for the explicit decomposition of the P- and S-waves. We can accurately obtain the propagation directions of pure P- and S-waves, assuming that there is only one set of P-wave and S-wave on the same imaging point at the same time. Then, based on the idea of vector dot product cross-correlation, we present a more precise source-free P-SV converted-wave imaging condition.

Shabelansky et al. (2017) gave a source-free converted-wave imaging condition:

$$I_{PS(x,y,z)} = \frac{\sum_0^{t_{max}} \boldsymbol{P}_R(x,y,z,t)\boldsymbol{S}_R(x,y,z,t)}{\sum_0^{t_{max}} \boldsymbol{P}_R^2(x,y,z,t)} \tag{4}$$

where I_{PS} is the converted-wave migration result, $\boldsymbol{P}_R$ and $\boldsymbol{S}_R$ are the P-wavefield and the converted S-wavefield of the receiver, respectively. t represents time, and t_{max} is the maximum recording length, and x, y, z are the three spatial coordinates of the rectangular coordinate system.

To improve the stability and amplitude fidelity of **Eq. 4**, Shabelansky et al. (2017) further modified it as follows:

$$I_{PS(x,y,z)} = \frac{\sum_0^{t_{max}} 4\boldsymbol{P}_R(x,y,z,t)\boldsymbol{S}_R(x,y,z,t)}{\sum_0^{t_{max}} \left(\boldsymbol{P}_R^2(x,y,z,t) + 2\left|\boldsymbol{P}_R(x,y,z,t)\boldsymbol{S}_R(x,y,z,t)\right| + \boldsymbol{S}_R^2(x,y,z,t)\right)} \tag{5}$$

Eq. 5 represents a source-free imaging condition, which does not need to calculate, store, and reconstruct the source-wavefield, know the source position, and set the source wavelet.

When there is only one subsurface reflection interface, the imaging result of **Eq. 5** represents the ratio of the S-wave reflection coefficient to the P-wave reflection coefficient in the case of P-wave incidence. However, when there are multiple subsurface reflection interfaces, due to the influence of the interlayer multiple reflections or conversions, the imaging result of **Eq. 5** fails to indicate the reflection coefficient ratio of S-wave and P-wave accurately. Therefore, if only the up-going waves in the receiver-wavefield are used for the cross-correlation operation during the imaging process, the influence of the multiple reflections and conversions on the imaging results can be reduced, and the migration accuracy can be improved. Consequently, we modified **Eq. 5** as follows:

$$I_{PS(x,y,z)} = \frac{\sum_0^{t_{max}} 4\boldsymbol{P}_R^u(x,y,z,t)\boldsymbol{S}_R^u(x,y,z,t)}{\sum_0^{t_{max}} \left(\begin{array}{l}\boldsymbol{P}_R^u(x,y,z,t)\boldsymbol{P}_R^u(x,y,z,t) + 2\left|\boldsymbol{P}_R^u(x,y,z,t)\boldsymbol{S}_R^u(x,y,z,t)\right| \\ + \boldsymbol{S}_R^u(x,y,z,t)\boldsymbol{S}_R^u(x,y,z,t)\end{array}\right)} \tag{6}$$

where the superscript u represents the up-going wavefield of the receiver.

NUMERICAL TESTS

Two-Dimensional Marmousi2 Elastic Model

To demonstrate the effectiveness of our method, we test it with the synthetic multi-component seismic data of the partial Marmousi2 model (Martin et al., 2006). The model is of the size of 6,500 × 3,505 m with a spatial grid of $\Delta x = \Delta z = 5$ m. It was stimulated by the finite-difference method with the 100-layer PML absorbing boundaries. We generate 100 P-wave sources located at a depth of 5 m below the sea surface with a horizontal interval of 65 m using a Ricker wavelet with a dominant frequency of 35 Hz. We compute the synthetic

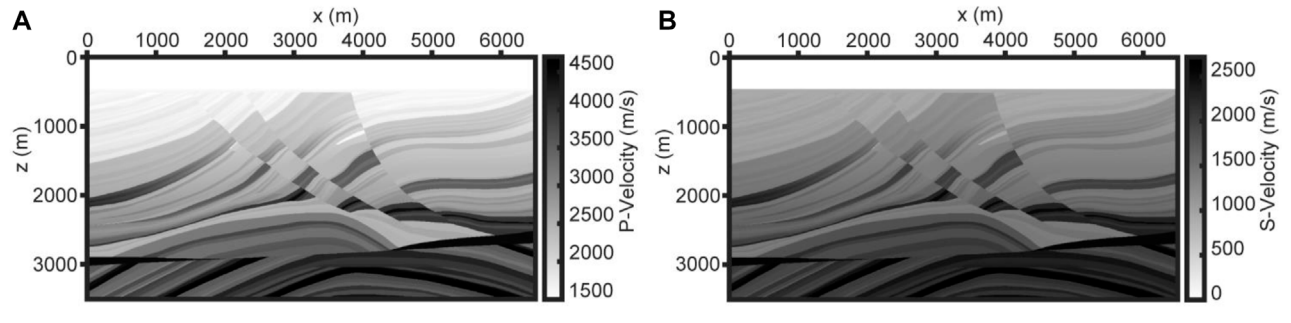

FIGURE 5 | Partial Marmousi2 velocity models of **(A)** P-wave and **(B)** S-wave.

seismogram up to 4 s length with the time-stepping interval of 0.5 ms. The receiver array is located on the seafloor at 455 m depth, with a total of 1,300 traces and an interval of 5 m. The first shot is at the coordinate of $x = 0$ m. The receiver array is fixed, and the shots roll one by one. Consequently, we can obtain the multi-component synthetic seismogram of 100 shots.

Figure 4 shows the RTM images obtained by using different equations and imaging conditions. **Figure 4A** and **Figure 4B** both use the first-order velocity-stress equations with the cross-correlation imaging condition of the source- and receiver-wavefields applied. The difference between the two is that **Figure 4B** performs wavefield separation according to the propagation directions of P- and S-wavefields before cross-correlation imaging, and then only wavefields with opposite propagation directions are involved in imaging, while **Figure 4A** allows all wavefields of the same or different propagation directions in P- or S-wavefields to be used in imaging. **Figure 4A** does not separate the directions of P-and S-wavefields, resulting in stronger low-wavenumber imaging artifacts than **Figure 4B**. The migration image of **Figure 4C** is obtained by decomposing the wavefield into the P-wavefield and S-wavefield, and separating the propagation directions of the P-wavefield and S-wavefield based on the velocity-dilatation-rotation equations, and applying the source-free imaging condition. There is no impact of source extrapolation, and the method we proposed shows a high imaging accuracy and a larger imaging range (**Figure 4C**).

Since the first-order velocity-stress elastic wave equations can only obtain the Poynting vector of the mixed wavefield, the vector can only acquire the propagation directions of the mixed wavefield, rather than that of the pure P-wave or the pure S-wave. However, the propagation directions of mixed wavefield are not consistent with that of pure P-wave or pure S-wave. Therefore, using mixed wavefield propagation directions to correct the S-wave polarity may result in incorrect polarity, lower quality of migration images, unclear structure, and destruction of the event continuity in the migration image. On the contrary, the Poynting vector of P-wave and S-wave obtained by the first-order velocity-dilatation-rotation equations can accurately represent P- and S-wave propagation directions, respectively. In turn, more accurate P-SV converted-wave migration results can be obtained.

In terms of computational efficiency, the source-free converted-wave imaging condition does not need source-wavefield extrapolation, storage, and reconstruction, which dramatically decreases the calculation cost and temporary file storage amount. Using one-shot migration of the model shown in **Figure 5** as an example, the calculation time of source-free converted-wave imaging condition is more than 2.5 times faster than that of conventional cross-correlation imaging condition under the same hardware condition.

Three-Dimensional SEG/EAEG Salt Model

We also test our method on a 3D SEG/EAEG salt model as shown in **Figure 6**. The model is of the size of 3,000 × 3,000 × 2,010 m, with the spatial grid of $\Delta x = \Delta y = \Delta z = 10$ m. The PML absorbing boundaries are set to 30 layers. The time-stepping interval is 0.35 ms. We generate P-wave sources located at 10 m depth, using the Ricker wavelet with a dominant frequency of 35 Hz. A total of seven shot lines are set up with a line interval of 400 m. Each shot line is generated from the left of the model with a shot interval of 100 m. There are 30 shots in each shot line, for a total of 210 shots. The data is recorded by 151 multi-component receiver lines located on the ground with the receiver line interval of 20 m. There are 301 traces at the group interval of 10 m on each receiver line. During the data acquisition process, the shot is moved while the receiver array remains fixed.

The converted-wave migration image that uses the imaging condition proposed in this study (**Figure 7B**) is clearer and more accurate than the vector field dot product cross-correlation (Wang and He, 2017) migration image (**Figure 7A**) in the three-dimensional case. **Figure 7B** can accurately utilize subsurface media with no obvious low-wavenumber imaging artifacts in the migration image. The interfaces in the migration image are continuous. The correct subsurface structure and the geological interface can be observed. The improvements both in the accuracy and resolution of the image further demonstrate the imaging ability of our method.

Advantage Analysis

The first-order velocity-dilatation-rotation elastic wave equations can realize the automatic decoupling of the P- and S-waves, accurately indicate the propagation directions of

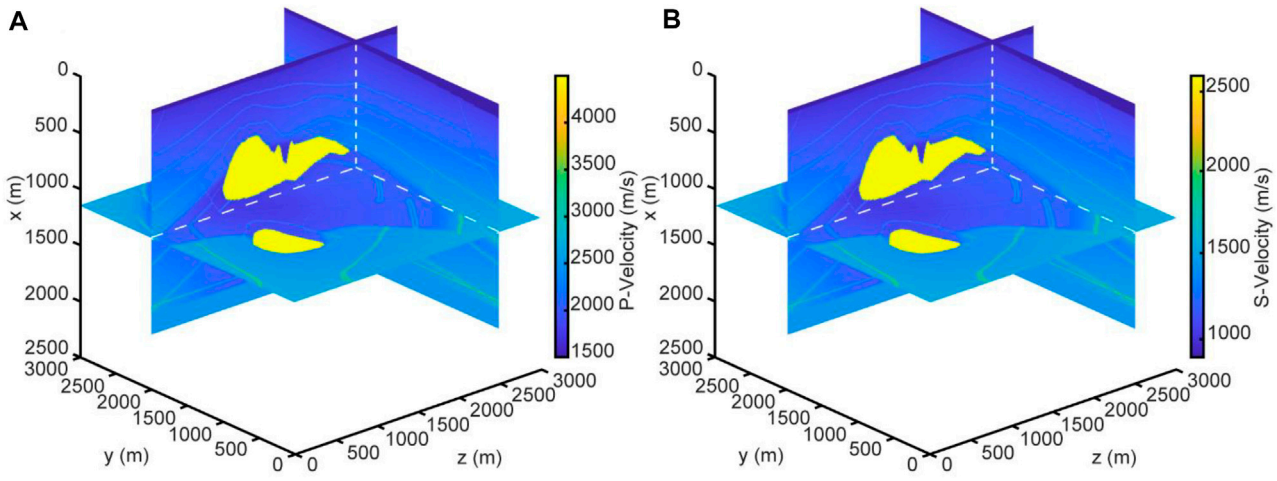

FIGURE 6 | Partial SEG/EAEG salt velocity models of **(A)** P-wave and **(B)** S-wave.

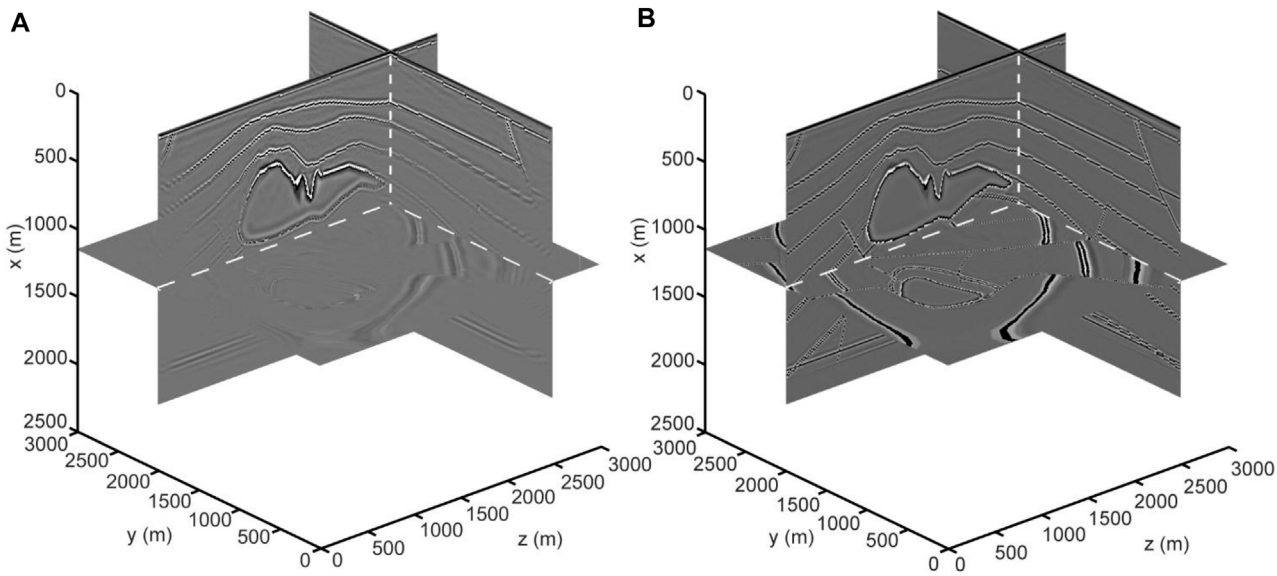

FIGURE 7 | (A) The migration image using the vector field dot product cross-correlation imaging condition by Wang and He (2017). **(B)** The migration image using the imaging condition of **Eq. 6**. Both two migration images use the first-order velocity-dilatation-rotation equations.

the P-wave and S-wave, and further suppress the low-wavenumber imaging artifacts. The migration image obtained by source-free converted-wave imaging condition shows less low-wavenumber imaging artifacts and more continuous horizons, and therefore potentially more accurate images of the subsurface.

The method proposed in this study also has obvious advantages in computing efficiency. Taking the three-dimensional SEG/EAEG salt model shown in **Figure 6** as an example, the calculation and storage cost required to migrate one-shot are shown in **Table 1**. Under the model shown in **Figure 6**, the computational cost of our method is reduced to about one-third of that of the traditional algorithm.

DISCUSSION

The converted-wave imaging method in this paper relies on an assumption: the source of multi-component exploration only excites the P-wave, while all the S-wave in multi-component recordings is converted from the P-wave. When the measured

TABLE 1 | Comparison of the migration computational efficiency of the one-shot between the velocity-stress equations and velocity-dilatation-rotation equations.

	The first-order velocity-stress elastic wave equations	The first-order velocity-dilatation-rotation elastic wave equations
Addition and subtraction	10.15918×10^{13}	3.71507×10^{13}
Multiplication and division	9.78224×10^{13}	2.79862×10^{13}

data does not meet this assumption (i.e., the excitation source excites P-wave and S-wave at the same time), it is necessary to develop a new approach to utilize the reflected S-wave and converted S-wave, and this method is no longer suitable. This algorithm also relies on the assumption that there is only one set of P-wave or S-wave at one imaging point at the same time, therefore when multiple sets of the P-wave or the S-wave are present at a certain imaging point at the same time, potential errors would be generated by our method.

The method in this paper can only be used for the P-SV converted-wave RTM, but the process of multi-component seismic data includes the imaging of both converted-wave and reflected P-wave. Therefore, the imaging results can be further improved by combining our method with the application of the acoustic RTM method for reflected P-waves.

CONCLUSION

We present a P-SV converted-wave RTM method based on the first-order velocity-dilatation-rotation elastic wave equations and the source-free imaging condition. It has the following advantages. 1) It is suitable for multi-component data imaging of both active- and passive-sources. 2) The ERTM computational cost is reduced to one-third of the conventional algorithm as it is no longer necessary to calculate, store and reconstruct the source-wavefield. 3) The first-order velocity-dilatation-rotation elastic wave equations include both a scalar P-wave parameter and a parameter for particle vibration velocity vector caused by dilatation motion. Therefore, the proposed algorithm can handle both pressure and three-component particle velocity data.

DATA AVAILABILITY STATEMENT

The raw data supporting the conclusions of this article will be made available by the authors, without undue reservation.

AUTHOR CONTRIBUTIONS

BH developed the idea for the study, BH, XY, and XS performed the research, BH and XY wrote the manuscript. The three authors are the executors of the specific work and contribute to the manuscript.

FUNDING

The research was financially supported by the National Natural Science Foundation of China (No. 41674118) and the Fundamental Research Funds for the Central Universities of China (No. 201964017).

REFERENCES

Bao, H., Li, M., and Zhang, M. (2021). Efficient Implementation of Wave-Equation Reverse Time Migration Based on Large Memory Nodes. *Geophy. Prosp. Petrol.* 60 (5), 732–737. doi:10.3969/j.issn.1000-1441.2021.05.004

Bian, D., Wang, X., Yang, W., Yang, Z., and Wang, J. (2017). 3D Converted Wave Imaging. *OGP* 52 (Suppl. 2), 91–97. doi:10.13810/j.cnki.issn.1000-7210.2017.S2.016

Biot, M. A. (1956). Theory of Propagation of Elastic Waves in a Fluid-Saturated Porous Solid. I. Low-Frequency Range. *The J. Acoust. Soc. America* 28 (2), 168–178. doi:10.1121/1.1908239

Chang, W. F., and McMechan, G. A. (1994). 3-D Elastic Prestack, Reverse-Time Depth Migration. *Geophysics* 59 (4), 597–609. doi:10.1190/1.1443620

Chattopadhyay, S., and McMechan, G. A. (2008). Imaging Conditions for Prestack Reverse-Time Migration. *Geophysics* 73 (3), S81–S89. doi:10.1190/1.2903822

Claerbout, J. F. (1971). Toward a Unified Theory of Reflector Mapping. *Geophysics* 36, 467–481. doi:10.1190/1.1440185

Clapp, R. G. (2009). "Reverse Time Migration with Random Boundaries," in *SEG Technical Program Expanded Abstracts 2009* (Houston, United States: Society of Exploration Geophysicists), 2809–2813. doi:10.1190/1.3255432

Dellinger, J., and Etgen, J. (1990). Wave-field Separation in Two-Dimensional Anisotropic media. *Geophysics* 55 (5), 914–919. doi:10.1190/1.1442906

Dong, L., Ma, Z., and Cao, J. (2000a). A Study on Stability of the Staggered-Grid High-Order Difference Method of First-Order Elastic Wave Equation. *Chin. J. Geophys.* 43 (6), 411–419. (in Chinese). doi:10.1002/cjg2.107

Dong, L., Ma, Z., Cao, J., Wang, H., Geng, J., Lei, B., et al. (2000b). A Staggered-Grid High-Order Difference Method of One-Order Elastic Wave Equation. *Chin. J. Geophys.* 43 (3), 411–419. (in Chinese). doi:10.1002/cjg2.107

Du, Q., Gong, X., Zhu, Y., Fang, G., and Zhang, Q. (2012a). "PS Wave Imaging in 3D Elastic Reverse-Time Migration," in *SEG Technical Program Expanded Abstracts 2009* (Houston, United States: Society of Exploration Geophysicists). doi:10.1190/segam2012-0107.1

Du, Q., Zhu, Y., and Ba, J. (2012b). Polarity Reversal Correction for Elastic Reverse Time Migration. *Geophysics* 77 (2), S31–S41. doi:10.1190/geo2011-0348.1

Du, Q., Gong, X., Zhang, M., Zhu, Y., and Fang, G. (2014). 3D PS-Wave Imaging with Elastic Reverse-Time Migration. *Geophysics* 79 (5), S173–S184. doi:10.1190/geo2013-0253.1

Du, Q., Gong, X., Guo, C., Zhao, Q., Wang, C., and Li, X.-y. (2017). Vector-based Elastic Reverse Time Migration Based on Scalar Imaging Condition. *Geophysics* 82 (2), S111–S127. doi:10.1190/GEO2016-0146.1

He, B., and Zhang, H. (2006). Vector Prestack Depth Migration of Multi-Component Wavefield. *OGP* 41 (4), 369–374. doi:10.3321/j.issn:1000-7210.2006.04.003

Liu, F., Zhang, G., Morton, S. A., and Leveille, J. P. (2011). An Effective Imaging Condition for Reverse-Time Migration Using Wavefield Decomposition. *Geophysics* 76 (1), S29–S39. doi:10.1190/1.3533914

Martin, G. S., Wiley, R., and Marfurt, K. J. (2006). Marmousi2: An Elastic Upgrade for Marmousi. *The Leading Edge* 25 (2), 156–166. doi:10.1190/1.2172306

Murphy, W. F., III (1982). Effects of Partial Water Saturation on Attenuation in Massilon sandstone and Vycor Porous Glass. *J. Acoust. Soc. America* 71 (6), 1458–1468. doi:10.1121/1.387843

Poynting, J. H. (1884). XV. On the Transfer of Energy in the Electromagnetic Field. *Phil. Trans. R. Soc.* 175, 343–361. doi:10.1098/rstl.1884.0016

Shabelansky, A. H., Malcolm, A. E., Fehler, M. C., Shang, X., and Rodi, W. L. (2015). Source-independent Full Wavefield Converted-phase Elastic Migration Velocity Analysis. *Geophys. J. Int.* 200 (2), 954–968. doi:10.1093/gji/ggu450

Shabelansky, A. H., Malcolm, A., and Fehler, M. (2017). Converted-wave Seismic Imaging: Amplitude-Balancing Source-independent Imaging Conditions. *Geophysics* 82 (2), S99–S109. doi:10.1190/GEO2015-0167.1

Shang, X., de Hoop, M. V., and van der Hilst, R. D. (2012). Beyond Receiver Functions: Passive Source Reverse Time Migration and Inverse Scattering of Converted Waves. *Geophys. Res. Lett.* 39 (15), L15308. doi:10.1029/2012GL052289

Shen, J. (2017). Application of Multi-Card GPU in 3D Elastic Wave Reverse-Time Migration (RTM). *Coal Geology. China* 29 (03), 65–71. doi:10.3936/j.issn.1674-1803.2017.03.14

Stewart, R. R., Gaiser, J. E., Brown, R. J., and Lawton, D. C. (2003). Converted-wave Seismic Exploration: Applications. *Geophysics* 68 (1), 40–57. doi:10.1190/1.1543193

Sun, R., McMechan, G. A., Hsiao, H. H., and Chow, J. (2004). Separating P- and S-Waves in Prestack 3D Elastic Seismograms Using Divergence and Curl. *Geophysics* 69 (1), 286–297. doi:10.1190/1.1649396

Sun, R., McMechan, G. A., Lee, C.-S., Chow, J., and Chen, C.-H. (2006). Prestack Scalar Reverse-Time Depth Migration of 3D Elastic Seismic Data. *Geophysics* 71 (5), S199–S207. doi:10.1190/1.2227519

Sun, R., and McMechan, G. A. (2001). Scalar Reverse-Time Depth Migration of Prestack Elastic Seismic Data. *Geophysics* 66 (5), 1519–1527. doi:10.1190/1.1487098

Tang, H.-G., He, B.-S., and Mou, H.-B. (2016). P- and S-Wave Energy Flux Density Vectors. *Geophysics* 81 (6), T357–T368. doi:10.1190/geo2016-0245.1

Wang, D., Xin, K., Li, Y., Gao, J., and Wu, X. (2006). An Experimental Study of Influence of Water Saturation on Velocity and Attenuation in sandstone under Stratum Conditions. *Chin. J. Geophys.* 49 (3), 908–914. (in Chinese). doi:10.1002/cjg2.896

Wang, P., and He, B. (2017). Vector Field Dot Product Cross-Correlation Imaging Based on 3D Elastic Wave Separation. *OGP* 52 (3), 477–483. doi:10.13810/j.cnki.issn.1000-7210.2017.03.009

Wang, W., and McMechan, G. A. (2015). Vector-based Elastic Reverse Time Migration. *Geophysics* 80 (6), S245–S258. doi:10.1190/GEO2014-0620.1

Whitemore, N. D. (1983). "Iterative Depth Migration by Backward Time Propagation," in *SEG Technical Program Expanded Abstracts 1983* (Houston, United States: Society of Exploration Geophysicists), 382–385. doi:10.1190/1.1893867

Wu, G., and Qin, H. (2014). Elastic Reverse Time Migration in Isotropic Medium Based on Random Boundary. *Prog. Geophys.* 29 (4), 1815–1821. (in Chinese). doi:10.6038/pg20140444

Xiao, X., and Schuster, G. T. (2009). Local Migration with Extrapolated VSP Green's Functions. *Geophysics* 74 (1), SI15–SI26. doi:10.1190/1.3026619

Xue, D. (2013). Imaging Condition of Prestack Reverse-Time Migration. *OGP* 48 (2), 222–227. doi:10.13810/j.cnki.issn.1000-7210.2013.02.018

Yan, J., and Sava, P. (2008). Isotropic Angle-Domain Elastic Reverse-Time Migration. *Geophysics* 73 (6), S229–S239. doi:10.1190/1.2981241

Yan, J., and Sava, P. (2009). Elastic Wave-Mode Separation for VTI media. *Geophysics* 74 (5), WB19–WB32. doi:10.1190/1.3184014

Yang, H., Ba, J., Tang, J., Nie, J., and Lu, M. (2006). Development of Conventional Geophysical Methods in Oil/gas Exploration. *OGP* 41 (2), 231–236. doi:10.3321/j.issn:1000-7210.2006.02.023

Yoon, K., and Marfurt, K. J. (2006). Reverse-time Migration Using the Poynting Vector. *Exploration Geophys.* 37 (1), 102–107. doi:10.1071/eg06102

Yu, F., Liu, B., Fan, J., and Li, Z. (2018). Analysis of Noise Suppression Effect of Several Angle Imaging Conditions in Reverse Time Migration. *Prog. Geophys.* 33 (1), 0297–0303. (in Chinese). doi:10.6038/pg2018BB0018

Zhang, H., Feng, X., Fu, C., Sun, H., Wang, X., and Lu, Y. (2021). Noise Suppression during Elastic Reverse Time Migration in the Dip-Angle Domain Using a Convolutional Neural Network. *Geophy. Prosp. Petrol.* 60 (3), 376–384. doi:10.3969/j.issn.1000-1441.2021.03.003

Conflict of Interest: The authors declare that the research was conducted in the absence of any commercial or financial relationships that could be construed as a potential conflict of interest.

Publisher's Note: All claims expressed in this article are solely those of the authors and do not necessarily represent those of their affiliated organizations, or those of the publisher, the editors and the reviewers. Any product that may be evaluated in this article, or claim that may be made by its manufacturer, is not guaranteed or endorsed by the publisher.

Advantages of publishing in Frontiers

OPEN ACCESS
Articles are free to read for greatest visibility and readership

FAST PUBLICATION
Around 90 days from submission to decision

HIGH QUALITY PEER-REVIEW
Rigorous, collaborative, and constructive peer-review

TRANSPARENT PEER-REVIEW
Editors and reviewers acknowledged by name on published articles

Frontiers
Avenue du Tribunal-Fédéral 34
1005 Lausanne | Switzerland

Visit us: www.frontiersin.org
Contact us: frontiersin.org/about/contact

REPRODUCIBILITY OF RESEARCH
Support open data and methods to enhance research reproducibility

DIGITAL PUBLISHING
Articles designed for optimal readership across devices

FOLLOW US
@frontiersin

IMPACT METRICS
Advanced article metrics track visibility across digital media

EXTENSIVE PROMOTION
Marketing and promotion of impactful research

LOOP RESEARCH NETWORK
Our network increases your article's readership